

ABSTRACT

STEVENS, ERIC CHRISTOPHER. From Novel Processes to Industrially Relevant Applications: Atomic Layer Deposition of Metal, Metal Oxide, and Metal Carbide Thin Films. (Under the direction of Dr. Gregory N. Parsons).

The demand for faster electronic devices with better storage capacity, all without being prohibitively expensive, requires innovations in process design and chemistry. Atomic layer deposition (ALD) is one such process which allows for thin films of material to be deposited with sub-nanometer thickness control. ALD relies on self-limiting chemical reactions, which leads to uniform, pin-hole free, and conformal coatings on substrates with complex and three-dimensional architectures.

We investigated a novel ALD process for the deposition of tin (Sn) metal using a vapor phase reducing agent and a metal halide precursor. This study marked the first thermal (i.e., without plasma) ALD process for elemental Sn, where the mechanism and growth properties as a function of temperature were studied using *in situ* methods. Sn metal films have a broad range of applications from nanowire transistors to anode materials for lithium ion batteries.

In a similar fashion, we also studied the use of a novel ALD precursor, tungsten (V) chloride, to deposit tungsten carbide (WC) thin films, using trimethyl aluminum as a co-reagent. *In situ* studies revealed key information regarding the likely reaction pathways as well as saturation behavior at different temperatures. The deposited WC films were doped with aluminum and had low Cl impurities. WC films have many applications in the semiconductor industry due to their chemical stability, hardness, and high conductivity.

We also investigated area-selective ALD of metal oxide and metal nitride materials on amorphous carbon (aC) substrates, deposited on 300 mm silicon wafers, for use in advanced patterning applications. Without any treatment to as-formed aC substrates, uninhibited ALD

growth of titanium oxide (TiO_2), hafnium oxide (HfO_2), and titanium nitride (TiN) was observed. The use of a hydrogen plasma pretreatment on aC removed oxygen species and passivated the surface with C-H groups, leading to a nucleation delay for TiO_2 , HfO_2 , and TiN . We showed that the use of water as a co-reagent in metal oxide ALD leads to significant nucleation site generation, while the ammonia co-reagent in TiN ALD resulted in enhanced selectivity.

We applied two different models to describe the nucleation behavior of metal oxide and metal nitride ALD on plasma-treated aC. The best fit of the experimental data was obtained using a modification based on the Avrami Equation, which assumed random dispersion of nucleation sites on the surface increasing at some rate. The insights gained from the model fit show that water plays a key role in the generation of new nucleation sites for metal oxide ALD. This model can be applied to other ALD processes to gain valuable information regarding the nucleation behavior as well as potential selectivity losses.

We demonstrated the use of plasma pre-treatments to selectively deactivate aC lines in a sub-50 nm aC/ Si_3N_4 line/space patterned structure on 300 mm substrates. ALD films of TiN and TiO_2 were deposited on Si_3N_4 spaces, with particle formation on aC lines. Nucleation density was observed to be greater on the tops and corners of aC lines, implying optimization in the pattern formation is needed to realize maximum selectivity. Furthermore, aC lines were selectively removed using oxygen plasma to give sub-50 nm patterned lines TiN on Si_3N_4 . Post-process cleans steps are likely to remove undesired particles which may form during ALD processing.

© Copyright 2018 by Eric Christopher Stevens

All Rights Reserved

From Novel Processes to Industry-Relevant Applications: Atomic Layer Deposition of Metal,
Metal Oxide, and Metal Carbide Thin-Films.

by
Eric Christopher Stevens

A dissertation submitted to the Graduate Faculty of
North Carolina State University
in partial fulfillment of the
requirements for the degree of
Doctor of Philosophy

Chemical Engineering

Raleigh, North Carolina

2018

APPROVED BY:

Dr. Gregory N. Parsons
Committee Chair

Dr. Michael D. Dickey

Dr. Saad Khan

Dr. Fanxing Li

DEDICATION

I dedicate this work to my incredible wife, Amy. She is my rock and the love of my life.

Without her, I would not be here today. Thank you, Amy. This is for you.

BIOGRAPHY

Eric Stevens was born and raised in Phoenix, AZ, to Chuck and Margaret Stevens. Eric attended Arizona State University (Go Devils) in Tempe, AZ, where he studied chemical engineering. Eric gained valuable research experience under the mentorship of Professor Lenore Dai, where he worked on the integration of silicon ribbons with stimuli responsive hydrogels. While at Arizona State, Eric was a teaching assistant for lower and upper division chemical engineering courses, as well as a tutor for organic chemistry. Eric decided to pursue graduate school following the completion of an internship at Pacific Northwest National Laboratory. Under the direction of Dr. Carlos Fraga, Eric designed and implemented a novel, chemical forensic technique to identify trace impurities in chemical warfare agents and establish a direct link to the respective manufacturer using two-dimensional gas chromatography/time-of-flight mass spectrometry.

In Fall 2013, Eric began his Ph.D. in chemical engineering under the direction of Professor Gregory Parsons at North Carolina State University in Raleigh, NC. Eric's research was mainly focused on development of new atomic layer deposition processes for deposition of metal and metal carbide thin films. Eric continued his studies at IMEC in Leuven, Belgium, under the mentorship of Professor Annelies Delabie. At IMEC, Eric studied the use of atomic layer deposition for advanced patterning applications relevant to the semiconductor industry. Eric will join the Research and Development team at ASM America in Phoenix, AZ, after graduation.

Outside of research, Eric enjoys hiking and camping with his wife Amy and dog Pinot "Mr. Grigio" Stevens. Eric and Amy love to travel and experiencing new cultures together. During his free time, Eric also enjoys playing guitar, wood working, and playing basketball.

ACKNOWLEDGMENTS

To my advisor Professor Gregory Parsons, thank you for your guidance and support throughout this process. You have molded me into a researcher and scientist, constantly encouraging me to find answers to challenging problems. Thank you for sticking by me through everything and helping me with a slight nudge here and a carefully crafted “...” in your emails. I am honored to be one of your students and future colleague in the ALD community.

To Professor Annelies Delabie, thank you for giving me the opportunity to conduct research at IMEC. That experience was both challenging and gezellig (did I use this in the correct context?), and one that had a profound impact on my future and for that I am extremely grateful to you and entire team at IMEC, including Yoann, BT, Efrain, Sven, and Elie. Dank u wel voor alles!

To Professor Lenore Dai, thank you for your support and guidance during my time at ASU. You helped me tremendously along the way, without you I wouldn't have likely pursued graduate school.

To Mr. Mariner, thank you for piquing my interest in chemistry and steering me towards a major in Chemical Engineering. You gave me a passion for teaching and I aim to make STEM outreach a major part of my life going forward. With regards to breaking things and setting them on fire... you also gave me that passion as well.

A special thanks to my fellow classmates and friends at NC State: Wenyi, Jenny, Mariah, Jason, Adam, Ryan, and Ishan. It has been a long journey, but we finally made it. All the long nights working on transport and perturbation theory were well worth it in the end!

To my parents, Chuck and Margaret, thank you for instilling a sense of curiosity and encouraging my success in school. Without your support and guidance, I would not be the person I am today. You've been incredible parents to me and I hope you know just how appreciative I am

of the sacrifices you made for my future. I hope to be half the person you both are in the future. Thank you and I love both you so much.

To the rest of my family, Matt, Lauren, Shawn, Gina, Daniel, Jim, and Lisa, thank you for your love and support through this, and for all the less than exciting conversations you all endured regarding my research. Although I am the youngest of the three brothers, I feel that I am the favorite. I wanted that to be in writing for future generations to know. Joking aside, your support has no bounds and for that I am grateful. Love you guys.

Lastly, to Amy. Thank you. From encouraging me during those first few discussions about pursuing graduate school, to moving across the country and starting our married life together in North Carolina, to crossing off a bucket list item as we lived, worked, and explored in Europe, and navigating through our toughest times – thank you for being my partner. Your unconditional love and support provided me with hope and a renewed vigor going into the next day. You've been my shoulder to cry on, my hand to hold, my ear to listen, and my light in the darkest times. Without you, I would have never reached this point and for that I am grateful. I cherish the moments we shared during this journey and I am ecstatic to experience the next chapter in our lives. Thank you for always making me the luckiest guy in the room. Love you, Cherish.

TABLE OF CONTENTS

LIST OF TABLES	xiii
LIST OF FIGURES	xiv
Chapter 1: Introduction and Background	1
1.1 Atomic Layer Deposition Background and Applications	2
1.2 Basic Principles of Atomic Layer Deposition	3
1.2.1 Surface Reactions in Atomic Layer Deposition	3
1.2.2 Thermodynamics of Atomic Layer Deposition	4
1.2.3 Growth Rate Versus Temperature	5
1.2.4 Nucleation and Growth Modes.....	5
1.3 Materials Deposited Using Atomic Layer Deposition	6
1.3.1 Atomic Layer Deposition of Metal Oxides.....	6
1.3.2 Atomic Layer Deposition of Metals	7
1.3.3 Atomic Layer Deposition of Metal Carbides.....	8
1.4 Area-Selective Atomic Layer Deposition	9
1.5 Figures for Chapter 1	11
1.6 References	15
Chapter 2: Thermal Atomic Layer Deposition of Sn Metal Using SnCl₄ and a Vapor Phase Silyl Dihydropyrazine Reducing Agent	27
2.1 Abstract	28
2.2 Introduction.....	29
2.3 Experimental	30
2.3.1 Reactor Setup	30

2.3.2	ALD Precursors and Delivery.....	31
2.3.3	Substrate Preparation	32
2.3.4	<i>In situ</i> Characterization.....	33
2.3.5	<i>Ex situ</i> Characterization	34
2.4	Results.....	35
2.4.1	Quartz Crystal Microbalance	35
2.4.2	Growth Rate on QCM Substrates	37
2.4.3	Film Morphology on QCM and Si Substrates	38
2.4.4	Film Composition	39
2.4.4.1	ToF-SIMS Depth Profiling	39
2.4.4.2	XPS Depth Profiling	40
2.4.5	<i>In situ</i> Reaction Monitoring by Quadrupole Mass Spectrometry	41
2.4.5.1	Characteristic Mass Fragments of Unreacted SnCl ₄ and DHP.....	41
2.4.5.2	<i>In situ</i> Reaction Analysis during SnCl ₄ /DHP Processing.....	42
2.5	Discussion.....	43
2.5.1	Proposed SnCl ₄ /DHP Reaction Mechanism	43
2.5.1.1	SnCl ₄ Adsorption	43
2.5.1.2	DHP Desilylation and Pyrazine Elimination	44
2.5.2	Growth Saturation.....	45
2.5.3	Film Composition	47
2.6	Conclusions.....	48
2.7	Acknowledgements.....	49
2.8	Figures for Chapter 2	50

2.9 Tables for Chapter 2.....	61
2.10 References	62
Chapter 3: Thermal Atomic Layer Deposition of Tungsten Carbide by WCl₆ and Trimethyl Aluminum.....	66
3.1 Abstract.....	67
3.2 Introduction.....	67
3.3 Experimental.....	68
3.3.1 ALD Reactor Setup.....	68
3.3.2 ALD Precursors and Delivery.....	69
3.3.3 Substrate Preparation and <i>in situ</i> QCM	69
3.3.4 <i>Ex situ</i> Characterization	70
3.4 Results.....	71
3.4.1 Temperature Dependence and on Film Growth by QCM.....	71
3.4.2 Dose Saturation.....	72
3.4.3 Growth Rate from QCM.....	73
3.4.4 Film Composition	74
3.4.5 Thermodynamic Modeling.....	76
3.5 Discussion.....	76
3.6 Conclusions.....	79
3.7 Acknowledgements.....	80
3.8 Figures for Chapter 3	81
3.9 Tables for Chapter 3.....	90
3.10 References	93

Chapter 4: Growth Inhibition of TiN, TiO₂, and HfO₂ on Plasma-Treated Amorphous

Carbon by Area-Selective Atomic Layer Deposition	97
4.1 Abstract.....	98
4.2 Introduction.....	99
4.3 Experimental.....	101
4.3.1 Substrate Preparation, Plasma and ALD Processing	101
4.3.2 Characterization	102
4.4 Results and Discussion	103
4.4.1 ALD on Untreated aC Substrates.....	103
4.4.2 aC Surface Composition and Modification Using Plasma Exposures.....	104
4.4.3 Optimization of H ₂ Plasma Conditions	106
4.4.4 Nucleation and Growth of TiO ₂ , HfO ₂ , and TiN ALD on Plasma-Treated aC and Si ₃ N ₄ Substrates	108
4.4.5 Selectivity Loss of Plasma-Treated Carbon.....	111
4.5 Conclusions.....	112
4.6 Acknowledgements.....	113
4.7 Figures for Chapter 4	114
4.8 Tables for Chapter 4.....	123
4.9 References.....	125

Chapter 5: Modeling the Nucleation of TiO₂, HfO₂ and TiN Atomic Layer Deposition

on Plasma-Treated Amorphous Carbon	129
5.1 Abstract.....	130
5.2 Introduction.....	131

5.3 Experimental	132
5.3.1 aC Substrate Preparation	132
5.3.2 Atomic Layer Deposition and H ₂ Plasma Processing	132
5.3.3 Characterization	133
5.3.4 Models	134
5.3.4.1 Island Growth Model	134
5.3.4.2 Modified Island Growth Model - Avrami Equation	135
5.4 Results and Discussion	137
5.4.1 Particle Analysis from SEM	137
5.4.2 Island Growth Model	139
5.4.3 Modified Island Growth Model - Avrami Equation	141
5.5 Conclusions	144
5.6 Acknowledgements	144
5.7 Figures for Chapter 5	145
5.8 Tables for Chapter 5	160
5.9 References	162

Chapter 6: Area-Selective Atomic Layer Deposition of TiN and TiO₂ in Sub-50 nm

aC/Si₃N₄ Patterns for Advanced Patterning Applications	165
6.1 Abstract	166
6.2 Introduction	166
6.3 Experimental	168
6.3.1 Materials, Plasma, and ALD Processing	168
6.3.2 Sub-50 nm Pattern Formation	169

6.3.3	Characterization	170
6.4	Results and Discussion	170
6.4.1	Formation and Plasma Treatment Processing of Sub-50 nm aC/Si ₃ N ₄ Patterned Structures	170
6.4.2	TiO ₂ and TiN ALD for Bottom-Up Fill in Sub-50nm aC/Si ₃ N ₄ Patterned Structures	172
6.4.2.1	Film Thickness and Growth Per Cycle	172
6.4.2.2	Angle-Resolved XPS to Assess Selectivity	173
6.4.2.3	Nucleation Differences for Pattern vs. Blanket Substrates	174
6.4.2.4	Tone Reversal by Selective aC Removal	174
6.5	Conclusions	175
6.6	Acknowledgements	176
6.7	Figures for Chapter 6	177
6.8	Tables for Chapter 6	185
6.9	References	186
	Appendices	190
	Appendix A1: Thermal Chemical Vapor Etch Selectivity of TiO₂ versus Al₂O₃ Using Vapor Phase WCl₅	191
A1.1	Experimental	192
A1.1.1	ALD Precursors and Delivery	192
A1.1.2	<i>In situ</i> QCM	193
A1.2	Results and Discussion	193
A1.3	Figures for Appendix A1	197

A1.4 References	202
Appendix A2: <i>In Situ</i> Study of Titanium Carbide by Thermal ALD	203
A2.1 Experimental	204
A2.1.1 ALD Precursors and Delivery	204
A2.1.2 <i>In situ</i> QCM	205
A2.2 Results and Discussion.....	205
A2.3 Figures for Appendix A2	209
A2.4 References	215

LIST OF TABLES

Table 2.1	Film Impurity Content from XPS Analysis vs. Deposition Temperature.	61
Table 3.1	GPC from Average Mass Change during WCl_5/TMA for $\rho(\alpha-WC)=15.6 \text{ g/cm}^3$...	90
Table 3.2	GPC from Average Mass Change during WCl_5/TMA for $\rho(\alpha-W_2C)=16.6 \text{ g/cm}^3$...	91
Table 3.3	Mass Ratio vs. WCl_5/TMA Reaction Pathway.....	92
Table 4.1	TiO_2 , HfO_2 , and TiN Bulk Film Properties.	123
Table 4.2	C 1s Peak Deconvolution for Plasma Treated aC.	124
Table 5.1	Island Growth Model Parameters for TiO_2 , HfO_2 , and TiN ALD.....	160
Table 5.2	Modified Island Growth Model Parameters for TiO_2 , HfO_2 , and TiN ALD.....	161
Table 6.1	Dimensions for Untreated and Plasma-Treated aC/ Si_3N_4 Patterns	185

LIST OF FIGURES

- Figure 1.1 Schematic of Al_2O_3 by ALD using $\text{Al}(\text{CH}_3)_3$ and H_2O precursors. Exposure of a reactive substrate (-OH groups) to $\text{Al}(\text{CH}_3)_3$ will result in a complete reaction of all available surface sites, giving off CH_4 byproducts and forming Al-O bonds. After purging excess reactant and byproducts using inert gas, H_2O can be exposed to the newly terminated surface ($\text{Al}-\text{CH}_3$), releasing CH_4 byproducts. Following another purge step, this process can be repeated in a cyclic manner until the desired film thickness is reached..... 11
- Figure 1.2 Quantum chemical calculations of the anticipated reaction pathways and associated energetics during the reaction of $\text{Al}(\text{CH}_3)_3 + \text{H}_2\text{O}$. a) shows the first half-reaction of gas-phase $\text{Al}(\text{CH}_3)_3$ reacting with $\text{Al}-\text{OH}^*$ surface sites. b) shows the second half-reaction of gas-phase H_2O with $\text{Al}-\text{CH}_3^*$ surface sites. Figure reproduced from Ref 54 12
- Figure 1.3 Growth rate as a function of deposition temperature for ALD processing. For most ALD processes, there exists an ALD window, which is a range of temperatures where the film growth rate is constant. Outside of this window, the growth can vary depending on the temperature and specific reaction chemistry..... 13
- Figure 1.4 Schematic of the three growth modes typically observed during ALD: a) layer-by-layer (Frank-van der Merwe), b) island (Volmer-Weber), and c) layer-plus-island (Stranski-Krastanov) growth..... 14
- Figure 2.1 Homemade, hot wall ALD reactor with direct-port and charge cell precursor delivery. N_2 carrier and purge gas was used, with an operating pressure of 1.5 Torr. *In situ* QCM and QMS capabilities were used to monitor the mass uptake and reaction byproducts, respectively, during ALD processing..... 50
- Figure 2.2 Mass change, measured by QCM, as a function of deposition time during $\text{SnCl}_4/\text{N}_2/\text{DHP}/\text{N}_2$ (2s/40s/2s/40s) processing at a) 130 °C for 650 cycles and b) 170 °C for 500 cycles. Depositions were carried out on as-received Au-coated QCM crystals. Inset graphs show 3 cycles of $\text{SnCl}_4/\text{N}_2/\text{DHP}/\text{N}_2$ within linear mass uptake regions, with solid arrows indicating SnCl_4 and DHP dosing. 51

- Figure 2.3 a) Mass change vs. deposition time, obtained by *in situ* QCM, during multiple consecutive SnCl₄/DHP exposures as a function of the deposition temperature, 150 (top, black line) and 210 °C (bottom, red line). b) Magnified region from a) to show sub-dose behavior. Solid arrows indicate the instance of 2 second SnCl₄ and DHP doses, separated by 100 and 200 second N₂ purges for depositions carried out at 150 and 210 °C, respectively..... 52
- Figure 2.4 Mass change, obtained by QCM, showing the average mass uptake per cycle obtained during SnCl₄/DHP depositions at 130, 150, 170, 190, 210 °C. The reported mass change is an average of the values obtained with saturated consecutive exposures, at a given temperature..... 53
- Figure 2.5 Top-down SEM images of a) as-received Au-coated QCM crystal, b) 1000 cycles of SnCl₄/DHP deposited at 150 °C on Au-coated QCM crystal, c) 1000 cycles of SnCl₄/DHP deposited at 190 °C on Au-coated QCM crystal. Scale bars 2 μm..... 54
- Figure 2.6 a) Cross-sectional SEM image of the Si-H/Sn/TiN/TiO₂ sample deposited at 190 °C (1500 cycles SnCl₄/DHP, 1300 cycles TDMAT/NH₃, 1500 cycles TTiP/TiCl₄) and cut using a Focused Ion Beam. The platinum bar was used to protective the area of interest during ion milling. Sn films show good thickness uniformity over the micron length scales. b) Magnified SEM image of a). The average thickness of the Sn layer was 41 ± 1 nm and the total capping layer thickness was 129 ± 2 nm..... 55
- Figure 2.7 a) ToF-SIMS results of the Si-H/Sn/TiN/TiO₂ sample used for FIB SEM. Layers were labeled and color coded as follows: “Capping Layer TiO₂ and TiN” – yellow, “Sn” – grey, “Si” – purple. The ions tracked for the capping layer were TiO₂⁻ (orange), O₂⁻ (red), ³⁷Cl⁻ (teal), and CN⁻ (pink). The Sn⁻ (grey), SiO₂⁻ (green), and SnO₂⁻ (blue) were used to identify the Sn region. b) O, C, N, and Cl impurities within the Sn region... .. 56
- Figure 2.8 a) XPS survey scans of the Si-H/Sn/TiN/TiO₂ stack deposited at 190°C, with offset spectra for visual clarity. Each line represents the resulting survey scan of the same sample after 20 – 159 minutes Ar sputtering. After roughly 120

minutes of sputtering (red line), the Sn 3d peaks between 500 - 480 eV start to increase in intensity. A maximum in the Sn 3d peak intensity most likely occurs between 125 – 159 minutes of sputtering. After 159 minutes of sputtering, the Sn 3d peak intensity decreases accompanied with a rise Si 2p peak intensity, indicative of the underlying Si substrate. b) High resolution scans of the Sn 3d 5/2 region showing Sn-Sn (485 eV) and Sn-O (486.7 eV) chemical bonds as a function of Ar sputter time of the same samples in a). Spectra offset for visual clarity..... 57

Figure 2.9 Analog mass spectrometry scans from direct sampling of each individual charge cell (maintained at 120 °C), and thus the unreacted SnCl₄ and DHP species. a) SnCl₄ mass fragmentation patterns for 50 consecutive doses, separated by N₂ purges. Most prominent peak observed at m/z = 224, with predicted structure of the SnCl₄ mass fragment shown. b) DHP mass fragmentation patterns for 50 consecutive doses, separated by N₂ purges. Most prominent peak observed at m/z = 146, with predicted structure of the DHP mass fragment shown..... 58

Figure 2.10 QMS data during SnCl₄/DHP processing at 190 °C on Si substrates for 5 sub-doses of SnCl₄ followed by 5 sub-doses of DHP, separated by N₂ purges. Most prominent mass fragments a) m/z 224 (black) and b) 146 (green) shown with their respective predicted structures. c) SnCl₄/DHP dosing sequence corresponding to the QMS data in a) and b)..... 59

Figure 2.11 Proposed reaction mechanism between DHP and two surface-bound SnCl_x species. 1) SnCl₄ exposure and subsequent densification gives a Sn–Cl surface. 2) DHP is exposed to the Sn–Cl surface, breaking Si–N bonds on the DHP to give off TMS–Cl byproducts. 3) Intermediate ring structure which can donate electrons to create a Sn-Sn bond and eliminate pyrazine. 4) One Sn–Sn bond formed per DHP molecule..... 60

Figure 3.1 QCM results showing the mass change (ng/cm²) versus process time (minutes) for a) 100 cycles of WCl₅/N₂/TMA/N₂, with dose times 1s/30s/1s/30s, at 150 °C and b) 50 cycles [WCl₅/N₂]₅/[TMA/N₂]₅, with dose times [1s/30s]₅/[1s/30s]₅, at 150 °C. c) and d) are magnified images of a) and b),

respectively, showing 3 cycles, with WCl_5 and TMA doses indicated with arrows.	81
Figure 3.2 QCM results showing the mass change (ng/cm^2) versus process time (minutes) for a) 100 cycles of $WCl_5/N_2/TMA/N_2$, with dose times 1s/30s/1s/30s, at 300 °C and b) 100 cycles $[WCl_5/N_2] \times 5/[TMA/N_2] \times 5$, with dose times $[1s/30s] \times 5/[1s/30s] \times 5$, at 300 °C. c) and d) are magnified images of a) and b), respectively, showing 3 cycles, with WCl_5 and TMA doses indicated with arrows	82
Figure 3.3 Average mass change per cycle ($ng/cm^2/cycle$), obtained from QCM results, versus deposition temperatures 150, 200, 250, 300, and 325 °C for $WCl_5/N_2/TMA/N_2$ (black squares) and $[WCl_5/N_2] \times 5/[TMA/N_2] \times 5$ (red circles). ...	83
Figure 3.4 WCl_5/TMA ratio (y-axis) of the averaged mass change obtained by QCM during WCl_5 and TMA cycling. The number of WCl_5 (1, 3, 5 on x-axis) and TMA (1–black squares, 3–red circles, 5–blue triangles) sub-doses were varied for deposition temperatures of a) 150 °C, b) 200 °C, c) 250 °C, d) 300 °C, and e) 325 °C	84
Figure 3.5 Elemental depth profile, obtained using XPS with Ar sputtering, for a) 200 cycles of $[WCl_5/N_2] \times 2/[TMA/N_2] \times 2$ at 200 °C and b) 400 cycles of $[WCl_5/N_2] \times 2/[TMA/N_2] \times 2$ at 300 °C deposited on Si with native oxide. Species shown, with units of atomic percent, are: W (blue triangles), O (black squares), C (red circles), Al (pink upside-down triangles), Cl (green diamonds), and Si (navy blue left-triangles)	85
Figure 3.6 High resolution scans of the W 4f region, obtained using XPS with Ar sputtering (representative sputtering times indicated above each designated line), for a) 200 cycles of $[WCl_5/N_2] \times 2/[TMA/N_2] \times 2$ at 200 °C, and b) 400 cycles of $[WCl_5/N_2] \times 2/[TMA/N_2] \times 2$ at 300 °C deposited on Si with native oxide. Raw spectra offset for visual clarity. Expected peaks for WO_3 doublet at ~36 and 38 eV and WC_x doublet at ~32 and 34 eV are indicated above raw spectra.....	86

- Figure 3.7 High resolution scans of the C 1s region, obtained using XPS with Ar sputtering (representative sputtering times indicated above each designated line), for a) 200 cycles of $[\text{WCl}_5/\text{N}_2] \times 2 / [\text{TMA}/\text{N}_2] \times 2$ at 200 °C, and b) 400 cycles of $[\text{WCl}_5/\text{N}_2] \times 2 / [\text{TMA}/\text{N}_2] \times 2$ at 300 °C deposited on Si with native oxide. Raw spectra offset for visual clarity. Expected peaks for C–C, W–C, and Al–C bonding at ~284., ~283.5, and 282.2 eV, respectively, are indicated above raw spectra..... 87
- Figure 3.8 High resolution scans of the Al 2p region, obtained using XPS with Ar sputtering (representative sputtering times indicated above each designated line), for a) 200 cycles of $[\text{WCl}_5/\text{N}_2] \times 2 / [\text{TMA}/\text{N}_2] \times 2$ at 200 °C, and b) 400 cycles of $[\text{WCl}_5/\text{N}_2] \times 2 / [\text{TMA}/\text{N}_2] \times 2$ at 300 °C deposited on Si with native oxide. Raw spectra offset for visual clarity. Expected peaks for Al–O and Al–C bonding at ~75 and ~73.5 eV, respectively, are indicated above raw spectra..... 88
- Figure 3.9 Predicted equilibrium species from the gas phase reaction of 1 mole of WCl_5 and 1.5 moles of $\text{Al}(\text{CH}_3)_3$ from temperatures ranging 25 – 400 °C and pressure of 2 mbar. Only species with an equilibrium concentration greater than 1 mmol are shown. The following are the species expected at equilibrium, with their anticipated phase indicated as either (g) for gas or (s) for solid, $\text{CH}_4(\text{g})$ (black), $\text{AlCl}_3(\text{g})$ (red), $\text{WC}(\text{s})$ (blue), $\text{AlCl}_3(\text{s})$ (pink), Al_2Cl_6 (green), and $\text{HCl}(\text{g})$ (orange)..... 89
- Figure 4.1 Ti and Hf content, measured by RBS, for TiO_2 (blue circles), HfO_2 (red triangles), and TiN (black squares) ALD films deposited on untreated aC (closed shapes) and Si_3N_4 (open shapes) versus the number of ALD cycles..... 114
- Figure 4.2 Oxygen concentration determined by XPS depth profiling of 100 nm aC films deposited on Si wafers. Untreated aC sample (green upside-down triangles) represents as-deposited films with no plasma processing. aC films were treated with hydrogen plasma for 100W 50s (black triangles), 200W 50s (red diamonds), and 400W 50s (blue circles) 115
- Figure 4.3 High resolution XPS scans of the C 1s region for untreated aC (black line), 400W 50s plasma treated aC with 20 minutes air exposure after processing (red

line), and the same 400W 50s treated aC sample measured after 1 week of air exposure. C–C, C–O, and C=O bonding types can be ascribed to peak energies of 284 – 285, 286, and 288 eV, respectively. C–C sp^2 and sp^3 bonding hybridization was indicated at 284 and 285 eV, respectively. 116

Figure 4.4 a) Resulting content of Ti (by RBS) on aC substrates for 50 (orange square), 100 (black triangles), 200 (red diamonds), and 400W (blue circles) plasma power for 10, 50, and 100s exposure times followed by 30 cycles of TiO₂ ALD at 250°C. A 0W (green triangle) treatment represents untreated aC when no plasma was used, thus serving as the control sample. The RBS detection limit for Ti was determined to be $\sim 8 \times 10^{13}$ at/cm² for the tool..... 117

Figure 4.5 Ti or Hf content from RBS, in units of atoms/cm², obtained after ALD growth on untreated aC (black squares), plasma-treated Si₃N₄ (blue triangles), and plasma-treated aC (red circles) substrates for a) TiO₂ by Ti(OCH₃)₄/H₂O at 250°C b) HfO₂ by HfCl₄/H₂O at 300°C c) TiN by TiCl₄/NH₃ at 390°C..... 118

Figure 4.6 Top-down SEM images obtained for ALD a) TiO₂, b) HfO₂, c) TiN films for various numbers of cycles after plasma treatment on aC blanket substrates. All scale bars are 100 nm 119

Figure 4.7 a) Particle density (1/cm²) and b) nuclei areal surface coverage (from SEM image analysis) as a function of the amount of material deposited (obtained from RBS measurements) for HfO₂ (red squares), TiO₂ (black squares), and TiN (blue triangles) on 400W 20s H₂ plasma-treated aC. The corresponding number of cycles for the particle density and areal coverage of TiO₂ and HfO₂, from left to right, are 20, 30, 60, 90, 120, and 200 cycles. Similarly, the corresponding number of cycles for TiN, from left to right, are 200, 320, 480, 640 cycles..... 120

Figure 4.8 Top down SEM images of plasma-treated aC blanket substrates with a) 0, b) 1, c) 10, and d) 20 2s H₂O exposures (with 4s Ar purges) at 250°C followed by 150 cycles of TiN ALD. Scale bars 100 nm..... 121

Figure 4.9 a) Particle density (1/cm²) and b) nuclei areal surface coverage as a function of the amount of material deposited (obtained from RBS measurements) on 400W

20s H ₂ plasma-treated aC. Plasma treated aC substrates subjected to 1, 10, and 20 H ₂ O water exposures (2s dose, 4s Ar purge) followed by 150 cycles of TiN ALD (open blue triangles). Plasma-treated aC substrates not subjected to H ₂ O, with 200 and 320 cy TiN ALD are also given for reference (closed blue triangles)	122
Figure 5.1 Top down SEM images of TiO ₂ particles on plasma-treated aC substrates subjected to a) 30, b) 60, c) 90, d) 120, and e) 200 cycles of Ti(OCH ₃) ₄ + H ₂ O at 250 °C. Included under each SEM image are overlaid particle outlines (shown in green) generated from particle analysis in ImageJ. All scale bars are 50 nm	145
Figure 5.2 Top down SEM images of HfO ₂ particles on plasma-treated aC substrates subjected to a) 30, b) 60, c) 90, d) 120, and e) 200 cycles of HfCl ₄ + H ₂ O at 300 °C. Included under each SEM image are overlaid particle outlines (shown in green) generated from particle analysis in ImageJ. All scale bars are 50 nm.	146
Figure 5.3 Top down SEM images of TiN particles on plasma-treated aC substrates subjected to a) 200, b) 320, c) 480, and d) 640 cycles of TiCl ₄ + NH ₃ at 390 °C. Included under each SEM image are overlaid particle outlines (shown in green) generated from particle analysis in ImageJ. All scale bars are 50 nm	147
Figure 5.4 Areal surface coverage of identified a) TiO ₂ and HfO ₂ , and b) TiN particles from top-down SEM images in Figures 5.1 (TiO ₂), 5.2 (HfO ₂), and 5.3 (TiN).....	148
Figure 5.5 TiO ₂ particle size distributions, calculated using ImageJ, given as particle count versus radius on plasma-treated aC substrates for 30 (black), 60 (red), 90 (blue), and 120 (green) cycles of Ti(OCH ₃) ₄ + H ₂ O at 250 °C. Total particle counts were normalized over an area of 1 cm ² . The theoretical particle radius (r _n [*]), indicated using a vertical line at the expected radius, was estimated assuming a growth per cycle of 0.043 nm/cy (from spectroscopic ellipsometry measurements).....	149
Figure 5.6 HfO ₂ particle size distributions, calculated using ImageJ, given as particle count versus radius on plasma-treated aC substrates for 30 (black), 60 (red), 90 (blue), and 120 (green) cycles of HfCl ₄ + H ₂ O at 300 °C. Total particle counts were	

normalized over an area of 1 cm^2 . The theoretical particle radius (r_n^*), indicated using a vertical line at the expected radius, was estimated assuming a growth per cycle of 0.05 nm/cy (from spectroscopic ellipsometry measurements). 150

Figure 5.7 TiN particle size distributions, calculated using ImageJ, given as particle count versus radius on plasma-treated aC substrates for 200 (black), 320 (red), 480 (blue), and 640 (green) cycles of $\text{TiCl}_4 + \text{NH}_3$ at $390 \text{ }^\circ\text{C}$. Total particle counts were normalized over an area of 1 cm^2 . The theoretical particle radius (r_n^*), indicated using a vertical line at the expected radius, was estimated assuming a growth per cycle of 0.031 nm/cy (from spectroscopic ellipsometry measurements). 151

Figure 5.8 TiO_2 island surface fraction as a function of ALD cycling on plasma-treated aC. Black squares are areal coverage of TiO_2 islands calculated from SEM images in Figure 5.1, while the dotted and dashed lines correspond to the resulting fit using the Island Growth Model with layer closure parameter, n_c , equal to 150 and 180 cycles, respectively. 152

Figure 5.9 HfO_2 island surface fraction as a function of ALD cycling on plasma-treated aC. Black circles are data points from areal coverage of HfO_2 islands calculated from SEM images in Figure 5.2, while the dotted, dot-dashed, and dashed lines correspond to the resulting fit using the Island Growth Model with layer closure parameter, n_c , equal to 100, 120, and 150 cycles, respectively 153

Figure 5.10 TiN island surface fraction as a function of ALD cycling on plasma-treated aC. Black triangles are data points from areal coverage of TiN islands calculated from SEM images in Figure 5.3, while the dotted, dot-dashed, and dashed lines correspond to the resulting fit using the Island Growth Model with layer closure parameter, n_c , equal to 800, 1000, and 1300 cycles, respectively. 154

Figure 5.11 TiN island surface fraction as a function of ALD cycling on plasma-treated aC. Black triangles indicate data points from experiment, while the short-dashed, dotted, and dashed lines correspond to the resulting fit using the Avrami Equation assuming constant initial nucleation density, N_0 , equal to 1×10^{-4} ,

<p>1×10^{-3}, and $2 \times 10^{-3} \text{ nm}^{-2}$, respectively. For the model fits shown, the rate of nucleation generation parameter, \dot{N}, was set to zero.....</p>	155
<p>Figure 5.12 TiN island surface fraction as a function of ALD cycling on plasma-treated aC. Black triangles indicate data points from experiment, while the dotted and dashed lines correspond to the resulting fit using the Avrami Equation with nucleation functions given by N_1 and N_2, respectively.....</p>	156
<p>Figure 5.13 TiO₂ island surface fraction as a function of ALD cycling on plasma-treated aC. Black squares indicate data points from experiment, while the dotted and dot-dashed lines correspond to the resulting fit using the Avrami Equation with nucleation functions given by N_1 and N_2, respectively.....</p>	157
<p>Figure 5.14 HfO₂ island surface fraction as a function of ALD cycling on plasma-treated aC. Black circles indicate data points from experiment, while the dotted and dashed lines correspond to the resulting fit using the Avrami Equation with nucleation functions given by N_1 and N_2, respectively</p>	158
<p>Figure 5.15 a) HfO₂ surface fraction data (black circles) with best fit using the Avrami modification (dot-dashed line) with $N_0 = 2.5 \times 10^{-2} \text{ nm}^{-2}$. Also shown is the fit calculated from the Island Growth Model (dotted line) using $N_0 = 2.5 \times 10^{-2} \text{ nm}^{-2}$. b) HfO₂ surface fraction data (black circles) with best fit using Island Growth Model (dotted line) with $N_0 = 5.8 \times 10^{-3} \text{ nm}^{-2}$. Also shown is the fit calculated from the Avrami modification using $N_0 = 5.8 \times 10^{-3} \text{ nm}^{-2}$.....</p>	159
<p>Figure 6.1 Schematic showing the steps involved in formation of aC/Si₃N₄ line/space patterns (Steps 1 – 4), where APF is an aC film. Steps 5 – 7 show the patterns after plasma, ALD, and APF strip processing, respectively.....</p>	177
<p>Figure 6.2 30° tilt and cross-sectional SEM images of aC/Si₃N₄ patterned substrates after lithography and etch steps followed by a) no treatment, b) 400W 20s H₂ plasma, and c) 400W 50s H₂ plasma. Target pattern dimensions were aC line width of 45 nm, height of 75 nm, and Si₃N₄ trench width of 45 nm. All scale bars 100 nm</p>	178

Figure 6.3 TEM images of aC/Si ₃ N ₄ patterns subjected to 400W 20s H ₂ plasma treatments at 300 °C followed by a) 30 cycles and b) 75 cycles of Ti(OCH ₃) ₄ + H ₂ O (ALD TiO ₂) at 250 °C	179
Figure 6.4 TEM images of the aC/Si ₃ N ₄ patterns subjected to 400W 20s H ₂ plasma at 300 °C followed by a) 200 cycles, b) 320 cycles, and 480 cycles of TiCl ₄ + NH ₃ (ALD TiN) at 390 °C.....	180
Figure 6.5 TiN thickness, measured from cross-sectional TEM images on Si ₃ N ₄ spaces (red circles) and aC lines (blue triangles) in aC/Si ₃ N ₄ line/space patterns subjected to 400W 20s plasma and 200, 320, and 480 cycles of TiCl ₄ /NH ₃ at 390 °C. Also shown is TiN thickness obtained by spectroscopic ellipsometry on Si ₃ N ₄ blanket substrates (black squares)	181
Figure 6.6 a) Schematic showing aC/Si ₃ N ₄ line/space patterns oriented such that the photoelectrons generated during X-ray exposure are collected perpendicular to aC lines. Angle resolved XPS was utilized, with photoelectron collection angles $22^\circ \leq \theta \leq 78^\circ$. For $\theta > \theta^*$, photoelectrons generated from Si ₃ N ₄ spaces need to travel through adjacent aC lines. b) Resulting Ti at.%, with XPS detector perpendicular to aC lines, from plasma-treated aC/Si ₃ N ₄ line/space patterns subjected to 96 (black squares), 200 (blue triangles), 320 (green diamonds), and 480 (red circles) cycles of TiCl ₄ /NH ₃ at 390 °C. θ^* indicated at $\sim 35^\circ$ based on pattern geometry	182
Figure 6.7 Top-down SEM images of 400W 20s H ₂ plasma-treated a) aC/Si ₃ N ₄ (tops of aC lines shown in image) patterned substrate followed by 320 cycles of TiN ALD, b) aC blanket substrate followed by 320 cycles of TiN ALD, and c) aC blanket substrate followed by 480 cycles of TiN ALD. All scale bars 50 nm.....	183
Figure 6.8 Tilted and cross-sectional SEM images of aC/Si ₃ N ₄ substrates subjected 400W 20s H ₂ plasma exposure, a) 320 and b) 480 cycles of TiN ALD, and 60 seconds O ₂ plasma. Resulting structures are TiN patterned on Si ₃ N ₄ with TiN particle contamination remaining in aC vacancies.....	184

Figure A1.1 Predicted equilibrium species from the reaction of 2 moles of $\text{WCl}_5(\text{g})$ and 1 moles of $\text{TiO}_2(\text{s})$ from temperatures ranging 25 – 500 °C and pressure of 2 mbar. Only species with an equilibrium concentration greater than 1 mmol are shown. The following are the species expected at equilibrium, with their anticipated phase indicated as either (g) for gas or (s) for solid, $\text{WOCl}_3(\text{s})$ (black), $\text{WOCl}_3(\text{g})$ (red), $\text{TiCl}_4(\text{g})$ (blue), $\text{WOCl}_4(\text{g})$ (green), and $\text{WOCl}_2(\text{g})$ (brown)..... 197

Figure A1.2 a) After 100 cycles of $\text{TiCl}_4 + \text{H}_2\text{O}$ at 300 °C, 10 consecutive, 1 second doses of WCl_5 , separated by 30 second purges. Linear etch rate of -40 $\text{ng}/\text{cm}^2/\text{cy}$. b) same as from Figure A1.1 but with vertical line indicating the etch temperature in a)..... 198

Figure A1.3 a) After 100 cycles of $\text{TiCl}_4 + \text{H}_2\text{O}$ at 250 °C, 10 consecutive, 1 second doses of WCl_5 , separated by 30 second purges. Linear etch rate of -25 $\text{ng}/\text{cm}^2/\text{cy}$, with a decrease in etch rate to 10 $\text{ng}/\text{cm}^2/\text{cy}$ for the 9th and 10th dose. 25 minutes of N_2 purging, then 10 consecutive, 1 second doses of WCl_5 , separated by 30 second purges. b) same as from Figure A1.1 but with vertical line indicating the etch temperature in a)..... 199

Figure A1.4 100 cycles of $\text{Al}(\text{CH}_3)_3 + \text{H}_2\text{O}$ (black) and $\text{TiCl}_4 + \text{H}_2\text{O}$ (red) at 300 °C deposited on Au-coated QCM substrates followed by 30 and 50 consecutive, 1 second doses of WCl_5 , separated by 30 second N_2 purges, respectively 200

Figure A1.5 Magnified etching regions from Figure A1.4. a) 100 cycles of $\text{Al}(\text{CH}_3)_3 + \text{H}_2\text{O}$ followed by 30 consecutive, 1 second doses of WCl_5 , separated by 30 second N_2 purges. b) $\text{TiCl}_4 + \text{H}_2\text{O}$ (red) at 300 °C followed by 50 consecutive, 1 second doses of WCl_5 , separated by 30 second N_2 purges 201

Figure A2.1 Predicted equilibrium species from the reaction of 1 mole of $\text{TiCl}_4(\text{g})$ and 1 mole of $\text{Al}(\text{CH}_3)_3(\text{g})$ from temperatures ranging 25 – 400 °C and pressure of 2 mbar. Only species with an equilibrium concentration greater than 1 mmol are shown. The following are the species expected at equilibrium, with their anticipated phase indicated as either (g) for gas or (s) for solid: $\text{CH}_4(\text{s})$ (black), $\text{TiC}(\text{s})$ (red), $\text{AlCl}_3(\text{g})$ (pink), $\text{AlCl}_3(\text{s})$ (green), and $\text{Al}_2\text{Cl}_6(\text{g})$ (blue)..... 209

Figure A2.2 QCM results showing the mass change (ng/cm^2) versus process time (minutes) for 200 cycles of $\text{TiCl}_4/\text{N}_2/\text{TMA}/\text{N}_2$, with dose times 1s/30s/1s/30s, at 350 °C (black), 300 °C (blue), and 250 °C (red). For each temperature, the average mass change per cycle is given above the corresponding curve in units of $\text{ng}/\text{cm}^2/\text{cy}$... 210

Figure A2.3 QCM results showing the magnified mass change (ng/cm^2) versus process time (minutes) from Figure A2.2 for 200 cycles of $\text{TiCl}_4/\text{N}_2/\text{TMA}/\text{N}_2$, with dose times 1s/30s/1s/30s, at a) 350 °C (black), b) 300 °C (blue), and c) 250 °C (red). For each deposition temperature, a representative TiCl_4 and TMA dose are shown with arrows, along with the average mass change 211

Figure A2.4 QCM results showing the mass change (ng/cm^2) versus process time (minutes) for 5 sub-doses, i.e., $(\text{TiCl}_4/\text{N}_2) \times 5 / (\text{TMA}/\text{N}_2) \times 5$, with dose times $(1\text{s}/30\text{s}) \times 5 / (1\text{s}/30\text{s}) \times 5$, at a) 350 °C (black), b) 300 °C (blue), c) 250 °C (red), and d) 200 °C (green). For each deposition temperature, representative TiCl_4 and TMA doses are indicated with arrows, along with the cumulative mass change 212

Figure A2.5 QCM results showing the average mass change (ng/cm^2) versus number of a) TiCl_4 of b) TMA sub-doses. Data were averaged from over at least 50 cycles of $(\text{TiCl}_4/\text{N}_2) \times 5 / (\text{TMA}/\text{N}_2) \times 5$, with dose times $(1\text{s}/30\text{s}) \times 5 / (1\text{s}/30\text{s}) \times 5$, at 350 °C (black upside-down triangles), 300 °C (red triangles), 250 °C (blue circles) and 200 °C (green squares) 213

Figure A2.6 Ratio of the averaged mass changes (absolute value), obtained from QCM, during 5 sub doses of TiCl_4/TMA at 200, 250, 300, and 350 °C. Data were averaged from over at least 50 cycles of $(\text{TiCl}_4/\text{N}_2) \times 5 / (\text{TMA}/\text{N}_2) \times 5$, with dose times $(1\text{s}/30\text{s}) \times 5 / (1\text{s}/30\text{s}) \times 5$ 214

CHAPTER 1: INTRODUCTION AND BACKGROUND

CHAPTER 1. Introduction and Background

Eric C. Stevens,[†]

[†]Department of Chemical and Biomolecular Engineering, North Carolina State University, 911 Partners Way, Raleigh NC 27695

1.1 Atomic Layer Deposition Background and Applications

Since being first introduced in the 1970s,¹ Atomic layer deposition (ALD), previously referred to as atomic layer epitaxy or ALE, has seen broad adaptation for a variety of uses in the semiconductor industry. ALD has been described as the so-called sister method to chemical vapor deposition, but with some important distinctions. ALD is a vapor phase method to deposit thin films of solid material utilizing sequential, self-limiting half reactions.² The surface chemistry involved in ALD ranges from ligand exchange,³⁻⁵ combustion,^{6,7} and oxidation-reduction,⁸⁻¹¹ among others. The key advantages of ALD are angstrom-level control over thickness,¹²⁻¹⁴ smooth and conformal coverage in high aspect ratio structures,¹⁵⁻¹⁷ free of pin-holes,¹⁸⁻²⁰ and scalable to large volume manufacturing.^{21,22}

In the semiconductor industry, the use of ALD to deposit thin films has played a pivotal role in the continued device scaling since the 45 nm node (2007), when Intel first adapted using ALD to deposit high-k metal gates.^{23,24} In the years that followed, ALD has made its mark in the industry and has been widely adapted in both front-end-of-line (FEOL) and back-end-of-line (BEOL) processing.²⁵⁻²⁷ Continued progress toward gate-all-around (GAA)²⁸ and other 3D device architectures^{29,30} only furthers the increased use of ALD in the industry. For example, area-selective ALD has been proposed as an alternative to traditional lithographic patterning techniques.³¹⁻³³ In using ALD to pattern the desired material, continued device scaling can be

achieved with a reduction in line-edge roughness, pattern misalignment, and non-uniformity in high aspect ratio structures.

Beyond the semiconductor industry, ALD has seen rapid expansion in the areas such as solar cells,^{34–38} electrochemical storage,^{39–41} textiles,^{42–44} and catalysis,^{45–47} among others. With a broad application base of atomic layer deposition, continued research is required to match the rapid rise in technological demand. The motivation for this work is to further understand novel processes on a fundamental level and investigate the challenges involved for potential industrial adaptation.

1.2 Basic Principles of Atomic Layer Deposition

1.2.1 Surface Reactions in Atomic Layer Deposition

In a typical ALD process, two vapor-phase reagents are sequentially exposed to a heated substrate under low pressure, separated by inert gas purge steps. Figure 1.1 shows a cartoon depicting the reaction of trimethyl aluminum ($\text{Al}(\text{CH}_3)_3$, abbreviated TMA) and water (H_2O). This reaction proceeds by first exposing TMA to a reactive surface, here given as a hydroxyl-terminated substrate ($-\text{OH}$). A ligand exchange reaction takes place between the TMA and $-\text{OH}$ surface, forming an Al-O bond and giving off methane (CH_4) as a byproduct. This is considered the first half-reaction, which self-saturates after an excess of TMA has reacted with all accessible $-\text{OH}$ groups. Following this first half-reaction step, an inert gas purge (typically nitrogen, N_2 , or argon, Ar) is used to remove any unreacted TMA or CH_4 byproducts.

The second half reaction proceeds by an excess exposure of H_2O to the now methyl-terminated surface, forming Al-OH groups and giving off CH_4 as a byproduct. Again, an inert gas is used to purge the system of excess H_2O and CH_4 . The combination of these two half cycles constitutes one ALD cycle, which can be repeated in the same cyclic manner to give films with Angstrom-level thickness control. The self-limiting nature, via the making and breaking of

chemical bonds, of these half reactions is what gives the ALD process the distinctive features of conformal and uniform films. The uniform and conformal nature of this deposition process is also extended to substrates with complex geometries and high aspect ratios.^{48–52}

1.2.2. Thermodynamics of Atomic Layer Deposition

The thermodynamics of the ALD reactions have been studied previously using TMA and H₂O as a model system to produce aluminum oxide (Al₂O₃).^{33,53,54} Quantum chemical calculations of the TMA and H₂O half reactions are shown in Figures 1.2.⁵⁴ From these calculations, each half reaction was determined to be exothermic, with the overall reaction sequence also being exothermic. The driving force for these reactions is the formation of strong Al-O bonds. For the TMA half reaction, the breaking of Al-C bonds leads to an energy barrier for formation of Al-O bonds. It follows that a similar energy barrier exists for the H₂O half reaction. Due to the overall downhill thermodynamics of the reaction, these energy barriers are surmountable with the aid of heat, but has also been demonstrated to proceed at low temperature.⁵⁵ These findings are in good alignment with other reports of a negative change in the Gibbs free energy, corresponding to favorable thermodynamics in the TMA+H₂O reaction.³³ Similar findings have been demonstrated for other ALD processes, with a general trend of exothermic reactions with a negative change in the Gibbs free energy.^{56–58}

1.2.3 Growth Rate Versus Temperature

For a typical ALD process, there exists an ALD temperature window (see Figure 1.3), where the growth rate per cycle (GPC) is constant over a specific temperature range.¹² Usually the temperature window is large enough that small fluctuations in the deposition temperature will not affect the GPC (as long as the fluctuations are within the specified ALD window). Outside of the ALD window, the GPC varies depending on the temperature and specific reaction chemistry used.

For example, at lower temperatures, growth may be much higher than within the window due to direct condensation of the vapor-phase precursors on the reactive surface. Alternatively, at lower temperatures, insufficient thermal energy is available to overcome reaction energy barriers. For temperatures exceeding the ALD window, precursor desorption (without reacting with the surface groups) or precursor dissociation in the gas phase or on the surface may cause a non-constant relationship between the GPC and deposition temperature.

1.2.4 Nucleation and Growth Modes

Most ALD processes can be divided into three separate growth modes: layer-by-layer, island, and layer-plus-island growth.⁵⁹ Figure 1.4 shows a schematic of the three growth modes during the initial nucleation on a given substrate. Layer-by-layer growth, also referred to as Frank-van der Merwe growth, proceeds via two-dimensional stacking of material, which typically occurs when the atoms of the deposited material are strongly bound to the substrate. This type of growth mode is usually associated with most ALD processes due to the self-limiting nature of the ALD chemistry.⁵⁹ Island growth, or Volmer-Weber growth,⁵⁹ is usually observed when the deposited material exhibits stronger bonding to itself rather than the substrate.⁶⁰ This type of growth is widely observed during the nucleation of metals on oxide surfaces metal oxide on hydrogen terminated silicon.^{6,61-63} For an ALD process, islands will continue to grow radially, in three dimensions, and at a constant growth rate until the islands coalesce into a film.⁶⁴ After which, layer-by-layer growth is typically observed on the coalesced film. Layer-plus-island growth, also known as Stranski-Krastanov growth, has been observed for systems when strain energy due to lattice mismatch will trigger a change from layer-by-layer to island growth.⁶⁵⁻⁶⁷ For an ALD process, the island growth would again proceed until coalescence, followed by two-dimensional layer-by-layer growth. Depending on the material system, this transient growth mode can proceed in perpetuity.

Of special interest for this work is the modeling of the island growth mode during atomic layer deposition processing. As will be presented in Section 1.4, understanding the nucleation and growth behavior during area-selective atomic layer deposition is very important to broader adaptation in the semiconductor industry and beyond.

1.3 Materials Deposited Using Atomic Layer Deposition

Specifically regarding microelectronics, ALD has been applied to deposit high-k gate oxides, high-k memory capacitor dielectrics, and nitrides and metals for electrode and interconnect materials.^{39,41,68-72} Of specific interest to this dissertation are ALD processes for metal oxides, pure metals, and metal carbides.

1.3.1 Atomic Layer Deposition of Metal Oxides

High-k gate oxides by ALD have been one of the most well studied processes, as the chemistry is usually straightforward and very thermodynamically favorable.⁶⁸ The use of a thin film with a high dielectric constant stems from the need for very thin (sub 10 nm) barriers to tunneling currents in metal-oxide semiconductor field effect transistors (MOSFETs), where silicon oxide (SiO_2) is the traditionally used material.¹³ A film with a greater dielectric constant has a larger so-called equivalent oxide thickness (EOS), which is defined as the equivalent thickness of SiO_2 that would be required to produce the same electron tunnel barrier effect.¹³ Aluminum oxide (Al_2O_3), hafnium oxide (HfO_2), and zirconium oxide (ZrO_2) are all materials that have been explored as high-k replacements for SiO_2 .⁷³ Most metal oxide deposition processes used in the industry involve a ligand exchange reaction mechanism, with metal halide, metal organic precursors typically reacting with water, oxygen, or oxygen plasma.⁷⁴

1.3.2 Atomic Layer Deposition of Metals

ALD has been studied for deposition of metal films for interconnects,⁷⁵ contact plugs,⁷⁶ seed layers,⁷⁷ diffusion barriers.⁷¹ In addition, noble metals and high- and low-workfunction metals have been used for dynamic random access memory and dual-gate metal-oxide-semiconductor field effect transistors.⁷⁸⁻⁸¹ Metal ALD typically proceeds via combustion reactions (e.g., noble metals), oxidation-reduction reactions, or radical initiated reactions.^{6,7,57,62,82}

With many of these applications, comes many challenges associated with metal ALD. These challenges arise from the lack of well-known 1) reaction mechanisms (most vary from the well-studied ligand exchange reactions), 2) nucleation and growth mechanisms on surfaces that do not contain reactive sites (e.g., -OH or -CH₃ groups), and 3) lack of strong vapor-phase reducing agents that can reduce metal precursors completely to their elemental state. Plasma-enhanced ALD (PE-ALD) has been used to try and circumvent some of these challenges to deposit metal films.⁸³⁻⁸⁵ Plasma sources are used to generate high energy radicals, which facilitate reactions that are not currently possible by traditional ALD methods. This method has been used to deposit metals such as Ta, Si, and Ge.⁸³ The key drawback for PE-ALD is radical recombination, which can limit conformality in high aspect ratio structures.⁸³ Another consideration is substrate and film damage, with a possible increase in contamination from highly reactive radical species.⁸³ Therefore, a thermal ALD process has many advantages over plasma-enhanced ALD, yet more research and characterization is required to expand the types of metals deposited as well as reduce impurity content.

1.3.3 Atomic Layer Deposition of Metal Carbides

Metal carbide materials by ALD are a relatively new compared to that of metal oxide and pure metal thin films. Metal carbides have many applications that make them attractive for

adaption into the semiconductor industry as diffusion barriers,^{72,86,87} adhesion layers,⁸⁸ and potential gate metal replacements.⁸⁹⁻⁹³ Of specific interest to this work is tungsten carbide. The unique properties of tungsten carbide (WC, W₂C, or WC₂) lead to a variety of important uses for WC thin films, with a wide range of applications. Some recent studies have suggested use of WC as low-cost alternatives for noble metals in catalysis,⁹⁴⁻⁹⁷ diffusion barriers,^{86,98,99} and hard coatings due to high strength, hardness, and stability.^{100,101} Typically, WC thin films are deposited using sputter deposition,^{102,103,88} chemical vapor deposition (CVD),¹⁰⁴⁻¹⁰⁶ and recently atomic layer deposition (ALD).^{87,107-109}

Concerning ALD of WC, PE-ALD processes have been demonstrated previously to deposit WC thin films.¹⁰⁸ As discussed in the previous section, plasma-based processing can provide limitations due to substrate damage and conformality variance in high aspect ratio structures.¹¹⁰⁻¹¹² Therefore, thermal ALD of WC is of interest to expand adaptation into transistor and memory applications. Thermal ALD processing of WC has not been extensively studied in the research community, with thermal ALD of WC by WCl₆ and Al(CH₃)₃ being the most recent development.⁸⁷ This study was very promising for applications as Cu diffusion barriers, with resistivity values of 1500 μΩ-cm at 375 °C. Yet, an understanding of the *in situ* growth behavior and possible reaction mechanisms were not demonstrated experimentally and would greatly benefit the broader adaptation of these processes in the semiconductor industry.

1.4 Area-Selective Atomic Layer Deposition

Area-selective ALD refers for a process in which ALD is inhibited on one substrate (or substrates), while growth is unaffected on another substrate (or substrates). Area-selective ALD has been demonstrated in various forms in the literature.³¹ In some cases, ALD does not proceed readily on a given substrate due to thermodynamic or kinetic barriers which exist inherently in the

system. These types of ALD processes are usually referred to as inherently selective ALD, which have been shown for Co,¹¹³ Ru,⁶² Ni,¹¹⁴ W,¹¹⁵ TiO₂¹¹⁶ thin films on specific substrates. These types of processes are usually preferred due to less processing steps but are typically limited in the breadth of materials and substrates.

To expand the types of ALD thin films deposited selectively, the use of blocking layers, such as self-assembled monolayer (or SAMs), have been used^{117,118} Such blocking layers will selectively adsorb to specific substrates and not others. These types of processes rely on the use of specific precursors with ligands that remain mostly unreactive to ALD precursors.¹¹⁹ For the case of SAMs, these molecules have long carbon chains, which were shown previously to be hydrophobic and thus very efficient at inhibiting metal oxide ALD. These types of processes are often limited in terms of deposition temperature, due to desorption of inhibitor molecules, and thus also the types of ALD processes that can be used in conjunction with these blocking layers.¹²⁰ A similar concept to the blocking layers is the use of a masking layer, which is typically a patterned film which can be used as a template for area-selective ALD. These materials are usually polymers,^{121,122} but have also been shown to work with aC hard mask materials.⁷⁷ Of special interest to this work is the use of aC thin films as sacrificial templates to enable area-selective ALD due to their widespread use in current patterning efforts and easy removal (using oxygen or oxygen plasma).¹²³

1.5 Figures for Chapter 1

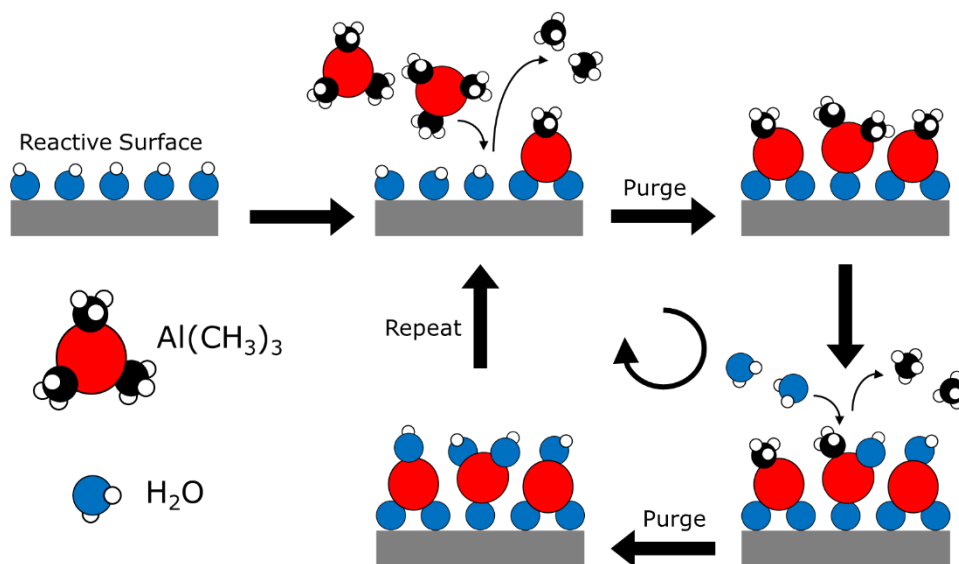


Figure 1.1: Schematic of Al₂O₃ by ALD using Al(CH₃)₃ and H₂O precursors. Exposure of a reactive substrate (-OH groups) to Al(CH₃)₃ will result in a complete reaction of all available surface sites, giving off CH₄ byproducts and forming Al-O bonds. After purging excess reactant and byproducts using inert gas, H₂O can be exposed to the newly terminated surface (Al-CH₃), releasing CH₄ byproducts. Following another purge step, this process can be repeated in a cyclic manner until the desired film thickness is reached.

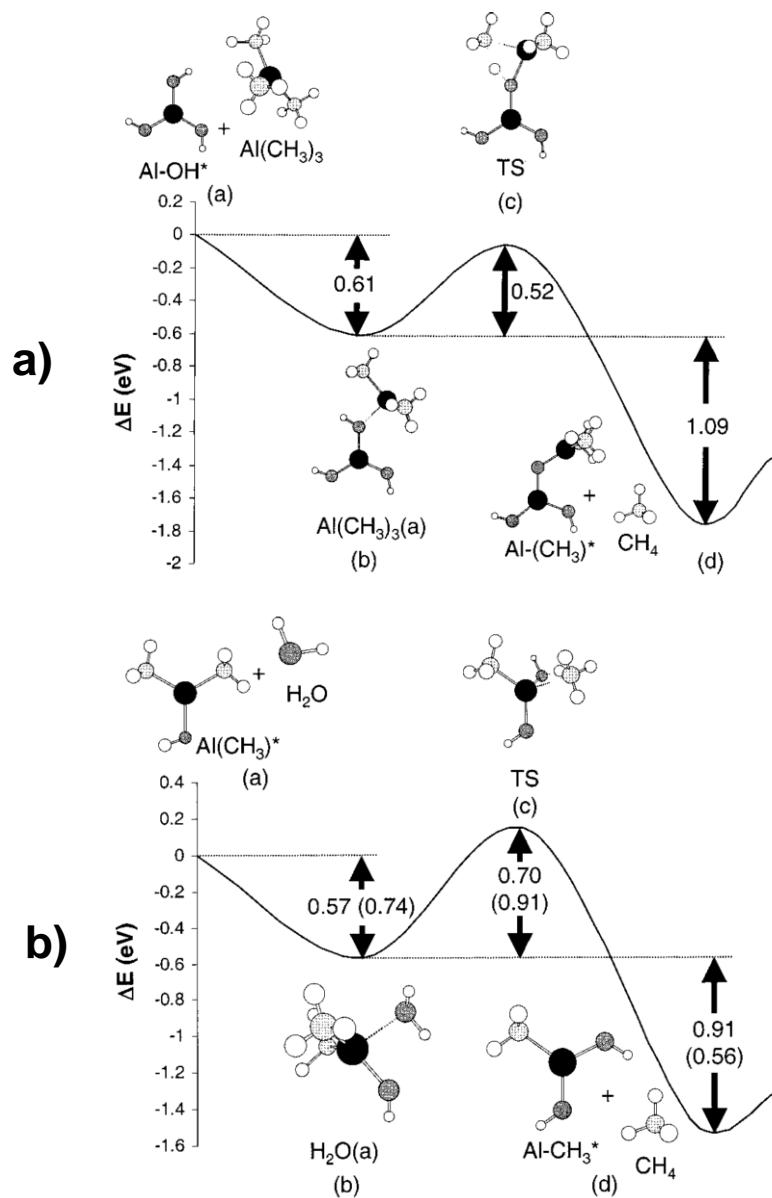


Figure 1.2: Quantum chemical calculations of the anticipated reaction pathways and associated energetics during the reaction of $\text{Al}(\text{CH}_3)_3 + \text{H}_2\text{O}$. a) shows the first half-reaction of gas-phase $\text{Al}(\text{CH}_3)_3$ reacting with Al-OH^* surface sites. b) shows the second half-reaction of gas-phase H_2O with $\text{Al}-(\text{CH}_3)^*$ surface sites. Figure reproduced from Ref 54.

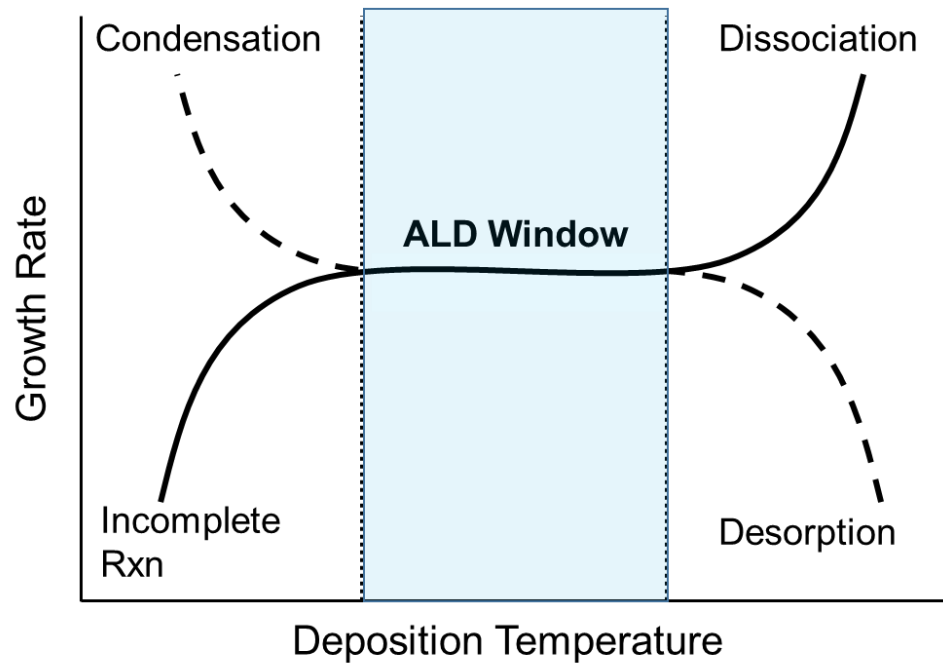


Figure 1.3: Growth rate as a function of deposition temperature for ALD processing. For most ALD processes, there exists an ALD window, which is a range of temperatures where the film growth rate is constant. Outside of this window, the growth can vary depending on the temperature and specific reaction chemistry.

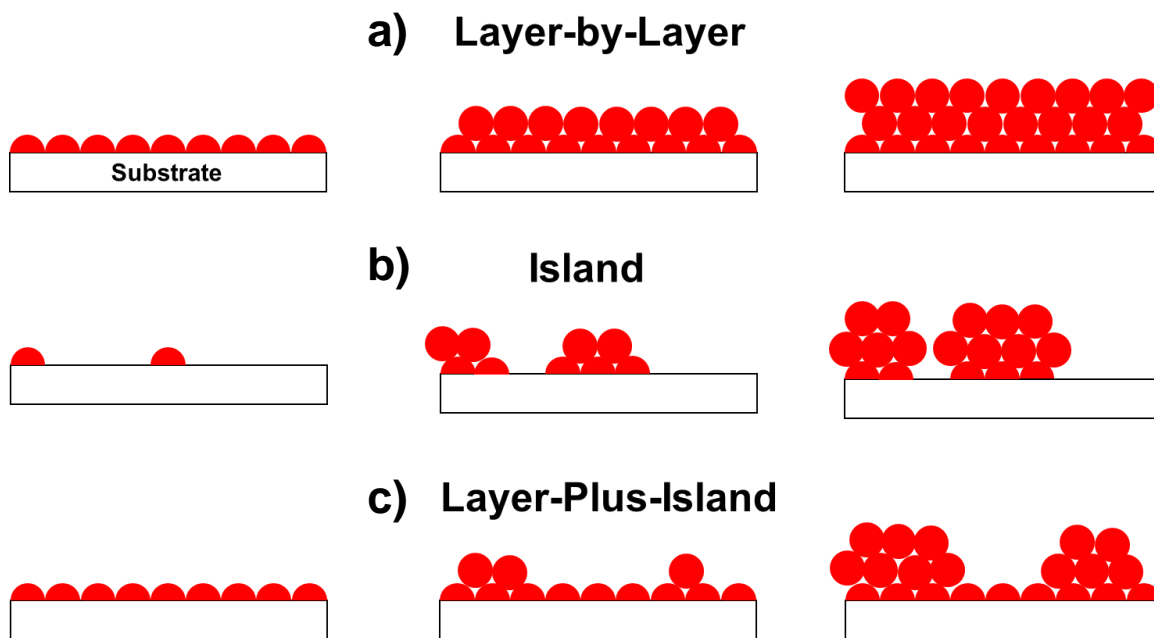


Figure 1.4: Schematic of the three growth modes typically observed during ALD: a) layer-by-layer (Frank-van der Merwe), b) island (Volmer-Weber), and c) layer-plus-island (Stranski-Krastanov) growth.

1.6 References

- (1) Suntola, T.; Antson, J. Method for Producing Compound Thin Films. U.S. Patent #4,058,430, 1977.
- (2) Higashi, G. S.; Fleming, C. G. Sequential Surface Chemical Reaction Limited Growth of High Quality Al₂O₃ Dielectrics. *Appl. Phys. Lett.* **1989**, *55* (19), 1963–1965.
- (3) Delabie, A.; Sioncke, S.; Rip, J.; Van Elshocht, S.; Caymax, M.; Pourtois, G.; Pierloot, K. Mechanisms for the Trimethylaluminum Reaction in Aluminum Oxide Atomic Layer Deposition on Sulfur Passivated Germanium. *J. Phys. Chem. C* **2011**, *115* (35), 17523–17532.
- (4) Mullings, M. N.; Hägglund, C.; Tanskanen, J. T.; Yee, Y.; Geyer, S.; Bent, S. F. Thin Film Characterization of Zinc Tin Oxide Deposited by Thermal Atomic Layer Deposition. *Thin Solid Films* **2014**, *556*, 186–194.
- (5) Xie, Q.; Jiang, Y.-L.; Detavernier, C.; Deduytsche, D.; Meirhaeghe, R. L. Van; Ru, G.-P.; Li, B.-Z.; Qu, X.-P. Atomic Layer Deposition of TiO₂ from Tetrakis-Dimethyl-Amido Titanium or Ti Isopropoxide Precursors and H₂O. *J. Appl. Phys.* **2007**, *102* (8), 83521.
- (6) Aaltonen, T.; Ritala, M.; Sajavaara, T.; Keinonen, J.; Leskelä, M. Atomic Layer Deposition of Platinum Thin Films. *Chem. Mater.* **2003**, *15* (9), 1924–1928.
- (7) Aaltonen, T.; Ritala, M.; Tung, Y.-L.; Chi, Y.; Arstila, K.; Meinander, K.; Leskelä, M. Atomic Layer Deposition of Noble Metals: Exploration of the Low Limit of the Deposition Temperature. *J. Mater. Res.* **2004**, *19* (11), 3353–3358.
- (8) Klesko, J. P.; Thrush, C. M.; Winter, C. H. Thermal Atomic Layer Deposition of Titanium Films Using Titanium Tetrachloride and 2-Methyl-1,4-Bis(trimethylsilyl)-2,5-Cyclohexadiene or 1,4-Bis(trimethylsilyl)-1,4-Dihydropyrazine.
- (9) Klaus, J. W.; Ferro, S. J.; George, S. M. Atomic Layer Deposition of Tungsten Using Sequential Surface Chemistry with a Sacrificial Stripping Reaction. *Thin Solid Films* **2000**, *360* (1–2), 145–153.
- (10) Elam, J. W.; Schuisky, M.; Ferguson, J. D.; George, S. M. Surface Chemistry and Film Growth during TiN Atomic Layer Deposition Using TDMAT and NH₃. *Thin Solid Films* **2003**, *436* (2), 145–156.
- (11) Musschoot, J.; Xie, Q.; Deduytsche, D.; Van den Berghe, S.; Van Meirhaeghe, R. L.; Detavernier, C. Atomic Layer Deposition of Titanium Nitride from TDMAT Precursor. *Microelectron. Eng.* **2009**, *86* (1), 72–77.
- (12) Miikkulainen, V.; Leskelä, M.; Ritala, M.; Puurunen, R. L. Crystallinity of Inorganic Films Grown by Atomic Layer Deposition: Overview and General Trends. *Journal of Applied Physics*. 2013.

- (13) Jeong, S. J.; Gu, Y.; Heo, J.; Yang, J.; Lee, C. S.; Lee, M. H.; Lee, Y.; Kim, H.; Park, S.; Hwang, S. Thickness Scaling of Atomic-Layer-Deposited HfO₂ Films and Their Application to Wafer-Scale Graphene Tunnelling Transistors. *Sci. Rep.* **2016**, *6* (1), 20907.
- (14) Chai, Z.; Liu, Y.; Li, J.; Lu, X.; He, D. Ultra-Thin Al₂O₃ Films Grown by Atomic Layer Deposition for Corrosion Protection of Copper.
- (15) Gordon, R. G.; Hausmann, D.; Kim, E.; Shepard, J. A Kinetic Model for Step Coverage by Atomic Layer Deposition in Narrow Holes or Trenches. *Chem. Vap. Depos.* **2003**, *9* (2), 73–78.
- (16) Liu, K.-I.; Kei, C.-C.; Mishra, M.; Chen, P.-H.; Liu, W.-S.; Perng, T.-P. Uniform Coating of TiO₂ on High Aspect Ratio Substrates with Complex Morphology by Vertical Forced-Flow Atomic Layer Deposition. *RSC Adv.* **2017**, *7* (55), 34730–34735.
- (17) Pellin, M. J.; Elam, J. W.; Libera, J. A.; Martinson, A. B.; Hupp, J. T. Transparent Conducting Oxides at High Aspect Ratios by ALD. In *ECS Transactions*; ECS, 2007; Vol. 3, pp 243–247.
- (18) Litvinov, J.; Wang, Y. J.; George, J.; Chinwangso, P.; Brankovic, S.; Willson, R. C.; Litvinov, D. Development of Pinhole-Free Amorphous Aluminum Oxide Protective Layers for Biomedical Device Applications. *Surf. Coatings Technol.* **2013**, *224*, 101–108.
- (19) Zhang, W.; Dong, J. C.; Li, C. Y.; Chen, S.; Zhan, C.; Panneerselvam, R.; Yang, Z. L.; Li, J. F.; Zhou, Y. L. Large Scale Synthesis of Pinhole-Free Shell-Isolated Nanoparticles (SHINs) Using Improved Atomic Layer Deposition (ALD) Method for Practical Applications. *J. Raman Spectrosc.* **2015**, *46* (12), 1200–1204.
- (20) Wan, Z.; Zhang, T. F.; Ding, J. C.; Kim, C. M.; Park, S. W.; Yang, Y.; Kim, K. H.; Kwon, S. H. Enhanced Corrosion Resistance of PVD-CrN Coatings by ALD Sealing Layers. *Nanoscale Res. Lett.* **2017**, *12* (248), 1–8.
- (21) Poodt, P.; Lankhorst, A.; Roozeboom, F.; Spee, K.; Maas, D.; Vermeer, A. High-Speed Spatial Atomic-Layer Deposition of Aluminum Oxide Layers for Solar Cell Passivation. *Adv. Mater.* **2010**, *22* (32), 3564–3567.
- (22) Poodt, P.; Cameron, D. C.; Dickey, E.; George, S. M.; Kuznetsov, V.; Parsons, G. N.; Roozeboom, F.; Sundaram, G.; Vermeer, A. Spatial Atomic Layer Deposition: A Route towards Further Industrialization of Atomic Layer Deposition. *J. Vac. Sci. Technol. A Vacuum, Surfaces, Film.* **2012**, *30* (1), 10802.
- (23) Mistry, K.; Allen, C.; Auth, C.; Beattie, B.; Bergstrom, D.; Bost, M.; Brazier, M.; Buehler, M.; Cappellani, A.; Chau, R.; Choi, C.; Ding, G.; Fischer, K.; Ghani, T.; Grover, R.; Han, W.; Hanken, D.; Hattendorf, M.; He, J.; Hicks, J.; Huessner, R.; Ingerly, D.; Jain, P.; James, R.; Jong, L.; Joshi, S.; Kenyon, C.; Kuhn, K.; Lee, K.; Liu, H.; Maiz, J.; McIntyre, B.; Moon, P.; Neiryneck, J.; Pae, S.; Parker, C.; Parsons, D.; Prasad, C.; Pipes, L.; Prince, M.; Ranade, P.; Reynolds, T.; Sandford, J.; Shifren, L.; Sebastian, J.; Seiple, J.; Simon, D.; Sivakumar, S.; Smith, P.; Thomas, C.; Troeger, T.; Vandervoorn, P.; Williams, S.; Zawadzki, K. A

- 45nm Logic Technology with High-k+Metal Gate Transistors, Strained Silicon, 9 Cu Interconnect Layers, 193nm Dry Patterning, and 100% Pb-Free Packaging. In *IEEE International Electron Devices Meeting*; 2007; pp 247–250.
- (24) Sneh, O.; Clark-Phelps, R. B.; Londergan, A. R.; Winkler, J.; Seidel, T. E. Thin Film Atomic Layer Deposition Equipment for Semiconductor Processing. *Thin Solid Films* **2002**, *402*, 248–261.
- (25) Belyansky, M.; Conti, R.; Khan, S.; Zhou, X.; Klymko, N.; Yao, Y.; Madan, A.; Tai, L.; Flaitz, P.; Ando, T. Atomic Layer Deposition of Sidewall Spacers: Process, Equipment and Integration Challenges in State-of-the-Art Logic Technologies. *Silicon Compat. Mater. Process. Technol. Adv. Integr. Circuits Emerg. Appl.* **2014**, *61* (39), 39–45.
- (26) Koh, W.; Kumar, D.; Li, W.-M.; Sprey, H.; Leuven, N. V; Raaijmakers, I. J. Meeting the Cu Diffusion Barrier Challenge Using ALD Tungsten Nitride Carbide. *Solid State Technol.* **2005**, *48* (6), 54–58.
- (27) Nogami, T.; Chae, M.; Penny, C.; Shaw, T.; Shobha, H.; Li, J.; Cohen, S.; Hu, C. K.; Zhang, X.; He, M.; Tanwar, K.; Patlolla, R.; Chen, S. T.; Kelly, J.; Lin, X.; Straten, O.; Simon, A.; Motoyama, K.; Bonilla, G.; Huang, E.; Spooner, T.; Edelstein, D. Performance of Ultrathin Alternative Diffusion Barrier Metals for next - Generation BEOL Technologies, and Their Effects on Reliability. In *2014 IEEE International Interconnect Technology Conference*; IEEE, 2014; pp 223–226.
- (28) Chu, C.-L.; Chen, B.-Y.; Fuh, Y.-K. Capacitive Effective Thickness of a Few Nanometers by Atomic Layer Deposition and Device Performance in Ge Gate-All-around Fin Field Effect Transistors. *J. Micro/ Nanolithography, MEMS, MOEMS* **2015**, *14* (4), 44501.
- (29) Liu, W.; Chikkadi, K.; Lee, S. W.; Hierold, C.; Haluska, M. Improving Non-Suspended Carbon Nanotube FET Performance by Using an Alumina Protective Layer. *Sensors Actuators, B Chem.* **2014**, *198*, 479–486.
- (30) Bakir, M.; Meindl, J. *Integrated Interconnect Technologies for 3D Nanoelectronic Systems*, 1st ed.; Artech House, Inc. Norwood, MA, USA, 2008.
- (31) Mackus, A. J. M.; Bol, A. A.; Kessels, W. M. M. The Use of Atomic Layer Deposition in Advanced Nanopatterning.
- (32) Chang, L.; Litvinov, D. Nanoimprint Lithography Tone Reversal Process Using Poly(methyl Methacrylate) and Hydrogen Silsesquioxane. *J. Vac. Sci. Technol. B, Nanotechnol. Microelectron. Mater. Process. Meas. Phenom.* **2017**, *35* (4), 41603.
- (33) Longo, R. C.; Owen, J. H. G.; McDonnell, S.; Dick, D.; Ballard, J. B.; Randall, J. N.; Wallace, R. M.; Chabal, Y. J.; Cho, K. Toward Atomic-Scale Patterned Atomic Layer Deposition: Reactions of Al₂O₃ Precursors on a Si(001) Surface with Mixed Functionalizations. *J. Phys. Chem. C* **2016**, *120* (5), 2628–2641.
- (34) Chandiran, A. K.; Yella, A.; Mayer, M. T.; Gao, P.; Nazeeruddin, M. K.; Grätzel, M. Sub-

- Nanometer Conformal TiO₂ Blocking Layer for High Efficiency Solid-State Perovskite Absorber Solar Cells. *Adv. Mater.* **2014**, *26*, 4309–4312.
- (35) Niu, W.; Li, X.; Karuturi, S. K.; Fam, D. W.; Fan, H.; Shrestha, S.; Wong, L. H.; Tok, A. I. Y. Applications of Atomic Layer Deposition in Solar Cells. *Nanotechnology* **2015**, *26* (6), 64001.
- (36) Kobayashi, T.; Kumazawa, T.; Jehl Li Kao, Z.; Nakada, T. Cu(In,Ga)Se₂ Thin Film Solar Cells with a Combined ALD-Zn(O,S) Buffer and MOCVD-ZnO:B Window Layers. *Sol. Energy Mater. Sol. Cells* **2013**, *119*, 129–133.
- (37) Huang, H.; Lv, J.; Bao, Y.; Xuan, R.; Sun, S.; Sneek, S.; Li, S.; Modanese, C.; Savin, H.; Wang, A.; Zhao, J. 20.8% Industrial PERC Solar Cell: ALD Al₂O₃ Rear Surface Passivation, Efficiency Loss Mechanisms Analysis and Roadmap to 24%. *Sol. Energy Mater. Sol. Cells* **2017**, *161*, 14–30.
- (38) Zardetto, V.; Di Giacomo, F.; Mohammed, M. A.; Lucarelli, G.; Razza, S.; D'Epifanio, A.; Licoccia, S.; Kessels, W. M. M.; Di Carlo, A.; Brown, T. M.; Creatore, M. Opportunities of Atomic Layer Deposition for Perovskite Solar Cells. *ECS Trans.* **2015**, *69* (7), 15–22.
- (39) Assaud, L.; Hanbücken, M.; Santinacci, L. Atomic Layer Deposition of TiN/Al₂O₃/TiN Nanolaminates for Capacitor Applications. *ECS Trans.* **2012**, *50* (13), 151.
- (40) Daubert, J. S.; Wang, R.; Ovental, J. S.; Barton, H. F.; Rajagopalan, R.; Augustyn, V.; Parsons, G. N. Intrinsic Limitations of Atomic Layer Deposition for Pseudocapacitive Metal Oxides in Porous Electrochemical Capacitor Electrodes. *J. Mater. Chem. A* **2017**, *5* (25), 13086–13097.
- (41) Hudec, B.; Hušeková, K.; Dobročka, E.; Aarik, J.; Rammula, R.; Kasikov, A.; Tarre, A.; Vincze, A.; Fröhlich, K. Atomic Layer Deposition Grown Metal-Insulator-Metal Capacitors with RuO₂ Electrodes and Al-Doped Rutile TiO₂ Dielectric Layer. *J. Vac. Sci. Technol. B* **2011**, *29* (1), 01AC09.
- (42) Iii, W. J. S.; Jur, J. S.; Parsons, G. N. Bi-Layer Al₂O₃/ZnO Atomic Layer Deposition for Controllable Conductive Coatings on Polypropylene Nonwoven Fiber Mats. *J. Appl. Phys.* **2013**, *113* (19), 194303.
- (43) Jur, J. S.; Sweet, W. J.; Oldham, C. J.; Parsons, G. N. Atomic Layer Deposition of Conductive Coatings on Cotton, Paper, and Synthetic Fibers: Conductivity Analysis and Functional Chemical Sensing Using “All-Fiber” Capacitors. *Adv. Funct. Mater.* **2011**, *21* (11), 1993–2002.
- (44) Kalanyan, B.; Oldham, C. J.; Sweet, W. J.; Parsons, G. N. Highly Conductive and Flexible Nylon-6 Nonwoven Fiber Mats Formed Using Tungsten Atomic Layer Deposition. *ACS Appl. Mater. Interfaces* **2013**, *5* (11), 5253–5259.
- (45) Ramachandran, R. K.; Detavernier, C.; Dendooven, J. Atomic Layer Deposition for Catalysis. In *Nanotechnology in Catalysis*; Wiley-VCH Verlag GmbH & Co. KGaA:

Weinheim, Germany, 2017; pp 335–358.

- (46) Singh, J. A.; Yang, N.; Bent, S. F. Nanoengineering Heterogeneous Catalysts by Atomic Layer Deposition. *Annu. Rev. Chem. Biomol. Eng.* **2017**, *8* (1), 41–62.
- (47) O'Neill, B. J.; Jackson, D. H. K.; Lee, J.; Canlas, C.; Stair, P. C.; Marshall, C. L.; Elam, J. W.; Kuech, T. F.; Dumesic, J. A.; Huber, G. W. Catalyst Design with Atomic Layer Deposition. *ACS Catal.* **2015**, *5* (3), 1804–1825.
- (48) Karuturi, S. K.; Liu, L.; Su, L. T.; Zhao, Y.; Fan, H. J.; Ge, X.; He, S.; Yoong, A. T. I. Kinetics of Stop-Flow Atomic Layer Deposition for High Aspect Ratio Template Filling through Photonic Band Gap Measurements. *J. Phys. Chem. C* **2010**, *114* (35), 14843–14848.
- (49) Dendooven, J.; Goris, B.; Devloo-Casier, K.; Levrau, E.; Biermans, E.; Baklanov, M. R.; Ludwig, K. F.; Voort, P. Van Der; Bals, S.; Detavernier, C. Tuning the Pore Size of Ink-Bottle Mesopores by Atomic Layer Deposition. *Chem. Mater.* **2012**, *24* (11), 1992–1994.
- (50) Tien, T.-C.; Pan, F.-M.; Wang, L.-P.; Tsai, F.-Y.; Lin, C. Growth Mode Transition of Atomic Layer Deposited Al₂O₃ on Porous TiO₂ Electrodes of Dye-Sensitized Solar Cells. *Thin Solid Films* **2012**, *520*, 1745–1750.
- (51) Verdonck, P.; Delabie, A.; Swerts, J.; Farrell, L.; Baklanov, M. R.; Tielens, H.; Van Besien, E.; Witters, T.; Nyns, L.; Van Elshocht, S. Chemisorption of ALD Precursors in and on Porous Low-K Films. *Microelectron. Eng.* **2013**, *106*, 81–84.
- (52) Brizé, V.; Prieur, T.; Violet, P.; Artaud, L.; Berthomé, G.; Blanquet, E.; Boichot, R.; Coindeau, S.; Doisneau, B.; Farcy, A.; Mantoux, A.; Nuta, I.; Pons, M.; Volpi, F. Developments of TaN ALD Process for 3D Conformal Coatings. *Chem. Vap. Depos.* **2011**, *17* (10–12), 284–295.
- (53) Travis, C. D.; Adomaitis, R. A. Modeling Alumina Atomic Layer Deposition Reaction Kinetics during the Trimethylaluminum Exposure. *Theor. Chem. Acc.* **2014**, *133* (1), 3–11.
- (54) Widjaja, Y.; Musgrave, C. B. Quantum Chemical Study of the Mechanism of Aluminum Oxide Atomic Layer Deposition. *Appl. Phys. Lett.* **2002**, *80* (18), 3304–3306.
- (55) Taewook, N.; Jae-Min, K.; Min-Kyu, K.; Hyungjun, K.; Woo-Hee, K. Low-Temperature Atomic Layer Deposition of TiO₂, Al₂O₃, and ZnO Thin Films. *J. Korean Phys. Soc.* **2011**, *59* (21), 452–457.
- (56) Violet, P.; Blanquet, E.; Monnier, D.; Nuta, I.; Chatillon, C. Experimental Thermodynamics for the Evaluation of ALD Growth Processes. *Surf. Coatings Technol.* **2009**, *204* (6–7), 882–886.
- (57) Li, W.-M. Recent Developments of Atomic Layer Deposition Processes for Metallization. *Chem. Vap. Depos.* **2013**.
- (58) Musgrave, C. Introduction to ALD. In *Atomic Layer Deposition of Nanostructured*

Materials; Pinna, N., Knez, M., Eds.; 2012; pp 1–22.

- (59) George, S. M. Atomic Layer Deposition: An Overview. *Chem. Rev.* **2010**, *110* (1), 111–131.
- (60) Elofsson, V.; Lü, B.; Magnfält, D.; Münger, E. P.; Sarakinos, K.; L€e, B.; Magnf, D.; Alt, €; M€e Unger, E. P. Unravelling the Physical Mechanisms That Determine Microstructural Evolution of Ultrathin Volmer-Weber Films. *J. Appl. Phys.* **2014**, *116* (4), 44302.
- (61) Kerrigan, M. M.; Klesko, J. P.; Winter, C. H. Low Temperature, Selective Atomic Layer Deposition of Cobalt Metal Films Using Bis(1,4-Di-Tert-Butyl-1,3-Diazadienyl)cobalt and Alkylamine Precursors.
- (62) Aaltonen, T.; Ritala, M.; Arstila, K.; Keinonen, J.; Leskelä, M. Atomic Layer Deposition of Ruthenium Thin Films from Ru(thd)₃ and Oxygen. *Chem. Vap. Depos.* **2004**, *10* (4), 215–219.
- (63) Puurunen, R. L.; Vandervorst, W.; Besling, W. F. A.; Richard, O.; Bender, H.; Conard, T.; Zhao, C.; Delabie, A.; Caymax, M.; De Gendt, S.; Heyns, M.; Viitanen, M. M.; De Ridder, M.; Brongersma, H. H.; Tamminga, Y.; Dao, T.; De Win, T.; Verheijen, M.; Kaiser, M.; Tuominen, M. Island Growth in the Atomic Layer Deposition of Zirconium Oxide and Aluminum Oxide on Hydrogen-Terminated Silicon: Growth Mode Modeling and Transmission Electron Microscopy. *J. Appl. Phys.* **2004**, *96* (9), 4878–4889.
- (64) Hagen, D. J.; Connolly, J.; Povey, I. M.; Rushworth, S.; Pemble, M. E. Island Coalescence during Film Growth: An Underestimated Limitation of Cu ALD. *Adv. Mater. Interfaces* **2017**, *4* (18), 1700274.
- (65) Baskaran, A.; Smereka, P. Mechanisms of Stranski-Krastanov Growth Direct Formation of Quantum-Sized Dots from Uniform Coherent Islands of InGaAs on GaAs Surfaces Multidimensional Quantum Well Laser and Temperature Dependence of Its Threshold Current Mechanisms of Stranski-Krastanov Growth. *J. Appl. Phys. Appl. Phys. Lett. Appl. Phys. Lett. Am. J. Phys. Appl. Phys. Lett. Appl. Phys. Lett. Appl. Phys. Lett.* **2012**, *111* (40).
- (66) Ossicini, S.; Memeo, R.; Ciccacci, F. AES Analysis of the Growth Mechanism of Metal Layers on Metal Surfaces. *J. Vac. Sci. Technol. A* **1985**, *3* (2), 387–391.
- (67) Puurunen, R. L. Random Deposition as a Growth Mode in Atomic Layer Deposition. *Chem. Vap. Depos.* **2004**, *10* (3), 159–170.
- (68) Leskelä, M.; Ritala, M. Atomic Layer Deposition Chemistry: Recent Developments and Future Challenges. *Angew. Chemie Int. Ed.* **2003**, *42* (45), 5548–5554.
- (69) Liyanage, L. S.; Cott, D. J.; Delabie, A.; Elshocht, S. Van; Bao, Z.; Wong, H.-S. P. Atomic Layer Deposition of High- K Dielectrics on Single-Walled Carbon Nanotubes: A Raman Study. *Nanotechnology* **2013**, *24* (24), 245703.
- (70) Liu, X.; Ramanathan, S.; Lee, E.; Seidel, T. E. Atomic Layer Deposition of Aluminum

Nitride Thin Films from Trimethyl Aluminum (TMA) and Ammonia; MRS Online Proceedings Library; 2004; Vol. 811.

- (71) Rossnagel, S. M.; Sherman, A.; Turner, F. Plasma-Enhanced Atomic Layer Deposition of Ta and Ti for Interconnect Diffusion Barriers. *J. Vac. Sci. Technol. B* **2000**, *18* (4), 2016–2020.
- (72) Volders, H.; Tö Kei, Z.; Bender, H.; Brijs, B.; Caluwaerts, R.; Carbonell, L.; Conard, T.; Drijbooms, C.; Franquet, A.; Garaud, S.; Hoflijck, I.; Moussa, A.; Sinapi, F.; Travaly, Y.; Vanhaeren, D.; Verecke, G.; Zhao, C.; Li, W.-M.; Sprey, H.; Jonas, A. M. Materials Characterization of WN X C Y , WN X and WC X Films for Advanced Barriers. **2007**.
- (73) Gierałowska, S.; Wachnicki, Ł.; Witkowski, B. S.; Godlewski, M.; Guziewicz, E. Properties of Thin Films of High-K Oxides Grown by Atomic Layer Deposition at Low Temperature for Electronic Applications. *Opt. Appl.* **2013**, *43* (1), 17–25.
- (74) Miikkulainen, V.; Leskela, M.; Ritala, M.; Puurunen, R. L. Crystallinity of Inorganic Films Grown by Atomic Layer Deposition: Overview and General Trends. *J. Appl. Phys.* **2013**, *113* (2), 21301.
- (75) Gordon, P. G.; Kurek, A.; Barry, S. T. Trends in Copper Precursor Development for CVD and ALD Applications. *ECS J. Solid State Sci. Technol.* **2015**, *4* (1), N3188–N3197.
- (76) Luoh, T.; Su, C. T.; Yang, T. H.; Chen, K. C.; Lu, C. Y. Advanced Tungsten Plug Process for beyond Nanometer Technology. *Microelectron. Eng.* **2008**, *85* (8), 1739–1747.
- (77) Zyulkov, I.; Krishtab, M.; De Gendt, S.; Armini, S. Selective Ru ALD as a Catalyst for Sub-Seven-Nanometer Bottom-Up Metal Interconnects. *ACS Appl. Mater. Interfaces* **2017**, *9* (36), 31031–31041.
- (78) Knisley, T. J.; Kalutarage, L. C.; Winter, C. H. Precursors and Chemistry for the Atomic Layer Deposition of Metallic First Row Transition Metal Films. *Coordination Chemistry Reviews*. 2013.
- (79) Goldstein, D. N. Surface Chemistry of the Atomic Layer Deposition Of Metals and Group III Oxides. *Thesis* **2009**.
- (80) Kim, H. Atomic Layer Deposition of Metal and Nitride Thin Films: Current Research Efforts and Applications for Semiconductor Device Processing. *J. Vac. Sci. Technol. B Microelectron. Nanom. Struct.* **2003**, *21* (6), 2231.
- (81) Hamalainen, J.; Ritala, M.; Leskela, M. Atomic Layer Deposition of Noble Metals and Their Oxides. *Chem. Mater.* **2014**, *26*, 786–801.
- (82) Kalanyan, B.; Losego, M. D.; Oldham, C. J.; Parsons, G. N. Low-Temperature Atomic Layer Deposition of Tungsten Using Tungsten Hexafluoride and Highly-Diluted Silane in Argon. *Chem. Vap. Depos.* **2013**, *19* (4–6), 161–166.

- (83) Profijt, H. B.; Potts, S. E.; van de Sanden, M. C. M.; Kessels, W. M. M. Plasma-Assisted Atomic Layer Deposition: Basics, Opportunities, and Challenges. *J. Vac. Sci. Technol. A Vacuum, Surfaces, Film.* **2011**.
- (84) Yoon, J.; Song, J.-G.; Kim, H.; Lee, H.-B.-R. Plasma-Enhanced Atomic Layer Deposition of Co on Metal Surfaces. *Surf. Coat. Technol.* **2015**, *264*, 60–65.
- (85) Wu, L.; Eisenbraun, E. Hydrogen Plasma-Enhanced Atomic Layer Deposition of Copper Thin Films. *J. Vac. Sci. Technol. B Microelectron. Nanom. Struct.* **2007**, *25* (6), 2581.
- (86) Mustain, H. A.; Brown, W. D.; Ang, S. S. Tungsten Carbide as a Diffusion Barrier on Silicon Nitride Active-Metal-Brazed Substrates for Silicon Carbide Power Devices. *J. Electron. Packag.* **2009**, *131* (3), 34502.
- (87) Blakeney, K. J.; Winter, C. H. Thermal Atomic Layer Deposition of Tungsten Carbide Films from WCl_6 and $AlMe_3$. *J. Vac. Sci. Technol. A Vacuum, Surfaces, Film.* **2018**, *36* (1), 01A104.
- (88) Gubisch, M.; Liu, Y.; Spiess, L.; Romanus, H.; Krischok, S.; Ecke, G.; Schaefer, J. A.; Knedlik, C. Nanoscale Multilayer WC/C Coatings Developed for Nanopositioning: Part I. Microstructures and Mechanical Properties. **2005**.
- (89) Xiang, J.; Ding, Y.; Du, L.; Li, J.; Wang, W.; Zhao, C. Growth Mechanism of Atomic-Layer-Deposited TiAlC Metal Gate Based on $TiCl_4$ and TMA Precursors. *Chinese Phys. B* **2016**, *25* (3), 37308.
- (90) Xiang, J.; Ding, Y.; Du, L.; Li, J.; Wang, W.; Zhao, C. Growth Mechanism of Atomic-Layer-Deposited TiAlC Metal Gate Based on $TiCl_4$ and TMA Precursors. *Chinese Phys. B* **2016**, *25* (3), 37308.
- (91) Xiang, J.; Ding, Y.; Du, L.; Xu, C.; Li, T.; Wang, X.; Li, J.; Zhao, C. Investigation of N Type Metal TiAlC by Thermal Atomic Layer Deposition Using $TiCl_4$ and TEA as Precursors. *ECS J. Solid State Sci. Technol.* **2016**, *5* (5), P299–P303.
- (92) Xiang, J.; Li, T.; Wang, X.; Du, L.; Ding, Y.; Wang, W.; Li, J.; Zhao, C. Thermal Atomic Layer Deposition of TaAlC with $TaCl_5$ and TMA as Precursors. *ECS J. Solid State Sci. Technol.* **2016**, *5* (10), P633–P636.
- (93) Xiang, J.; Wang, X.; Li, T.; Gao, J.; Han, K.; Yu, J.; Wang, W.; Li, J.; Zhao, C. Investigation of Thermal Atomic Layer Deposited TaAlC with Low Effective Work-Function on HfO_2 Dielectric Using $TaCl_5$ and TEA as Precursors. *ECS J. Solid State Sci. Technol.* **2017**, *6* (1), P38–P41.
- (94) Levy, R. B.; Boudart, M. Platinum-Like Behavior of Tungsten Carbide in Surface Catalysis. *Science* (80-.). **1973**, *181* (4099), 547–549.
- (95) Yang, X.; Kimmel, Y. C.; Fu, J.; Koel, B. E.; Chen, J. G. Activation of Tungsten Carbide Catalysts by Use of an Oxygen Plasma Pretreatment. *ACS Catal.* **2012**, *2* (5), 765–769.

- (96) Yang, X. G.; Wang, C. Y. Nanostructured Tungsten Carbide Catalysts for Polymer Electrolyte Fuel Cells. *Appl. Phys. Lett.* **2005**, *86* (22), 1–3.
- (97) Rodella, C. B.; Barrett, D. H.; Moya, S. F.; Figueroa, S. J. A.; Pimenta, M. T. B.; Curvelo, A. A. S.; Teixeira da Silva, V. Physical and Chemical Studies of Tungsten Carbide Catalysts: Effects of Ni Promotion and Sulphonated Carbon. *RSC Adv.* **2015**, *5* (30), 23874–23885.
- (98) Jinn Wang, S.; Yi Tsai, H.; Chung Sun, S. Characterization of Tungsten Carbide as Diffusion Barrier for Cu Metallization. *Jpn. J. Appl. Phys.* **2001**, *40* (4B), 2642–2649.
- (99) Ghaisas, S. Diffusion Barrier Performance of Pulsed Laser Deposited Amorphous Tungsten Carbide Films. *J. Appl. Phys.* **1991**, *70* (12), 7626–7628.
- (100) Polini, R. Chemically Vapour Deposited Diamond Coatings on Cemented Tungsten Carbides: Substrate Pretreatments, Adhesion and Cutting Performance. *Thin Solid Films* **2006**, *515* (1), 4–13.
- (101) Lee, H. C.; Gurland, J. Hardness and Deformation of Cemented Tungsten Carbide. *Mater. Sci. Eng.* **1978**, *33* (1), 125–133.
- (102) Endrino, J. L.; Nainaparampil, J. J.; Krzanowski, J. E. Magnetron Sputter Deposition of WC-Ag and TiC-Ag Coatings and Their Frictional Properties in Vacuum Environments. *Scr. Mater.* **2002**, *47* (9), 613–618.
- (103) Eser, E.; Ogilvie, R. E.; Taylor, K. A. Structural and Compositional Characterization of Sputter-deposited WC+Co Films. *J. Vac. Sci. Technol.* **1978**, *15* (2), 396–400.
- (104) Xue, Z.; Caulton, K.; Chisholm, M. Low-Pressure Chemical Vapor Deposition of Tungsten Carbide Thin Films. *Chem. Mater* **1991**, *3*, 384–386.
- (105) Jipa, I.; Heinemann, F. W.; Schneider, A.; Popovska, N.; Siddiqi, M. A.; Siddiqui, R. A.; Atakan, B.; Marbach, H.; Papp, C.; Steinrück, H.-P.; Zenneck, U. [Cis-(1,3-Diene)₂W(CO)₂] Complexes as MOCVD Precursors for the Deposition of Thin Tungsten - Tungsten Carbide Films. *Chem. Vap. Depos.* **2010**, *16* (7–9), 239–247.
- (106) Pawbake, A.; Waykar, R.; Jadhavar, A.; Kulkarni, R.; Waman, V.; Date, A.; Late, D.; Pathan, H.; Jadhkar, S. Wide Band Gap and Conducting Tungsten Carbide (WC) Thin Films Prepared by Hot Wire Chemical Vapor Deposition (HW-CVD) Method. **2016**.
- (107) Kim, J. B.; Jang, B.; Lee, H.-J.; Han, W. S.; Lee, D.-J.; Lee, H.-B.-R.; Hong, T. E.; Kim, S.-H. A Controlled Growth of WN_x and WC_x Thin Films Prepared by Atomic Layer Deposition Tungsten Nitride Tungsten Carbide N₂H₂ Plasma Phase Microstructure. *Mater. Lett.* **2016**, *168*, 218–222.
- (108) Kim, D.-H.; Kim, Y. J.; Song, Y. S.; Lee, B.-T.; Kim, J. H.; Suh, S.; Gordon, R. Characteristics of Tungsten Carbide Films Prepared by Plasma-Assisted ALD Using Bis(tert-Butylimido)bis(dimethylamido)tungsten. *J. Electrochem. Soc.* **2003**, *150* (10),

C740.

- (109) Beom Kim, J.; KimWon Seok HanDo-Joong Lee, S.-H.; Kim, S.-H.; Seok Han, W.; Lee, D.-J. Atomic Layer Deposited Nanocrystalline Tungsten Carbides Thin Films as a Metal Gate and Diffusion Barrier for Cu Metallization. *J. Vac. Sci. Technol. A Vacuum, Surfaces, Film.* **2016**, *34* (35), 41504–1.
- (110) Profijt, H. B.; Potts, S. E.; Sanden, M. C. M. van de; Kessels, W. M. M. Plasma-Assisted Atomic Layer Deposition: Basics, Opportunities, and Challenges. *J. Vac. Sci. Technol. A* **2011**, *29* (5), 50801.
- (111) Bor-Wen Chan; Baw-Ching Perng; Sheu, L.; Yuan-Hung Chiu; Han-Jan Tao. Plasma Induced Substrate Damage in High Dose Implant Resist Strip Process. In *8th International Symposium Plasma- and Process-Induced Damage*; IEEE, 2003; pp 73–76.
- (112) Kaminaga, U.; Matsushita, T.; Kohra, K. Surface Damage on Si Substrates Caused by Reactive Sputter Etching. *Jpn. J. Appl. Phys.* **1981**, *20* (5), 893–900.
- (113) Kerrigan, M. M.; Klesko, J. P.; Winter, C. H. Low Temperature, Selective Atomic Layer Deposition of Cobalt Metal Films Using Bis(1,4-Di- *Tert* -Butyl-1,3-Diazadienyl)cobalt and Alkylamine Precursors. *Chem. Mater.* **2017**, *29* (17), 7458–7466.
- (114) Kim, W.-H.; Lee, H.-B.-R.; Heo, K.; Lee, Y. K.; Chung, T.-M.; Kim, C. G.; Hong, S.; Heo, J.; Kim, H. Atomic Layer Deposition of Ni Thin Films and Application to Area-Selective Deposition. *J. Electrochem. Soc.* **2011**, *158* (1), D1–D5.
- (115) Lemaire, P. C.; King, M.; Parsons, G. N. Understanding Inherent Substrate Selectivity during Atomic Layer Deposition: Effect of Surface Preparation, Hydroxyl Density, and Metal Oxide Composition on Nucleation Mechanisms during Tungsten ALD. *J. Chem. Phys.* **2017**, *146* (5), 52811.
- (116) Atanasov, S. E.; Kalanyan, B.; Parsons, G. N. Inherent Substrate-Dependent Growth Initiation and Selective-Area Atomic Layer Deposition of TiO₂ Using “water-Free” Metal-Halide/metal Alkoxide Reactants. *J. Vac. Sci. Technol. A Vacuum, Surfaces, Film.* **2016**, *34* (1), 01A148.
- (117) Zhang, W.; Engstrom, J. R. Effect of Substrate Composition on Atomic Layer Deposition Using Self-Assembled Monolayers as Blocking Layers. *J. Vac. Sci. Technol. A* **2016**, *34* (1), 01A107.
- (118) Fang, M.; Ho, J. C. Area-Selective Atomic Layer Deposition: Conformal Coating, Subnanometer Thickness Control, and Smart Positioning. *ACS Nano* **2015**, *9* (9), 8651–8654.
- (119) Marnett, A.; Merckx, M. J. M.; Karasulu, B.; Roozeboom, F.; Kessels, W. E. M. M.; MacKus, A. J. M. Area-Selective Atomic Layer Deposition of SiO₂ Using Acetylacetone as a Chemoselective Inhibitor in an ABC-Type Cycle. *ACS Nano* **2017**, *11* (9), 9303–9311.

- (120) Xu, Y.; Musgrave, C. B. A DFT Study of the Al₂O₃ Atomic Layer Deposition on SAMs : Effect of SAM Termination. *Chem. Mater.* **2004**, *16*, 646–653.
- (121) Färm, E.; Kemell, M.; Santala, E.; Ritala, M.; Leskelä, M. Selective-Area Atomic Layer Deposition Using Poly(vinyl Pyrrolidone) as a Passivation Layer. *J. Electrochem. Soc.* **2010**, *157* (1), K10–K14.
- (122) Vervuurt, R. H. J.; Sharma, A.; Jiao, Y.; Kessels, W. M. M.; Bol, A. A. Area-Selective Atomic Layer Deposition of Platinum Using Photosensitive Polyimide. *Nanotechnology* **2016**, *27* (40), 405302.
- (123) G. A. Antonellia, S. Reddyb, P. Subramoniumb, J. Henrib, J. Simsb, J. O’loughlinb, N.; Shammac, D. Schlosserc, T. Mountsiere, W. Guod, and H. S. Patterning with Amorphous Carbon Thin Films. *ECS Trans.* **2011**, *35* (4), 701.

**CHAPTER 2: THERMAL ATOMIC LAYER
DEPOSITION OF SN METAL USING SnCl_4 AND A
VAPOR PHASE SILYL DIHYDROPYRAZINE
REDUCING AGENT**

CHAPTER 2: Thermal Atomic Layer Deposition of Sn Metal Using SnCl₄ and a Vapor Phase Silyl Dihydropyrazine Reducing Agent

Eric C. Stevens,^{†‡} Moataz Bellah Mousa,^{†‡} Gregory N. Parsons^{*,†}

[†]Department of Chemical and Biomolecular Engineering, North Carolina State University, 911
Partners Way, Raleigh NC 27695

[‡]These authors contributed equally to this work

2.1 Abstract

This work explores a novel, thermal ALD process to deposit tin metal at low temperature. We employ 1,4-bis(trimethylsilyl)-1,4-dihydropyrazine (DHP) as a reducing agent, to reduce SnCl₄ on silicon substrates. We explored a range of temperatures between 130 and 210 °C to determine the ALD window, which was found to be 170 – 210 °C. We show that this process yields a growth rate of ~0.3 angstroms per cycle at 190 °C. Furthermore, XPS results showed that the film impurity content is significantly reduced by operating at elevated temperatures (e.g., 190 vs 130 °C). The reaction mechanism was explored using *in situ* mass spectrometry and *in situ* quartz crystal microbalance (QCM). Within the ALD temperature window, the QCM results showed a saturated mass gain during the SnCl₄ exposure, and a net mass loss during the DHP dose. Consistent with the QCM results, *in situ* mass spectroscopy data indicate that the DHP exposure step removes surface Cl via formation of volatile trimethylsilyl chloride and pyrazine byproducts, effectively reducing the oxidation state of surface-bound Sn. This work is the first thermal Sn metal ALD process to be reported in literature and the oxidation/reduction chemistry presented here may be applied to other metal precursors, increasing the applicability of metal ALD use in industry.

2.2 Introduction

Tin is an intriguing metal that boasts various applications spanning multiple fields. For example, Sn has been proposed as a candidate material for confinement modulated gap nanowire transistors.^{1,2} Electronic structure calculations¹ suggest that when Sn is confined in nanowire structures less than 5 nm diameter, it undergoes a transition from semimetal to semiconductor, thereby providing an alternative approach to atomic scale transistor scaling.

Tin is also used as an anode for lithium ion batteries.³ Key advantages including an exceptionally high gravimetric capacity (959 mAh/g),⁴ good electrical conductivity (9.17×10^4 S/cm),³ and high Li-ion diffusivity (5.9×10^{-7} cm²/s).⁵ The major drawback for Sn anodes is the large volume expansion (~225%) upon Li-ion insertion, leading to a loss of electrical contact and physical cracking.³ This drawback can be addressed by controlling the metal film thickness,⁶ nanostructure,^{7,8,9} and morphology.^{10,11} Typically, Sn films are deposited on anodes by either electroplating¹¹ or physical vapor deposition¹² but the increasing need for 3D battery architectures and porous anode scaffolds¹³ challenges the coating limits of these techniques. The ability to deposit conformal Sn thin films by a thermally-driven atomic layer deposition (ALD) process could help address these limitations.

In this work, we investigate 1,4-bis(trimethylsilyl)-1,4-dihydropyrazine (abbreviated as DHP) as a vapor-phase reducing agent for Sn ALD from tin (IV) tetrachloride (SnCl₄). First synthesized by Saito et al.,¹⁴ DHP and its derivatives have been used for the salt-free reduction of chloride-containing transition metal complexes. Saito showed that DHP can reduce liquid phase transition metal complexes to a lower oxidation state, but did not explore their efficacy in reduction of vapor phase species.¹⁴ Klesko et al.¹⁵ previously utilized DHP as a vapor phase reducing agent to reduce TiCl₄ to elemental Ti. We propose that DHP can also be used to form Sn metal films via

a thermal ALD process at temperatures below the melting point of Sn (231.9 °C). The hallmark ALD characteristics of precursor exposure saturation, saturated growth conditions vs number of cycles, and ALD temperature window were investigated. Deposited films were tested for thickness uniformity and film purity. As a key addition to the understanding of DHP-based metal ALD, we utilized *in situ* analysis tools to characterize the ALD half-reactions, allowing us to propose a detailed reaction sequence that is consistent with the resulting material properties.

2.3 Experimental

2.3.1 Reactor Setup

All ALD experiments were conducted in a homemade, hot wall, reactor operating in the viscous flow regime. Figure 2.1 shows the reactor schematic. All reactor lines were resistively heated to ~100 °C to prevent precursor condensation during the delivery process. The deposition chamber (~3.5 cm diameter 316 stainless steel tube) was resistively heated using a proportional–integral–derivative (PID) temperature controller. The maximum deposition temperature tested was 210 °C to avoid additional film morphology changes near melting point of bulk Sn at 231.9 °C.¹⁶ The charge cell, indicated in Figure 2.1, allowed for direct precursor charge into a known volume, where the pressure could be measured using a MKS Baratron capacitance manometer. The charge cell delivery allowed for consistent and controlled precursor exposures by continuously monitoring the precursor partial pressure. Dry and clean charge cell volumes were obtained by equipping each charge cell with a separate mechanical pump. The reactor also utilized *in situ* quartz crystal microbalance (QCM) and quadrupole mass spectrometry (QMS) capabilities to monitor the process during ALD processing. Research grade nitrogen (99.999%, Machine & Welding Supply Company) was further purified (Entegris Gate-Keeper) and used as the carrier and purge gas at an operating pressure of ~1.5 Torr.

2.3.2 ALD Precursors and Delivery

DHP was obtained from industry partners and was transferred, in a N₂-filled glovebox, into a quartz bubbler vessel for ALD experiments. The bubbler was connected to the ALD reactor and, prior to initiation of ALD experiments, pumped down for ~5 minutes, at room temperature, to remove excess N₂ and ensure consistent dosing of DHP into the reactor chamber. The DHP bubbler was heated resistively and maintained at ~65-70 °C via a PID temperature controller, to maintain a precursor pressure of ~1.3 Torr to the charge cell. A typical DHP dosing sequence consisted of 1) pump down the charge cell until the pressure was below 100 mTorr, 2) close pneumatic valve to charge cell pump, 3) charge DHP into charge cell for 3 seconds or until charge cell pressure reads ~1.3 Torr, 4) close DHP bottle and open charge cell N₂, 5) dose DHP into deposition chamber for 3-5 seconds using the charge cell N₂ as the carrier gas, 6) purge deposition chamber and charge cell for 50 seconds with their respective N₂ streams.

Tin (IV) chloride (SnCl₄) was purchased from Strem and used as received. SnCl₄ was selected as the metal precursor because it has a suitable vapor pressure of 18.6 Torr @ 20 °C¹⁷ and good thermal stability (up to at least 500 °C).¹⁸ The SnCl₄ vessel was not heated, but the delivery lines were kept at ~100 °C. The dosing sequence for SnCl₄ also incorporated the charge cell delivery, as was used for the DHP, but with a 1 second precursor charge and 3 second dose into the deposition chamber.

For some experiments, deposited Sn layers were directly coated in the same deposition reactor with capping layers consisting of titanium nitride (TiN) followed by titanium dioxide (TiO₂) ALD at 190 °C. These layers were used to limit Sn surface oxidation and adventitious carbon contamination upon exposure to air. TiN and TiO₂ precursors were obtained from Strem and used as received. TiN was deposited directly on top of the Sn layer by tetrakis(dimethylamido)

titanium (TDMAT) and NH_3 , with the TDMAT source temperature resistively heated to 45 °C with a dosing scheme of TDMAT/ N_2 / NH_3 / N_2 :4s/50s/6s/100s. A TiO_2 film was then deposited using the titanium (IV) chloride (TiCl_4) and titanium tetraisopropoxide (TTiP), with the TTiP source temperature resistively heated to 80 °C, (TTiP/ N_2 / TiCl_4 / N_2 : 2s/50s/1s/50s). Based on our own analysis and previous reports of TiN ¹⁹ and TiO_2 ^{20,21} growth rates, we expect that 1300 cycles of TDMAT/ NH_3 produced ~ 80 nm of TiN , and 1500 cycles of TTiP/ TiCl_4 led to ~45 nm of TiO_2 based on cross-sectional SEM measurements.

2.3.3 Substrate Preparation

For *ex situ* analysis, silicon (100) with native oxide substrates were utilized. Si wafers (WRS Materials) were diced into 1 cm × 1 cm pieces using a diamond scribe. To remove the native oxide and form hydrogen terminated silicon (Si-H), the cleaved Si pieces were dipped into a dilute hydrofluoric acid (dHF) solution (7% by volume) for 30 seconds, then rinsed and stored in deionized water. Prior to deposition, cleaved Si pieces were cleaned in hot piranha solution (1:1 H_2SO_4 : H_2O_2 v/v) for 30 minutes to remove organic species, followed by a deionized water rinse. Cleaned Si substrates were placed on a stainless-steel sample holder specifically designed for substrates to be in the center line of the reactor as well as in the center of the ceramic heater (location of thermocouple probe during temperature calibrations), inserted into the reactor, and pumped down to the reactor base pressure ~0.01 Torr. Before deposition began, the samples and sample holder were thermally stabilized for 30 minutes in the reactor under dry N_2 flow at the operating pressure of 1.5 Torr and the desired deposition temperature, between 130 – 210 °C.

To inhibit film oxidation when removing the Si samples for ex-situ analysis, a capping layer was deposited prior to removal of the samples. The capping layer consisted of two films. A TiN ALD film was deposited directly on the Sn film using TDMAT/ NH_3 at 190 °C, followed by a

TiO₂ ALD film using TiCl₄/TTiP at 190 °C. Due to previous reports²² of porosity for TiN films deposited below 200 °C, a waterless TiO₂ ALD process was used to fill the pores in the TiN film. Using ALD processes for pore filling has been well represented in the literature.^{23–26} Selection of TiO₂ specifically was due to the well-studied, waterless deposition process using readily available precursors in our lab.²⁰

For QCM analysis, Au-coated quartz crystals (Inficon, 6 MHz AT-cut quartz, 0.55” diameter, unpolished) were used as received. Before starting deposition runs, the QCM sensor was held in the reactor for \simeq 4 to 6 hours under dry N₂ flow at the operating pressure of 1.5 Torr to allow the sensor to reach thermal equilibrium at the desired deposition temperature. Thermal equilibrium was reached after changes in steady-state QCM frequency were less than \sim 0.5 Hz over 30 minutes. Higher temperatures required longer equilibration times.

2.3.4 *In situ* Characterization

For QCM experiments, a commercial QCM assembly (Cool Drawer, Inficon) was specially modified to allow a constant flow of \sim 0.3 Torr of N₂ to purge the back side of the quartz crystal. This modification prevented unwanted deposition during ALD processing on the electrode contacts. The modified QCM assembly was inserted into the ALD reactor, with the sensor head containing the QCM crystal positioned in the center of the deposition chamber. Mass change measurements were recorded using an Inficon SQM-160 controller at a sampling rate of 10 Hz.

In situ mass spectrometry characterization relied on a MKS Vision 2000c QMS equipped with a triple-filtered quadrupole with a mass range of 1-300 amu. Sampled gases were ionized using a thoriated iridium filament and detected using an electron multiplier (referenced against a Faraday cup detector) with a gain of 100. Calibration of the ionized gas partial pressures was performed with a capacitance manometer.

To maximize conductance of gaseous species during sampling, the lines connecting the reactor exhaust to the QMS inlet had an outside diameter of 2.75 inches. Additionally, these lines were maintained at ~100 °C to prevent undesired precursor condensation and maintain effective purging. Furthermore, the QMS sampling volume was heated to 85 °C. The reported mass fragments for the reactants and products were identified with the aid of NIST mass spectrometry database.²⁷

For direct sampling of the unreacted SnCl₄ and DHP molecules, the data were collected by directly connecting the QMS to the respective precursor charge cell. Charge cell temperatures were maintained at 120 °C to prevent undesired precursor contamination during charge sequences. Prior to collecting data, SnCl₄ or DHP were pulsed directly through the QMS system for at least 50, 1 second sub-doses, separated by 5 second N₂ purges. This method was used such that the resulting spectra should represent characteristic ion fragments for each precursor in the unreacted state. Data were then collected continuously from 20 to 240 m/z during precursor sub-doses.

To monitor the reactants and products during SnCl₄/DHP processing, the QMS was connected to the outlet of the reactor so that all exhaust gas passed through the sampling chamber before going to the rotary vacuum pump. Prior to collecting data, at least 200 cycles of SnCl₄ and DHP were used to condition the reactor walls.

2.3.5 *Ex situ* Characterization

Cross-sectional SEM images were taken of the Si/Sn/TiN/TiO₂ samples using focused ion beam (FIB) and a FEI Verios 460L scanning electron microscope (SEM). For the FIB processing, a 25 μm × 2 μm × 2 μm bar of platinum was deposited while the sample was inside the FIB SEM chamber to protect the area of interest from destruction during the ion milling process. After the

milled channels were prepared in the FIB, the samples were transferred to the Verios SEM for high resolution cross-sectional imaging.

Compositional analysis was performed using a SPECS X-ray photoelectron spectroscopy (XPS) system with a PHOIBOS 150 analyzer. An Al K α X-ray source operated at 400 W was used to generate the X-ray beam and Ar ions were used for the sputtering through the deposited layers. The gathered data was shifted accordingly by referencing the adventitious carbon peak (C 1s) to 284.8 eV. CasaXPS software was used to plot the spectra and determine the elemental concentrations. The NIST XPS database²⁸ was used for peak identification. Sn film composition was also characterized using time of flight secondary ion mass spectrometry (ToF-SIMS) on a TOF.SIMS5 (ION TOF, Inc. Chestnut Ridge, NY). The ToF-SIMS instrument utilized a 10 nA, 1 KeV Cs⁺ ion for depth profiling over a 200 \times 200 μm^2 area. Film analysis used a 0.2 pA Bi₃⁺ primary ion beam to analyze a 50 \times 50 μm^2 area within the sputtered region.

2.4 Results

2.4.1 Quartz Crystal Microbalance

Figure 2.2 shows the resulting mass change during SnCl₄/DHP exposures on untreated, Au-coated QCM crystals using SnCl₄/N₂/DHP/N₂ exposure times of 2s/40s/2s/40s, respectively at a) 130 °C and b) 170 °C. For depositions at 130 °C, the average mass uptake per cycle was non-linear for the first 500 cycles, indicative of a nucleation delay. After approximately 500 cycles, the average mass change increased to ~ 1000 ng/cm²/cycle and was linear for the remaining cycles. The inset in Figure 2.2 a) shows 3 cycles of SnCl₄/DHP at 130 °C, with the individual dose indicated by an arrow, within the region where the mass change per cycle was shown to be linear. The SnCl₄ dose resulted in a mass gain, while the DHP dose resulted in a mass loss. As discussed below, the large mass change at 130°C corresponds to film growth outside the ALD temperature window.

For depositions at 170 °C, growth incubation on Au proceeded over the first 200 cycles, followed by linear mass uptake of ~ 200 ng/cm²/cycle. The inset in Figure 2.2 b) shows 3 cycles of SnCl₄/DHP at 170 °C, within the region where the mass change per cycle was linear. Similar to that observed at 130 °C, SnCl₄ dosing resulted in a mass gain, while DHP dosing resulted in a mass loss.

Figure 2.3 shows other QCM results collected at 150 and 210°C. Prior to recording this data, the Au-coated QCM substrates were exposed to at least 500 (at 150 °C) and 200 (at 210 °C) cycles of SnCl₄/DHP to reduce the potential impacts of film nucleation. The data shows the mass change using multiple, consecutive 2 second sub-doses of SnCl₄ or DHP, where each sub-dose was followed by 100 second (for 150 °C) or 200 second (for 210 °C) N₂ purges. Other data (not shown) confirms that similar trends were observed for purge times exceeding 40 seconds between doses.

Figure 2.3 a) shows 5 total SnCl₄/DHP cycles, with each cycle consisting of 10 (at 150 °C) and 5 (at 210 °C) consecutive SnCl₄ sub-doses, followed by 5 consecutive DHP sub-doses. Figure 2.3 b) shows a zoomed in region from Figure 2.3 a), where SnCl₄ and DHP sub-doses are indicated with arrows. At 150 °C, the first SnCl₄ sub-dose resulted in $\sim 25\%$ of the total mass gain measured for all 10 SnCl₄ sub-doses, with $\sim 80\%$ of the total mass gain occurring after 7 SnCl₄ sub-doses. The first DHP sub-dose resulted in $\sim 70\%$ of the total mass decrease for all 5 DHP sub-doses. The average mass change per cycle for 10 SnCl₄ and 5 DHP sub-doses at 150 °C was 430 ± 50 ng/cm²/cy.

The data in Figure 2.3 also shows that for growth at 210 °C, the mass gain during the SnCl₄ sub-doses produces saturation behavior, with $> 90\%$ of the mass gain occurring within the first two SnCl₄ sub-dose. Likewise, for the DHP doses, the first DHP sub-dose resulted in $\sim 95\%$ of the

total mass decrease. The average mass change per cycle at 210 °C for 5 SnCl₄ and 5 DHP sub-doses was 250 ± 10 ng/cm²/cy.

The net mass change from QCM in Figure 2.3 and data sets at other temperatures collected during steady state saturated growth conditions (after nucleation on Au-coated crystals) was analyzed, and the results are shown in Figure 2.4. Saturation was determined when the resulting mass change during SnCl₄ and DHP sub-doses reached > 95% of the total mass change. For temperatures between 170 and 210°C, the growth rate was nearly constant at ~ 250 ng/cm²/cycle. To confirm the observed trend, deposition was performed at least twice at each temperature. Error bars in Figure 2.4 represent the standard deviation in the average growth rate obtained from separate runs, showing good repeatability in our reactor system. Reduction of the substrate temperature led to a net higher growth rate and more significant run-to-run variance.

2.4.2 Growth Rate on QCM Substrates

The mass uptake values from QCM analysis, coupled with the expected bulk density of Sn ($\rho_{\text{Sn}} = 7.3$ g/cm³), can be used to estimate the SnCl₄/DHP growth thickness per cycle (GPC). The value of ~ 250 nm/cm²/cycle corresponds to ~2.7 Å/cy. The GPC value can be compared to the ideal thickness of a Sn monolayer, t_m calculated using equation (2.1), where the Sn atomic weight, $MW_{\text{Sn}} = 118.71$ g/mol, and $N_A = 6.022 \times 10^{23}$ molecules/mol:

$$t_m = [MW/(N_A \times \rho)]^{1/3} \quad (2.1)$$

From eq. 2.1, the bulk Sn monolayer thickness is ~3Å, indicating that the observed steady-state mass uptake of 250 nm/cm²/cycle measured by QCM between 170 and 210°C corresponds to ~0.9 monolayer/cy.

2.4.3 Film Morphology on QCM and Si Substrates

The films deposited on quartz substrates were analyzed by SEM, and the images are shown in Figure 2.5. Figure 2.5 a) shows an as-received, Au-coated QCM crystal, and b) and c) show the resulting films after 1000 cycles of the SnCl₄/DHP sequence at 150 °C and 190°C, respectively. For depositions at both temperatures, the resulting films were continuous and appear to conform to the rough QCM substrate. At 150°C, particles with diameter of several hundred nanometers can be observed distributed across the surface, with a broad distribution of particle size. Conversely, for depositions performed at 190°C, similar surface particles were not observed.

We also characterized the films using cross-sectional SEM imaging, as shown in Figure 2.6. For these samples, the metal deposition was performed on hydrogen-terminated silicon wafers. In the same reactor, the with a capping layer was then deposited, consisting ALD of TiN followed by ALD TiO₂ using conditions described in the experimental section. This film stack is denoted as Si-H/Sn/TiN/TiO₂. In Figure 2.6, the Sn layer was deposited using 1500 cycles of SnCl₄/DHP at 190 °C. Figure 2.6 a) shows good film uniformity of the deposited Sn layer within the ~ 1 micron lateral scale of the image. Magnified images in Figure 2.6 b) show that 1500 cycles lead to a metal thickness of 41 ± 1 nm. Based on the expected steady state growth rate of ~3 Å/cycle, the observed thickness suggests that on the Si-H surface, a long incubation period (> 1000 cycles) was needed before achieving steady-state growth.

In Figure 2.6 b), it is noteworthy that the TiO₂ and the TiN layers were not discernable from one another via cross-sectional SEM, probably due to interlayer mixing from the pore filling process. The Pt bar was used as a reference, as well as to protect the desired imaging area during ion milling.

2.4.4 Film Composition

To better understand the quality of the deposited films, samples from the same run as that shown in Figure 2.6 (without the Pt overcoat) were used ToF SIMS and XPS analysis.

2.4.4.1 ToF-SIMS Depth Profiling

Figure 2.7 shows the secondary ion counts, obtained via ToF-SIMS, revealing an estimate of the species present within deposited films and their interfaces. Figure 2.7 a) shows four distinct layers present in the sample.

The first layer was ascribed to TiO_2 , with maximum values of TiO_2^- , O_2^- , and $^{37}\text{Cl}^-$ ions detected from 0 – 150 seconds sputtering. The Cl was attributed to the TiCl_4 coreagent. A drop in $^{37}\text{Cl}^-$ around 150 seconds, coupled with a rise in CN^- is attributed to a transition from TiO_2 to TiN , where the CN^- originated from the amino ligands on the TDMAT precursor.

A third layer corresponds to the deposited Sn, indicated by the Sn^- ion counts between 225 – 300 seconds. The Sn^- signal began to rise around 120 seconds of sputtering, which corresponds with the start of the TiN layer. The overlap between the Sn and TiN layer is likely due to porosity of the TiN films. The Sn ions reach a maximum around 240 seconds of sputtering and remains nearly constant until about 300 seconds. The substrate silicon layer is observed by the rise of Si^{2-} secondary ions coupled with the decrease in Sn^- .

Figure 2.7 b) shows the ion counts for potential impurities (SnO_2^- , CN^- , and $^{37}\text{Cl}^-$) within the Sn layer. The SnO_2^- intensity tracks well with the SiO_2^- signal, reaching a maximum near the Sn/Si interface. Maxima for the CN^- and $^{37}\text{Cl}^-$ ions coincide also appear to reach a maximum near the Sn/Si interface. Secondary ion count intensity for CN^- , $^{37}\text{Cl}^-$, and SnO_2^- appear to decrease near the Sn/capping layer interface.

2.4.4.2 XPS Depth Profiling

Figure 2.8 shows the XPS spectra as a function of Ar sputtering time for the same samples analyzed in Figures 6 and 7. After 20 minutes of sputtering to remove adventitious carbon, the survey scans in Figure 2.8 a) shown no discernable Cl 1s signal. Ti 2p and O 1s peaks were observed at 459 and 531 eV, respectively, which corresponded with the TiO₂ portion of the capping layer.

After 120 minutes of sputtering, Sn 3d peaks emerged in the region between 494 and 485 eV. These peaks were observed during all sputter times analyzed (up to 159 minutes), reaching an apparent maximum around 125 – 130 minutes.

After 159 minutes of sputtering, the increasing intensity of the Si 2p peak at 150 eV is indicative of the Sn/Si interface. The small peaks around 319 and 243 eV were assigned to Ar 1s and 2p, respectively, due to ion implantation during the sputtering process. It is important to note that the Ti 2p and O 1s peaks were observed at all sputter times investigated. It was later discovered that the XPS analysis area was unintentionally shifted to the edge of the sputtered area on the sample, leading to edge effects and Ti and O appearing to persist throughout the Sn layer. The presence of Sn 3d peaks between 120 – 159 minutes sputtering in the survey scans gives a rough estimate of the bounds of the Sn layer.

High resolution scans of the Sn 3d, N 1s, C 1s, and Cl 2p regions were performed to obtain elemental concentrations within the Sn layer. Figure 2.8 b) shows the Sn 3d 5/2 region where Sn-Sn and Sn-O bonds were identified at binding energies of 485 and 486.7 eV, respectively. After 20 minutes of sputtering, Sn 3d peaks were not discernable from noise, indicative of the capping layer. Increased sputtering time from 120 to 130 minutes resulted in decrease in the Sn-O peak intensity, coupled with an increase in the Sn-Sn peak intensity. The maximum ratio of Sn-Sn/Sn-O peak

area was observed after 130 minutes of sputtering. After sputtering 159 minutes, the ratio of the Sn–Sn/Sn–O peak area decreases. This result supports a SnO_x region at the Si/Sn interface.

C, Cl, and N impurities were quantified using high resolution scans of the C 1s, Cl 2p, and N 1s after 130 minutes sputtering. Table 1 shows the resulting impurity percentages for films deposited at 130 °C and 190 °C. The peak area as well as the relative sensitivity factor were considered when calculating the impurity percentages using CasaXPS software. At 130 °C, the Sn film contained 5 at.% C, 13 at.% Cl, and 9 at.% N impurities. Conversely, at 190 °C those impurities decreased to 3 at.% C, 2 at.% Cl, and 4 at.% N. The atomic percent of oxygen in the Sn layer could not be determined unambiguously due to the oxygen present in the capping layer.

2.4.5 *In situ* Reaction Monitoring by Quadrupole Mass Spectrometry

In situ quadrupole mass spectrometry was utilized to better understand the half reactions during SnCl₄ and DHP exposures. For these experiments, the reactor temperature was set at 190 °C, and reactant dose sequences were described in the experimental section.

2.4.5.1 Characteristic Mass Fragments of Unreacted SnCl₄ and DHP

Figure 2.9 a) and b) show mass fragmentation patterns for SnCl₄ and DHP, respectively, collected by the mass spectrometer under constant reactant dosing into the deposition chamber.

In Figure 2.9 a), the largest peak was observed at $m/z = 224$, ascribed to SnCl₃⁺, an expected electron impact fragment of SnCl₄. Likewise, in Figure 2.9 b) the most prominent peak occurs at $m/z = 146$, consistent with ionized hexamethyl disilane, which is a likely fragment product of DHP. We choose the peaks at $m/z = 224$ and 146 to monitor SnCl₄ and DHP species, respectively, because of the favorable signal amplitude and because these peaks do not overlap with other expected reactants or byproducts.

2.4.5.2 *In situ* Reaction Analysis during SnCl₄/DHP Processing

Figure 2.10 shows the measured partial pressure at $m/z = 224$ and 146 as a function of time, collected during steady-state deposition at $190\text{ }^{\circ}\text{C}$ using 5 sub-doses of each SnCl₄ and DHP, separated by N₂ purges. The dosing sequence was shown in Figure 2.10 c).

In Figure 2.10 a) the first SnCl₄ sub-dose produces no measurable signal at $m/z = 224$. During the following sub-doses, a peak appears and increases to saturation during the third sub-dose. Figure 2.10 b) shows no detectable signals for DHP at $m/z = 146$ or any other peaks shown in Figure 2.9 a) during any SnCl₄ sub-doses.

During DHP exposures, Figure 2.10 b) shows the first DHP sub-dose produces a signal at $m/z = 146$, followed by a less intense signal, which appears to saturate, during the 2nd to 5th sub-doses. During DHP sub-dosing, no signal was observed related to SnCl₄ fragments shown in Figure 2.9 a).

Potential reaction byproducts produced during the SnCl₄/DHP reaction include TMS-Cl and pyrazine. From the NIST mass spectroscopy database,²⁸ TMS-Cl is expected to give peaks at $m/z = 65, 73, 74, 77, 93,$ and 95 , and pyrazine at $m/z = 53$ and 80 . To observe these products, we chose to monitor peaks at 93 and 80 , respectively, since they showed the most prominent signal-to-noise ratio. The QMS results for TMS-Cl and pyrazine (not shown) were convoluted due to overlap with mass fragments of the parent DHP molecule shown in Figure 2.9 b). Other potential reaction by-product signals, including $m/z = 188$ for 1-chloro, 4-trimethylsilyl dihydropyrazine, and $m/z = 50$ for chloromethane, were also collected, but the intensity was too small to be discerned from noise for all DHP and SnCl₄ sub-dose and purge steps.

2.5 Discussion

2.5.1 Proposed SnCl₄/DHP Reaction Mechanism

Based on the observed growth rate and the in-situ mass spectroscopy results, we hypothesize the reaction mechanism for Sn ALD using SnCl₄ and DHP in Figure 2.11. During the SnCl₄ dose step, the SnCl₄ is anticipated to adsorb on the deposition substrate, possibly through electrostatic interactions between the electron-rich metal surface and the positively charged Sn⁴⁺ in SnCl₄. During the DHP exposure step, available Cl species on the growth surface promote cleavage of Si-N bonds in the DHP, forming thermodynamically favored Si-Cl bonds (i.e. trimethylchlorosilane) and heterocyclic aromatic pyrazine. The removal of Cl atoms results in the donation of electrons to form a Sn-Sn bond. Subsequent formation of Sn-Sn bonds is expected to occur until all DHP is consumed or the surface Cl species are not accessible to the DHP molecule. The following sections describe the how each key step in this process relates to the observed experimental results.

2.5.1.1 SnCl₄ Adsorption

The QCM results in Figures 2 and 3 show mass gain upon SnCl₄ exposure step during steady-state growth, consistent with adsorption of the metal halide precursor. Within the ALD window (i.e. at 190°C used for QCM), the mass uptake saturates after the first 2 second SnCl₄ sub-dose. Likewise, the *in situ* QMS results in Figure 2.10 are consistent with consumption of the SnCl₄ precursor during the first sub-dose step. The SnCl₄ adsorption step within the ALD window is consistent with models of other reactant systems during ALD, including for example, redox active Cu(II) precursor dissociation during Cu ALD.²⁹

At lower temperatures, outside the ALD window (i.e., 150°C), Figure 2.3 shows excess mass uptake during SnCl₄ sub-doses, and ToF-SIMS (Figure 2.7) and XPS (Figure 2.8) show excess Cl, consistent with incomplete Cl desorption.

2.5.1.2 DHP Desilylation and Pyrazine Elimination

QCM results in Figures 2 and 3 show mass loss during DHP exposure, which we ascribe to loss of surface Cl forming Sn-Sn bonds and volatile trimethyl chlorosilane and pyrazine, as shown in Figure 2.11. The XPS results in Table 1 show a decrease in Cl impurities with increased temperature, indicating more efficient removal of Cl by DHP at elevated deposition temperatures. Klesko et al.¹⁵ hypothesized that since the proposed DHP intermediate ring structure is antiaromatic (i.e., $8\pi e^-$ in the ring structure), the driving force for the metallic surface reduction lies in the negative reduction potential of the DHP dianion ($E_{1/2}$ -2.32 V vs. ferrocene) formed during the desilylation process.

In Figure 2.10 b), the peak at $m/z = 146$ was relatively large during the first sub-dose and decreased to saturation during subsequent sub-dosing. This result would imply that $m/z = 146$ is not only a fragment of the unreacted DHP precursor (Figure 2.9 b), but also a byproduct of the SnCl₄/DHP process. The propensity to form the hexamethyl disilane structure shown in Figure 2.10 b) is thus more likely to proceed during Sn ALD processing than during DHP doses only. As a byproduct of the reaction, QMS results for the $m/z = 146$ peak in Figure 2.10 b) are consistent with those observed with QCM in Figure 2.3 b). Namely, a single DHP sub-dose is sufficient to reduce the surface within the ALD temperature window (e.g.t, 190 °C). Thus, $m/z = 146$, which we ascribe to hexamethyl disilane, is a key reaction byproduct during SnCl₄/DHP processing. The formation of such a mass fragment was not further investigated but could be due to downstream reactions of unreacted DHP and/or reaction byproducts (TMS-Cl and pyrazine).

It may also be possible that the DHP molecule does not bridge two adjacent Sn-Cl sites, but instead only removes one chlorine. This absorption step would likely prevent further absorption on adjacent Sn-Cl sites due to steric hindrance of the bulky remaining DHP structure.

This would also lead to increased Cl, C, and N impurities in the deposited Sn film. Since an increase in the Cl, C, and N impurities was measured at lower deposition temperatures (Figure 2.8), incomplete DHP surface reactions are likely more probable at lower temperature.

Decreasing C and N contamination with increasing temperature (Figure 2.8) may result from more effective pyrazine desorption during N₂ purging. Greater C and N impurities at lower temperatures observed by XPS are indicative of increased pyrazine incorporation into the film. At higher deposition temperatures, less C and N impurities were observed experimentally, which indicates more effective pyrazine desorption.

Lone pair electrons on the N species make pyrazine a weak Lewis base, and may contribute to undesired surface interactions. The incorporation of pyrazine species should be observable during the DHP dose via QCM, yet a net mass loss was observed at both low and high deposition temperatures. Thus, it is likely that excess DHP and as-formed pyrazine are removed during N₂ purging.

2.5.2 Growth Saturation

A region of constant mass uptake per cycle was observed via QCM for deposition temperatures 170 to 210°C (maximum tested temperature), which suggests an ALD window in this temperature range (Figure 2.4). Furthermore, saturated reaction behavior was observed for multiple sub-doses of both SnCl₄ and DHP within the ALD window by QCM (Figures 3 and 4) and QMS (Figure 2.10).

The large mass uptake measured by QCM was ascribed to the increased surface area due to large particles observed on Au-coated QCM substrates (Figure 2.5). Large agglomeration of Sn metal has been previously observed during thin film deposition.^{30,31} For example, Sn films deposited by CVD using Sn[N(SiCH₃)₂]₂ on HF-dipped Si substrates at 350 °C resulted in thick

films with the top surface covered with Sn spheres 500 nm – 7.5 μ m in diameter.³⁰ According to Wang et. al.,³¹ epitaxial growth of Sn metal on Si substrates revealed Sn island growth with continuous layers between islands. This is an example of Stranski-Krastanov growth, where the formation of islands occurs in order to reduce the crystal strain energy.³² Such a growth mechanism would explain the formation of large agglomeration of surface Sn particles observed in this work during ALD processing at low temperatures. Furthermore, for Sn-Al films deposited by co-evaporation, increasing Sn content from 0 to 10 % was shown to increase the average crystal grain size by a factor of at least 5, with films proceeding via an island growth mode.³³

For this work, Sn spheres were observed during ALD processing at 150 °C leading to rough surface morphology. Conversely, depositions at higher temperatures (i.e., 190 °C) would promote greater surface diffusion, facilitating island coalescence. The nucleation and growth regimes of the SnCl₄/DHP process requires further study to better understand the discrepancy in expected thickness values calculated from the mass change on Au-coated QCM substrates and cross-sectional SEM observations on H-terminated Si

In addition to Sn surface agglomerates contributing to the surface area available to ALD, unpolished QCM crystals were previously shown to have at least 16% larger surface area than the geometric surface area (assuming a planar substrate).³⁴ Rough QCM deposition surfaces, which can be seen in Figure 2.5 b), would contribute to the larger net mass gain per cycle observed by QCM as this increases the active area available to ALD precursors.^{34–37} Including the 16% increase in active surface area, the average mass change can be adjusted and the resulting GPC at 190 °C decreases from 2.7 Å/cy (0.9 monolayer/cy) to 2.3 Å/cy (0.77 monolayer/cy).

The density of the Sn films was not measured but could also be a contributing factor to the SnO₂ observed throughout the film. Thus, a capping layer would need to be used to prevent film

oxidation, should a metallic Sn layer be desired. Furthermore, the use of an N-free reducing agent would presumably remove N impurities from the film, which could increase film quality and density. Such a reducing agent was explored, and compared with DHP, by Klesko et al.¹⁵

2.5.3 Film Composition

ToF-SIMS (Figure 2.7) and XPS (Figure 2.8) data confirm the presence of Sn metal for films deposited at 190 °C. As discussed previously, there may be an interfacial SnO₂/SiO₂ layer present at the interface between the Si and Sn film. The maxima of the SnO₂⁻ and SiO₂⁻ peaks in Figure 2.7 b) occur at nearly the same sputtering times as the corresponding CN⁻ and ³⁷Cl⁻ maxima, which may be due to incomplete surface reactions, leaving behind C, N, and Cl impurities. This implies that the Sn film has a higher impurity concentration near the oxide interface but decreases as the film thickness increases.

The impurity content at the Sn/Si interface appears to be, in part, due to starting surface of the Si substrate. Since an HF clean was used to remove the ~ 2 nm native oxide, leaving the surface hydrogen terminated, the oxygen contamination most likely occurred once the sample was loaded into the reactor. Using the QMS, the partial pressure of H₂O was measured, using the m/z 18 peak, to be ~ 0.002 Torr. This value can be attributed to the background H₂O in the reactor. Since samples were allowed to reach a thermal equilibrium under N₂, with pressure 1.5 Torr, for at least 30 minutes, a partial oxidation of the Si surface is possible.

The observation of Sn–O throughout the Sn layer was in part attributed to edge effects during XPS analysis. Analyzing a region which contains part of the sputtered edge would provide information from range of film depths. Furthermore, it is possible that there could be some mixing effects from the TiO₂ layer which may be oxidizing the Sn films during Ar sputtering to give SnO_x. To rule out this mixing phenomenon, a non-oxide capping layer would be needed. The reactor used

for this study was not suitable to deposit such a capping layer due to precursor and temperature constraints.

The Sn/Si and Sn/Capping Layer interfacial regions shown in Figure 2.7 are expected to be exaggerated. Previous studies have shown that atomic mixing and recoil implantation are readily observed at film interfaces.³⁸ Knowledge of this phenomena makes accurately assigning layer interfaces to specific sputtering times difficult. For example, TiO₂ looks to extend well into the Sn layer, yet the sputtering yields of the two materials at the interface are most likely responsible for the interfacial blending. It is also apparent that the O₂⁻ counts track with that of the TiO₂⁻, implying that oxygen from the capping layer undergoes atomic mixing and recoil implantation and may not be present throughout the Sn film.

2.6 Conclusions

This work demonstrated the first thermal ALD process for depositing Sn metal from SnCl₄ and DHP. ALD process parameters were determined, such as an ALD window between 170 – 210 °C (maximum temperature tested), saturated linear mass uptake (~200 ng/cm²/cy), a growth rate of ~0.3 Å/cy, and good thickness uniformity over tens of microns. An oxidation/reduction mechanism was proposed for the DHP and SnCl₄ system. Firstly, SnCl₄ densified on the substrate followed by an exposure of the DHP reducing agent. The DHP underwent a desilylation process, removing Cl groups from the surface bound Sn-Cl, giving off volatile TMS-Cl and forming an intermediate DHP ring structure. The intermediate species, which is an anti-aromatic ring structure, donates electrons to form a Sn-Sn bond and eliminate as aromatic pyrazine.

This mechanism was tested using *in situ* QCM and QMS experiments. Within the ALD window, the SnCl₄ appeared to densify on the starting surface leading to a mass increase, and saturated after 1- 2 consecutive sub-doses. No other reactants or products were observed during

SnCl₄ dosing, confirming SnCl₄ adsorption and surface densification. DHP sub-doses also revealed saturated reaction conditions, with a net mass loss was observed, indicative of Cl removal via TMS-Cl byproducts. Since a net mass loss was observed for the DHP dose, it can be assumed that the intermediate species is removed before the subsequent SnCl₄ dose and most likely eliminated as pyrazine. At temperatures below the ALD window, desorption of excess SnCl₄ was slower than at higher temperature.

The film purity of the deposited films was analyzed using ToF-SIMS and XPS. A lower concentration of C, N, and Cl impurities was observed for Sn films deposited at 190 °C (3 at.% C, 4 at.% N, and 2 at.% Cl) compared to those at 130 °C (5 at.% C, 9 at.% N, and 13 at.% Cl). At low temperature, the higher impurity percentages are most likely due to incomplete SnCl₄ desorption, which then introduces steric hindrance effects for Cl removal by DHP. Furthermore, the aromatic pyrazine molecule produced during the elimination process is a weak Lewis base, which may lead further incorporation into the film at lower temperatures. The oxidation/reduction chemistry presented here may be applied to other metal precursors and may increase the applicability of metal ALD for a variety of purposes.

2.7 Acknowledgements

The authors acknowledge the financial support from the Semiconductor Research Corporation (SRC task# 2401.001) and the National Defense Science and Engineering Fellowship Program. Acknowledgement is also due to the Analytical Instrumentation Facility (AIF) at North Carolina State University, which is supported by the State of North Carolina and the National Science Foundation, and Duke's Shared Materials Instrumentation Facility.

2.8 Figures for Chapter 2

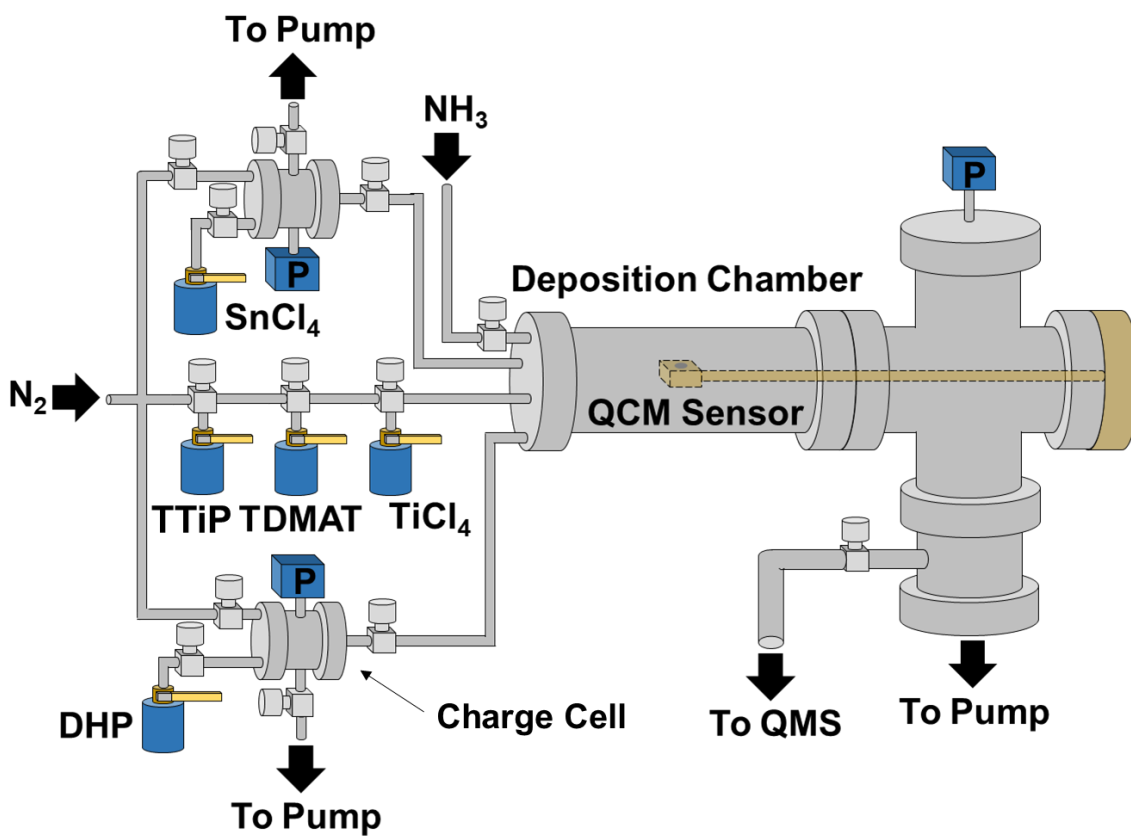


Figure 2.1: Homemade, hot wall ALD reactor with direct-port and charge cell precursor delivery. N_2 carrier and purge gas was used, with an operating pressure of 1.5 Torr. *In situ* QCM and QMS capabilities were used to monitor the mass uptake and reaction byproducts, respectively, during ALD processing.

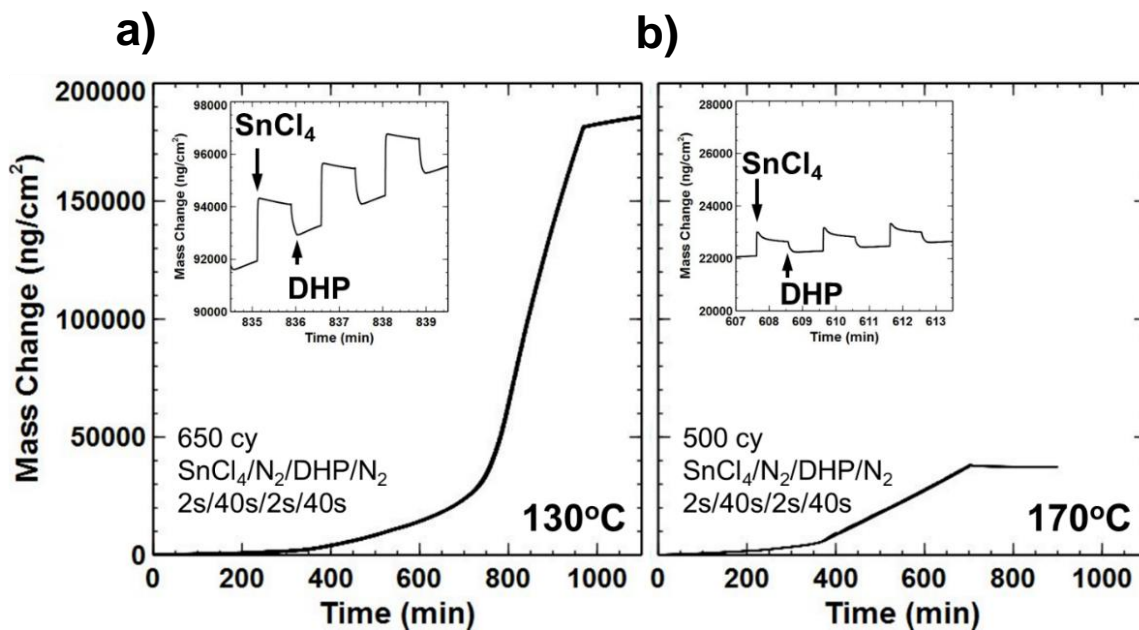


Figure 2.2: Mass change, measured by QCM, as a function of deposition time during SnCl₄/N₂/DHP/N₂ (2s/40s/2s/40s) processing at a) 130 °C for 650 cycles and b) 170 °C for 500 cycles. Depositions were carried out on as-received Au-coated QCM crystals. Inset graphs show 3 cycles of SnCl₄/N₂/DHP/N₂ within linear mass uptake regions, with solid arrows indicating SnCl₄ and DHP dosing.

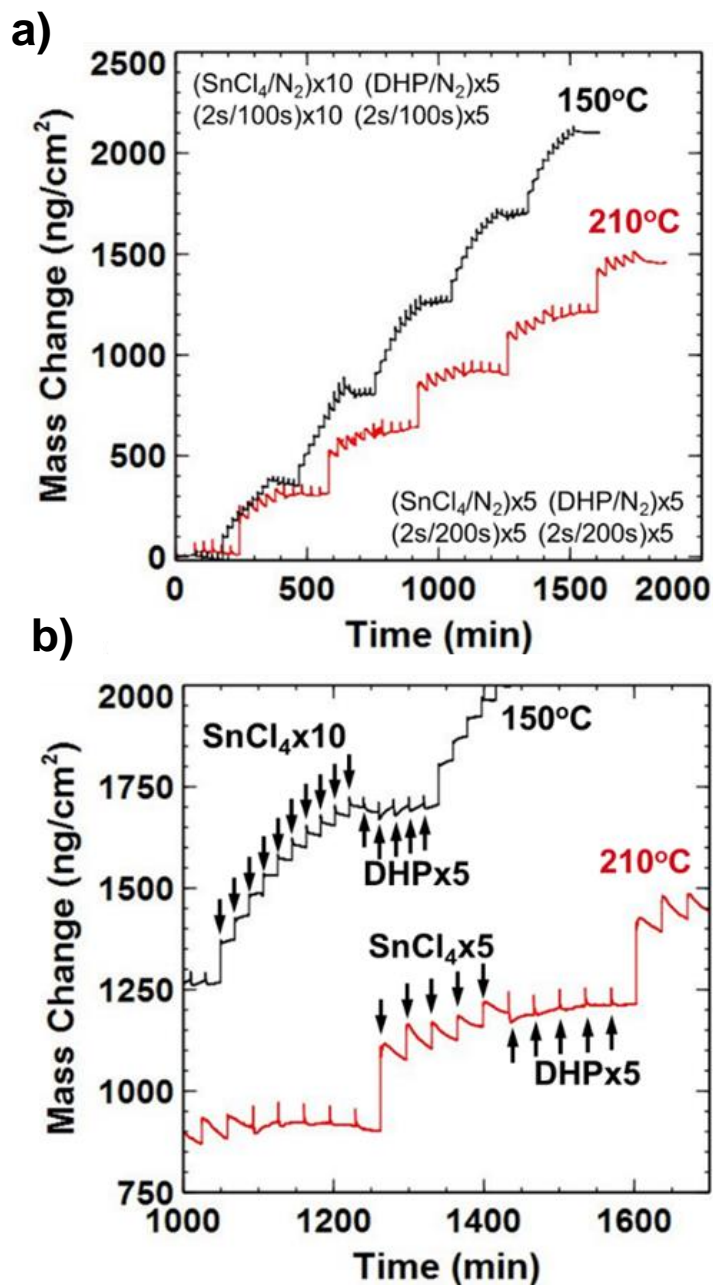


Figure 2.3: a) Mass change vs. deposition time, obtained by *in situ* QCM, during multiple consecutive SnCl₄/DHP exposures as a function of the deposition temperature, 150 (top, black line) and 210 °C (bottom, red line). b) Magnified region from a) to show sub-dose behavior. Solid arrows indicate the instance of 2 second SnCl₄ and DHP doses, separated by 100 and 200 second N₂ purges for depositions carried out at 150 and 210 °C, respectively.

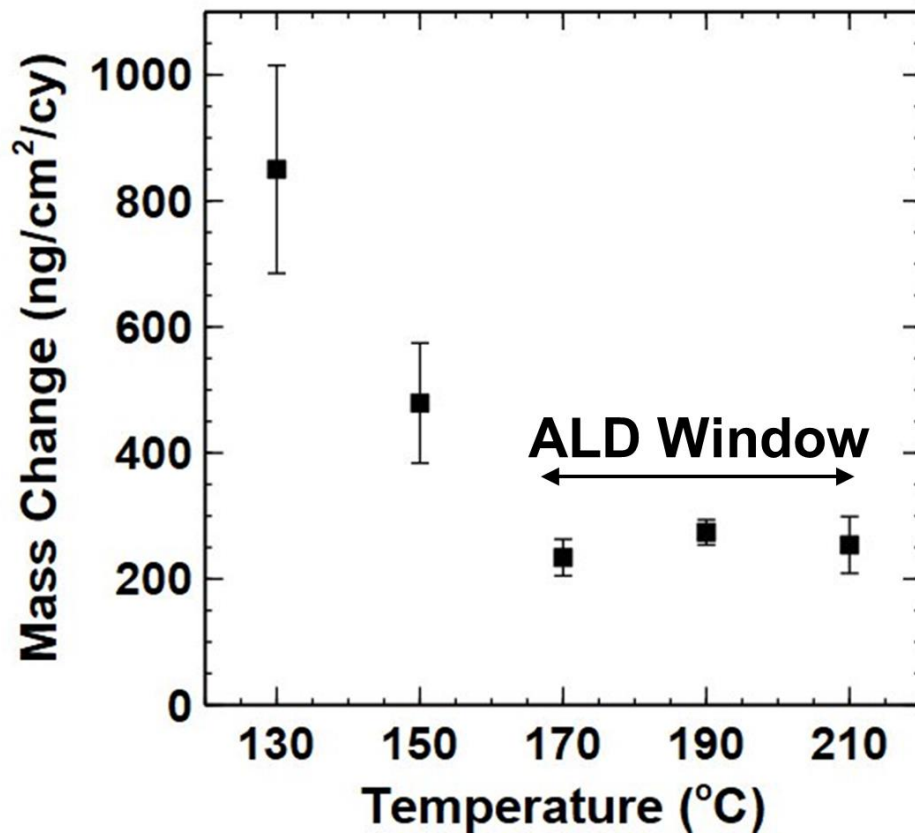


Figure 2.4: Mass change, obtained by QCM, showing the average mass uptake per cycle obtained during SnCl₄/DHP depositions at 130, 150, 170, 190, 210 °C. The reported mass change is an average of the values obtained with saturated consecutive exposures, at a given temperature.

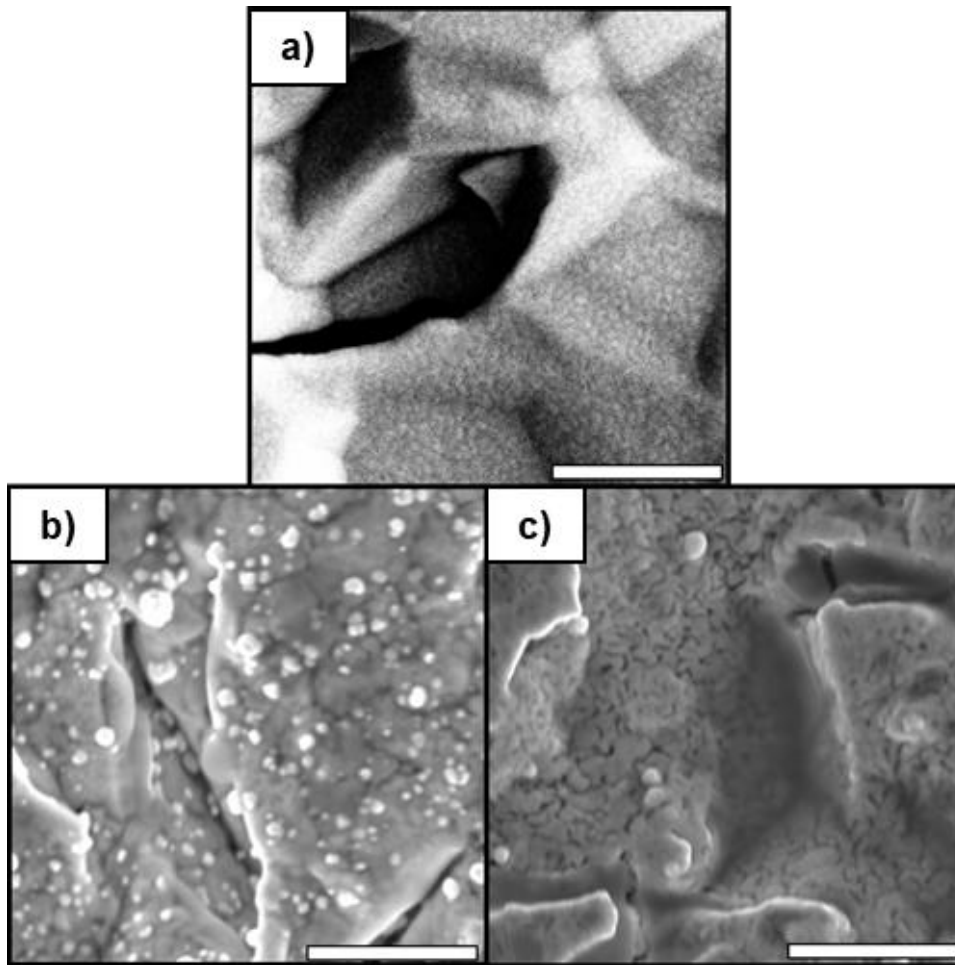


Figure 2.5: Top-down SEM images of a) as-received Au-coated QCM crystal, b) 1000 cycles of SnCl₄/DHP deposited at 150 °C on Au-coated QCM crystal, c) 1000 cycles of SnCl₄/DHP deposited at 190 °C on Au-coated QCM crystal. Scale bars 2 μm.

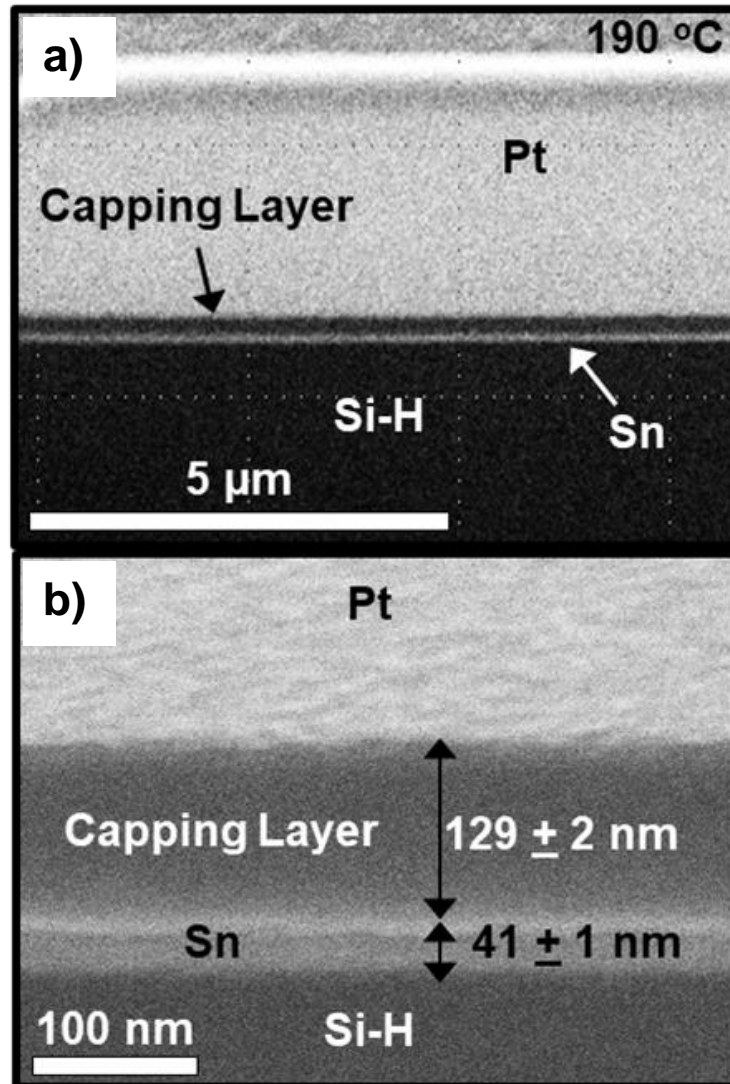


Figure 2.6: a) Cross-sectional SEM image of the Si-H/Sn/TiN/TiO₂ sample deposited at 190 °C (1500 cycles SnCl₄/DHP, 1300 cycles TDMAT/NH₃, 1500 cycles TTiP/TiCl₄) and cut using a Focused Ion Beam. The platinum bar was used to protective the area of interest during ion milling. Sn films show good thickness uniformity over the micron length scales. b) Magnified SEM image of a). The average thickness of the Sn layer was 41 ± 1 nm and the total capping layer thickness was 129 ± 2 nm.

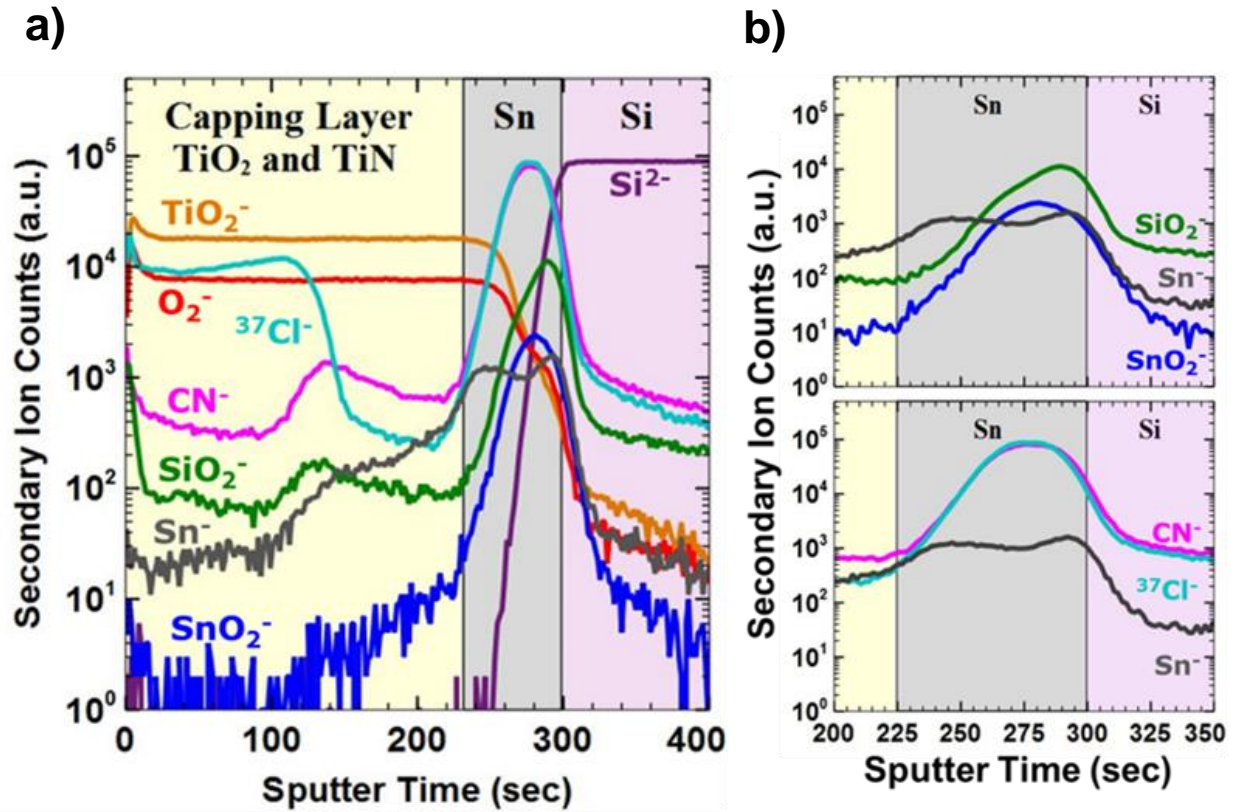


Figure 2.7: a) ToF-SIMS results of the Si-H/Sn/TiN/TiO₂ sample used for FIB SEM. Layers were labeled and color coded as follows: “Capping Layer TiO₂ and TiN” – yellow, “Sn” – grey, “Si” – purple. The ions tracked for the capping layer were TiO₂⁻ (orange), O₂⁻ (red), ³⁷Cl⁻ (teal), and CN⁻ (pink). The Sn⁻ (grey), SiO₂⁻ (green), and SnO₂⁻ (blue) were used to identify the Sn region. b) O, C, N, and Cl impurities within the Sn region.

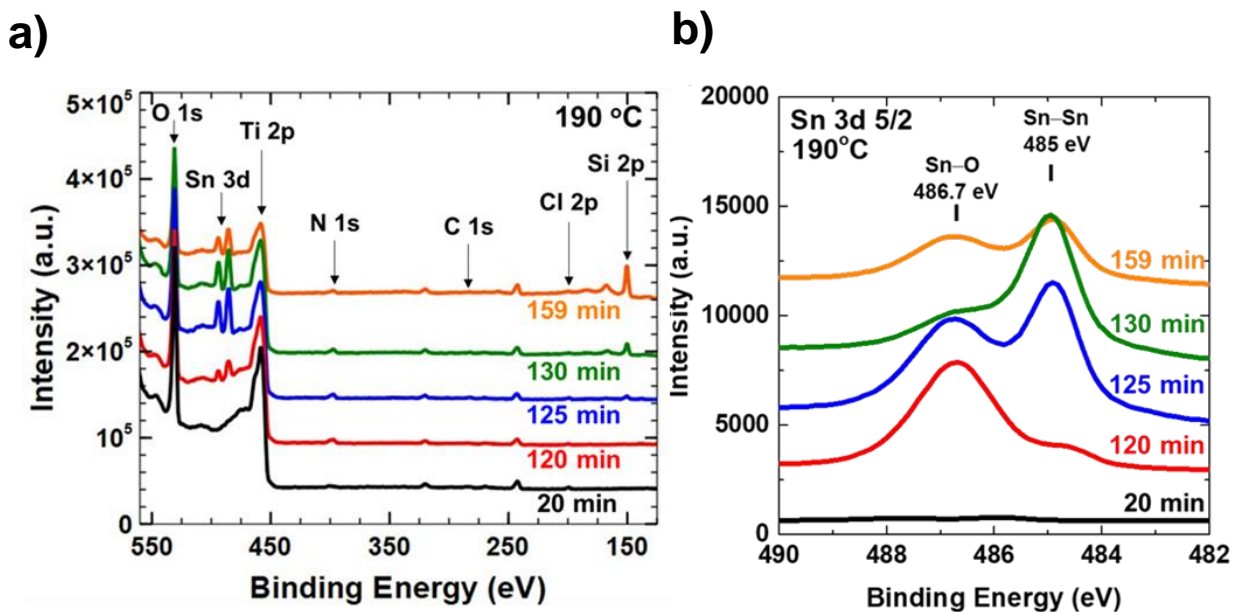


Figure 2.8: a) XPS survey scans of the Si-H/Sn/TiN/TiO₂ stack deposited at 190°C, with offset spectra for visual clarity. Each line represents the resulting survey scan of the same sample after 20 – 159 minutes Ar sputtering. After roughly 120 minutes of sputtering (red line), the Sn 3d peaks between 500 - 480 eV start to increase in intensity. A maximum in the Sn 3d peak intensity most likely occurs between 125 – 159 minutes of sputtering. After 159 minutes of sputtering, the Sn 3d peak intensity decreases accompanied with a rise Si 2p peak intensity, indicative of the underlying Si substrate. b) High resolution scans of the Sn 3d 5/2 region showing Sn-Sn (485 eV) and Sn-O (486.7 eV) chemical bonds as a function of Ar sputter time of the same samples in a). Spectra offset for visual clarity.

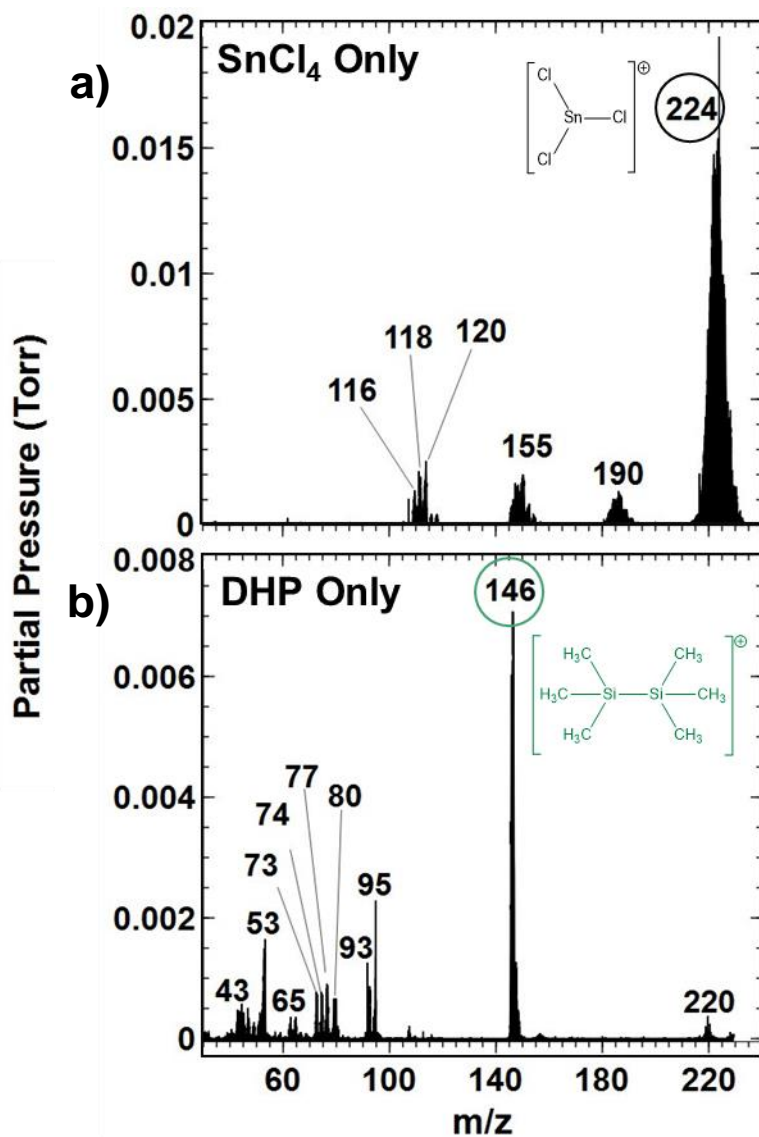


Figure 2.9: Analog mass spectrometry scans from direct sampling of each individual charge cell (maintained at 120 °C), and thus the unreacted SnCl₄ and DHP species. a) SnCl₄ mass fragmentation patterns for 50 consecutive doses, separated by N₂ purges. Most prominent peak observed at m/z = 224, with predicted structure of the SnCl₄ mass fragment shown. b) DHP mass fragmentation patterns for 50 consecutive doses, separated by N₂ purges. Most prominent peak observed at m/z = 146, with predicted structure of the DHP mass fragment shown.

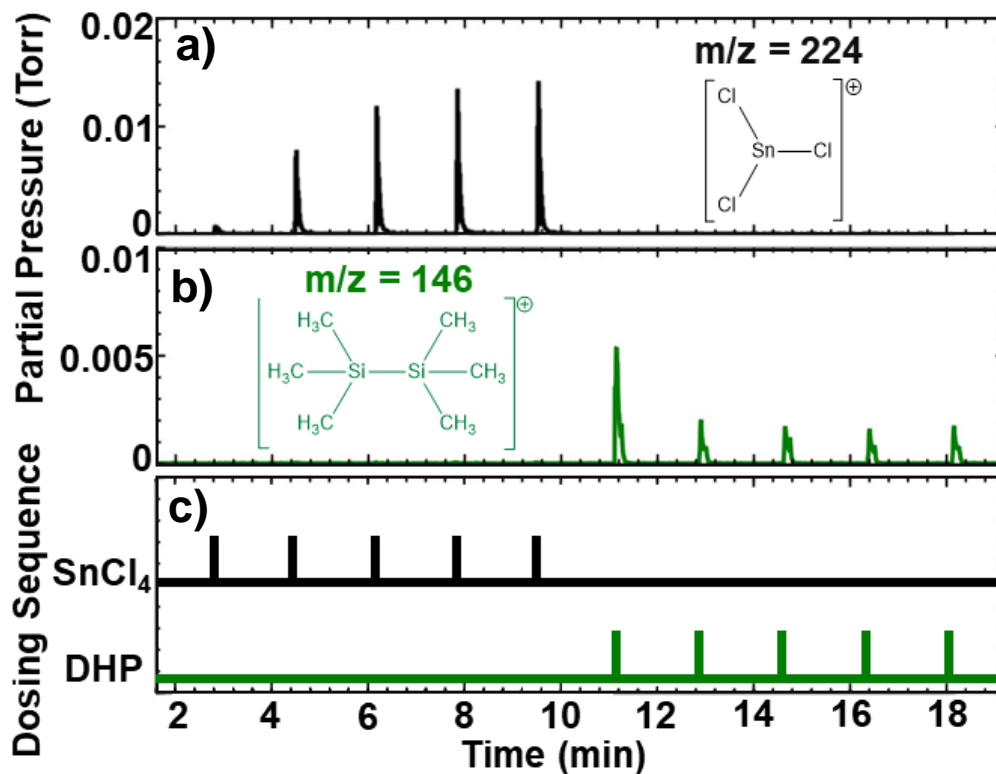


Figure 2.10: QMS data during SnCl₄/DHP processing at 190 °C on Si substrates for 5 sub-doses of SnCl₄ followed by 5 sub-doses of DHP, separated by N₂ purges. Most prominent mass fragments a) $m/z = 224$ (black) and b) 146 (green) shown with their respective predicted structures. c) SnCl₄/DHP dosing sequence corresponding to the QMS data in a) and b).

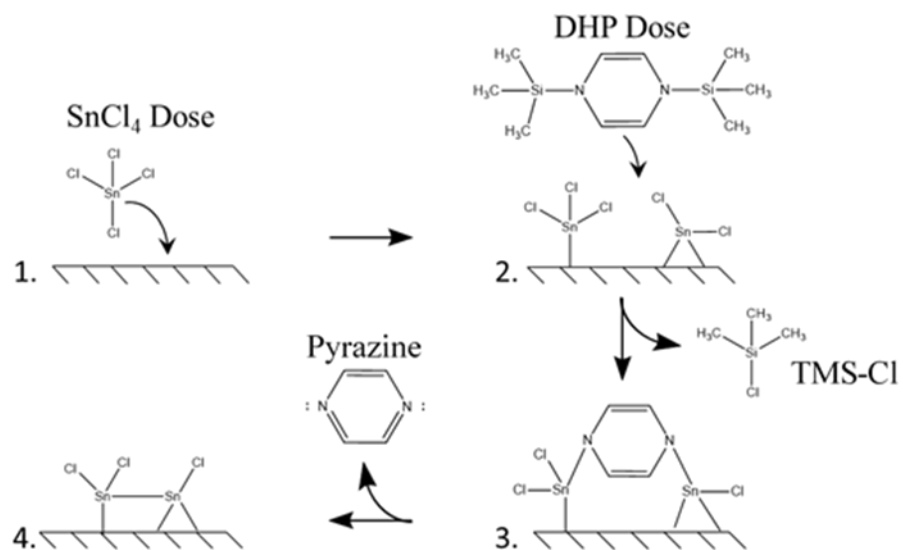


Figure 2.11: Proposed reaction mechanism between DHP and two surface-bound SnCl_x species.

1) SnCl₄ exposure and subsequent densification gives a Sn-Cl surface. 2) DHP is exposed to the Sn-Cl surface, breaking Si-N bonds on the DHP to give off TMS-Cl byproducts. 3) Intermediate ring structure which can donate electrons to create a Sn-Sn bond and eliminate pyrazine. 4) One Sn-Sn bond formed per DHP molecule.

2.9 Tables for Chapter 2

Table 2.1: Film Impurity Content from XPS Analysis vs. Deposition Temperature

Element	130 °C Atomic%	190 °C Atomic%
Cl	13 ± 2.0	2 ± 0.4
N	9 ± 1.5	4 ± 0.5
C	5 ± 1.2	3 ± 0.4

2.10 References

- (1) Ansari, L.; Fagas, G.; Colinge, J. P.; Greer, J. C. A Proposed Confinement Modulated Gap Nanowire Transistor Based on a Metal (Tin). *Nano Lett.* 2012, 12, 2222–2227.
- (2) Ansari, L.; Fagas, G.; Greer, J. C. Strain Induced Effects on Electronic Structure of Semi-Metallic and Semiconducting Tin Nanowires. *Appl. Phys. Lett.* 2014, 105, 123105.
- (3) Whiteley, J. M.; Kim, J. W.; Kang, C. S.; Cho, J. S.; Oh, K. H.; Lee, S.-H. Tin Networked Electrode Providing Enhanced Volumetric Capacity and Pressureless Operation for All-Solid-State Li-Ion Batteries. *J. Electrochem. Soc.* 2015, 162 (4), 711–715.
- (4) Goward, G. R.; Taylor, N. J.; Souza, D. C. S.; Nazar, L. F. The True Crystal Structure of Li_{17}M_4 (M=Ge, Sn, Pb)-Revised from Li_{22}M_5 . *J. Alloys Compd.* 2001, 329, 82–91.
- (5) Anani, A.; Crouch-Baker, S.; Huggins, R. A. Kinetic and Thermodynamic Parameters of Several Binary Lithium Alloy Negative Electrode Materials at Ambient Temperature. *J. Electrochem. Soc.* 1987, 134 (12), 3098–3102.
- (6) Li, J.; Dozier, A. K.; Li, Y.; Yang, F.; Cheng, Y.-T. Crack Pattern Formation in Thin Film Lithium-Ion Battery Electrodes. *J. Electrochem. Soc.* 2011, 158 (6), A689–A694.
- (7) Liu, Z.; Deng, B.; Cheng, G. J.; Deng, H.; Mukherjee, P. P. Mesoscale Elucidation of Laser-Assisted Chemical Deposition of Sn Nanostructured Electrodes. *J. Appl. Phys.* 2015, 117 (21), 214301.
- (8) Alaf, M.; Gultekin, D.; Akbulut, H. Tin/Tin oxide (Sn/SnO_2) Nanocomposites Thin Films as Negative-Electrode Materials for Li-Ion Batteries. *123* (2), 323–325.
- (9) Han, J.; Kong, D.; Lv, W.; Tang, D.-M.; Han, D.; Zhang, C.; Liu, D.; Xiao, Z.; Zhang, X.; Xiao, J.; He, X.; Hsia, F.-C.; Zhang, C.; Tao, Y.; Golberg, D.; Kang, F.; Zhi, L.; Yang, Q.-H. Caging Tin Oxide in Three-Dimensional Graphene Networks for Superior Volumetric Lithium Storage. *Nat. Commun.* 2018, 9 (1), 402.
- (10) Goodenough, J. B.; Kim, Y. Challenges for Rechargeable Li Batteries. *Chemistry of Materials.* 2010.
- (11) Ui, K.; Kikuchi, S.; Kadoma, Y.; Kumagai, N.; Ito, S. Electrochemical Characteristics of Sn Film Prepared by Pulse Electrodeposition Method as Negative Electrode for Lithium Secondary Batteries. *J. Power Sources* 2009, 189 (1), 224–229.
- (12) Hu, R. Z.; Zeng, M. Q.; Zhu, M. Cyclic Durable High-Capacity $\text{Sn}/\text{Cu}_6\text{Sn}_5$ Composite Thin Film Anodes for Lithium Ion Batteries Prepared by Electron-Beam Evaporation Deposition. *Electrochim. Acta* 2009, 54 (10), 2843–2850.
- (13) Arthur, T. S.; Bates, D. J.; Cirigliano, N.; Johnson, D. C.; Malati, P.; Mosby, J. M.; Perre, E.; Rawls, M. T.; Prieto, A. L.; Dunn, B. Three-Dimensional Electrodes and Battery Architectures. *MRS Bull.* 2011, 36, 523–531.

- (14) Saito, T.; Nishiyama, H.; Tanahashi, H.; Kawakita, K.; Tsurugi, H.; Mashima, K. 1,4-Bis(trimethylsilyl)-1,4-Diaza-2,5-Cyclohexadienes as Strong Salt-Free Reductants for Generating Low-Valent Early Transition Metals with Electron-Donating Ligands. *J. Am. Chem. Soc.* 2014.
- (15) Klesko, J. P.; Thrush, C. M.; Winter, C. H. Thermal Atomic Layer Deposition of Titanium Films Using Titanium Tetrachloride and 2-Methyl-1,4-Bis(trimethylsilyl)-2,5-Cyclohexadiene or 1,4-Bis(trimethylsilyl)-1,4-Dihydropyrazine. *Chem. Mater.* 2015, 27, 4918–4921.
- (16) Haynes, W. M. *Handbook of Chemistry and Physics*, 96th ed.; Taylor and Francis Group, 2015.
- (17) Tin (IV) Chloride (Anhydrous); International Chemical Safety Card No. 0953 (U.S. National Version); National Institute for Occupational Safety and Health, Centers for Disease Control and Prevention: Atlanta, GA, 2001, <http://www.cdc.gov/niosh/ipcsneng/nen>.
- (18) Nazarov, D. V.; Bobrysheva, N. P.; Osmolovskaya, O. M.; Osmolovsky, M. G.; Smirnov, V. M. Atomic Layer Deposition of Tin Dioxide Nanofilms: A Review. *Rev. Adv. Mater. Sci.* 2015, 40, 262–275.
- (19) Musschoot, J.; Xie, Q.; Deduytsche, D.; Van den Berghe, S.; Van Meirhaeghe, R. L.; Detavernier, C. Atomic Layer Deposition of Titanium Nitride from TDMAT Precursor. *Microelectron. Eng.* 2009, 86 (1), 72–77.
- (20) Atanasov, S. E.; Kalanyan, B.; Parsons, G. N. Inherent Substrate-Dependent Growth Initiation and Selective-Area Atomic Layer Deposition of TiO₂ Using “water-Free” Metal-Halide/metal Alkoxide Reactants. *J. Vac. Sci. Technol. A Vacuum, Surfaces, Film.* 2016, 34 (1), 01A148.
- (21) Anderson, V. R.; Cavanagh, A. S.; Abdulagatov, A. I.; Gibbs, Z. M.; George, S. M. Waterless TiO₂ Atomic Layer Deposition Using Titanium Tetrachloride and Titanium Tetraisopropoxide. *J. Vac. Sci. Technol. A Vacuum, Surfaces, Film.* 2014, 32 (1), 01A114.
- (22) Elam, J. W.; Schuisky, M.; Ferguson, J. D.; George, S. M. Surface Chemistry and Film Growth during TiN Atomic Layer Deposition Using TDMAT and NH₃. *Thin Solid Films* 2003, 436, 145–156.
- (23) Levrau, E.; Devloo-Casier, K.; Dendooven, J.; Ludwig, K. F.; Verdonck, P.; Meersschant, J.; Baklanov, M. R.; Detavernier, C. Atomic Layer Deposition of TiO₂ on Surface Modified Nanoporous Low- K Films. *Langmuir* 2013, 29 (39), 12284–12289.
- (24) Abell, T.; Schuhmacher, J.; Tokei, Z.; Travaly, Y.; Maex, K. Lateral Solvent Diffusion Characterization of Low K Dielectric Plasma Damage and ALD Barrier Film Closure. *Microelectron. Eng.* 2005, 82 (3–4 SPEC. ISS.), 411–415.

- (25) Karuturi, S. K.; Liu, L.; Su, L. T.; Zhao, Y.; Fan, H. J.; Ge, X.; He, S.; Yoong, A. T. I. Kinetics of Stop-Flow Atomic Layer Deposition for High Aspect Ratio Template Filling through Photonic Band Gap Measurements. *J. Phys. Chem. C* 2010, 114 (35), 14843–14848.
- (26) Liu, Y.; Gibbs, M.; Perkins, C. L.; Tolentino, J.; Zarghami, M. H.; Bustamante, J.; Law, M. Robust, Functional Nanocrystal Solids by Infilling with Atomic Layer Deposition. *Nano Lett.* 2011, 11 (12), 5349–5355.
- (27) Linstrom, P.; Mallard, W. G. NIST Chemistry WebBook, NIST Standard Reference Database Number 69 Gaithersburg MD, 20899: National Institute of Standards and Technology; 2015.
- (28) NIST X-Ray Photoelectron Spectroscopy Database, Version 4.1; National Institute of Standards and Technology: Gaithersburg MD, 20899.
- (29) Dey, G.; Elliot, S. D. Quantum Chemical Study of the Effect of Precursor Stereochemistry on Dissociative Chemisorption and Surface Redox Reactions during the Atomic Layer Deposition of the Transition Metal Copper. *J. Phys. Chem. C* 2015, 119, 5914–5927.
- (30) Baxter, D. V.; Chisholm, M. H.; Gama, G. J.; Hector, A. L.; Parkin, I. P. Low Pressure Chemical Vapor Deposition of Metallic Films of Iron, Manganese, Cobalt, Copper, Germanium and Tin Employing Bis(trimethyl)silylamido Complexes, $M(N(SiMe_3)_2)_n$. *Chem. Vap. Depos.* 1995, 1 (2), 49–51.
- (31) Wang, L. L.; Ma, X. C.; Ji, S. H.; Fu, Y. S.; Shen, Q. T.; Jia, J. F.; Kelly, K. F.; Xue, Q. K. Epitaxial Growth and Quantum Well States Study of Sn Thin Films on Sn Induced Si(111)-(23×23) R30° Surface. *Phys. Rev. B - Condens. Matter Mater. Phys.* 2008, 77 (20).
- (32) Baskaran, A.; Smereka, P. Mechanisms of Stranski-Krastanov Growth Direct Formation of Quantum-Sized Dots from Uniform Coherent Islands of InGaAs on GaAs Surfaces Multidimensional Quantum Well Laser and Temperature Dependence of Its Threshold Current Mechanisms of Stranski-Krastanov Growth. *J. Appl. Phys.* 2012, 111 (40).
- (33) Petrov, I.; Barna, P. B.; Hultman, L.; Greene, J. E. Microstructural Evolution during Film Growth. *J. Vac. Sci. Technol. A Vacuum, Surfaces, Film.* 2003, 21 (5), S117–S128.
- (34) Elam, J. W.; Groner, M. D.; George, S. M. Viscous Flow Reactor with Quartz Crystal Microbalance for Thin Film Growth by Atomic Layer Deposition. *Rev. Sci. Instrum.* 2002, 73 (8), 2981–2987.
- (35) Rechendorff, K.; Hovgaard, M. B.; Foss, M.; Besenbacher, F. Influence of Surface Roughness on Quartz Crystal Microbalance Measurements in Liquids. *J. Appl. Phys.* 2007, 101 (11), 114502.
- (36) Daikhin, L.; Michael Urbakh. Influence of Surface Roughness on the Quartz Crystal Microbalance Response in a Solution New Configuration for QCM Studies. *Faraday Discuss.* 1997, 107 (0), 27–38.

- (37) Yousfi, E. B.; Fouache, J.; Lincot, D. Study of Atomic Layer Epitaxy of Zinc Oxide by in-Situ Quartz Crystal Microgravimetry. *Appl. Surf. Sci.* 2000, 153 (4), 223–234.
- (38) Ignatova, V. A.; Möller, W.; Conard, T.; Vandervorst, W.; Gijbels, R. Interpretation of ToF-SIMS Depth Profiles from Ultrashallow High-K Dielectric Stacks Assisted by Hybrid Collisional Computer Simulation. *Appl. Phys. A Mater. Sci. Process.* 2005, 81 (1), 71–77.

**CHAPTER 3: THERMAL ATOMIC LAYER DEPOSITION
OF TUNGSTEN CARBIDE BY WCl_5 AND TRIMETHYL
ALUMINUM**

CHAPTER 3. Thermal Atomic Layer Deposition of Tungsten Carbide by WCl_5 and Trimethyl Aluminum

Eric C. Stevens,[†] Gregory N. Parsons^{*,†}

[†]Department of Chemical and Biomolecular Engineering, North Carolina State University, 911 Partners Way, Raleigh NC 27695

3.1 Abstract

A new thermal atomic layer deposition process to deposit tungsten carbide is demonstrated using tungsten (V) chloride and trimethyl aluminum from 150 to 325 °C. *In situ* monitoring of the reactions using quartz crystal microbalance showed saturation growth conditions from 300 – 325 °C, with an estimated growth rate of ~0.12 nm/cycle, corresponding to ~0.5 monolayers/cycle. Composition analysis of the deposited films showed a W:C ratio 2:1, implying the formation of W_2C at 300 °C, with ~13 at.% aluminum incorporation and ≤ 2 at.% chlorine. Deposited films were amorphous at all deposition temperatures. From the experimental data, a reaction mechanism is proposed for tungsten carbide formation. The use of the reported films as diffusion barrier layers would be advantageous due to the higher density and amorphous carbide formed W_2C .

3.2 Introduction

The unique properties of tungsten carbide (WC) lead to a variety of important uses for WC thin films, with a wide range of applications such as inexpensive replacements for Pt and other catalysts,¹⁻⁴ diffusion barriers,⁵⁻⁷ and industrial hard coatings due to high strength, hardness, and chemical and thermal stability.^{8,9} WC films are deposited in a range of ways such as high-temperature carbonation of tungsten oxide using CH_4 and H_2 ,¹⁰ sputter deposition,¹¹⁻¹³ chemical vapor deposition (CVD),¹⁴⁻¹⁶ and atomic layer deposition (ALD).¹⁷⁻²⁰

Concerning the continued scaling of the semiconductor and memory industries,²¹ the ever-increasing need for high-purity films, with controllable film thickness and conformal coating-

ability on the nanometer scale furthers the demand for new WC ALD processes. Plasma-assisted ALD processes by bis(tert-butylimido)bis(dimethylamido)tungsten for thin-film W_2C 250 °C was shown previously.¹⁹ Plasma-based processing typically is limited when considering high aspect ratio structures, where radical recombination is increasingly probable as the aspect ratio increases.²² Furthermore, plasma processing can sometimes lead to substrate damage, which could lead to unacceptable defect formation, hindering performance for microelectronic devices.^{23,24}

Thermal ALD processing of tungsten carbide thin films has been demonstrated previously using WF_6 and $H_2Si(C_2H_5)_2$, yet the use of WF_6 causes generation of HF species, which can lead to undesired etching/damage to other components in semiconductor devices. The investigation of thermal WC ALD films with fluorine-free precursors is a necessary to advance the adoption into the semiconductor industry. Recently, thermal ALD of WCl_6 and $Al(CH_3)_3$ was shown to deposit high-purity, amorphous WC films with a growth rate of 0.15 – 0.18 nm/cycle between 275 and 350 °C.¹⁷ This study was very promising for applications as Cu diffusion barriers, with resistivity values of 1500 $\mu\Omega$ -cm at 375 °C. An understanding of the *in situ* growth behavior and possible reaction mechanisms were not demonstrated experimentally.

This work presents the findings of a new thermal ALD process for depositing WC, and possibly W_2C , thin-films using WCl_5 and $Al(CH_3)_3$. Furthermore, we study the reactions *in situ* to gain insights on possible reaction pathways for the formation of tungsten oxide.

3.3 Experimental

3.3.1 Reactor Setup

All ALD experiments were conducted in a homemade, hot wall, reactor operating in the viscous flow regime. All reactor lines were resistively heated to ~150–170 °C to prevent precursor condensation during the delivery process. The deposition chamber (~3.5 cm diameter 316 stainless steel tube) was resistively heated using a proportional–integral–derivative (PID) temperature

controller. The reactor utilized *in situ* QCM to monitor the process during ALD processing. The deposition temperature range tested was 150 – 325 °C, with the upper bound held below 350 °C for consistent and reliable use of quartz crystal microbalance (QCM) instrumentation. Research grade nitrogen (99.999%, Machine & Welding Supply Company) was further purified (Entegris Gate-Keeper) and used as the carrier and purge gas at an operating pressure of ~1.5 Torr.

3.3.2 ALD Precursors and Delivery

Tungsten (V) chloride (WCl_5) was obtained from industry partners and was transferred, in a N_2 -filled glovebox, into a stainless-steel vessel for ALD experiments. The WCl_5 vessel was connected to the ALD reactor and, prior to initiation of ALD experiments, pumped down for ~5 minutes, at room temperature, to remove excess N_2 and ensure consistent dosing into the reactor chamber. The WCl_5 vessel was heated resistively and maintained at ~145 °C via a PID temperature controller. WCl_5 was dosed into the deposition chamber via a three-way valve, with N_2 as the carrier gas. Trimethyl aluminum ($\text{Al}(\text{CH}_3)_3$, or TMA) was purchased from Strem and used as received. The TMA vessel was not heated, but the delivery lines were kept at ~150 – 170 °C. TMA was dosed into the deposition chamber via a three-way valve, with N_2 as the carrier gas. For saturation experiments, multiple consecutive sub-doses of each precursor were employed. For example, for 2-sub doses of each precursor, denoted as $\text{WCl}_5 \times 2 / \text{TMA} \times 2$, the following dosing sequence was used: [1s WCl_5 /30s N_2 /1s WCl_5 /30s N_2] followed by [1s TMA/30s N_2 /1s TMA/30s N_2].

3.3.3 Substrate Preparation and *in situ* QCM

For *ex situ* analysis, silicon (100) with native oxide substrates were utilized. Si wafers (WRS Materials) were diced into 1 cm × 1 cm pieces using a diamond scribe. Prior to deposition, cleaved Si pieces were cleaned in hot piranha solution (1:1 H_2SO_4 : H_2O_2 by volume) for 30 minutes to remove organic species, followed by a deionized water rinse. Cleaned Si substrates were placed

on a stainless-steel sample holder specifically designed for substrates to be in the center line of the reactor as well as in the center of the ceramic heater (location of thermocouple probe during temperature calibrations), inserted into the reactor, and pumped down to the reactor base pressure ~ 0.01 Torr. Before commencing deposition, the samples and sample holder were dried for at least 30 minutes in the reactor, under dry N_2 flow (operating pressure of 1.5 Torr) and the desired deposition temperature, between 150 – 325 °C.

For QCM analysis, Au-coated quartz crystals (Inficon, 6 MHz AT-cut quartz, 0.55” diameter, unpolished) were used as received. A commercial QCM assembly (Cool Drawer, Inficon) was specially modified to allow a constant flow of ~ 0.3 Torr of N_2 to purge the back side of the quartz crystal. This modification prevented unwanted deposition during ALD processing on the electrode contacts. The modified QCM assembly was inserted into the ALD reactor, with the sensor head containing the QCM crystal positioned in the center of the deposition chamber. Before starting deposition runs, the QCM sensor was held in the reactor for $\simeq 4$ to 6 hours under dry N_2 flow at the operating pressure of 1.5 Torr to allow the sensor to reach thermal equilibrium at the desired deposition temperature. Thermal equilibrium was reached after changes in steady-state QCM frequency were less than ~ 0.5 Hz over 30 minutes. Higher temperatures (i.e., $> 300^\circ\text{C}$) required longer equilibration times. For QCM experiments, Mass change measurements were recorded using an Inficon SQM-160 controller at a sampling rate of 10 Hz.

3.3.4 *Ex situ* Characterization

Compositional analysis was performed using a SPECS X-ray photoelectron spectroscopy (XPS) system with a PHOIBOS 150 analyzer. An Al $K\alpha$ X-ray source operated at 400 W was used to generate the X-ray beam and Ar ions were used for the sputtering through the deposited layers. CasaXPS software was used to plot the spectra perform composition analysis. High resolution scans of the W 4f, C 1s, O 1s, Al 2p, Cl 2p, and Si 2p regions were utilized for calculations of

elemental concentrations, considering the relative sensitivity factors given in CasaXPS and the XPS NIST database.²⁵ The NIST XPS database²⁵ was used for some peak identification, while other peaks were identified from the literature.

3.4 Results

3.4.1 Temperature Dependence and on Film Growth by QCM

The temperature dependence of the WCl_5 /TMA reaction was explored using QCM. Figures 3.1 and 3.2 show the mass change, measured by QCM, at 150 and 300 °C, respectively, deposited on two separate Au-coated QCM substrates (as received). For single exposures of WCl_5 /TMA deposited at 150 (Fig. 3.1 a) and 300 °C (Fig. 3.2 a), the average mass uptake per cycle was linear from the first cycle, with values of 210 and 170 $ng/cm^2/cy$, respectively. Increasing the number of consecutive exposures to 5 sub doses of each WCl_5 and TMA, separated by N_2 purges, the average mass uptake per cycle increased to 480 and 230 $ng/cm^2/cy$ for 150 (Fig. 3.1 b) and 300 °C (Fig. 3.2 b), respectively.

To better understand the mass changes during individual doses, the curves shown in Figures 3.1 and 3.2 a) and b) were magnified to show three cycles of WCl_5 /TMA, giving the data shown in Figures 3.1 and 3.2 c) and d). For both temperatures, WCl_5 exposures resulted in a mass gain, while TMA doses resulted in a mass loss. Figure 3.1 d) shows that at 150 °C, the mass increase from the first WCl_5 sub-dose resulted in ~65% of the total mass gain over the 5 sub-doses. Approximately 90% of the total mass gain was reached after the third WCl_5 sub-dose. For TMA doses, the mass decrease during the first TMA sub-dose accounted for ~64% of the total mass loss, with 91% occurring after the third sub-dose. Figure 3.2 d) shows that at 300 °C, the mass increase from the first and second WCl_5 sub-doses resulted in ~70% and 87% of the total mass gain over the 5 sub-doses. For TMA doses, the mass decrease during the first and second sub-dose accounted for ~72% and 90% of the total mass loss.

The average mass change per cycle as a function of deposition temperature (150 – 325 °C) is shown in Figure 3.3. For single exposures, denoted $WCl_5 \times 1 / TMA \times 1$, the averaged mass change was ~ 200 and $150 \text{ ng/cm}^2/\text{cycle}$ for depositions between 150-200 °C and 300-325°C, respectively. For five consecutive sub-doses, denoted $WCl_5 \times 5 / TMA \times 5$, the averaged mass change was as large as $\sim 500 \text{ ng/cm}^2/\text{cycle}$ at 150 °C, decreasing to $\sim 210 \text{ ng/cm}^2$ at 300-325°C. Error bars in Figure 3.3 represent the standard deviation in the average mass change per cycle obtained from separate runs, showing good repeatability.

3.4.2 Dose Saturation

The dose saturation behavior was investigated further by investigating the individual mass change behavior during WCl_5 and TMA sub-doses. A full factorial design of experiments was conducted using 1, 3, and 5 sub-doses of WCl_5 and TMA. The resulting mass gain and loss during WCl_5 and TMA sub-doses, respectively, were averaged over the entire run, which was typically 5-10 cycles. The ratio of the mass gain to mass loss is shown in Figure 3.4 as a function of WCl_5 and TMA sub-doses for deposition temperatures ranging 150 – 325 °C. For lower deposition temperatures (e.g., 150 °C) and low sub-doses (e.g., $WCl_5 \times 1 / TMA \times 1$), the mass gain to mass loss ratio was consistently greater than that for higher deposition temperatures and a greater number of sub-doses. The larger the mass ratio, the greater the mass gain during WCl_5 and/or the mass loss during TMA doses. The data imply dose saturation is reached using at least 3 sub-doses of each WCl_5 and TMA and deposition temperatures exceeding 200 °C.

3.4.3 Growth Rate From QCM

The average mass uptake (Δm) from Figure 3.3 and the density of tungsten carbide, can be used to estimate the expected growth rate per cycle (GPC), in units of nm/cycle, using Equation 3.1. Using the bulk densities of α -WC and α -W₂C of 15.6 and 16.6 g/cm³,²⁶ respectively, the

$$GPC = \Delta m \times \rho^{-1} \tag{3.1}$$

resulting GPC values as a function of temperature and sub-dosing are reported in Tables 3.1 and 3.2. The actual density of the deposited films is expected to be less than the bulk values, common for thin films deposited by ALD.^{27–29} Nevertheless, the calculated GPC values in Tables 3.1 and 3.2 give a good estimate to compare to other reports in the literature. This work found estimated GPC values for $\text{WCl}_5 \times 5 / \text{TMA} \times 5$ processing (which is assumed to be saturated based on QCM results), spanning ~ 0.12 to 0.3 nm/cycle for depositions at 325 and 150 °C, respectively. Previous reports found GPC values of $0.13 - 0.17$ nm/cycle ($250 - 375$ °C) for thermal ALD of $\text{WCl}_6 / \text{TMA}$ ¹⁷ and $0.04 - 0.11$ nm/cycle ($150 - 350$ °C) plasma-enhanced ALD of tungsten tris(3-hexyne) carbonyl and N_2 / H_2 plasma.²⁰ The GPC values estimated in this work compare well with WC ALD processes reported previously.

The theoretical monolayer thickness, t_m , of WC can be estimated using Equation 3.2:

$$t_m = [MW / (N_A \times \rho)]^{1/3} \quad (3.2)$$

where MW, N_A , and ρ are the molecular weight (WC - 195.9 g/mol, W_2C - 379.7 g/mol), Avagadro's number (6.022×10^{23} molecules/mol), and the density (α -WC - 15.6 , W_2C - 16.6 g/cm³), respectively. From Equation 3.2, the estimated monolayer thickness was calculated to be ~ 0.28 and 0.34 nm for WC and W_2C , respectively. Comparing the monolayer thickness estimates with the GPC values in Tables 3.1 and 3.2, we calculate a monolayer growth rate of ~ 0.5 (325 °C) and 1 (150°C) monolayer/cycle for WC and ~ 0.4 (325 °C) to 0.9 (150°C) monolayer/cycle for W_2C .

3.4.4 Film Composition

To gain insights into the film composition, 200 and 400 cycles of $\text{WCl}_5 \times 2 / \text{TMA} \times 2$ at 200 and 300 °C, respectively, were deposited on Si substrates with native oxide. Assuming a GPC of between $0.12 - 0.15$ nm/cy for $\text{WCl}_5 \times 2 / \text{TMA} \times 2$ dosing at 200°C , 200 cycles would correspond

to film roughly 27 nm thick. Assuming a GPC of between 0.09 – 0.11 nm/cy for $\text{WCl}_5 \times 2 / \text{TMA} \times 2$ dosing at 300°C, 400 cycles would correspond to film ~40 nm thick. Figure 3.5 a) and b) show the XPS elemental depth profiles obtained for samples deposited at 200 and 300 °C, respectively.

For the film deposited at 200 °C, Figure 3.5 a) shows the surface prior to sputtering (i.e., concentration at 0 minutes) contained ~35 at.% carbon, likely, in part from adventitious carbon. Also, ~37 at.% oxygen and 20 at.% tungsten implied oxidized tungsten, likely a result of ~24-hour air exposure during sample transfer for XPS analysis. WC films were also shown previously to oxidize in air.¹⁵ 1 minute of sputtering resulted in decreased carbon content to ~20 at.%, coupled with a decrease in oxygen to 25 at.% and increase in tungsten to 40 at.%, corresponding to removal of adventitious carbon and surface tungsten oxide, respectively. Due to the rise in silicon content to nearly 25 at.% after 10 minutes of sputtering, the elemental concentrations at 6 minutes of sputtering are likely indicative of the “bulk” film composition of 42 at.% tungsten, 20 at.% carbon, 10 at.% aluminum, 20 at.% oxygen, and 4 at.% chlorine. Within the film “bulk”, the ratios of W:C, W:O, and Al:O are ~2:1, 2:1, and 0.5:1, respectively.

For the film deposited at 300 °C, Figure 3.5 b) shows the as-deposited surface (i.e., concentration at 0 minutes) contained nearly the same elemental concentrations as for the film deposited at 200 °C. Due to the rise in silicon content to ~12 at.% after 40 minutes of sputtering, the elemental concentrations at between 16 and 40 minutes of sputtering are likely indicative of the “bulk” film composition of 43 at.% tungsten, 20 at.% carbon, 12 at.% aluminum, 16 at.% oxygen, and 2 at.% chlorine. Within the film “bulk”, the ratios of W:C, W:O, and Al:O are ~2:1, 2.7:1, and 0.75:1, respectively.

Figure 3.6 a) and b) show high resolution scans of the W 4f region for films deposited at 200 and 300 °C, respectively. For both deposition temperatures, doublet peaks at binding energies

of ~35.6 and 37.8 eV on the as-deposited films (i.e., 0 minutes sputtering) are likely from WO_3 species.^{30,31,10} After sputtering, these peaks decrease in intensity, while the intensity of a new doublet at binding energies of 31.6 and 33.8 eV is due to WC bonding.^{10,4} For increased sputter times, the films deposited at 200 °C had a greater WC/ WO_3 ratio (defined as the total area of the doublet for WC divided by the total area of the doublet for WO_3) than that for films deposited at 300 °C.

Figure 3.7 a) and b) show high resolution scans of the C 1s region for films deposited at 200 and 300 °C, respectively. For as-deposited films at both deposition temperatures, a peak at 284.5 eV indicates C-C bonding, likely from adventitious carbon species. After sputtering, the C 1s peak shifts to lower a lower binding energy. The presence of mostly W-C, with possible Al-C bonding, which result in binding energies of 282.8³² and 282 eV,^{33,34} respectively, are likely responsible for the peak shift observed at both deposition temperatures.

High resolution scans of the Al 2p region for WC films deposited at 200 and 300 °C are shown in Figure 3.8 a) and b), respectively. For as-deposited WC at both deposition temperatures, a peak at 74.5 eV could be due to Al-O (74.8 eV)³⁵ and/or Al-C (73.5 eV)³⁴ bonding. For films deposited at both temperatures, the peak increased in intensity and slightly broadened with increased Ar sputtering.

The crystallinity of the films was using XRD (data not shown) and was found to be amorphous, similar to previous studies of WC films deposited below 500 °C.^{17,15}

3.4.5 Thermodynamic Modeling

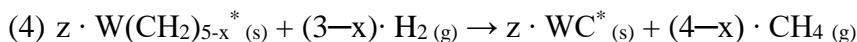
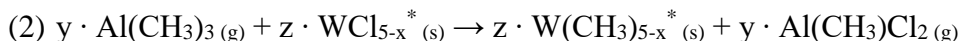
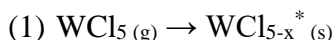
In order to understand the potential reaction pathways for WCl_5 and TMA, thermodynamic modeling was utilized via HSC Chemistry 7.1 software. Initial species were set to 5 moles N_2 , 1 mole $\text{WCl}_{5(g)}$ and 1.5 moles $\text{Al}(\text{CH}_3)_{3(g)}$ in a closed system, with constant pressure of 2 mbar. The temperature was increased from 25 to 400 °C, in 5 °C increments, with the Gibb free energy

minimized at each step to give the predicted species at equilibrium, shown in Figure 3.9. Any species with an equilibrium concentration less than 1 mmol was not shown.

At room temperature, $WCl_5(g)$ and $Al(CH_3)_3(g)$ react to give 1 mol of $WC(s)$, 0.75 mol of $AlCl_3(s)$, 2.5 mol of $CH_4(g)$, and 0.5 mol of $HCl(g)$. For temperatures above 75 °C, $AlCl_3(s)$ forms volatile $Al_2Cl_6(g)$, leaving only volatile reaction byproducts (excluding solid WC). For reaction temperatures exceeding 250 °C, the primary aluminum byproduct is $AlCl_3(g)$, rather than $Al_2Cl_6(g)$. It is important to note that this model is for a closed system, which does not consider the removal of species. In an ALD reaction, byproducts are removed after each half-reaction.

3.5 Discussion

Using the equilibrium species calculated in Figure 3.9, a possible reaction pathway for WCl_5/TMA can be given as a set of sub-reactions as follows:

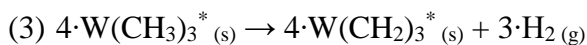
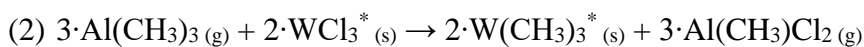
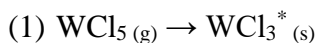


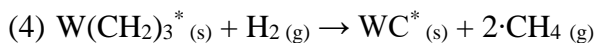
Step (1) indicates the WCl_5 adsorption step on the substrate, given as WCl_{5-x}^* , where dissociative adsorption is likely to occur, decreasing the number of available Cl groups by “x”. In this case, altering x changes the reaction stoichiometry, with y and z being the stoichiometric coefficients for Al-species and W-species, respectively. Similar precursor dissociation was observed previously for Cu ALD.^{36,37} Step (2) shows the reaction of TMA with the adsorbed WCl_{5-x}^* , which is predicted to yield a methylated W surface with $Al(CH_3)Cl_2(g)$, $AlCl_3(g)$, or $Al_2Cl_6(g)$ byproduct species. Step (3) shows α -hydride elimination, converting $W-CH_3$ species to $W=CH_2$ and $H_2(g)$, consistent with the mechanisms proposed for WC formation by WCl_6/TMA ALD¹⁷ and $((CH_3)_3CCH_2)_3W \equiv CC(CH_3)_3$ CVD.¹⁴ Since the oxidation state of tungsten in WC is (IV), such an

elimination is required to effectively reduce the oxidation state of tungsten from (V) to (IV). The final reaction, step (4) is the conversion to WC, possibly due to an intramolecular transfer, aided by the hydrogen produced in step (3) or hydrogen from nearby $WC(CH_2)_{5-x}^* (s)$ species to form of volatile $CH_4(g)$.^{17,38} For the latter case, the formation of W_2C may be the net result rather than WC. This step is not included but is likely to occur as evidenced by the W:C ratio of ~2:1 found by XPS in Figure 3.5.

Using the reactions defined in steps (1) – (4) above, the stoichiometry can be varied by first changing $x = 1, 2,$ and $3,$ which in turn dictates y and $z.$ Table 3.3 shows the estimated mass gain/mass loss ratio by performing a mass balance on the series of steps shown above (1) – (4) for $x = 1, 2,$ and $3.$ For $x = 1,$ 4 Cl groups are available for reaction with TMA, leading to more mass lost in the ligand exchange reaction from Cl to CH_3 groups. Accordingly, the ratio of mass gain to mass loss is lower than for $x = 2$ or $3,$ where 3 and 2 Cl groups, respectively, are available to react with TMA molecules.

Experimentally, Figure 3.4 shows that increasing temperature and number of sub-doses lead to a convergence in the total mass gain to loss ratio to ~4 – 5. Using the ratio calculated by employing a mass balance on the proposed reaction mechanism, this would imply an “x” value of roughly 2. This result means that most of the WCl_5 exposed to the surface will likely dissociate and adsorb as $WCl_3^* (s),$ thus allowing three Cl groups to react during the TMA half cycle. With this knowledge, a set of equations predicting the potential WCl_5/TMA reaction, with stoichiometry proposed based of experimental data, are given as follows:





For depositions at lower temperatures (e.g., ratio spanning 6 – 12 at 150 °C), dense packing of WCl_5 species decreases the number of available Cl species for subsequent reaction with TMA, thus increasing observed mass gain to loss ratio. Furthermore, inaccessible chlorine to TMA would lead to increased chlorine impurities at lower temperatures, which was observed experimentally by XPS as seen in Figure 3.5 a).

Figure 3.5 a) and b) show aluminum incorporation into the films, ~10 and 13 at.% on average for films deposited at 300 and 200 °C, respectively. Previous studies have shown aluminum content ranging from ~20 – 29 at.% for WCl_6/TMA at 325 – 375 °C,¹⁷ ~5 – 10 at.% for TiCl_4/TMA at 200 – 300 °C,³⁹ 10 – 13 at.% for HfCl_4/TMA at 270 °C,⁴⁰ 4 – 9 at.% for TaCl_5/TMA at 300 – 400 °C.^{41,42} Since TMA is well known to thermally decompose for temperatures ≥ 300 °C,^{43,44} Thus the ~10-13 at.% aluminum observed for films in this work is similar to the literature for metal carbide ALD using TMA. Furthermore, the chlorine observed in this work was quite low (~1 – 2 at.% at 300 °C) when compared to the studies listed above (5 – 20 at.%)^{39,40}. Similar chlorine impurity levels were found for WCl_6/TMA (1.3 at.% at 300 °C)¹⁷ and TaCl_5/TMA (2 - 4 at.% at 300 - 400 °C) which could be due to the difference in reduction potential for W (+0.1 V) versus that for Ta (-0.6 V), Ti (-1.63 V), and Hf (-1.55 V).⁴⁵ With highly negative reduction potentials for Ti and Hf, TMA reduction to form lower oxidation state carbides is more difficult than for W and Ta, leading to higher observed Cl impurities.

The presence of oxygen throughout the films, with steadily decreasing concentration with increased sputtering implies oxidation in air. Oxidation is likely a mixture of WO_3 and Al_2O_3 , with the latter more likely due to Al:O ratios of 0.75:1 and 0.5:1 for films deposited at 200 and 300 °C, respectively and the presence of Al – O bonding in the Al 2p XPS spectra (Figure 3.8). The

oxidized aluminum incorporated into the film was also observed previously for metal carbide films deposited using TMA.⁴⁰

3.6 Conclusions

Tungsten carbide films were deposited using a new thermal ALD process, with WCl_5 and $\text{Al}(\text{CH}_3)_3$ precursors at temperatures of 150 to 325 °C and 1.5 Torr. The film growth was monitored *in situ* by quartz crystal microbalance, revealing linear mass change per cycle for all tested temperatures. From the average mass change per cycle, the growth rate per cycle was calculated to be ~ 0.12 nm/cycle, corresponding to ~ 0.5 monolayers/cycle, for depositions at 300 – 325 °C. Using a full factorial design of experiments, the ratio of mass gain:loss was determined experimentally to converge at ~ 4 for films deposited at high temperature (e.g., 300 °C) and dose saturation. This ratio compared well with theoretical estimations using a mass balance on the predicted reaction species, indicating a probable reaction mechanism to give WC films. Composition analysis of the deposited films showed a W:C ratio 2:1, implying the formation of W_2C . Furthermore, 1 – 2 at.% chlorine impurities were observed for depositions at 300 °C. 10 – 13 at.% aluminum was measured in the films, likely due to thermal decomposition of the $\text{Al}(\text{CH}_3)_3$ precursor at higher temperatures.

3.7 Acknowledgements

The authors acknowledge the financial support from EMD Performance Materials, Ravi Kanjolia and Chuck Dezelah for technical conversations and insights, the Analytical Instrumentation Facility (AIF) at North Carolina State University, which is supported by the State of North Carolina and the National Science Foundation, and Duke's Shared Materials Instrumentation Facility.

3.8 Figures for Chapter 3

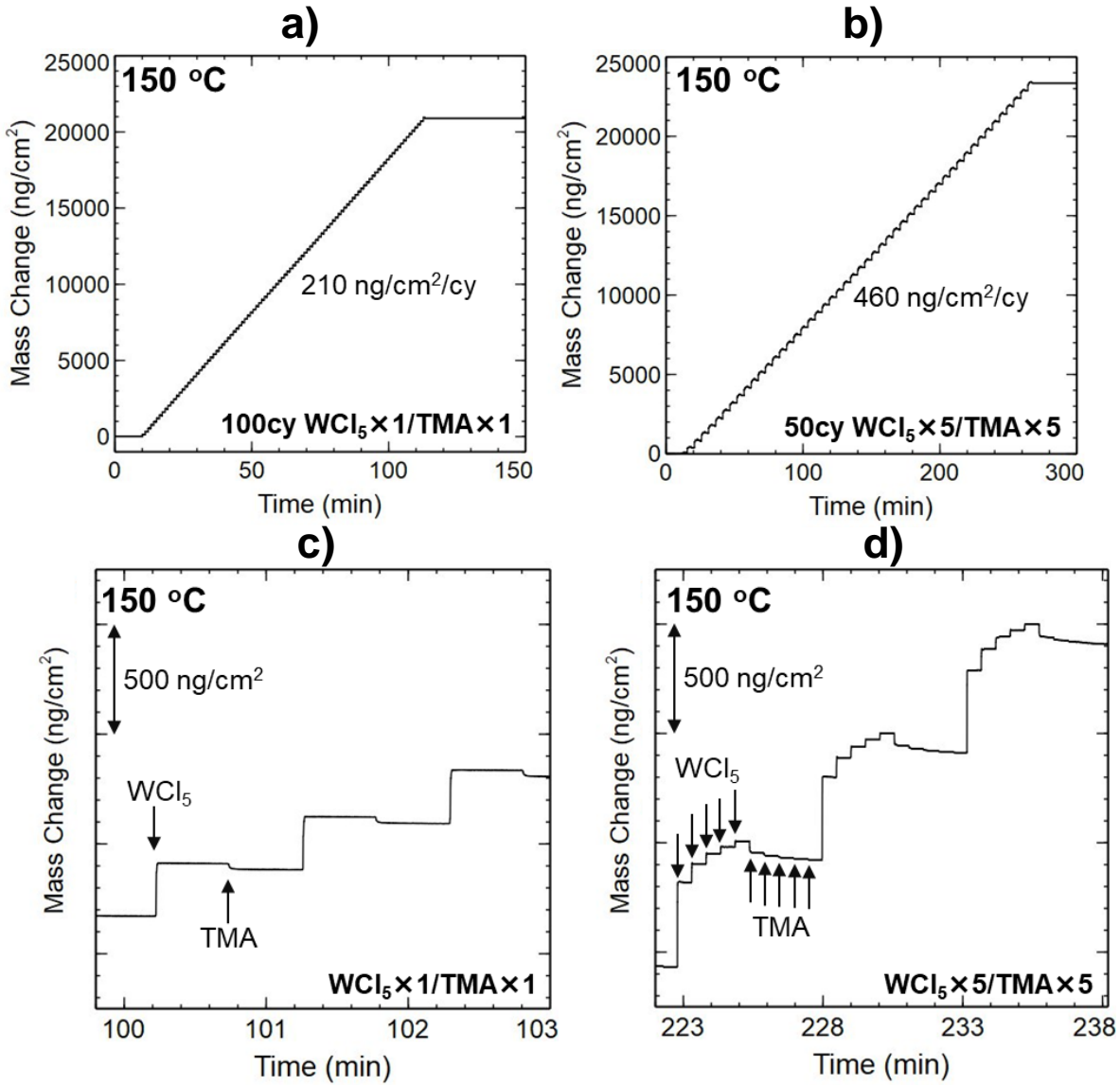


Figure 3.1: QCM results showing the mass change (ng/cm²) versus process time (minutes) for a) 100 cycles of WCl₅/N₂/TMA/N₂, with dose times 1s/30s/1s/30s, at 150 °C and b) 50 cycles [WCl₅/N₂]⁵/[TMA/N₂]⁵, with dose times [1s/30s]⁵/[1s/30s]⁵, at 150 °C. c) and d) are magnified images of a) and b), respectively, showing 3 cycles, with WCl₅ and TMA doses indicated with arrows.

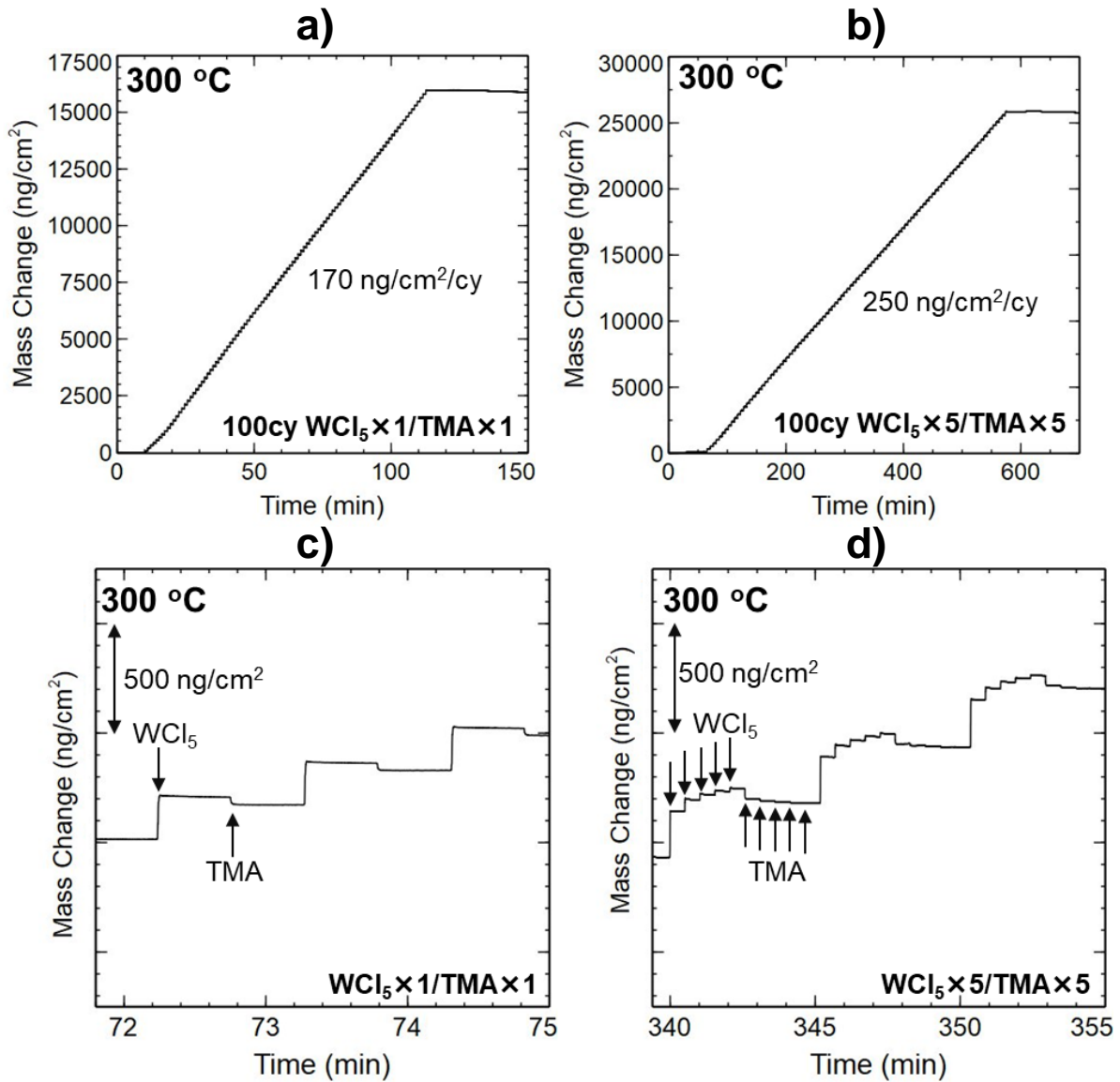


Figure 3.2: QCM results showing the mass change (ng/cm²) versus process time (minutes) for a) 100 cycles of WCl₅/N₂/TMA/N₂, with dose times 1s/30s/1s/30s, at 300 °C and b) 100 cycles [WCl₅/N₂]⁵/[TMA/N₂]⁵, with dose times [1s/30s]⁵/[1s/30s]⁵, at 300 °C. c) and d) are magnified images of a) and b), respectively, showing 3 cycles, with WCl₅ and TMA doses indicated with arrows.

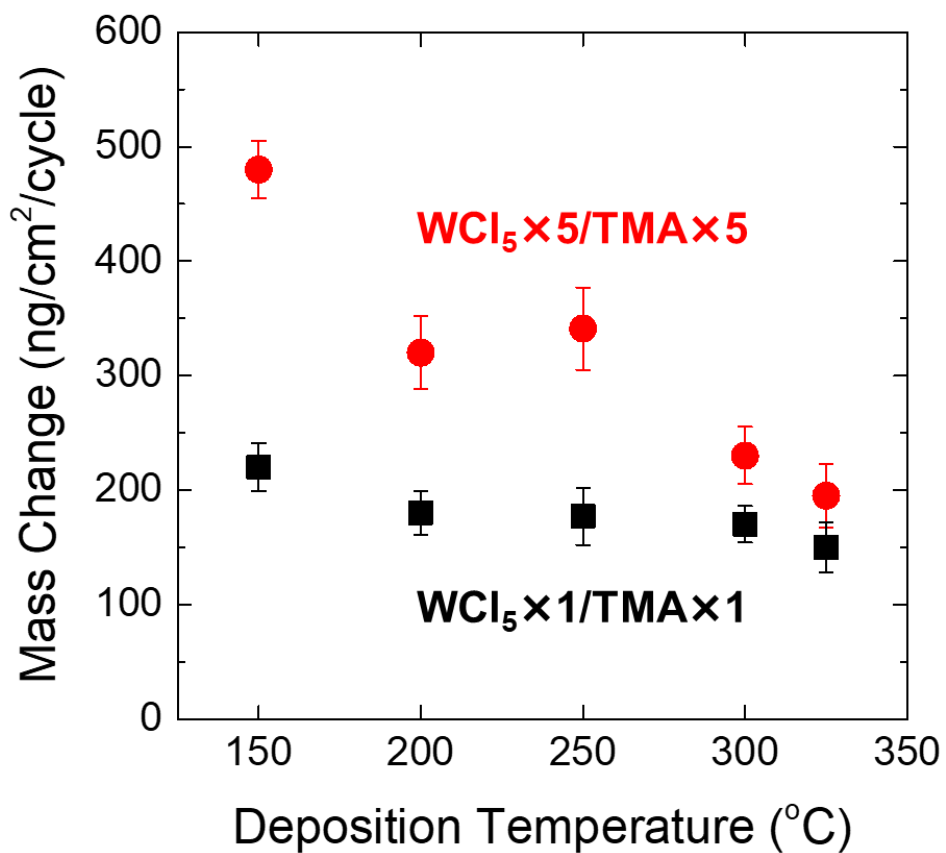


Figure 3.3: Average mass change per cycle (ng/cm²/cycle), obtained from QCM results, versus deposition temperatures 150, 200, 250, 300, and 325 °C for WCl₅/N₂/TMA/N₂ (black squares) and [WCl₅/N₂]⁵/[TMA/N₂]⁵ (red circles).

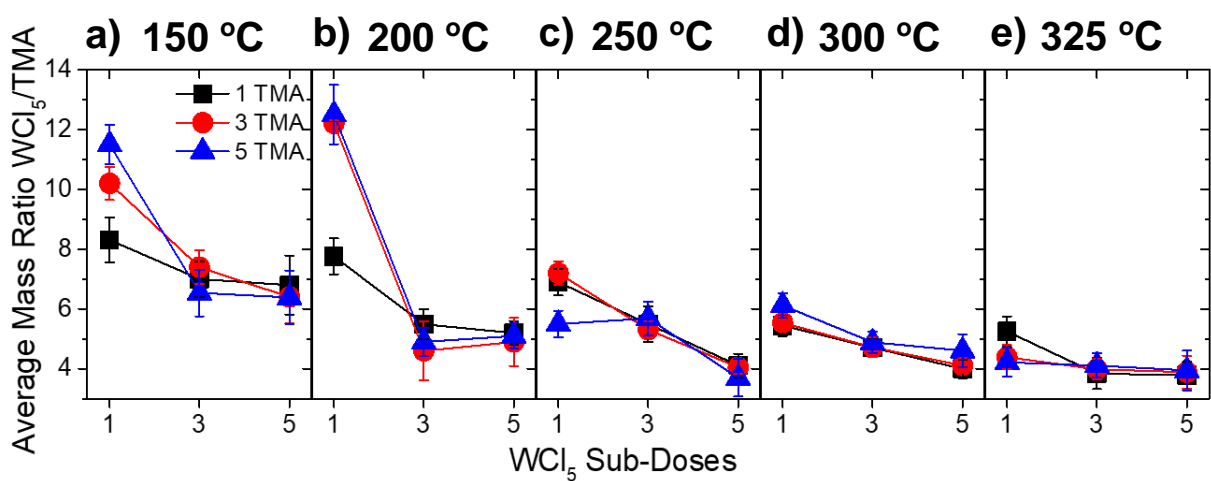


Figure 3.4: WCl_5/TMA ratio (y-axis) of the averaged mass change obtained by QCM during WCl_5 and TMA cycling. The number of WCl_5 (1, 3, 5 on x-axis) and TMA (1 – black squares, 3 – red circles, 5 – blue triangles) sub-doses were varied for deposition temperatures of a) 150 °C, b) 200 °C, c) 250 °C, d) 300 °C, and e) 325 °C.

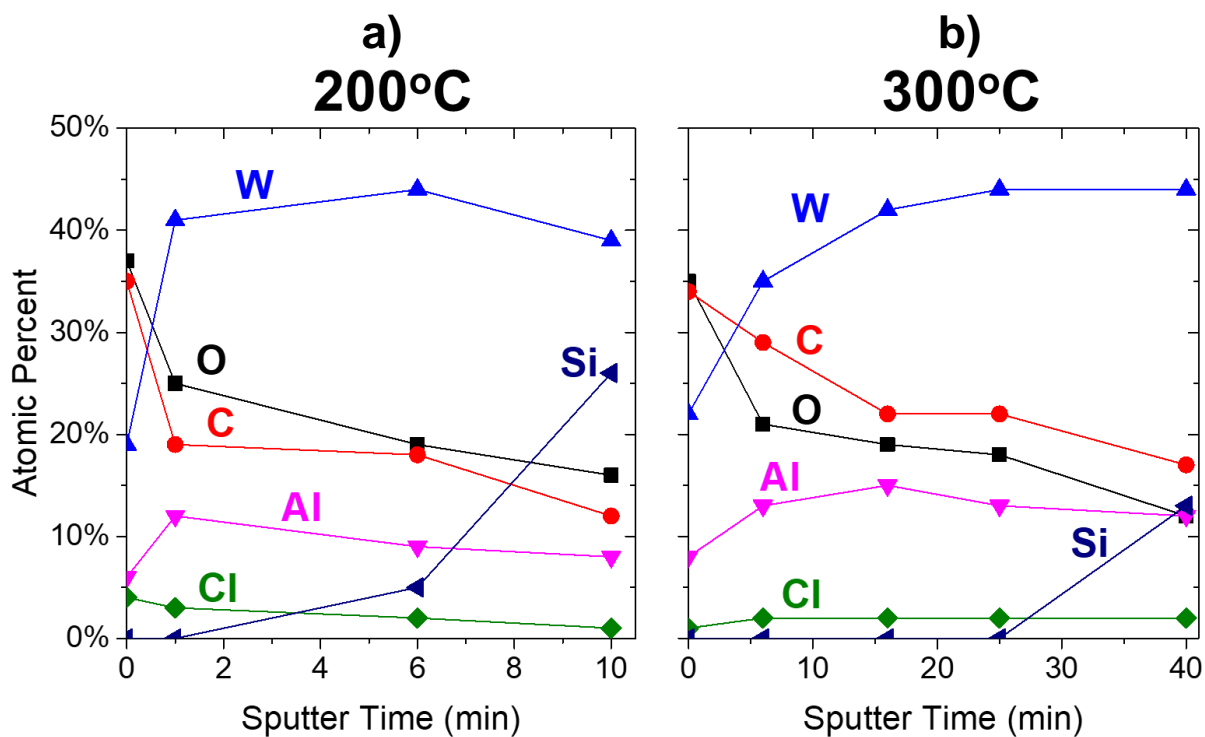


Figure 3.5: Elemental depth profile, obtained using XPS with Ar sputtering, for a) 200 cycles of $[\text{WCl}_5/\text{N}_2] \times 2 / [\text{TMA}/\text{N}_2] \times 2$ at 200 °C and b) 400 cycles of $[\text{WCl}_5/\text{N}_2] \times 2 / [\text{TMA}/\text{N}_2] \times 2$ at 300 °C deposited on Si with native oxide. Species shown, with units of atomic percent, are: W (blue triangles), O (black squares), C (red circles), Al (pink upside-down triangles), Cl (green diamonds), and Si (navy blue left-triangles).

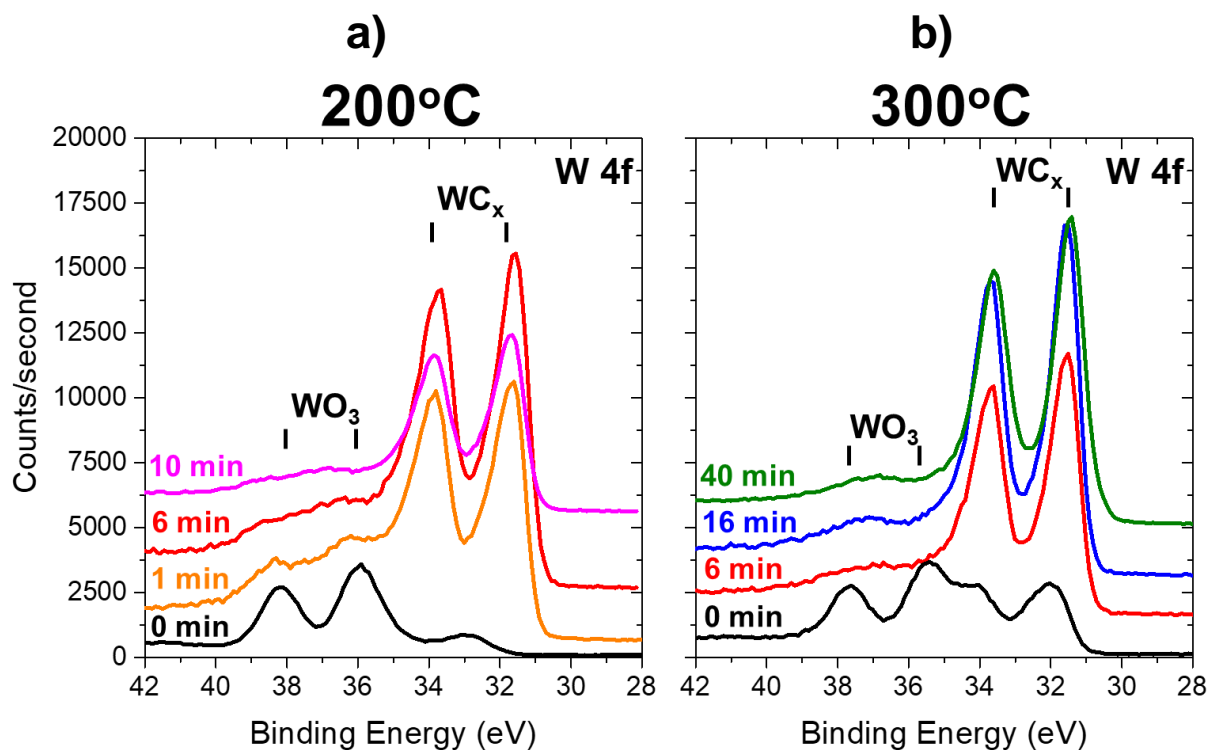


Figure 3.6: High resolution scans of the W 4f region, obtained using XPS with Ar sputtering (representative sputtering times indicated above each designated line), for a) 200 cycles of $[\text{WCl}_5/\text{N}_2] \times 2 / [\text{TMA}/\text{N}_2] \times 2$ at 200 °C, and b) 400 cycles of $[\text{WCl}_5/\text{N}_2] \times 2 / [\text{TMA}/\text{N}_2] \times 2$ at 300 °C deposited on Si with native oxide. Raw spectra offset for visual clarity. Expected peaks for WO_3 doublet at ~ 36 and 38 eV and WC_x doublet at ~ 32 and 34 eV are indicated above raw spectra.

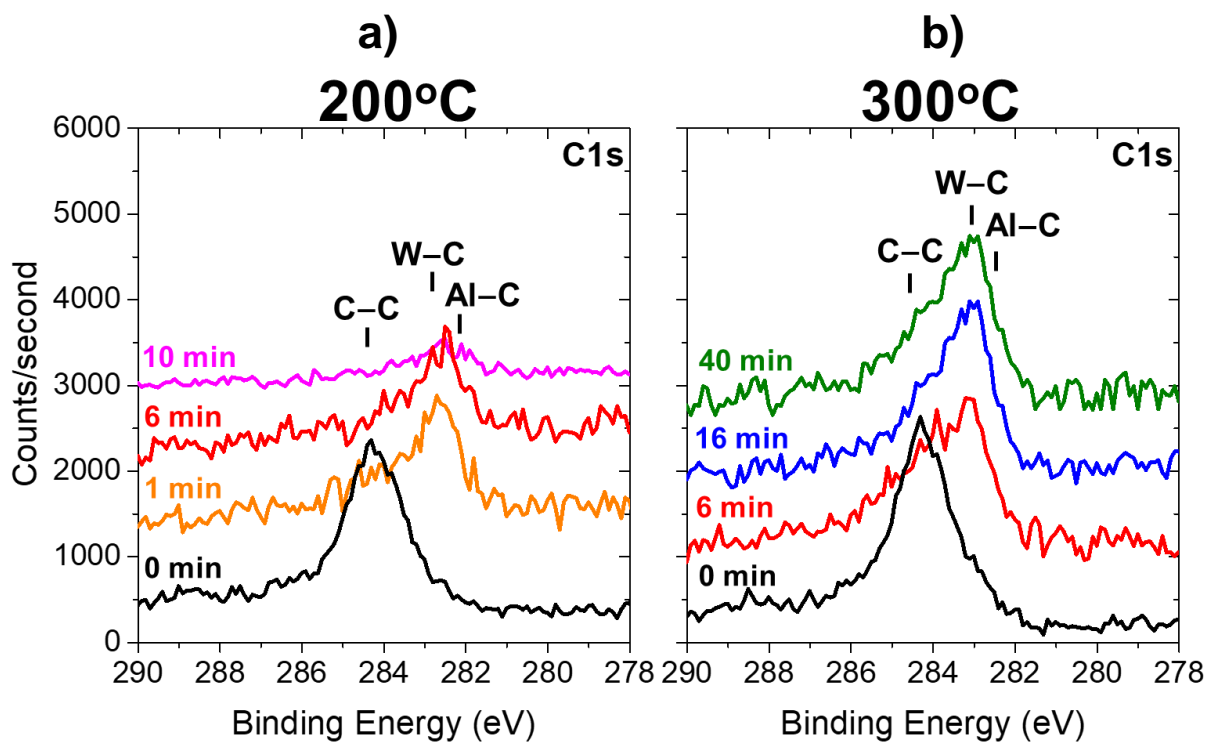


Figure 3.7: High resolution scans of the C 1s region, obtained using XPS with Ar sputtering (representative sputtering times indicated above each designated line), for a) 200 cycles of $[\text{WCl}_5/\text{N}_2] \times 2 / [\text{TMA}/\text{N}_2] \times 2$ at 200 °C, and b) 400 cycles of $[\text{WCl}_5/\text{N}_2] \times 2 / [\text{TMA}/\text{N}_2] \times 2$ at 300 °C deposited on Si with native oxide. Raw spectra offset for visual clarity. Expected peaks for C–C, W–C, and Al–C bonding at ~284., ~283.5, and 282.2 eV, respectively, are indicated above raw spectra.

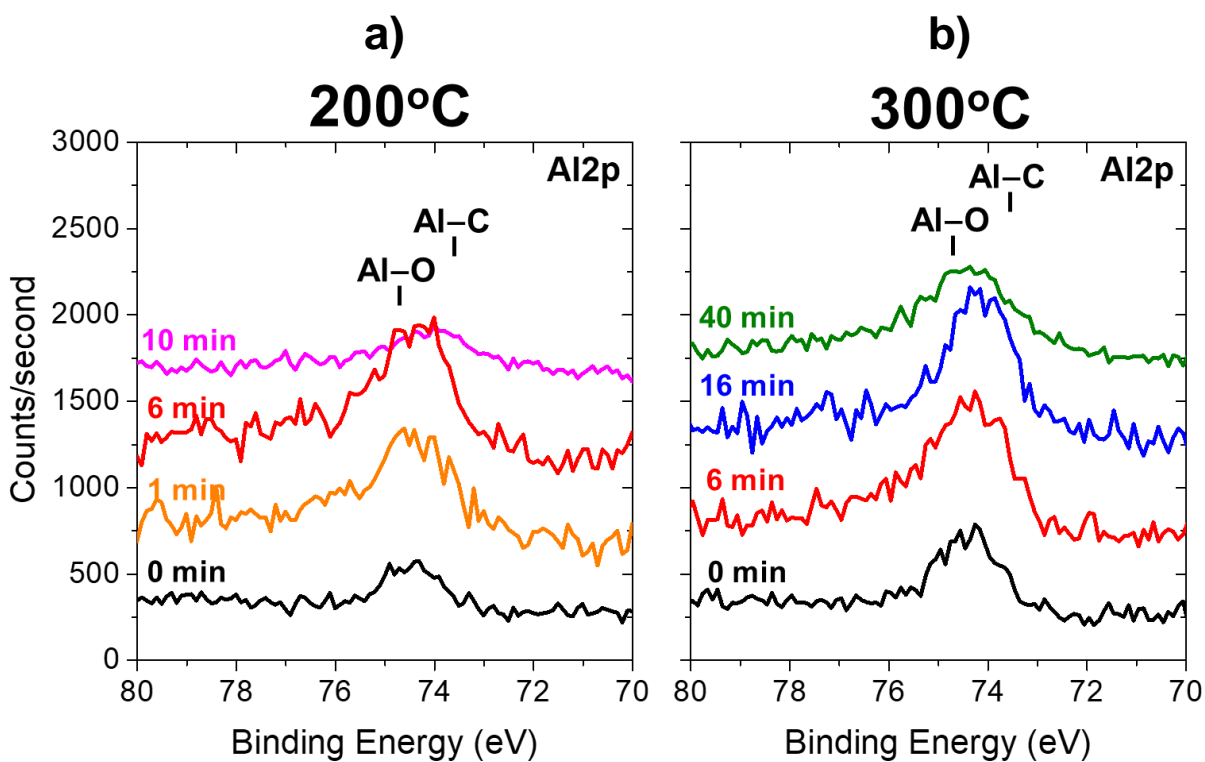


Figure 3.8: High resolution scans of the Al 2p region, obtained using XPS with Ar sputtering (representative sputtering times indicated above each designated line), for a) 200 cycles of $[\text{WCl}_5/\text{N}_2] \times 2 / [\text{TMA}/\text{N}_2] \times 2$ at 200 °C, and b) 400 cycles of $[\text{WCl}_5/\text{N}_2] \times 2 / [\text{TMA}/\text{N}_2] \times 2$ at 300 °C deposited on Si with native oxide. Raw spectra offset for visual clarity. Expected peaks for Al—O and Al—C bonding at ~ 75 and ~ 73.5 eV, respectively, are indicated above raw spectra.

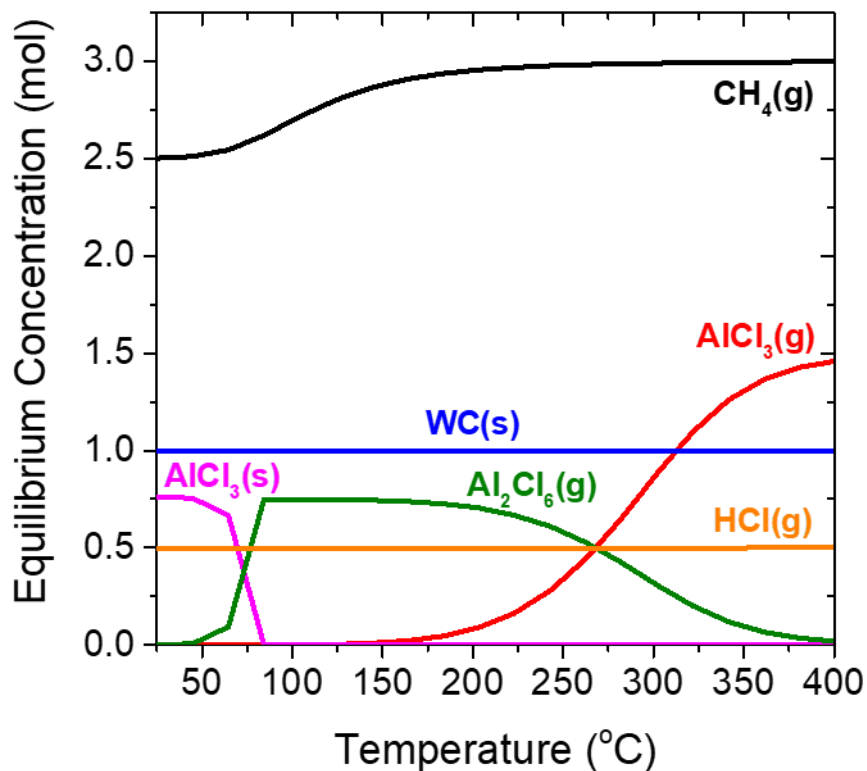


Figure 3.9: Predicted equilibrium species from the gas phase reaction of 1 mole of WCl_5 and 1.5 moles of $\text{Al}(\text{CH}_3)_3$ from temperatures ranging 25 – 400 °C and pressure of 2 mbar. Only species with an equilibrium concentration greater than 1 mmol are shown. The following are the species expected at equilibrium, with their anticipated phase indicated as either (g) for gas or (s) for solid, $\text{CH}_4(\text{g})$ (black), $\text{AlCl}_3(\text{g})$ (red), $\text{WC}(\text{s})$ (blue), $\text{AlCl}_3(\text{s})$ (pink), Al_2Cl_6 (green), and $\text{HCl}(\text{g})$ (orange).

3.9 Tables for Chapter 3

Table 3.1: GPC from Average Mass Change during WCl_5/TMA for $\rho(\alpha\text{-WC}) = 15.6 \text{ g/cm}^3$

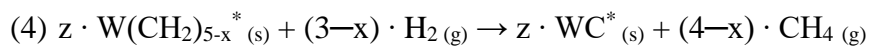
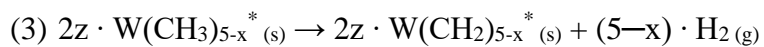
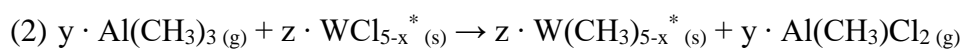
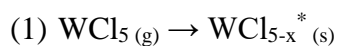
Temperature (°C)	Δm (ng/cm ² /cy)	GPC (nm/cy)	Δm (ng/cm ² /cy)	GPC (nm/cy)
	$\text{WCl}_5 \times 1 / \text{TMA} \times 1$	$\text{WCl}_5 \times 1 / \text{TMA} \times 1$	$\text{WCl}_5 \times 5 / \text{TMA} \times 5$	$\text{WCl}_5 \times 5 / \text{TMA} \times 5$
150	220	0.14	480	0.31
200	182	0.12	320	0.21
250	177	0.11	341	0.22
300	170	0.11	225	0.15
325	148	0.10	200	0.13

Table 3.2: GPC from Average Mass Change during WCl₅/TMA for $\rho(\alpha\text{-W}_2\text{C}) = 16.6 \text{ g/cm}^3$

Temperature (°C)	Δm (ng/cm ² /cy)	GPC (nm/cy)	Δm (ng/cm ² /cy)	GPC (nm/cy)
	WCl ₅ ×1/TMA×1	WCl ₅ ×1/TMA×1	WCl ₅ ×5/TMA×5	WCl ₅ ×5/TMA×5
150	220	0.13	480	0.29
200	182	0.11	320	0.19
250	177	0.11	341	0.21
300	170	0.10	225	0.14
325	148	0.09	200	0.12

Table 3.3: Mass Ratio vs. WCl_5 /TMA Reaction Pathway

x	Total Mass Gain (g/mol)	Total Mass Loss (g/mol)	<u>Total Mass Gain</u> <u>Total Mass Loss</u>
1	361	134	2.7
2	361	96	3.8
3	361	58	6.2



3.10 References

- (1) Levy, R. B.; Boudart, M. Platinum-Like Behavior of Tungsten Carbide in Surface Catalysis. *Science* (80-.). **1973**, *181* (4099), 547–549.
- (2) Yang, X.; Kimmel, Y. C.; Fu, J.; Koel, B. E.; Chen, J. G. Activation of Tungsten Carbide Catalysts by Use of an Oxygen Plasma Pretreatment. *ACS Catal.* **2012**, *2* (5), 765–769.
- (3) Yang, X. G.; Wang, C. Y. Nanostructured Tungsten Carbide Catalysts for Polymer Electrolyte Fuel Cells. *Appl. Phys. Lett.* **2005**, *86* (22), 1–3.
- (4) Rodella, C. B.; Barrett, D. H.; Moya, S. F.; Figueroa, S. J. A.; Pimenta, M. T. B.; Curvelo, A. A. S.; Teixeira da Silva, V. Physical and Chemical Studies of Tungsten Carbide Catalysts: Effects of Ni Promotion and Sulphonated Carbon. *RSC Adv.* **2015**, *5* (30), 23874–23885.
- (5) Mustain, H. A.; Brown, W. D.; Ang, S. S. Tungsten Carbide as a Diffusion Barrier on Silicon Nitride Active- Metal-Brazed Substrates for Silicon Carbide Power Devices. *J. Electron. Packag.* **2009**, *131* (3), 34502.
- (6) Jinn Wang, S.; Yi Tsai, H.; Chung Sun, S. Characterization of Tungsten Carbide as Diffusion Barrier for Cu Metallization. *Jpn. J. Appl. Phys.* **2001**, *40* (4B), 2642–2649.
- (7) Ghaisas, S. Diffusion Barrier Performance of Pulsed Laser Deposited Amorphous Tungsten Carbide Films. *J. Appl. Phys.* **1991**, *70* (12), 7626–7628.
- (8) Polini, R. Chemically Vapour Deposited Diamond Coatings on Cemented Tungsten Carbides: Substrate Pretreatments, Adhesion and Cutting Performance. *Thin Solid Films* **2006**, *515* (1), 4–13.
- (9) Lee, H. C.; Gurland, J. Hardness and Deformation of Cemented Tungsten Carbide. *Mater. Sci. Eng.* **1978**, *33* (1), 125–133.
- (10) Katrib, A.; Hemming, F.; Wehrer, P.; Hilaire, L.; Maire, G. The Multi-Structure of Oxidized-Reduced Tungsten Carbide Surfaces. *Catal. Letters* **1994**, *29*, 397–408.
- (11) Endrino, J. L.; Nainaparampil, J. J.; Krzanowski, J. E. Magnetron Sputter Deposition of WC-Ag and TiC-Ag Coatings and Their Frictional Properties in Vacuum Environments. *Scr. Mater.* **2002**, *47* (9), 613–618.
- (12) Eser, E.; Ogilvie, R. E.; Taylor, K. A. Structural and Compositional Characterization of Sputter-deposited WC+Co Films. *J. Vac. Sci. Technol.* **1978**, *15* (2), 396–400.
- (13) Gubisch, M.; Liu, Y.; Spiess, L.; Romanus, H.; Krischok, S.; Ecke, G.; Schaefer, J. A.; Knedlik, C. Nanoscale Multilayer WC/C Coatings Developed for Nanopositioning: Part I. Microstructures and Mechanical Properties. **2005**.
- (14) Xue, Z.; Caulton, K.; Chisholm, M. Low-Pressure Chemical Vapor Deposition of

- Tungsten Carbide Thin Films. *Chem. Mater* **1991**, *3*, 384–386.
- (15) Jipa, I.; Heinemann, F. W.; Schneider, A.; Popovska, N.; Siddiqi, M. A.; Siddiqui, R. A.; Atakan, B.; Marbach, H.; Papp, C.; Steinrück, H.-P.; Zenneck, U. [Cis-(1,3-Diene)₂W(CO)₂] Complexes as MOCVD Precursors for the Deposition of Thin Tungsten - Tungsten Carbide Films. *Chem. Vap. Depos.* **2010**, *16* (7–9), 239–247.
 - (16) Pawbake, A.; Waykar, R.; Jadhavar, A.; Kulkarni, R.; Waman, V.; Date, A.; Late, D.; Pathan, H.; Jadhkar, S. Wide Band Gap and Conducting Tungsten Carbide (WC) Thin Films Prepared by Hot Wire Chemical Vapor Deposition (HW-CVD) Method. **2016**.
 - (17) Blakeney, K. J.; Winter, C. H. Thermal Atomic Layer Deposition of Tungsten Carbide Films from WCl₆ and AlMe₃. *J. Vac. Sci. Technol. A Vacuum, Surfaces, Film.* **2018**, *36* (1), 01A104.
 - (18) Kim, J. B.; Jang, B.; Lee, H.-J.; Han, W. S.; Lee, D.-J.; Lee, H.-B.-R.; Hong, T. E.; Kim, S.-H. A Controlled Growth of WN_x and WC_x Thin Films Prepared by Atomic Layer Deposition Tungsten Nitride Tungsten Carbide N₂H₂ Plasma Phase Microstructure. *Mater. Lett.* **2016**, *168*, 218–222.
 - (19) Kim, D.-H.; Kim, Y. J.; Song, Y. S.; Lee, B.-T.; Kim, J. H.; Suh, S.; Gordon, R. Characteristics of Tungsten Carbide Films Prepared by Plasma-Assisted ALD Using Bis(tert-Butylimido)bis(dimethylamido)tungsten. *J. Electrochem. Soc.* **2003**, *150* (10), C740.
 - (20) Beom Kim, J.; KimWon Seok HanDo-Joong Lee, S.-H.; Kim, S.-H.; Seok Han, W.; Lee, D.-J. Atomic Layer Deposited Nanocrystalline Tungsten Carbides Thin Films as a Metal Gate and Diffusion Barrier for Cu Metallization. *J. Vac. Sci. Technol. A Vacuum, Surfaces, Film.* **2016**, *34* (35), 41504–1.
 - (21) International Technology Roadmap for Semiconductors, <http://public.itrs.net/Files/2001ITRS> http://mast-tech.com.tw/itrs_jan08.pdf.
 - (22) Profijt, H. B.; Potts, S. E.; Sanden, M. C. M. van de; Kessels, W. M. M. Plasma-Assisted Atomic Layer Deposition: Basics, Opportunities, and Challenges. *J. Vac. Sci. Technol. A* **2011**, *29* (5), 50801.
 - (23) Bor-Wen Chan; Baw-Ching Perng; Sheu, L.; Yuan-Hung Chiu; Han-Jan Tao. Plasma Induced Substrate Damage in High Dose Implant Resist Strip Process. In *8th International Symposium Plasma- and Process-Induced Damage*; IEEE, 2003; pp 73–76.
 - (24) Kaminaga, U.; Matsushita, T.; Kohra, K. Surface Damage on Si Substrates Caused by Reactive Sputter Etching. *Jpn. J. Appl. Phys.* **1981**, *20* (5), 893–900.
 - (25) NIST X-Ray Photoelectron Spectroscopy Database, Version 4.1; National Institute of Standards and Technology: Gathersburg MD, 20899.
 - (26) Suetin, D. V.; Shein, I. R.; Ivanovskii, A. L. Structural, Electronic Properties and Stability

- of Tungsten Mono- and Semi-Carbides: A First Principles Investigation. *J. Phys. Chem. Solids* **2009**, *70* (1), 64–71.
- (27) Etinger-Geller, Y.; Katsman, A.; Pokroy, B. Density of Nanometrically Thin Amorphous Films Varies by Thickness. *Chem. Mater.* **2017**, *29* (11), 4912–4919.
- (28) Coban, A.; Khawaja, E. E.; Durrani, S. M. A. Difference between Bulk and Thin Film Densities of Metal Oxide and Fluoride Films Studied by NRA Depth Profiling Techniques. *Nucl. Instruments Methods Phys. Res. B* **2002**, *194* (2), 171–176.
- (29) Gaskins, J. T.; Hopkins, P. E.; Merrill, D. R.; Bauers, S. R.; Hadland, E.; Johnson, D. C.; Koh, D.; Yum, J. H.; Banerjee, S.; Nordell, B. J.; Paquette, M. M.; Caruso, A. N.; Lanford, W. A.; Henry, P.; Ross, L.; Li, H.; Li, L.; French, M.; Rudolph, A. M.; King, S. W. Review—Investigation and Review of the Thermal, Mechanical, Electrical, Optical, and Structural Properties of Atomic Layer Deposited High- *K* Dielectrics: Beryllium Oxide, Aluminum Oxide, Hafnium Oxide, and Aluminum Nitride. *ECS J. Solid State Sci. Technol.* **2017**, *6* (10), N189–N208.
- (30) Nandi, D. K.; Sarkar, S. K. Atomic Layer Deposition of Tungsten Oxide for Solar Cell Application. *Energy Procedia* **2014**, *54*, 782–788.
- (31) Barreca, D.; Carta, G.; Gasparotto, A.; Rossetto, G.; Tondello, E.; Zanella, P. A Study of Nanophase Tungsten Oxides Thin Films by XPS. *Surf. Sci. Spectra* **2001**, *8* (4), 258–267.
- (32) Oya, Y.; Sato, M.; Li, X.; Yuyama, K.; Fujita, H.; Sakurada, S.; Uemura, Y.; Hatano, Y.; Yoshida, N.; Ashikawa, N.; Sagara, A.; Chikada, T. Impact of Temperature during He+ Implantation on Deuterium Retention in Tungsten, Tungsten with Carbon Deposit and Tungsten Carbide. *Phys. Scr.* **2016**, *2016* (T167), 14037.
- (33) Xiang, J.; Ding, Y.; Du, L.; Li, J.; Wang, W.; Zhao, C. Growth Mechanism of Atomic-Layer-Deposited TiAlC Metal Gate Based on TiCl₄ and TMA Precursors. *Chinese Phys. B* **2016**, *25* (3), 37308.
- (34) Hauert, R.; Patscheider, J.; Tobler, M.; Zehring, R. XPS Investigation of the a-C:H/Al Interface. *Surf. Sci.* **1993**, *292* (1), 121–129.
- (35) Figueiredo, N. M.; Carvalho, N. J. M.; Cavaleiro, A. An XPS Study of Au Alloyed Al-O Sputtered Coatings. *Appl. Surf. Sci.* **2011**, *257* (13), 5793–5798.
- (36) Dey, G.; Elliot, S. D. Quantum Chemical Study of the Effect of Precursor Stereochemistry on Dissociative Chemisorption and Surface Redox Reactions during the Atomic Layer Deposition of the Transition Metal Copper. *J. Phys. Chem. C* **2015**, *119*, 5914–5927.
- (37) Ma, Q.; Guo, H.; Gordon, R. G.; Zaera, F. Uptake of Copper Acetamidinate ALD Precursors on Nickel Surfaces. *Chem. Mater.* **2010**, *22* (2), 352–359.
- (38) Kim, T.; Zaera, F. Surface Chemistry of Pentakis(dimethylamido)tantalum on Ta Surfaces. *J. Phys. Chem. C* **2011**, *115* (16), 8240–8247.

- (39) Xiang, J.; Ding, Y.; Du, L.; Li, J.; Wang, W.; Zhao, C. Growth Mechanism of Atomic-Layer-Deposited TiAlC Metal Gate Based on TiCl_4 and TMA Precursors. *Chinese Phys. B* **2016**, *25* (3), 37308.
- (40) Lee, A.; Fuchigami, N.; Pisharoty, D.; Hong, Z.; Haywood, E.; Joshi, A.; Mujumdar, S.; Bodke, A.; Karlsson, O.; Kim, H.; Choi, K.; Besser, P. Atomic Layer Deposition of $\text{Hf}_x\text{Al}_y\text{C}_z$ as a Work Function Material in Metal Gate MOS Devices. *J. Vac. Sci. Technol. A Vacuum, Surfaces, Film.* **2014**, *32* (1), 01A118.
- (41) Xiang, J.; Li, T.; Wang, X.; Du, L.; Ding, Y.; Wang, W.; Li, J.; Zhao, C. Thermal Atomic Layer Deposition of TaAlC with TaCl_5 and TMA as Precursors. *ECS J. Solid State Sci. Technol.* **2016**, *5* (10), P633–P636.
- (42) Xiang, J.; Wang, X.; Li, T.; Gao, J.; Han, K.; Yu, J.; Wang, W.; Li, J.; Zhao, C. Investigation of Thermal Atomic Layer Deposited TaAlC with Low Effective Work-Function on HfO_2 Dielectric Using TaCl_5 and TEA as Precursors. *ECS J. Solid State Sci. Technol.* **2017**, *6* (1), P38–P41.
- (43) Puurunen, R. L.; Lindblad, M.; Root, A.; Outi I. Krause, A. Successive Reactions of Gaseous Trimethylaluminium and Ammonia on Porous Alumina. *Phys. Chem. Chem. Phys.* **2001**, *3* (6), 1093–1102.
- (44) Yamashita, S.; Watanuki, K.; Ishii, H.; Shiba, Y.; Kitano, M.; Shirai, Y.; Sugawa, S.; Ohmi, T. Dependence of the Decomposition of Trimethylaluminum on Oxygen Concentration. *J. Electrochem. Soc.* **2011**, *158* (2), H93.
- (45) Haynes, W. M. *Haynes, W. M. Handbook of Chemistry and Physics 96th Edition. Taylor and Francis Group, 2015, 96th ed.; 2015.*

**CHAPTER 4: GROWTH INHIBITION OF TiN, TiO₂,
AND HfO₂ ON PLASMA-TREATED AMORPHOUS
CARBON BY AREA-SELECTIVE ATOMIC LAYER
DEPOSITION**

CHAPTER 4. Growth Inhibition of TiN, TiO₂, and HfO₂ on Plasma-Treated Amorphous Carbon by Area-Selective Atomic Layer Deposition

Eric Stevens,^{†,‡,§} Yoann Tomczak,[†] BT Chan,[†] Efrain Altamirano Sanchez,[†] Gregory Parsons,[‡]
Annelies Delabie^{*,†,§}

[†] Imec, Kapeldreef 75, B-3001 Leuven, Belgium

[‡] Department of Chemical and Biomolecular Engineering, North Carolina State University, 911 Partners Way, Raleigh NC 27695

[§] KU Leuven (University of Leuven), Celestijnenlaan 200F, B-3001, Leuven, Belgium

4.1 Abstract

The demand for transistors and memory devices with smaller feature sizes and increasingly complex architectures furthers the need for advanced thin film patterning techniques. A pre-patterned, sacrificial layer can be used as a template for bottom-up fill of new materials which would otherwise be difficult to pattern using traditional top-down lithographic methods. This work investigates initial growth of TiN, TiO₂, and HfO₂ thin films during thermal atomic layer deposition (ALD) onto a high density, amorphous carbon (aC) sacrificial layer. ALD of TiN by TiCl₄/NH₃ at 390°C, TiO₂ by Ti(OCH₃)₄/H₂O at 250°C, and HfO₂ by HfCl₄/H₂O at 300°C on as-deposited aC films resulted in uninhibited, continuous thin film growth. We find that carbon surface reduction and passivation using a H₂ plasma resulted in delayed film coalescence for TiN, TiO₂, and HfO₂ on the aC. After 200 TiN cycles on H₂ plasma-treated aC, Rutherford backscattering spectrometry shows Ti levels below the detection limit (8×10^{13} at/cm²), whereas SiO₂ or Si₃N₄ substrates show TiN growth of ~6 nm, corresponding to a selectivity of ~200:1. Exposing plasma-treated aC to H₂O induces nucleation for TiN ALD, consistent with favorable nucleation on hydroxyl sites. Therefore, the H₂O co-reagent in TiO₂ and HfO₂ ALD contributes to loss of selectivity compared to TiN ALD using NH₃. We conclude that H₂O-based processes

should be avoided when using APF aC thin films, and maximum ALD selectivity can be achieved using a H₂ plasma treatment and water-free ALD processing.

4.2 Introduction

Fabrication of future nanoelectronic devices will require innovative and scalable patterning and coating techniques to transition to 3-D architectures. As a promising options for the 7 nm node and beyond, nanowire field effect transistors will require high precision patterning techniques of dielectric and metal materials, which may prove challenging using traditional lithography techniques.^{1,2} Furthermore, line-edge roughness and pattern misalignment are the prominent challenges for the patterning of sub 10 nm features.¹ One method to overcome these challenges is using a tone reversal process.³ A tone reversal process utilizes a sacrificial layer, such as a resist or amorphous carbon (aC), which is typically patterned using conventional lithography methods, followed by refilling the patterned regions with a desired hard mask material (e.g., TiN). This trench-filling deposition of the hard mask reverses the image, or tone, created by the initial lithography step. Tone reversal is used, for example, for self-aligned double patterning to extend the half-pitch resolution of patterns beyond the capabilities of traditional lithography tools.⁴ For highest precision, it is desirable to deposit the hard mask only within the spaces opened in the sacrificial patterning layer by area selective deposition.

Full realization of a single-step tone reversal will require new approaches to area-selective deposition of metal nitrides and oxides onto receptive surfaces without significant deposition onto sacrificial carbon. In this article, we describe and demonstrate controlled chemical plasma modification of amorphous carbon to achieve area-selective atomic layer deposition (ALD) of TiN onto silicon nitride, with minimal deposition on carbon materials patterned with sub-50 nm resolution, thus providing a new route to tone reversal without the need for plasma etch patterning.

Considering the nanoscale dimensions and complex geometries involved in patterning for next generation transistors, the study of aC and its interactions with ALD precursors is of particular interest. ALD is a vapor-phase deposition process that incorporates self-limiting half reactions to conformably deposit films with sub-nanometer thickness control.⁵ Since ALD relies on precursor chemisorption on the substrate, some ALD processes are inherently selective to specific surfaces (e.g., TiO₂ on SiH,⁶ W on SiO₂,⁷ and Co on C-doped SiO₂⁸). Additionally, some substrates can be chemically deactivated by surface reactions or physical adsorption of non-reactive species. This has been demonstrated using self-assembled monolayers as ALD blocking layers on Cu, SiO₂, and HfO₂ surfaces, among others.^{9–12}

The ALD nucleation and growth on carbon surfaces, including graphene^{13–16} and carbon nanotubes,^{17–21} has been studied previously. Typical studies seek to identify a means to chemically functionalize these carbon surfaces to promote ALD nucleation and facilitate uniform thin-films.¹⁹ The ALD growth inhibition on carbon substrates is less studied, specifically for aC substrates. Zhang et. al. showed that TiO₂ ALD on graphene only nucleated on surface defect sites at a deposition temperature of 200°C, implying that sp² hybridized carbon is inherently unreactive to TiO₂ ALD at the given process conditions.¹⁴ Similarly, single-walled carbon nanotubes were shown to have 1–3 at.% carboxylic acid defects sites,²² and additional functionalization was needed to minimize Fe₂O₃ ALD nucleation delays.¹⁷

This work seeks an in-depth understanding of the nucleation and growth behavior of metal oxide and metal nitride ALD on aC, specifically TiO₂, HfO₂, and TiN. Furthermore, the effects of surface pre-treatments on the nucleation density and growth regimes are investigated as a means to selectively deactivate aC to these ALD processes. We believe this work will lay the foundation

for applications in tone reversal patterning of dielectric-on-dielectric and metal-on-dielectric material systems.

4.3 Experimental

4.3.1 Substrate Preparation, Plasma and ALD Processing

The amorphous carbon material (aC) deposited and utilized in this study was Advanced Patterning Film (APF),²³ which is currently used in the industry for double patterning lithography to increase line density and decrease line-edge roughness.²⁴ The APF aC films were deposited on 300 mm Si (100) wafers in an Applied Materials Producer platform. High density aC was deposited by plasma enhanced chemical vapor deposition (PE-CVD) using acetylene (C_2H_2) at 400°C, producing films with a density of 1.5 g/cm³ and thickness of 100 nm. In this same reactor, Si_3N_4 films with a density of 2.56 g/cm³ and a thickness of 50 nm were deposited by PE-CVD at 400°C using silane (SiH_4) and mixture of ammonia (NH_3) and nitrogen (N_2) plasma.

Atomic layer deposition of TiO_2 and HfO_2 was performed in an ASM Polygon 8300 cluster tool, with three separate chambers for processing. Using this experimental setup, the APF aC deposited in the separate tool could be plasma-treated before being transferred to ALD processing without air breaks between chambers, thus removing the variability induced during air exposure during sample transfer.

The three chambers included an ASM EMERALD PE-ALD chamber, used for H_2 plasma treatments and TiN thermal ALD, and two ASM PULSAR cross-flow thermal ALD chambers, one for TiO_2 and another for HfO_2 . These materials were deposited using $Ti(OCH_3)_4/Ar/H_2O/Ar$ (4s/8s/2s/4s) at 250°C and $HfCl_4/N_2/H_2O/N_2$ (1s/3s/0.5s/3s) at 300°C, respectively. The reagent dose and purge times were selected such that linear growth with uniform thickness were observed across the entire 300 mm wafer.

In the ASM EMERALD PE-ALD chamber, a hydrogen plasma was generated at the showerhead top-electrode using a capacitively-coupled RF power source operated at 13.56 MHz. The wafer chuck was used as the counter electrode such that all plasma species were generated between the showerhead and substrate. The operating pressure was maintained at 2 Torr with an argon inert gas flow. The temperature of the bottom electrode, and thus the wafer, was set to 300°C, while the chamber walls and top electrode were maintained at 160°C. The plasma recipe began with a thermal equilibration time of 2 minutes under Ar flow. A 10 second, 10% H₂/Ar direct plasma exposure, with powers between 50 to 400W, was subjected to the wafer, followed by a 1 second Ar purge. This dosing sequence was repeated to give a total plasma exposure time of 20 seconds. Following the final exposure, the substrate was subjected to 60 seconds of 100% H₂ in an attempt to passivate the surface of dangling bonds.

During TiN ALD in the EMERALD chamber, the wafer chuck (bottom electrode) was heated to 390°C, while the walls and showerhead were kept at 160°C. TiN precursors, TiCl₄ and NH₃, were pulsed through the showerhead for 0.8s and 4s, respectively, separated by 1.5s Ar purges.

4.3.2 Characterization

Elemental depth profiling of pristine and plasma-treated aC substrates was measured by X-ray Photoelectron Spectroscopy (XPS) using a Theta300 system (Thermo Instruments). XPS measurements were carried out using a monochromatized Al K α X-ray source (1486.6 eV) with a spot size of 400 μ m. XPS depth profiling utilized Ar⁺ sputtering ions with an energy of 0.5-2.0 keV. Obtained XPS spectra were corrected to the C 1s peak at a binding energy of 284.5 eV. The total amount of metal oxide or metal nitride deposited on aC and Si₃N₄ coated Si wafers was determined by Rutherford Back Scattering (RBS), in a RBS400 system with a 1.52 MeV He⁺ ion beam. Etching of aC substrates as a function of H₂ plasma exposures was determined using

spectroscopic ellipsometry (SE) for 49 points on a 300 mm Si wafer (Aleris, KLA Tencor). TiO₂, HfO₂, and TiN particle size and areal density were found using images obtained from a scanning electron microscope (SEM, Hitachi SU8000) with a beam energy of 3 kV and a beam current of 10 pA.

4.4 Results and Discussion

4.4.1 ALD on Untreated aC Substrates

In order to understand how the untreated aC substrate affects nucleation and steady state ALD, TiO₂, HfO₂, and TiN were deposited on pristine (henceforth referred to as untreated) aC surfaces with varying numbers of cycles, and the atomic density of Ti or Hf on the surface was measured by RBS. Figure 4.1 shows the Ti and Hf content versus the number of ALD cycles on untreated aC for TiO₂, TiN, and HfO₂ ALD. For untreated aC substrates, a linear increase in the amount of material deposited versus the number of ALD cycles was detected, with a growth per cycle (GPC) of 1.23×10^{14} Ti atoms/cm²/cycle, 1.44×10^{14} Hf atoms/cm²/cycle, and 1.04×10^{14} Ti atoms/cm²/cycle for TiO₂, HfO₂, and TiN, respectively. Furthermore, the GPC on untreated aC was nearly identical to films grown on Si₃N₄ substrates. Data was not recorded below 96 cycles of TiN ALD, but extrapolation of the linear fit through the data implies an inherent delay in linear growth. This is likely due to an inherent nucleation delay, where film coalescence and steady state growth is likely to proceed via Volmer Weber, or island growth.²⁵

For each material “i” (where i = TiO₂, HfO₂, or TiN), Equation 4.1 can be used to convert the GPC obtained from RBS, GPC_i^{RBS} , with units of atoms/cm²/cy to GPC_i^* with units of nm/cy:

$$GPC_i^* = GPC_i^{RBS} \times \frac{MW_i}{\rho_i N_A} \quad (4.1)$$

where ρ_i is the bulk film density, MW_i is molecular mass, and N_A is Avogadro’s number. The resulting values are summarized in Table 1. For direct comparison, the table also includes values

for GPC_i^{SE} , the growth per cycle on Si substrates measured by spectroscopic ellipsometry (SE). The GPC_i^{SE} values are in agreement with GPC values reported in the literature for TiO_2 ,²⁶ HfO_2 ,²⁷ and TiN ²⁸ under the same deposition conditions. The values for GPC from RBS and SE agree well for TiO_2 and HfO_2 .

For TiN , the RBS value is somewhat less than the value from ellipsometry, which we ascribe to a film density that is less than that for bulk TiN (5.21 g/cm^3 ²⁹). The resulting GPC for TiO_2 , HfO_2 and TiN ALD on untreated aC substrates was similar to that on Si_3N_4 for all three materials. Thus, ALD growth is uninhibited for TiO_2 , HfO_2 , and TiN on untreated aC substrates. Furthermore, the untreated aC surface in this study was more reactive towards ALD than previously studied graphene or carbon nanotubes.^{14,17} Favorable ALD nucleation is ascribed (vide infra) to carbon-oxygen sites present on the as-prepared aC.

4.4.2 aC Surface Composition and Modification Using H_2 Plasma Exposures

When compared to SiO_2 or Si_3N_4 , the uninhibited ALD growth observed on untreated aC proves that surface modification is required to suppress nucleation. Surface oxygen species, specifically OH groups, are expected to be reactive sites for many ALD precursors^{5,30-32}, thus the oxygen content in the aC films was investigated. Surface modification was investigated by applying a 50 second, 10% H_2/Ar plasma exposure, with 100, 200, and 400W powers to 100 nm thick aC films deposited on Si wafers.

For this study, untreated and plasma-treated aC were transferred in air for XPS depth profile analysis. Figure 4.2 shows the surface oxygen concentration (measured by XPS) as a function of sputter depth (determined from ellipsometry) for untreated and plasma-treated aC films. Untreated aC films had a surface oxygen concentration of ~5.5 at.%, which corresponds to

a surface O-content of $\sim 2 \times 10^{15}$ O atoms/cm². After sputtering 1 – 2 nm into the film, the oxygen content saturates between ~ 0.5 and 1 at.%, which is likely the bulk oxygen content in aC films.

Considering that TiO₂ ALD proceeds without nucleation delay on untreated aC (Figure 4.1), $\sim 2 \times 10^{15}$ O atoms/cm² provided sufficient ALD reactive sites for film nucleation and growth commensurate with that for SiO₂ and Si₃N₄ substrates. Zhang et. al. also found that for SiO₂-coated MoS₂ layers, a surface oxygen concentration of 3×10^{15} O atoms/cm² was sufficient to enable atomic layer deposition of continuous Al₂O₃ and HfO₂ films.³³

Figure 4.2 shows that when untreated aC was exposed to a 50s H₂ plasma at 100 or 200W, the measured surface oxygen concentration decreased from 5.5 at.% to 3.5 at.%, while the measured bulk value remained unchanged. Similar surface oxygen content for 100 and 200W plasma treated aC may be due to a minimum threshold in the plasma density, which increases with plasma power, to remove surface oxygen. Increasing the plasma power to 400W resulted in a decrease in the measured surface oxygen content to ~ 2.5 at.%.

Decreasing initial oxygen content (before sputtering) with increasing plasma power can be ascribed to a better resistance to reoxidation for higher plasma powers during air break sample transfer. With a greater surface oxygen content which decreases to saturation below 1 at.%, aC films likely oxidized during transfer from the deposition chamber to the plasma chamber. Since these processes were carried out on separate tools, an air break was unavoidable. If aC films were to be deposited and transferred to ALD processing without an air-break, surface oxygen content would likely remain below 1 at.%.

Figure 4.3 shows high resolution XPS scans of the C 1s region for untreated and 400W 50s treated aC (which was exposed to air for 20 minutes during sample transfer) using XPS. Also shown is the same 400W treated sample remeasured after one week of air exposure. Shown in

Table 2, C 1s spectra were deconvoluted (data not shown) and the peak area was used to determine relative amounts of the C–C, C–O, and C=O bonding configurations, which were assigned using deconvoluted C 1s peak positions reported previously.^{34,35}

Untreated aC showed mostly C–C bonding, with the majority being sp² hybridized bonds. C–O and C=O bonding were also identified in roughly equal proportions. The addition of a 400W 50s plasma treatment, followed by a 20 min air exposure during sample transfer, resulted in a peak shift attributed to increased sp³ hybridized C–C bonding. Furthermore, C–O and C=O were reduced when compared to untreated aC. The 400W plasma-treated sample was remeasured following one week of air exposure. A similar proportion of sp²/sp³ hybridization was observed with an increase in C–O and C=O bonding. These results suggest that the extent of aC surface reoxidation following plasma treatment is dependent on the air exposure time. Previous findings show aC oxidation into CO or CO₂ with exposure to H₂O₂ during wet cleans steps.²⁴ Considering H₂O is a weaker oxidant than H₂O₂, the surface oxidation in the case of air exposed aC should be kinetically slower. We observe that 20 minutes of air exposure does not completely reoxidize the plasma-treated aC surface, suggesting surface termination of hydrophobic groups.

During the aC plasma treatment, H₂ plasma likely etches the aC, removing surface oxygen species, and forming hydrophobic –CH_x groups. Such a chemical change is expected to impede the nucleation ALD precursors during processing.^{6,30}

4.4.3 Optimization of H₂ Plasma Conditions

In order to probe the aC surface immediately following H₂ plasma treatments, an *in situ* experiment was conducted using TiO₂ ALD. Utilization of the ASM Polygon 8300 cluster tool allowed for air-free transfer of wafers, and thus no surface re-oxidation of the plasma-treated aC films, from the plasma processing chamber directly into a TiO₂ ALD deposition chamber. The amount of TiO₂ deposited on plasma-treated aC substrates could then be used to study the efficacy

of various plasma conditions in delaying ALD nucleation on aC substrates. The aC films were treated with various plasma treatments and transferred, without an air-break, to an adjacent chamber for TiO₂ ALD using Ti(OCH₃)₄ + H₂O at 250°C. Figure 4.4 a) shows the surface density of Ti atoms (measured by RBS) on aC substrates after various 10% H₂/Ar plasma treatments plotted as a function of the amount of aC etched (measured by ellipsometry). The H₂ plasma power (50, 100, 200, and 400W) and exposure time (10, 50, and 100s) were varied for a fixed number (30 cy) of Ti(OCH₃)₄ + H₂O cycles.

The etch rate of aC depended on the H₂ plasma conditions. No thickness change was detected by ellipsometry for aC films subjected to 50W 50s plasma treatments. Increasing the plasma power to 100, 200, and 400W resulted in a linear increase in aC etching. Furthermore, an increase in the exposure time, for a constant plasma power also led to a linear increase in the amount of aC etched. The aC etching byproducts are likely volatile hydrocarbons generated by reactive H₂ plasma exposures.

Results in Figure 4.3 show that the H₂ plasma power and exposure time significantly affected the amount of deposited TiO₂, suggesting that the rate of TiO₂ nucleation and growth can be slowed by decreasing O content and increasing -CH_x passivation. Compared with untreated aC (labelled as 0W), a 50W plasma for 50 seconds did not alter the amount of Ti detected by RBS, yielding a Ti content of $\sim 3 \times 10^{15}$ Ti atoms/cm². This amount of Ti was similar to that obtained after 30 cycles TiO₂ on an untreated aC substrate (see Figure 4.1) and resulted in a closed and continuous film. Increasing the plasma power to 100, 200, and 400W resulted in a decreasing Ti-content corresponding to delayed TiO₂ deposition. Plasma exposures of 200W for 100 seconds and 400W for 50 seconds resulted in a Ti content below the detection limit of the RBS instrument used for these experiments, which was $\sim 8 \times 10^{13}$ Ti atoms/cm².

For the same aC thickness loss, the amount of deposited Ti decreases with increasing plasma power. This further confirms that the H₂ plasma removes reactive surface oxygen species by etching the O-rich top layer and passivates the aC top surface, where the extent of this passivation increases with the H₂ plasma power.

For a desirable selective-area ALD process, the amount of aC etched should be as small as possible to decrease line-edge roughness and line placement error, while also maximizing nucleation inhibition. Since the amount of etched aC for the 400W 20s treatment was ~3-4 nm, compared to ~9 nm for the 400W 50s treatment, a 400W 20s treatment was selected as a “standard” pretreatment condition to assess nucleation during TiO₂, HfO₂, and TiN ALD.

4.4.4 Nucleation and Growth of TiO₂, HfO₂, and TiN ALD on Plasma-Treated aC and Si₃N₄ Substrates

As shown in Figure 4.3, the 400W 20s H₂ plasma treatment on aC removed surface oxygen with a minimal amount of C etching. Therefore, we explored this treatment condition on aC and Si₃N₄ as a means to modify nucleation for TiO₂, HfO₂, and TiN ALD. Figure 4.5 shows that a 400W plasma pre-treatment was sufficient to delay the onset of linear growth for all deposited films. All three materials grown on plasma-treated aC displayed an incubation period of 50 cycles, 45 cycles, and 320 cycles for TiO₂, HfO₂, and TiN, respectively. During this incubation period, the amount of material detected by RBS was at or below 1×10^{14} atoms/cm². The growth delay is most pronounced for the TiN ALD. For 320 cycles, the Ti content is reduced by two orders of magnitude by applying the H₂ plasma treatment, i.e. from 2.7×10^{16} atoms/cm², which corresponds to a 9 nm TiN layer, to 1×10^{14} atoms/cm², which corresponds to less than a monolayer.

While the H₂ plasma passivates the aC surface for TiO₂, HfO₂ and TiN ALD, it does not passivate the Si₃N₄ surface. The growth remains linear on H₂ plasma-treated Si₃N₄ (Figure 4.4), indicating that reactive sites for precursor adsorption remain present after the H₂ plasma treatment.

This is promising for area-selective deposition, as growth proceeds linearly on the H₂ plasma-treated Si₃N₄ surface, while it is significantly delayed on the H₂ plasma-treated aC surface. Using the Ti content measured by RBS for untreated and plasma-treated aC, an estimated selectivity of ~200:1 (untreated aC:plasma-treated aC) was obtained. Previous results of Si₃N₄ films treated with hydrogen plasma showed water contact angles of 65.5°,³⁶ which would still be classified as hydrophilic and thus explain the observed trend of steady state ALD growth on plasma-treated Si₃N₄.

To understand possible factors that may limit area-selective deposition, we studied the nucleation behavior on the passivated aC surface by investigating the morphology of the deposited materials as a function of the number of ALD cycles using SEM. The corresponding top-down SEM images for various cycles numbers deposited on aC substrates (corresponding to those from Figure 4.5) can be seen in Figure 4.6 a), b), and c). SEM reveals that after a certain number of cycles, the material exists in the form of small islands or particles rather than as a continuous film. An island growth mechanism can indeed be expected for substrate inhibited ALD.^{37,38} For aC substrates with less than 20 cycles of TiO₂ and HfO₂ and 200 cycles of TiN, particles could not be observed with the Hitachi SU8000 SEM. Figure 4.6 shows that for samples with Ti content below the RBS detection limit (~8x10¹³ atoms/cm²), for example 200 cycles TiN and 30 cycles TiO₂, islands are still observed by SEM. The islands shown for the 200 cycle TiN sample were not verified to be TiN and thus could be particles generated during sample cleaving or other adventitious contamination.

From the SEM images in Figure 4.6, the particle density and surface coverage can be obtained to better understand differences in the nucleation and growth behavior for the different ALD processes. Figure 4.7 shows the resulting particle density and surface coverage of TiO₂,

HfO₂, and TiN ALD on plasma-treated aC as a function of the amount of material deposited by RBS. Figure 4.7 a) shows that the nuclei density reaches a maximum for HfO₂ and TiO₂ for nearly the same amount of material deposited ($\sim 1 \times 10^{14}$ at/cm²), while the maximum nuclei density for TiN is delayed nearly two orders of magnitude ($\sim 1 \times 10^{16}$ at/cm²). Considering a similar maximum particle density for HfO₂ and TiO₂ ALD, for the same amount of deposited material, aC surface reoxidation during H₂O exposures is thus also comparable. It follows that H₂O exposures are the major contributing factor in the generation of nucleation sites of the plasma-treated aC, and that any differences resulting from HfCl₄ and Ti(OCH₃)₄ do not play a key role.

After reaching a maximum in nuclei density, there is a constant decrease in the density value, which implies partial island coalescence. For all three materials, nearby islands appear to coalesce prior to total film coalescence, which is indicative of a gradual decrease in nuclei.

For the same amount of material deposited, HfO₂ had the largest nuclei density on the plasma-treated aC for all cycle numbers. Furthermore, TiN had the smallest overall nuclei density up until a Ti content of 10^{16} at/cm², in line with the longest growth delay observed by RBS (Figure 4.4).

Figure 4.7 b) displays the surface coverage of the TiO₂, HfO₂, and TiN particles shown in Figure 4.6. The nuclei surface coverage for HfO₂ was consistently greater than that for TiO₂ or TiN for the same amount of material deposited, although the surface coverage for TiO₂ was nearly equal to that of HfO₂ for more than 120 cycles. Comparing the surface coverage for the same amount of material deposited implies that the TiN nuclei are larger and less dense than those for TiO₂ or HfO₂. This is again in line with the much longer growth delay for TiN, as observed by RBS (Figure 4.4). Larger and less dense nuclei could suggest a difference in the surface chemistry during ALD processing, as discussed in the following section.

The presence of nuclei in Figure 4.6 after just 20 cycles of TiO₂ or HfO₂ could be, in part due to surface damage incurred during plasma exposures. Such surface damage could be from ion bombardment and implantation during plasma exposures, since a direct plasma was used.³⁹ It is possible that surface damage could be reduced by using a remote plasma, where ions may be filtered out prior to contacting the surface and only radicals react. Since the nucleation appears to be different for TiN ALD, compared with TiO₂ and HfO₂, the aC surface damage due to plasma exposures is most likely not the dominant factor in the creation of nucleation sites. Thus, the dominant factors which lead to ALD nucleation on plasma-treated aC substrates is probably due to either residual surface oxygen (bulk was not O-free, ~1 at.%) and/or surface reoxidation due to H₂O exposures. The former is an inherent property of the aC material used in these experiments and could be avoided by using an oxygen-free aC alternative. The latter was investigated and reported in Section 4.6. In addition to H₂O, chemical or physical interactions with NH₃, TiCl₄, and Ti(OCH₃)₄ and the aC surface could lead to undesired nucleation. These precursor affects were not studied due to experimental limitations.

4.4.5 Selectivity Loss of Plasma-Treated aC

In comparing TiN to TiO₂ and HfO₂ ALD on plasma-treated aC, we hypothesize that H₂O plays a key role in the selectivity differences during increased cycling. Since TiN is a water-free process, we studied the effect of water exposure on nucleation of TiN. Figure 4.8 shows top down SEM images of plasma-treated aC substrates subjected to a) 0, b) 1, c) 10, and d) 20 H₂O exposures (2s dose, 4s Ar purge at 250°C) followed by 150 cycles of TiN ALD. TiN nuclei, if present, were not observed for the aC control (not subjected to H₂O). Introduction of water exposures after plasma treatment but before TiN ALD leads to visible nucleation.

The resulting particle density and nuclei areal coverage, obtained using image analysis on SEM images from Figure 4.8 are shown in Figure 4.9. Introduction of one H₂O exposure is

sufficient to induce TiN particle nucleation, with 20 H₂O exposures leading to a TiN particle density and areal coverage exceeding that of plasma-treated aC samples with 320 cy TiN ALD. Furthermore, introduction of new nucleation sites via H₂O exposures agrees with the results in Figure 4.2 showing oxidation of aC upon air exposure that reactivates the aC for TiN ALD.

From Figure 4.2, air exposure results in ~5.5% oxygen species being present within the top 1-2 nm of the untreated aC films. The H₂ plasma etches through the top few layers of aC to remove the oxygen, producing a hydrophobic surface termination that inhibits subsequent precursor adsorption. H₂O dosing during ALD eventually oxidizes the surface, leading to nucleation. Conversely, NH₃ based processes, such as TiN ALD will lead to increased selectivity, as observed in Figure 4.6. Since H₂O is more polar than NH₃, H₂O is expected to adsorb more readily on defect sites (generated during plasma treatment) or ~1 at.% bulk oxygen in aC films. These results confirm our hypothesis that selectivity loss during HfO₂ and TiO₂ ALD occurs via re-oxidation of the aC surface during H₂O exposure.

Regarding the Ti(OCH₃)₄, HfCl₄, and TiCl₄ precursors, differences in surface mobility and/or the surface adsorption of metal-organic versus metal-halide precursors could contribute to differences in selectivity. The -Cl and/or -OCH₃ ligands may play a significant role in the creation of defect sites, leading to subsequent H₂O or NH₃ adsorption. Considering that no Ti or N were detected by XPS for plasma-treated aC after 200 cycles of TiN, either the Cl-induced defect density is low and/or NH₃ adsorption on any Cl-induced defect sites is kinetically limiting.

4.5 Conclusions

In this work, we show that nucleation of HfO₂, TiO₂, and TiN during thermal ALD on aC surfaces can be affected using H₂ plasma pretreatment, where the H₂ plasma acts to remove surface oxygen and inhibit precursor adsorption. Similar H₂ plasma treatments on Si₃N₄ and SiO₂ substrates does not impede ALD nucleation, allowing inherent selective ALD of HfO₂, TiO₂, and

TiN to proceed on Si₃N₄ and SiO₂ with minimal deposition on aC. After treating aC with a H₂ plasma at 400W for 20s, 30 cycles of thermal TiO₂ ALD led to no detectable Ti on the aC by RBS analysis (with a detection limit of 8×10^{13} at/cm²).

We also found that using H₂O as a co-reagent for TiO₂ and HfO₂ ALD promote unwanted nucleation due to aC surface oxidation. Using NH₃ during TiN ALD allowed 200 cycles of growth, corresponding to ~6 nm on TiN on Si₃N₄ and SiO₂ substrates, without significant growth on aC. Thus, H₂O plays a key role in the surface reactivity to ALD precursors and should be avoided if long nucleation delays, with minimal defect generation are desired.

Due to experimental constraints, aC films were required to be deposited in a separate tool than where plasma and ALD processing was conducted. If aC films could be grown and transferred air-free for ALD processing, the nucleation and growth are expected to be affected. For water-based ALD processes, the effect should be minimal, due to the fast nucleation and steady-state film growth observed in Figure 4.1. Thus, for water-based ALD processing, a plasma treatment is required to inhibit ALD nucleation. For water-free processes, such as TiN by TiCl₄ and NH₃, the effects are less clear and require further investigation.

Overall, this work confirms and quantifies important capabilities for selective nucleation during ALD of metal oxides and nitrides on aC surfaces, and mechanistic understanding helps direct future research toward more highly selective processes that are scalable to high throughput manufacturing.

4.6 Acknowledgements

The authors thank Elie Schapmans (imec, Belgium) for assistance in the optimization of plasma processing with aC materials. The authors thank Thierry Conard, Johan Meersschant, and Christa Vrancken (imec, Belgium) for discussions involving characterization and data analysis.

4.7 Figures for Chapter 4

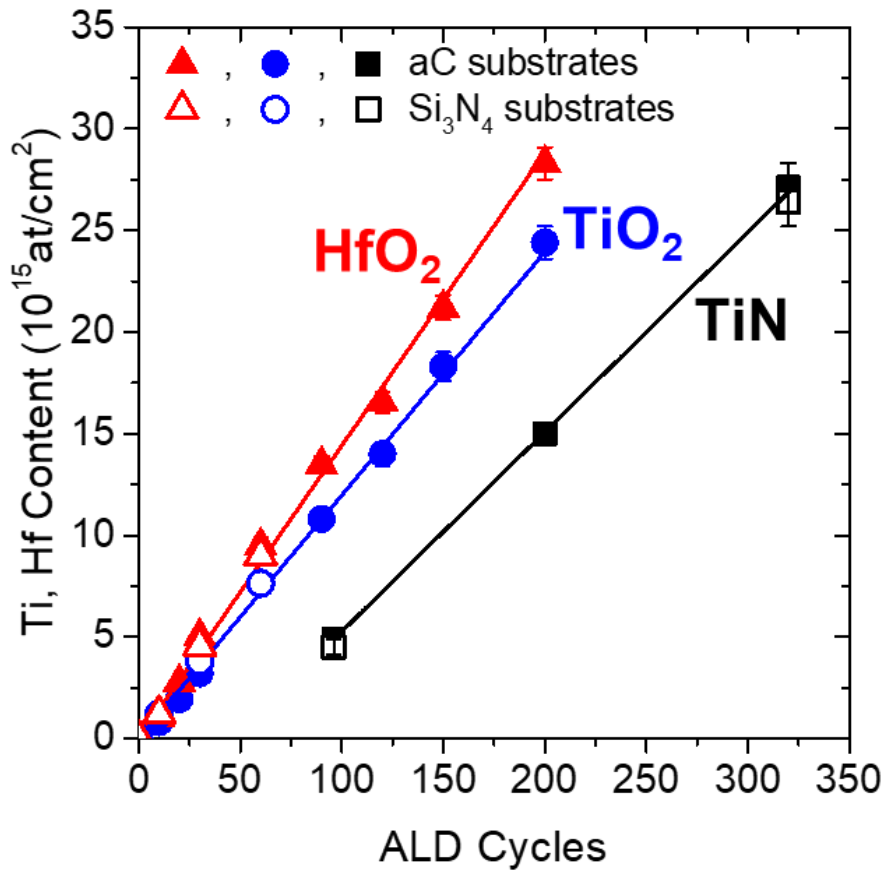


Figure 4.1: Ti and Hf content, measured by RBS, for TiO₂ (blue circles), HfO₂ (red triangles), and TiN (black squares) ALD films deposited on untreated aC (closed shapes) and Si₃N₄ (open shapes) versus the number of ALD cycles.

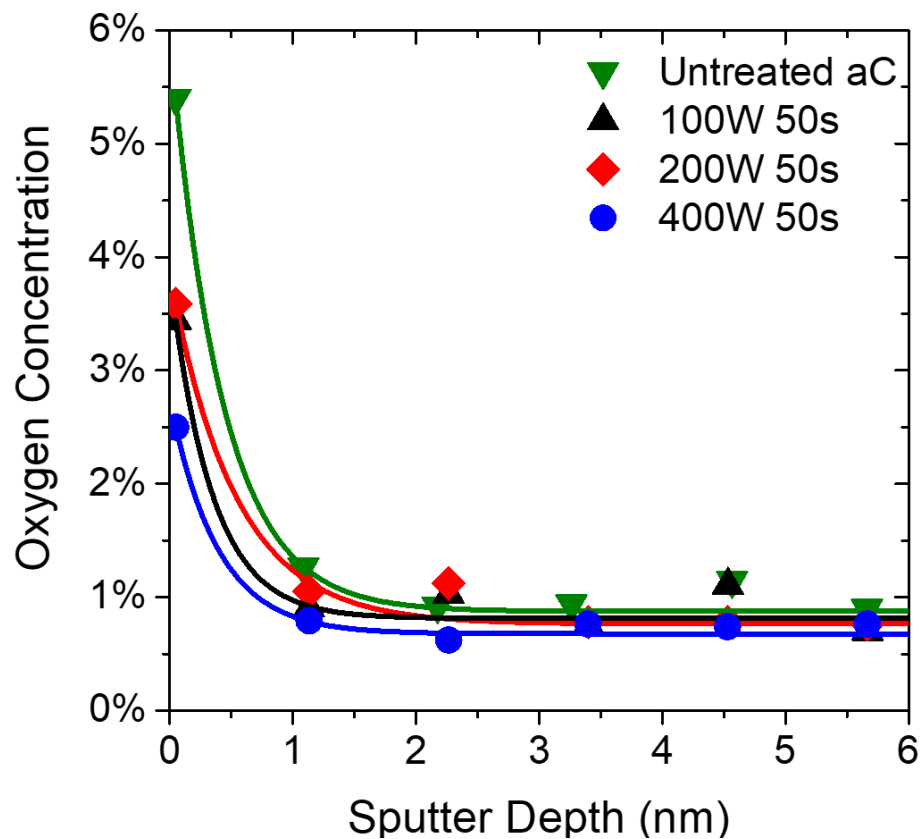


Figure 4.2: Oxygen concentration determined by XPS depth profiling of 100 nm aC films deposited on Si wafers. Untreated aC sample (green upside-down triangles) represents as-deposited films with no plasma processing. aC films were treated with hydrogen plasma for 100W 50s (black triangles), 200W 50s (red diamonds), and 400W 50s (blue circles).

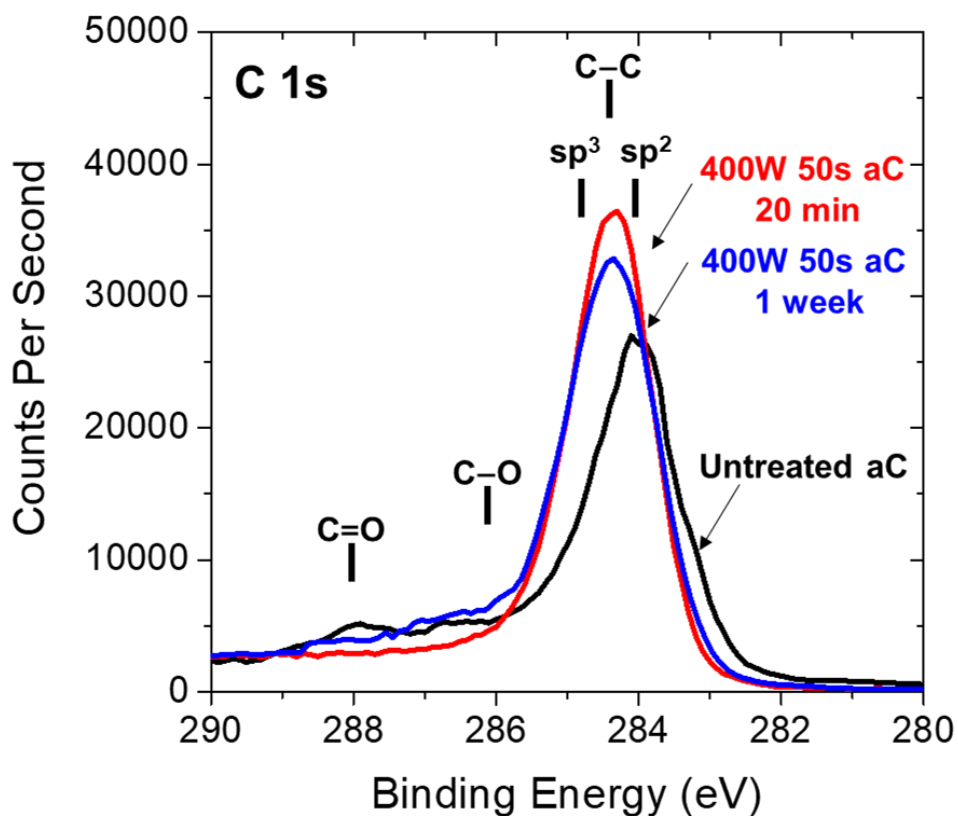


Figure 4.3: High resolution XPS scans of the C 1s region for untreated aC (black line), 400W 50s plasma treated aC with 20 minutes air exposure after processing (red line), and the same 400W 50s treated aC sample measured after 1 week of air exposure. C–C, C–O, and C=O bonding types can be ascribed to peak energies of 284 – 285, 286, and 288 eV, respectively. C–C sp² and sp³ bonding hybridization was indicated at 284 and 285 eV, respectively.

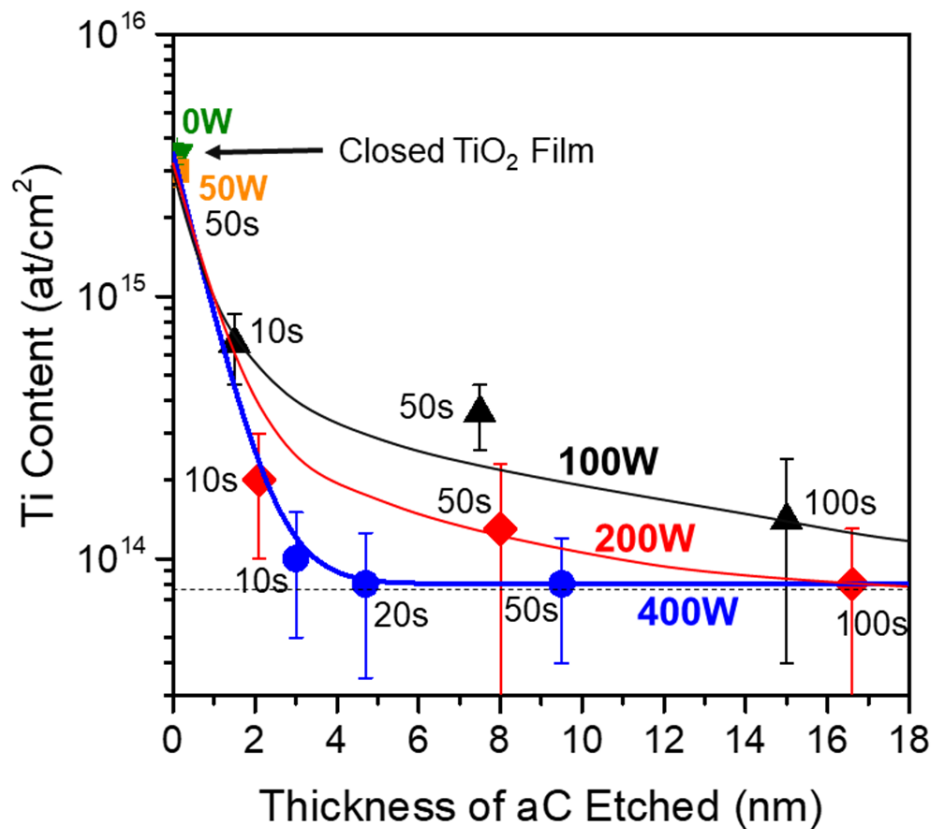


Figure 4.4: a) Resulting content of Ti (by RBS) on aC substrates for 50 (orange square), 100 (black triangles), 200 (red diamonds), and 400W (blue circles) plasma power for 10, 50, and 100s exposure times followed by 30 cycles of TiO₂ ALD at 250°C. A 0W (green triangle) treatment represents untreated aC when no plasma was used, thus serving as the control sample. The RBS detection limit for Ti was determined to be $\sim 8 \times 10^{13}$ at/cm² for the tool.

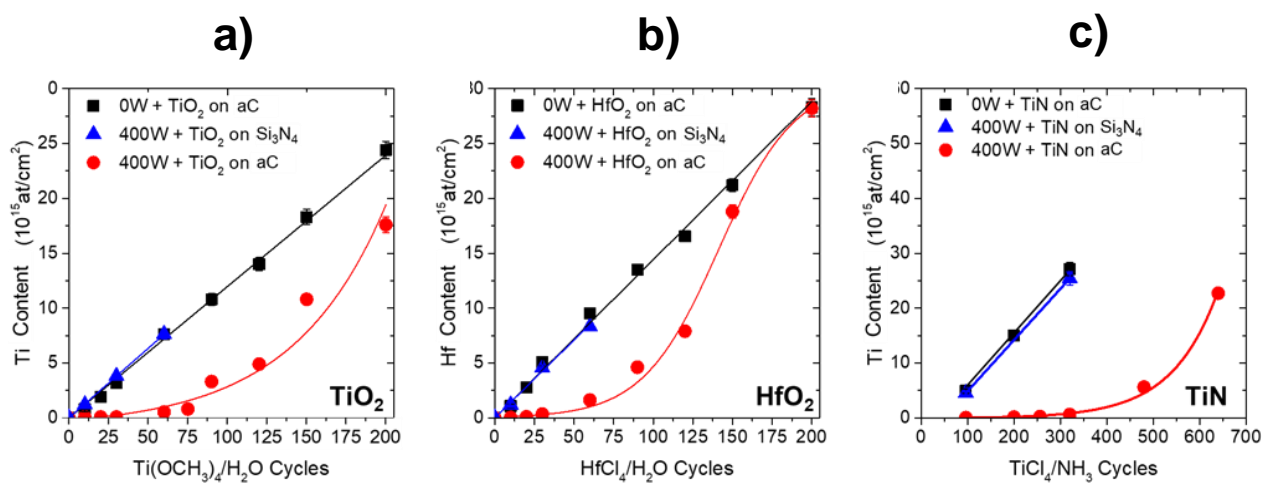


Figure 4.5: Ti or Hf content from RBS, in units of atoms/cm², obtained after ALD growth on untreated aC (black squares), plasma-treated Si₃N₄ (blue triangles), and plasma-treated aC (red circles) substrates for a) TiO₂ by Ti(OCH₃)₄/H₂O at 250°C b) HfO₂ by HfCl₄/H₂O at 300°C c) TiN by TiCl₄/NH₃ at 390°C.

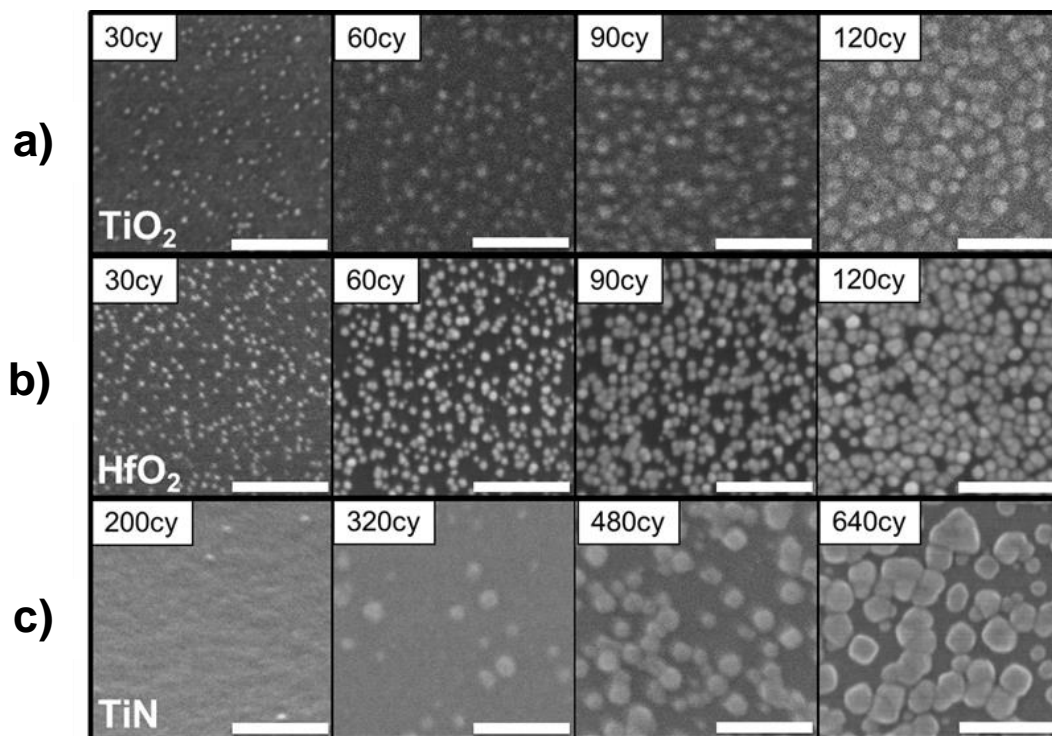


Figure 4.6: Top-down SEM images obtained for ALD a) TiO_2 , b) HfO_2 , c) TiN films for various numbers of cycles after plasma treatment on aC blanket substrates. All scale bars are 100 nm

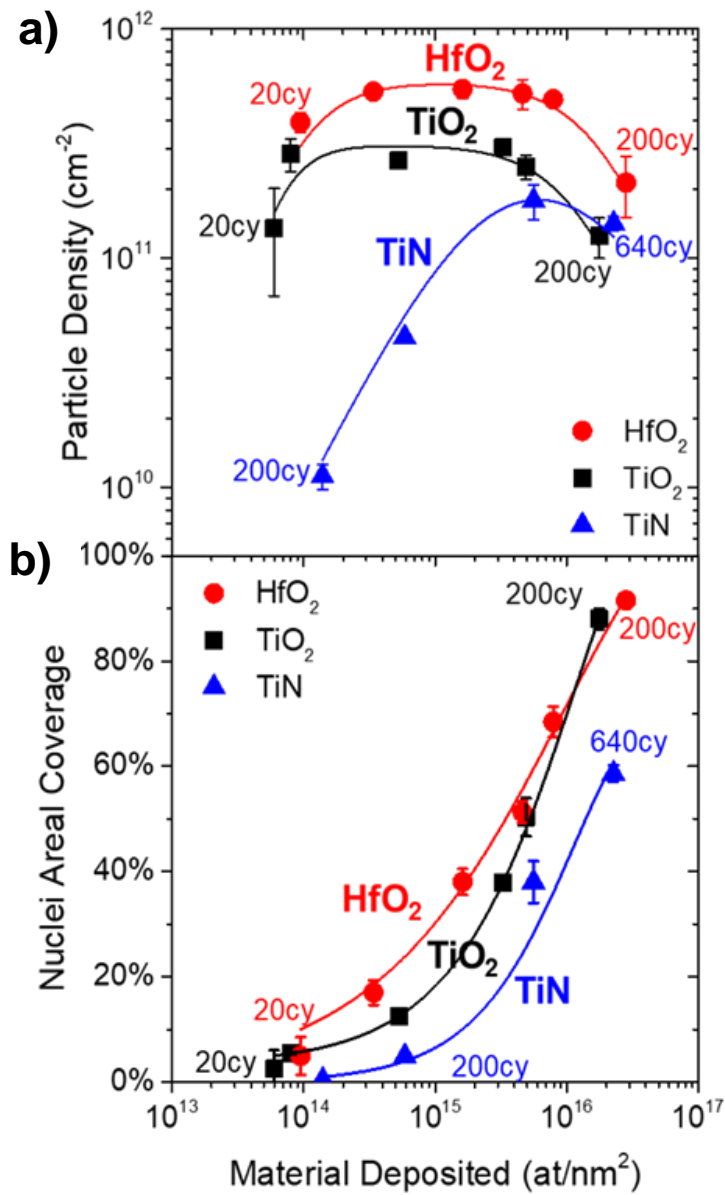


Figure 4.7: a) Particle density ($1/\text{cm}^2$) and b) nuclei areal surface coverage (from SEM image analysis) as a function of the amount of material deposited (obtained from RBS measurements) for HfO₂ (red squares), TiO₂ (black squares), and TiN (blue triangles) on 400W 20s H₂ plasma-treated aC. The corresponding number of cycles for the particle density and areal coverage of TiO₂ and HfO₂, from left to right, are 20, 30, 60, 90, 120, and 200 cycles. Similarly, the corresponding number of cycles for TiN, from left to right, are 200, 320, 480, 640 cycles.

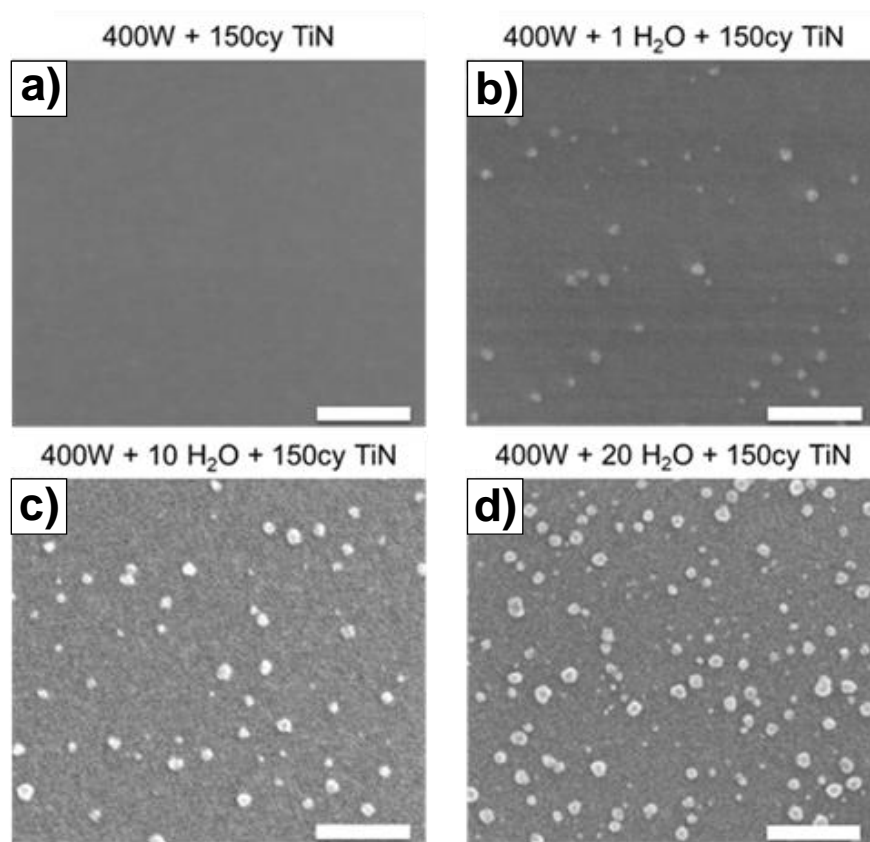


Figure 4.8: Top down SEM images of plasma-treated aC blanket substrates with a) 0, b) 1, c) 10, and d) 20 2s H₂O exposures (with 4s Ar purges) at 250°C followed by 150 cycles of TiN ALD. Scale bars 100 nm.

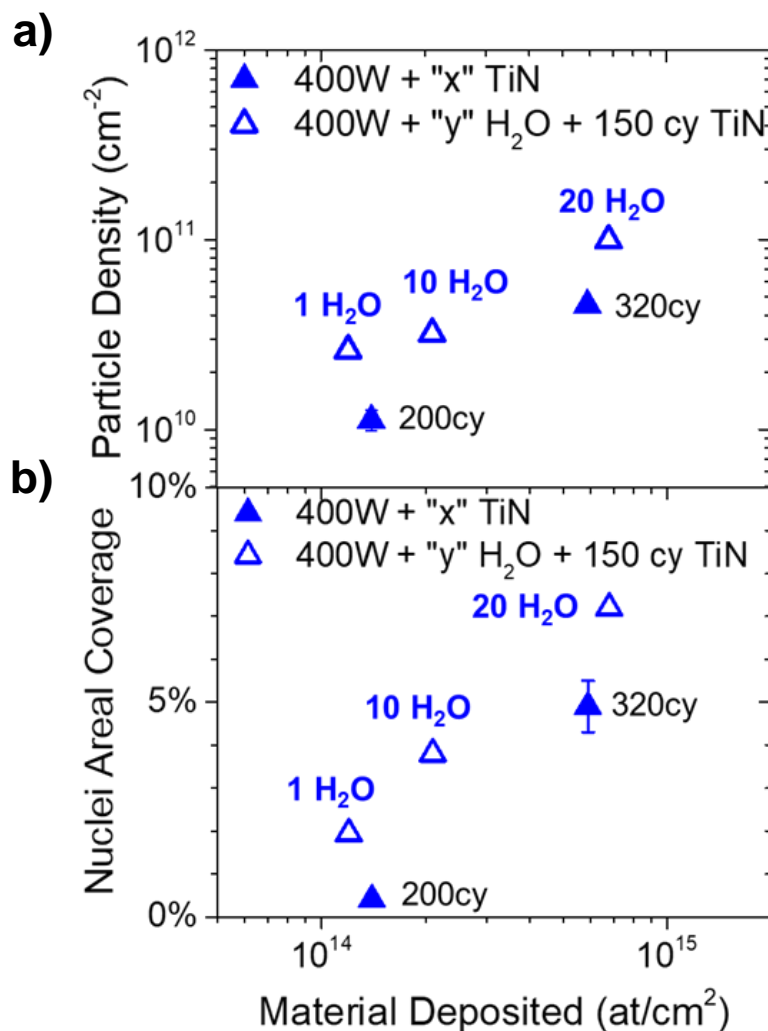


Figure 4.9: a) Particle density ($1/\text{cm}^2$) and b) nuclei areal surface coverage as a function of the amount of material deposited (obtained from RBS measurements) on 400W 20s H_2 plasma-treated aC. Plasma treated aC substrates subjected to 1, 10, and 20 H_2O water exposures (2s dose, 4s Ar purge) followed by 150 cycles of TiN ALD (open blue triangles). Plasma-treated aC substrates not subjected to H_2O , with 200 and 320 cy TiN ALD are also given for reference (closed blue triangles).

4.8 Tables for Chapter 4

Table 4.1 TiO₂, HfO₂, and TiN Bulk Film Properties

Parameter	TiO₂	HfO₂	TiN
ρ_i (g/cm ³) ref. ²⁹	3.9	9.7	5.2
MW _i (g/mol) ref. ²⁹	79.9	210.5	61.9
GPC_i^{RBS} (10 ¹⁴ at./cm ² /cy)	1.2	1.4	1.0
GPC_i^* (nm/cy)	0.04	0.05	0.02
GPC_i^{SE} (nm/cy)	0.043	0.050	0.031

Table 4.2 C 1s Peak Deconvolution for Plasma Treated aC

Sample	C–C sp²	C–C sp³	C–O	C=O
Untreated aC	57%	35.5%	4%	4.5%
400W 50s aC 20 minutes	39%	58%	2.5%	0.5%
400W 50s aC 1 week	35%	56%	5%	4%

4.9 References

- (1) Horiguchi, N.; Milenin, A. P.; Tao, Z.; Hubert, H.; Altamirano-Sanchez, E.; Veloso, A.; Witters, L.; Waldron, N.; -Å Ragnarsson, L.; Kim, M. S.; Kikuchi, Y.; Mertens, H. Patterning Challenges in Advanced Device Architectures: FinFETs to Nanowires. In *Advanced Etch Technology for Nanopatterning V*; 2016; p 978209.
- (2) Mameli, A.; Kuang, Y.; Aghaee, M.; Ande, C. K.; Karasulu, B.; Creatore, M.; Mackus, A. J. M.; Kessels, W. M. M.; Roozeboom, F. Area-Selective Atomic Layer Deposition of In₂O₃:H Using a μ -Plasma Printer for Local Area Activation. *Chem. Mater.* 2017, 29 (3), 921–925.
- (3) Yao, H.; Mullen, S.; Wolfer, E.; Mckenzie, D.; Dioses, A.; Rahman, D.; Cho, J.; Padmanaban, M.; Petermann, C.; Hong, S.; Mannaert, G.; Hopf, T.; De Simone, D.; Vangoidsenhoven, D.; Lorant, C.; Sebaai, F.; Sanchez, E. A. Spin-on Metal Oxides and Their Applications for Next Generation Lithography. *J. Photopolym. Sci. Technol.* 2016, 29 (1), 59–67.
- (4) Bencher, C.; Chen, Y.; Dai, H.; Montgomery, W.; Huli, L. 22nm Half-Pitch Patterning by CVD Spacer Self Alignment Double Patterning (SADP); *International Society for Optics and Photonics*, 2008; Vol. 6924, p 69244E.
- (5) Puurunen, R. Surface Chemistry of Atomic Layer Deposition: A Case Study for the Trimethylaluminum/ Water Process. *J. Appl. Phys.* 2005, 97, 121301.
- (6) Atanasov, S. E.; Kalanyan, B.; Parsons, G. N. Inherent Substrate-Dependent Growth Initiation and Selective-Area Atomic Layer Deposition of TiO₂ Using “water-Free” Metal-Halide/metal Alkoxide Reactants. *J. Vac. Sci. Technol. A Vacuum, Surfaces, Film.* 2016, 34 (1), 01A148.
- (7) Kalanyan, B.; Lemaire, P. C.; Atanasov, S. E.; Ritz, M. J.; Parsons, G. N. Using Hydrogen to Expand the Inherent Substrate Selectivity Window during Tungsten Atomic Layer Deposition. *Chem. Mater.* 2016, 28 (1), 117–126.
- (8) Kerrigan, M. M.; Klesko, J. P.; Winter, C. H. Low Temperature, Selective Atomic Layer Deposition of Cobalt Metal Films Using Bis(1,4-Di-Tert-Butyl-1,3-Diazadienyl)cobalt and Alkylamine Precursors. *Chem. Mater.* 2017, 29 (17), 7458–7466.
- (9) Zhang, W.; Engstrom, J. R. Effect of Substrate Composition on Atomic Layer Deposition Using Self-Assembled Monolayers as Blocking Layers. *J. Vac. Sci. Technol. A* 2016, 34 (1), 01A107.
- (10) Jiang, X.; Bent, S. F. Area-Selective ALD with Soft Lithographic Methods: Using Self-Assembled Monolayers to Direct Film Deposition. *J. Phys. Chem. C* 2009, 113 (41), 17613–17625.
- (11) Färm, E.; Kemell, M.; Ritala, M.; Leskelä, M. Selective-Area Atomic Layer Deposition with Microcontact Printed Self-Assembled Octadecyltrichlorosilane Monolayers as Mask Layers. *Thin Solid Films* 2008, 517 (2), 972–975.

- (12) Chopra, S. N.; Zhang, Z.; Kaihlanen, C.; Ekerdt, J. G. Selective Growth of Titanium Nitride on HfO₂ across Nanolines and Nanopillars. *Chem. Mater.* 2016, 28 (14), 4928–4934.
- (13) Vervuurt, R. H. J.; Karasulu, B.; Verheijen, M. A.; Kessels, W. M. M.; Bol, A. A. Uniform Atomic Layer Deposition of Al₂O₃ on Graphene by Reversible Hydrogen Plasma Functionalization. *Chem. Mater.* 2017, 29 (5), 2090–2100.
- (14) Zhang, Y.; Guerra-Nuñez, C.; Utke, I.; Michler, J.; Agrawal, P.; Rossell, M. D.; Erni, R. Atomic Layer Deposition of Titanium Oxide on Single-Layer Graphene: An Atomic-Scale Study toward Understanding Nucleation and Growth. *Chem. Mater.* 2017, 29 (5), 2232–2238.
- (15) Yang, L.; Jiang, L.; Fu, W.; Weimer, A. W.; Hu, X.; Zhou, Y. TiO₂ Quantum Dots Grown on Graphene by Atomic Layer Deposition as Advanced Photocatalytic Hybrid Materials. *Appl. Phys. A* 2017, 123 (6), 416.
- (16) Park, Y. H.; Kim, M. H.; Kim, S. Bin; Jung, H. J.; Chae, K.; Ahn, Y. H.; Park, J. Y.; Rotermund, F.; Lee, S. W. Enhanced Nucleation of High-K Dielectrics on Graphene by Atomic Layer Deposition. *Chem. Mater.* 2016, 28 (20), 7268–7275.
- (17) Meng, X.; Ionescu, M.; Banis, M. N.; Zhong, Y.; Liu, H.; Zhang, Y.; Sun, S.; Li, R.; Sun, X. Heterostructural Coaxial Nanotubes of CNT@Fe₂O₃ via Atomic Layer Deposition: Effects of Surface Functionalization and Nitrogen-Doping. *J. Nanoparticle Res.* 2011, 13 (3), 1207–1218.
- (18) Liyanage, L. S.; Cott, D. J.; Delabie, A.; Elshocht, S. Van; Bao, Z.; Wong, H.-S. P. Atomic Layer Deposition of High- K Dielectrics on Single-Walled Carbon Nanotubes: A Raman Study. *Nanotechnology* 2013, 24 (24), 245703.
- (19) Marichy, C.; Pinna, N. Carbon-Nanostructures Coated/decorated by Atomic Layer Deposition: Growth and Applications. *Coordination Chemistry Reviews.* 2013, pp 3232–3253.
- (20) Zhang, Y.; Guerra-Nuñez, C.; Li, M.; Michler, J.; Park, H. G.; Rossell, M. D.; Erni, R.; Utke, I. High Conformity and Large Domain Monocrystalline Anatase on Multiwall Carbon Nanotube Core-Shell Nanostructure: Synthesis, Structure, and Interface. *Chem. Mater.* 2016, 28 (10), 3488–3496.
- (21) Karg, M.; Lokare, K. S.; Limberg, C.; Clavel, G.; Pinna, N. Atomic Layer Deposition of Silica on Carbon Nanotubes. *Chem. Mater.* 2017, 29 (11), 4920–4931.
- (22) Hu, H.; Bhowmik, P.; Zhao, B.; Hamon, M. .; Itkis, M. .; Haddon, R. . Determination of the Acidic Sites of Purified Single-Walled Carbon Nanotubes by Acid–base Titration. *Chem. Phys. Lett.* 2001, 345 (1), 25–28.
- (23) Fairbairn, K.; Rice, M.; Weidman, T.; Ngai Ian, C. S.; Scot Latchford, I.; Bencher, C. D.; Wang, Y. M. Method for Depositing an Amorphous Carbon Layer. 6,573,030 B1, 2003.

- (24) Tai, H.; Liao, Y. M.; Liu, W. T.; Peng, W. C.; Ying, T. H. Novel Clean Concept of Advanced Patterning Film (Amorphous Carbon) for Beyond 2xnm Generation Self-Aligned Double-Patterning (SADP) Process. *ECS Trans.* 2014, 61 (3), 67–71.
- (25) Elofsson, V.; Lü, B.; Magnfält, D.; Münger, E. P.; Sarakinos, K.; L€e, B.; Magnf, D.; Alt, €; M€ Unger, E. P. Unravelling the Physical Mechanisms That Determine Microstructural Evolution of Ultrathin Volmer-Weber Films. *J. Appl. Phys.* 2014, 116 (4), 44302.
- (26) Pore, V.; Rahtu, A.; Leskelä, M.; Ritala, M.; Sajavaara, T.; Keinonen, J. Atomic Layer Deposition of Photocatalytic TiO₂ Thin Films from Titanium Tetramethoxide and Water. *Chem. Vap. Depos.* 2004, 10 (3), 143–148.
- (27) Aarik, J.; Aidla, A.; Kikas, A.; Käämbre, T.; Rammula, R.; Ritslaid, P.; Uustare, T.; Sammelselg, V. Effects of Precursors on Nucleation in Atomic Layer Deposition of HfO₂. *Appl. Surf. Sci.* 2004, 230 (1–4), 292–300.
- (28) Tiznado, H.; Zaera, F. Surface Chemistry in the Atomic Layer Deposition of TiN Films from TiCl₄ and Ammonia. *J. Phys. Chem. B* 2006, 110 (27), 13491–13498.
- (29) Haynes, W. M. Haynes, W. M. *Handbook of Chemistry and Physics* 96th Edition. Taylor and Francis Group, 2015, 96th ed.; 2015.
- (30) Lemaire, P. C.; King, M.; Parsons, G. N. Understanding Inherent Substrate Selectivity during Atomic Layer Deposition: Effect of Surface Preparation, Hydroxyl Density, and Metal Oxide Composition on Nucleation Mechanisms during Tungsten ALD. *J. Chem. Phys.* 2017, 146 (5), 52811.
- (31) Elliott, S. D.; Scarel, G.; Wiemer, C.; Fanciulli, M.; Pavia, G. Ozone-Based Atomic Layer Deposition of Alumina from TMA: Growth, Morphology, and Reaction Mechanism. *Chem. Mater.* 2006, 18 (16), 3764–3773.
- (32) Gharachorlou, A.; Detwiler, M. D.; Gu, X. K.; Mayr, L.; Klo; Tzer, B.; Greeley, J.; Reifengerger, R. G.; Delgass, W. N.; Ribeiro, F. H.; Zemlyanov, D. Y. Trimethylaluminum and Oxygen Atomic Layer Deposition on Hydroxyl-Free Cu(111). *ACS Appl. Mater. Interfaces* 2015, 7 (30), 16428–16439.
- (33) Zhang, H.; Arutchelvan, G.; Meersschaut, J.; Gaur, A.; Conard, T.; Bender, H.; Lin, D.; Asselberghs, I.; Heyns, M.; Radu, I.; Vandervorst, W.; Delabie, A. MoS₂ Functionalization with a Sub-Nm Thin SiO₂ Layer for Atomic Layer Deposition of High-κ Dielectrics. *Chem. Mater.* 2017, 29 (16), 6772–6780.
- (34) Dwivedi, N.; Yeo, R. J.; Satyanarayana, N.; Kundu, S.; Tripathy, S.; Bhatia, C. S. Understanding the Role of Nitrogen in Plasma-Assisted Surface Modification of Magnetic Recording Media with and without Ultrathin Carbon Overcoats. *Sci. Rep.* 2015, 5, 1–13.
- (35) Chu, P. K.; Li, L. Characterization of Amorphous and Nanocrystalline Carbon Films. *Mater. Chem. Phys.* 2006, 96 (2–3), 253–277.

- (36) Cheung, C.; Luo, K.; Li, D.; Ngo, P.; Dang, L.; Uyeda, J.; Wang, J.; Barsky, M. Silicon Nitride Surface Preparation to Prevent Photoresist Blister Defects. In CS Mantech; 2005; pp 1–2.
- (37) Puurunen, R.; Vandervorst, W.; Bender, H.; Conard, T.; Zhao, C.; Delabie, A.; Caymax, M.; De Gendt, S.; HeynsMinna, M.; de Ridder, M.; BrongersmaYde, H.; Dao, T.; de Win, T.; Verheijen, M.; KaiserMarko Tuominen, M. Island Growth in the Atomic Layer Deposition of Zirconium Oxide and Aluminum Oxide on Hydrogen-Terminated Silicon: Growth Mode Modeling and Transmission Electron Microscopy. *J. Appl. Phys.* 2004, 96, 4878.
- (38) Puurunen, R. L.; Vandervorst, W. Island Growth as a Growth Mode in Atomic Layer Deposition: A Phenomenological Model. *J. Appl. Phys.* 2004, 96 (12), 7686–7695.
- (39) Nakakubo, Y.; Eriguchi, K.; Ono, K. Characterization of Plasma Process-Induced Latent Defects in Surface and Interface Layer of Si Substrate. *ECS J. Solid State Sci. Technol.* 2015, 4 (6), N5077–N5083.
- (40) Xiang, J.; Ding, Y.; Du, L.; Li, J.; Wang, W.; Zhao, C. Growth Mechanism of Atomic-Layer-Deposited TiAlC Metal Gate Based on TiCl₄ and TMA Precursors. *Chinese Phys. B* 2016, 25 (3), 37308.

**CHAPTER 5: MODELING THE NUCLEATION OF TiO₂,
HfO₂ AND TiN ATOMIC LAYER DEPOSITION ON
PLASMA-TREATED AMORPHOUS CARBON**

CHAPTER 5. Modeling the Nucleation of TiO₂, HfO₂ and TiN Atomic Layer Deposition on Plasma-Treated Amorphous Carbon

Eric Stevens,^{†,‡,§} Yoann Tomczak,[†] Efrain Altamirano Sanchez,[†] Annelies Delabie,^{†,§} Gregory Parsons,^{*,‡}

[†] Imec, Kapeldreef 75, B-3001 Leuven, Belgium

[‡] Department of Chemical and Biomolecular Engineering, North Carolina State University, 911 Partners Way, Raleigh NC 27695

[§] KU Leuven (University of Leuven), Celestijnenlaan 200F, B-3001, Leuven, Belgium

5.1 Abstract

Understanding the nucleation during atomic layer deposition is very important for continued advances to be made in area-selective deposition. In this work, we apply a nucleation model to describe the atomic layer deposition of TiO₂, HfO₂, and TiN ALD on H₂-plasma treated aC. First, we apply the well-established Island Growth Model, which assumes periodic spacing of nuclei and no additional generation of nucleation sites. Then we modify the Island Growth Model according to the Avrami Equation, allowing random distribution of nucleation sites which increase at a constant rate. For TiN nucleation on plasma-treated aC, the modified Island Growth Model best fit the data, where the nucleation density was approximated using a linear expression with initial nucleation density of $1 \times 10^{-4} \text{ nm}^{-2}$ increasing at a rate of $3 \times 10^{-6} \text{ nm}^{-2} \text{ cy}^{-1}$. For TiO₂ and HfO₂ nucleation on plasma-treated aC, the modified Island Growth Model data best fit the data assuming a constant initial nucleation density of $1.8 \times 10^{-2} \text{ nm}^{-2}$ and $2.5 \times 10^{-2} \text{ nm}^{-2}$, respectively, and no additional site generation. The discrepancy is likely due H₂O absorption on plasma-treated aC for metal oxide ALD, leading to a roughly two order-of-magnitude increase in initial nucleation density. This work demonstrates that the modified Island Growth Model is a straightforward and

accurate method to model ALD nucleation phenomena and warrants further study for other area-selective ALD processes.

5.2 Introduction

The use of atomic layer deposition (ALD) in the semiconductor industry is well established,¹⁻⁴ and is quickly gaining attention for advanced patterning applications.^{5,6} ALD utilizes cyclic processing of self-limiting half reactions to grow thin films with sub-nm control over the thickness.^{7,8} Area-selective ALD is defined as a process which grows a film selectively to one substrate over another, for example TiO₂ on SiO₂ versus hydrogen-terminated Si⁹ and Co metal on Pt vs Si with native oxide.¹⁰ Understanding the nucleation during area-selective ALD on both the desired growth and non-growth substrates is extremely important to improve performance in accelerate adaptation of these processes into the industry.

Various models to describe nucleation in many different ALD processes have been investigated. For example, the well-established Island Growth Model was shown to accurately predict the nucleation and growth during Al₂O₃ and ZrO₂ on hydrogen-terminated Si (Si-H).^{11,12} Furthermore, an analytical model for island growth of different shapes was demonstrated previously.¹³ An underlying issue with these models is that they assume ordered distribution of nuclei on the surface, which is an appropriate assumption for some processes. These models would not be able to predict the growth of a species that is selectively grown (or not grown) on certain areas of a substrate. For example, Pt ALD was shown to selectively deposit only on graphene grain boundaries, leaving the rest of the graphene surface uncoated.¹⁴ A model describing island growth and coalescence on Cu ALD on TaN was described by Hagen et. al, but the complexity of the model required simulation in Matlab.¹⁵ Additionally, a kinetic model of Ru nucleation on SiO₂ and Si₃N₄ surfaces was also proposed, yet had many adjustable parameters which need to be

carefully defined or calculated (such as the rate at which nuclei capture monomers by surface diffusion).¹⁶

A kinetic model describing the phase transition during the nucleation and growth of a new phase on specific surface sites was described by Melvin Avrami.^{17–19} This model allows for calculations of nucleation phenomena for a random distribution of nucleation sites, which are allowed to vary as a function of time. Since being introduced in the late 1930s, the Avrami Equation was been applied in many ways^{20,21} but has yet to be applied to describe nucleation in selective deposition on aC substrates. Thus, we modify the Island Growth Model to compare fit results for the nucleation of TiO₂, HfO₂, and TiN ALD on plasma-treated aC substrates.

5.3 Experimental

5.3.1 aC Substrate Preparation

Substrates were prepared by depositing high-density amorphous carbon (Advanced Patterning Film)^{22,23} films on 300 mm Si (100) wafers by plasma-enhanced chemical vapor deposition (PE-CVD) using acetylene (C₂H₂) at 400°C in an Applied Materials Producer platform.

5.3.2 Atomic Layer Deposition and H₂ Plasma Processing

H₂ plasma exposures were used to remove oxygen species and terminate the aC surface with C-C and C-H bonds. Plasma and atomic layer deposition of TiO₂, HfO₂, and TiN were performed in an ASM Polygon 8300 cluster tool, allowing for plasma-treated substrates to be transferred without air breaks for ALD processing. TiO₂ and HfO₂ were deposited in an ASM PULSAR cross-flow thermal ALD chamber using Ti(OCH₃)₄/Ar/H₂O/Ar (4s/8s/2s/4s) at 250°C and HfCl₄/N₂/H₂O/N₂ (1s/3s/0.5s/3s) at 300°C, respectively. TiN depositions were performed in an ASM EMERALD PE-ALD chamber, the wafer chuck (bottom electrode) was heated to 390°C, while the walls and showerhead were kept at 160°C. TiN precursors, TiCl₄ and NH₃, were pulsed through the showerhead for 0.8s and 4s, respectively, separated by 1.5s Ar purges. The reagent

dose and purge times for TiO₂ and TiN were selected such that linear growth with uniform thickness were observed across the entire 300 mm wafer.

In the ASM EMERALD PE-ALD chamber, a capacitively-coupled hydrogen plasma was generated top-electrode (which was the gas delivery showerhead) using an RF power source at 13.56 MHz. The wafer chuck was used as the counter electrode such that all plasma species were generated between the showerhead and substrate. The operating pressure was maintained at 2 Torr with an argon inert gas flow. The temperature of the bottom electrode, and thus the wafer, was set to 300°C, while the chamber walls and top electrode were maintained at 160°C. The plasma recipe began with a thermal equilibration time of 2 minutes under Ar flow. A 10 second, 10% H₂/Ar direct plasma exposure, with powers between 50 to 400W, was subjected to the wafer, followed by a 1 second Ar purge. This dosing sequence was repeated to give a total plasma exposure time of 20 seconds. Following the final exposure, the substrate was subjected to 60 seconds of 100% H₂ to passivate the surface of any dangling bonds.

5.3.3 Characterization

Top-down images of TiO₂, HfO₂, and TiN particles were using a scanning electron microscope (SEM, Hitachi SU8000) with a beam energy of 3 kV, beam current of 10 pA, and no sputter deposition. Image analysis was performed on SEM images using ImageJ software, yielding particle density, particle size distribution, and surface coverage. Growth rate per cycle (GPC) of ALD thin films on untreated aC were determined using spectroscopic ellipsometry for 49 points on a 300 mm Si wafer (Aleris, KLA Tencor).

5.3.4 Models

5.3.4.1 Island Growth Model

The nucleation behavior of metal oxides on semiconductor substrates has been previously described by Puurunen and Vandervorst.¹¹ In the proposed model, the radius of a given island, $r(t)$, can be calculated using equation (5.1), where r_0 , t , and Δr correspond to the initial nuclei

$$r(t) = r_0 + t\Delta r \quad (5.1)$$

radius, cycle number, and growth rate per cycle (GPC) for the material. For an ALD process, Δr can be assumed to be constant over a certain temperature range, consistent with constant GPC values within the ALD temperature window of many ALD processes.^{24,25} Furthermore, r_0 is assumed to be constant, with a value of 0.5 nm based on previous experimental and modeling results.¹² In the model, Al_2O_3 nucleation on hydrogen-terminated Si (Si-H), Al_2O_3 is assumed to nucleate during the first ALD cycle only at surface defect sites. The defect sites here assumed to be ordered, with the distance between these defect sites, also referred to as the lattice constant, is assumed to be fixed for a given process. The lattice constant, b , is described in equation (5.2),

$$b = 2(r_0 + n_c\Delta r) \quad (5.2)$$

where n_c is defined as the number of ALD cycles at which the nuclei first coalesce. For this model, the adjustable parameters are n_c , r_0 , and Δr . Thus, the adjustable parameter for this model was n_c , and by definition, the lattice constant b .

The model describes three distinct island growth phases for metal oxide ALD on hydrogen-terminated Si substrates, and thus three different equations to calculate the surface fraction of islands. By applying assumption based on the system geometry, the surface fraction of the islands, as a function of cycle time, can be given by equations (5.3) – (5.5). Equation (5.3) shows the

$$S_{isl}^{(l)} = \pi \left(\frac{r(t)}{b} \right)^2 \quad (5.3)$$

surface fraction of islands in the first regime, which is defined while the radius of a given island is within the bounds of the lattice constant such that $r(t) \leq b/2$. These islands have initial radius r_0 and growth at a rate of Δr . Furthermore, this model assumes that no additional nucleation can take place in the spaces between initial nuclei. Once the islands have grown in radius to a value of $b/2$, adjacent islands have now touched, indicating the initial island coalescence point (i.e., when $t = n_c$). Equation (5.4) is used to calculate the surface fraction of islands in this second growth

$$S_{isl}^{(II)} = \pi \left(\frac{r(t)}{b} \right)^2 \left\{ \pi - 4 \left[\arccos \left(\frac{b}{2r(t)} \right) - \frac{b}{2r(t)} \sin \left(\arccos \left(\frac{b}{2r(t)} \right) \right) \right] \right\} \quad (5.4)$$

regime, where $b/2 \leq r(t) \leq b/\sqrt{2}$. After this point, the islands grow to fill the remaining space until a continuous film is formed and equation (5) holds, where the surface fraction is unity.

$$S_{isl}^{(III)} = 1 \quad (5.5)$$

These parameters used to describe TiO₂, HfO₂, and TiN ALD on plasma-treated aC are reported in Table 5.1. Two different n_c parameters were used to fit the data, which corresponded to two different lattice constants, b , for each material.

5.3.4.2 Modified Island Growth Model - Avrami Equation

A modification to the Island Growth Model was also applied to study to nucleation of ALD materials on aC films. Developed by Melvin Avrami,^{17,18} his mathematical equations can be used to describe the kinetics of a new phase material (e.g., islands growing on a surface) nucleating on a substrate surrounded by the old phase (i.e., gas or liquid of the material in question). The following section assumes the 2D form of the model, with parameters given in units widely used to describe ALD processes.

We explore two modifications to the Island Growth Model. The first assumption is that nucleation sites are randomly distributed across the substrate, which have an initial areal density

of N_0 , in units of nm^{-2} . The Island Growth Model makes a geometric simplification, where initial nuclei are periodically spaced with an initial radius. The first modification replaces the initial radius parameter, which is now assumed to be zero, and constant lattice spacing with the initial nuclei density (randomly distributed). The second assumption is that nucleation sites can be generated, yielding a nucleation rate, \dot{N} in units of $\text{nm}^{-2}\text{cy}^{-1}$. Nucleation sites are assumed to only be generated on the substrate where no islands are present. Radial growth occurs from nucleation sites, where the radius of a given island, $r(t)$ in units of nm, is given by equation (5.6), where t is the process time,

$$r(t) = t\Delta r \quad (5.6)$$

in units of cycles and Δr is the GPC for the nucleating material, in units of nm/cy. The GPC is assumed to be constant across the nucleating and continuous (i.e., thin-film ALD growth) phase and symmetric about the nucleation center point.

The surface fraction of islands as a function of time, $S_{isl}(t)$, can be described using equation (5.7), where $A_{isl}(t)$ and A_0 are the areas, in units of nm^{-2} , of the islands on the substrate

$$S_{isl}(t) = A_{isl}(t)/A_0 \quad (5.7)$$

(assuming two-dimensional growth) and the initial surface area of the substrate, respectively. At time dt , an isolated island grows to a radius of $r(t) + dr$. The change in island surface fraction can be described in equation (5.8), where $N(t)$ is the time dependent nucleation density, in units

$$dS_{isl} = \pi r(t)dr \cdot N(t)[1 - S_{isl}] \quad (5.8)$$

of nm^{-2} . Assuming the change in radius is constant and grows at the same rate as for ALD film growth at steady state, equation (5.8) can be rewritten to give equation (5.9), where r was rewritten in terms of cycle time, t , and the GPC, Δr :

$$dS_{isl} = \pi\Delta r^2tdt \cdot N(t)[1 - S_{isl}] \quad (5.9)$$

At this point, $N(t)$ needs to be defined and can be assumed to be constant, given by equation (5.10), or a function of t , given by equation (5.11):

$$N(t) \sim N_0 \quad (5.10)$$

$$N(t) \sim N_0 + \dot{N} \cdot t \quad (5.11)$$

where N_0 represents the initial nucleation density, with units nm^{-2} , and \dot{N} represents the constant generation rate of nucleation sites, with units $\text{nm}^{-2}\text{cy}^{-1}$. $N(t)$ can then be substituted into equation (5.9) and, after rearranging terms and integrating both sides of the equation, giving equations (5.12) and (5.13):

$$-\ln[1 - S_{isl}] = \pi \Delta r^2 \left[\frac{N_0 t^2}{2} \right], \text{ for } N(t) \sim N_0 \quad (5.12)$$

$$-\ln[1 - S_{isl}] = \pi \Delta r^2 \left[\frac{N_0 t^2}{2} + \frac{\dot{N} t^3}{3} \right], \text{ for } N(t) \sim N_0 + \dot{N} \cdot t \quad (5.13)$$

The initial condition, $S_{isl}(t = 0) = 0$ was applied to solve for the integration constant, which was found to be zero. Equations (5.12) and (5.13) can be simplified further to give an expression for S_{isl} , given by equations (5.14) and (5.15), respectively:

$$S_{isl} = 1 - \exp \left[-\pi \Delta r^2 \left[\frac{N_0 t^2}{2} \right] \right], \text{ for } N(t) \sim N_0 \quad (5.14)$$

$$S_{isl} = 1 - \exp \left[-\pi \Delta r^2 \left[\frac{N_0 t^2}{2} + \frac{\dot{N} t^3}{3} \right] \right], \text{ for } N(t) \sim N_0 + \dot{N} \cdot t \quad (5.15)$$

These expressions take on a familiar form of the well-known Avrami Equation demonstrated previously.¹⁷⁻²¹

5.4 Results and Discussion

5.4.1 Particle Analysis from SEM

Figures 5.1, 5.2, and 5.3 show the top-down SEM images on plasma-treated aC substrates subjected to TiO_2 , HfO_2 , and TiN ALD processing, respectively. From these images, the particles

were differentiated from the underlying aC substrate based on the pixel contrast, with resulting particle outlines overlaid on original images also shown in Figures 5.1, 5.2, and 5.3. The resulting surface coverage of the identified particles were also calculated and presented in Figure 5.4. For TiO₂ and HfO₂ processing, the particles were mostly coalesced, resulting in a surface coverage \geq 90% (Figure 5.4 a). Conversely, 680 cycles of TiN ALD on plasma-treated aC yielded a surface coverage of \sim 60% (Figure 5.4 b).

The particle size distributions at various cycle times were also calculated using ImageJ and shown in Figures 5.5, 5.6, and 5.7 for TiO₂, HfO₂, and TiN, respectively. During particle analysis, the image dimensions were normalized per cm² of analysis area to ensure the total particle counts for different cycle numbers were directly comparable. For reference, the theoretical particle radius (r^* in units of nm) was given as a function of the number of cycles for each ALD process. The r^* values were calculated assuming particle nucleation occurred during the first ALD cycle, followed by radial growth according to the GPC obtained from ellipsometry measurements of TiO₂, HfO₂, and TiN films on silicon with native oxide (see Δr in Table 5.1).

The particle size distributions for all three materials deposited on plasma-treated aC were initially narrow for low cycle numbers, followed by a broadening of the radial size for increasing numbers of ALD cycles. In comparing the measured particle radius, $r(t)$, with the theoretical radius, r^* , the relative time of nucleation on aC can be estimated. For a $r < r^*$, the likely nucleated after the first ALD cycle. For all three materials and every cycle number analyzed, particles with $r < r^*$ were observed, which implies continuous generation of nucleation sites during processing. From SEM images in Figures 5.1, 5.2 and 5.3, these smaller nuclei are more obvious for larger cycle numbers, where a large discrepancy in particle size is expected. For $r > r^*$, particles have likely coalesced with a neighboring particle to give a larger effective radius, assuming the Δr is constant in the

radial direction. Analysis of Figures 5.1, 5.2 and 5.3 also show increased particle coalescence for increased cycling. The image analysis software was, in some cases, able to differentiate merged particles with ones that have just began to touch. Since the analysis software was unable to consistently identify two or more coalesced particles with ones that are barely touching, the particle size distribution counts are considered rough estimations. Nevertheless, with some particles having coalesced or are close enough to begin coalescence, the distribution of nucleation sites on the surface is not ordered and periodic but instead random.

5.4.2 Island Growth Model

For the Island Growth Model, the parameters used for calculating the island surface fraction are given in Table 5.1. For each ALD process, the layer closure parameter, n_c , and thus the lattice spacing, b , were varied to assess the fit to the experimental data. Figure 5.8 shows the modeling results for TiO₂ ALD on plasma-treated aC. A model consistent with $n_c=150$ cycles best fit the data, with a standard error of 0.06. In order to fit the surface coverage of ~90% at 200 cycles, n_c was increased to 180 cycles, which underestimated the surface fraction for 90 – 120 cycles and increased the error to 0.09. Increasing the n_c parameter resulted in a ~30% decrease in the nucleation site density (see b^{-2} in Table 5.1) from 5.2×10^{-3} to $3.7 \times 10^{-3} \text{ nm}^{-2}$.

Figure 5.9 shows the modeling results for HfO₂ ALD on plasma-treated aC. A model consistent with $n_c=120$ cycles best fit the data, with a standard error of 0.10. n_c was increased to 150 cycles, which underestimated the surface fraction for 90 – 120 cycles and increased the error to 0.51. Decreasing n_c to 100 cycles resulted in a better fit for surface fractions less than 0.4 but also had an error of 0.14. The nucleation site density for $n_c = 100, 120, \text{ and } 150$ were calculated to be $8.1 \times 10^{-3}, 5.8 \times 10^{-3}, \text{ and } 3.8 \times 10^{-3} \text{ nm}^{-2}$, respectively.

Figure 5.10 shows the modeling results for TiN ALD on plasma-treated aC substrates. A model consistent with $n_c=800$ cycles best fit the data with an error of 0.08. Although using $n_c=800$ cycles resulted in the best fit, the model did not fit the data well less than 320 cycles (surface fraction < 0.05). To fit the surface fraction below 320 cycles, n_c was increased to 1000 and 1300 cycles, which then resulted in increased standard errors of 0.16 and 0.11, respectively. For $n_c = 1300$, the model best fit the data when the surface fraction was less than 0.05. The nucleation density for $n_c = 800, 100, \text{ and } 1300$ was calculated to be $5.1 \times 10^{-4}, 2.5 \times 10^{-4}, \text{ and } 1.5 \times 10^{-4} \text{ nm}^{-2}$.

Comparing the model results for metal oxide and metal nitride ALD, the nucleation density for TiN ALD was approximately an order of magnitude lower than that observed for TiO_2 and HfO_2 , corresponding to a longer delay prior to island coalescence. Furthermore, the model consistently fit either low or high surface fractions, corresponding to high or low n_c , respectively. For example, TiN nucleation required $n_c = 800$ and 1300 cycles, to best fit the data when $S_{isl} > 0.4$ and $S_{isl} < 0.05$, respectively.

A generation of additional nucleation sites is likely responsible for the incomplete fit of the experimental data. Additional nucleation sites generated during ALD processing would increase the measured island surface fraction with increased cycling. Furthermore, as surface fraction approaches unity, additional surface fraction from nucleation site generation is minimal compared to the size and coverage of existing particles. The likely difference in the rate of nucleation site generation is due to the use of H_2O as a co-reagent in the metal oxide chemistries, where the TiN process uses NH_3 . The increased polarity of H_2O is likely to adsorb more readily on the aC surface, leading to a higher probability of generating a new nucleation site (surface C-OH or other C-O species). These types of species have been shown to provide preferable nucleation over hydrogen-

terminated surfaces.²⁶⁻³⁰ Therefore, to best fit the experimental data, the model needs to be modified to allow for generation of additional nucleation sites.

5.4.3 Modified Island Growth Model - Avrami Equation

To directly compare with the unmodified Island Growth Model, the initial nucleation site density, N_0 , was first investigated for TiN nucleation without nucleation site generation. The results in Figure 5.11 show N_0 of $1 \times 10^{-4} \text{ nm}^{-2}$ and $2 \times 10^{-3} \text{ nm}^{-2}$ best fit the data for $t \leq 320$ cycles, with standard error 0.28, and $t \geq 480$ cycles, with standard error 0.10, respectively. The overall error was minimized to 0.09 in using $N_0 = 1 \times 10^{-3} \text{ nm}^{-2}$. Although initial nucleation density of $N_0 = 2.5 \times 10^{-4} \text{ nm}^{-2}$ gave the best fit of the data, the model did not adequately fit the data for low fractions. Since the best fit of the experimental data for low surface coverage (i.e., $S_{isl} < 0.05$) was calculated for $N_0 = 1 \times 10^{-4} \text{ nm}^{-2}$, the initial nucleation site density for plasma-treated aC prior to ALD was assumed to be on the order of $1 \times 10^{-4} \text{ nm}^{-2}$. Compared with the inverse square of the lattice parameter found in the Island Growth Model (Table 5.1), an initial nucleation site density on the order of 10^{-4} nm^{-2} was comparable. Similar to the unmodified Island Growth Model, adjusting the initial nucleation site density parameter lead to fits of either the low or high surface fraction data. This was expected since the differences in the unmodified and modified Island Growth Model are due to periodic and random distribution of initial nuclei, respectively. Thus, the addition of a nucleation site generation parameter is required.

Figure 5.12 shows the best fit results, which utilized $N_0 = 1 \times 10^{-4} \text{ nm}^{-2}$ (based on findings in Figure 5.11) and $\dot{N} = 3 \times 10^{-6} \text{ nm}^{-2} \text{ cy}^{-1}$, resulting in a standard error of 0.05. When compared to the best fit results for $\dot{N} = 0$ and $N_0 = 1 \times 10^{-3} \text{ nm}^{-2}$, a linear increase in nucleation density provides a good estimation of the surface fraction for TiN ALD, resulting in a ~44% reduction of the

standard error. Furthermore, using the modified Island Growth Model, with $\dot{N} = 3 \times 10^{-6} \text{ nm}^{-2} \text{ cy}^{-1}$ resulted in a ~38% decrease in the standard error over the unmodified model.

Figures 5.13 and 5.14 show the model fits for TiO_2 and HfO_2 , respectively, assuming both zero and non-zero \dot{N} . Using $N_0 = 1 \times 10^{-4} \text{ nm}^{-2}$ and $\dot{N} = 2.5 \times 10^{-4} \text{ nm}^{-2} \text{ cy}^{-1}$ (for TiO_2) and $\dot{N} = 4 \times 10^{-4} \text{ nm}^{-2} \text{ cy}^{-1}$ (for HfO_2) resulted in standard errors of 0.07 and 0.14, respectively. Interestingly, assuming $\dot{N} = 0$ and $N_0 = 1.8 \times 10^{-2} \text{ nm}^{-2}$ (for TiO_2) and $2.5 \times 10^{-2} \text{ nm}^{-2}$ (for HfO_2) reduced the standard error to 0.03 and 0.07, respectively. As established previously, $N_0 = 1 \times 10^{-4} \text{ nm}^{-2}$ is likely a good estimate of the initial nucleation density prior to ALD cycling on plasma-treated aC. Increasing the initial nucleation density two order-of-magnitude from this estimate resulted in the best model fits likely due rapid generation of nucleation sites in the early stages of ALD cycling. Thus, the N_0 parameter could feasibly start out at $\sim 1 \times 10^{-4} \text{ nm}^{-2}$, increasing to $\sim 1 \times 10^{-2} \text{ nm}^{-2}$ within the first 20 or 30 cycles. Since this rapid increase was not observed for TiN nucleation, the likely cause is due to using H_2O as a co-reagent for metal oxide ALD and NH_3 for TiN ALD. Thus, the less polar NH_3 instead leads to a more gradual increase in nucleation density and better selectivity on plasma-treated aC substrates. Improvements in the selectivity for TiO_2 and HfO_2 ALD would also be expected if a less polar co-reagent was utilized, for example using titanium isopropoxide as the oxygen source in TiO_2 ALD.^{27,31}

Figure 5.15 shows a comparison of the best fits for the a) Avrami-modified Island Growth Model and b) Island Growth Model. The resulting fit for the Island Growth Model, using the initial nucleation density found from the best fit Avrami modified model $N_0 = 2.5 \times 10^{-2} \text{ nm}^{-2}$ (corresponding to a $b = 6.32 \text{ nm}$), is shown in Figure 5.15 a). The Island Growth Model predicts layer closure after $n_c = 53$ cycles. The resulting fit for the Avrami modified model, using the initial nucleation density found from the best fit Island Growth Model $N_0 = 5.8 \times 10^{-3} \text{ nm}^{-2}$

(corresponding to a $b = 13.1$ nm and $n_c = 120$ cycles), is shown in Figure 5.15 b). In this case, the Avrami modified model drastically underestimates the surface fraction data. Herein lies the difference in the Avrami Equation, which assumes a random nucleation density versus periodic spacing. Compared with periodically spaced nuclei, a random distribution would lead to delay in the overall island coalescence (which was defined when $n = n_c$). In a random distribution, the nuclei will coalesce with nearby neighbors, which can vary on a substrate scale before total film coalescence is reached.

The modified Island Growth Model can likely also predict the island size distribution versus the number of cycles but was not calculated for this work. Qualitatively, the island size is expected to be dependent on the point at which a given island nucleated on the substrate. For nucleation generation equal to zero, all islands can be assumed to nucleate in the first cycle. Due to the random distribution, nearby neighbors are expected to coalesce and form larger island groups. This is readily observed for TiO_2 and HfO_2 , with tighter island size distributions mostly centered around the expected particle radius. Conversely, nucleation site generation would lead to a larger distribution in island size, which was observed for TiN ALD. This portion of the model requires further study before quantitative evaluations can be made for this system.

5.5 Conclusions

We demonstrated that the Island Growth Model, which assumes periodic spacing of islands and no additional generation of nucleation sites, does not accurately describe ALD nucleation on plasma-treated aC. In order to utilize this model, the lattice parameter needs to vary as a function of cycle number. With a variation in the lattice parameter, the periodicity of nucleation sites also is disrupted and the equations for calculating the surface fraction would also need to be altered.

Therefore, we propose a modification to the model in to more accurately describe the experimental data.

The Island Growth Model was modified by using the assumptions from the Avrami Equation. The key assumptions applied were (1) a random distribution of nucleation sites, and (2) a term to compensate for generation of additional sites. Modification of the Island Growth Model allowed for the most accurate fitting of experimental data for TiO₂, HfO₂, and TiN nucleation on plasma-treated aC, reducing the standard error 50%, 30%, and 38%, respectively. TiN data were best fit using an initial nucleation site density of $1 \times 10^{-4} \text{ nm}^{-2}$ increasing at a rate of $3 \times 10^{-6} \text{ nm}^{-2} \text{ cy}^{-1}$. TiO₂ and HfO₂ data were best fit assuming an initial nucleation site density of $\sim 2 \times 10^{-2} \text{ nm}^{-2}$, which implied the effects of H₂O absorption on aC as a key loss in selectivity.

This work shows that the Avrami Equation can be used to modify the Island Growth Model to accurately describe the nucleation of ALD on plasma-treated aC. In general, for ALD processes that are very selective, where nucleation site density is initially low and the generation is slow, a linear approximation of the nucleation site generation is likely sufficient. This modified model can be applied to other material systems and substrates with such complexity as precursor dependent generation rates of nucleation sites. The modifications presented here allow for a straightforward and accurate method to model ALD nucleation phenomena and should be further investigated further for various types of chemistries and substrates.

5.6 Acknowledgements

The authors thank Christa Vrancken (imec, Belgium) and SEM operators at IMEC for assistance in gathering SEM images. The authors thank Elie Schapmans (imec, Belgium) for assistance in operation and troubleshooting the Polygon 8300 tool.

5.7 Figures for Chapter 5

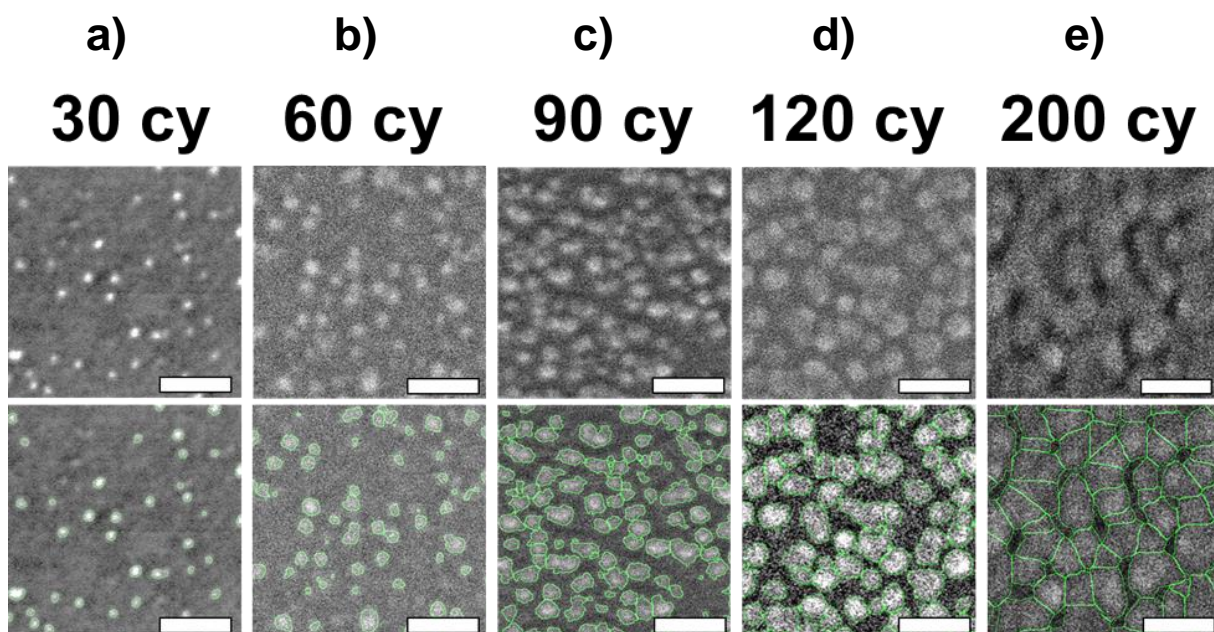


Figure 5.1: Top down SEM images of TiO_2 particles on plasma-treated aC substrates subjected to a) 30, b) 60, c) 90, d) 120, and e) 200 cycles of $\text{Ti}(\text{OCH}_3)_4 + \text{H}_2\text{O}$ at $250\text{ }^\circ\text{C}$. Included under each SEM image are overlaid particle outlines (shown in green) generated from particle analysis in ImageJ. All scale bars are 50 nm.

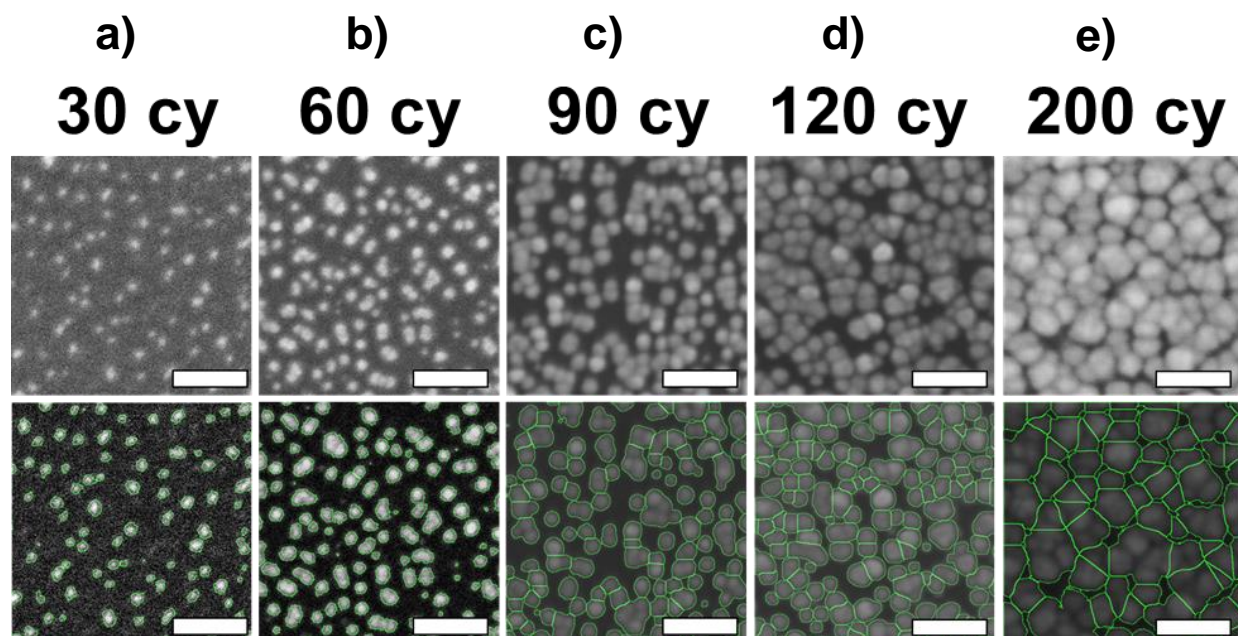


Figure 5.2: Top down SEM images of HfO₂ particles on plasma-treated aC substrates subjected to a) 30, b) 60, c) 90, d) 120, and e) 200 cycles of HfCl₄ + H₂O at 300 °C. Included under each SEM image are overlaid particle outlines (shown in green) generated from particle analysis in ImageJ. All scale bars are 50 nm.

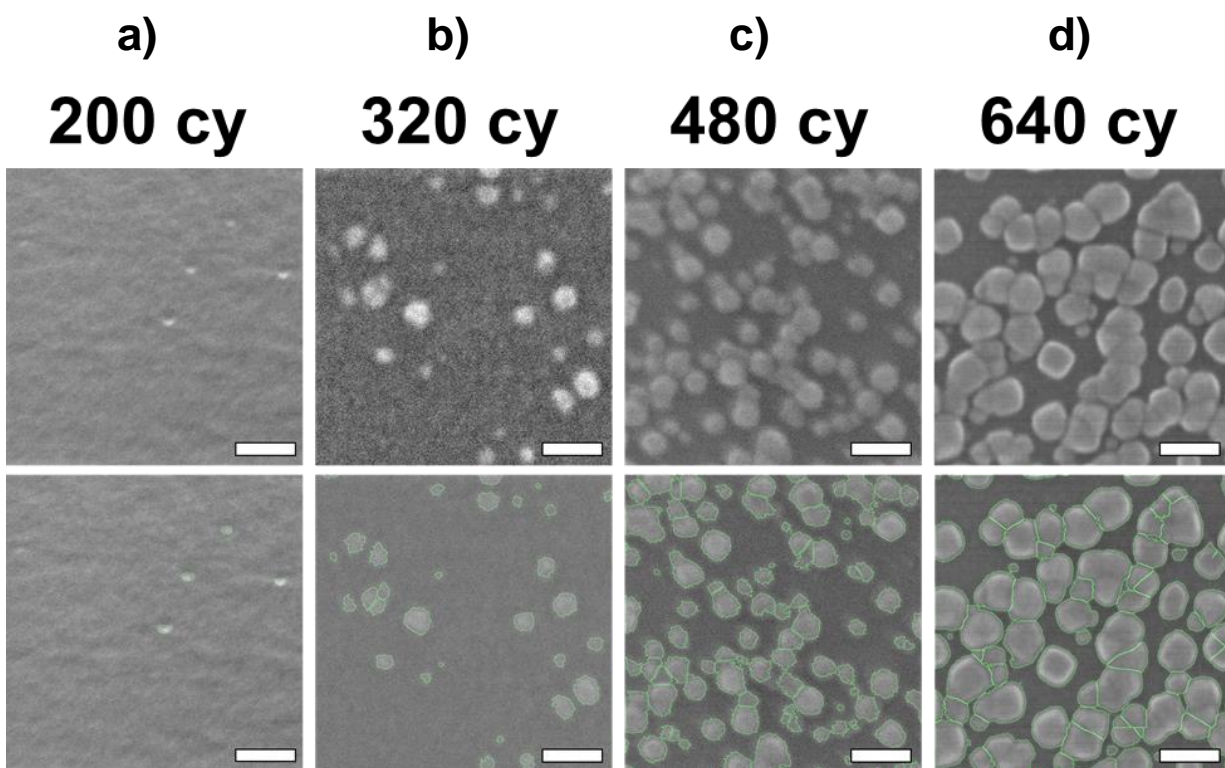


Figure 5.3: Top down SEM images of TiN particles on plasma-treated aC substrates subjected to a) 200, b) 320, c) 480, and d) 640 cycles of $\text{TiCl}_4 + \text{NH}_3$ at 390 °C. Included under each SEM image are overlaid particle outlines (shown in green) generated from particle analysis in ImageJ. All scale bars are 50 nm.

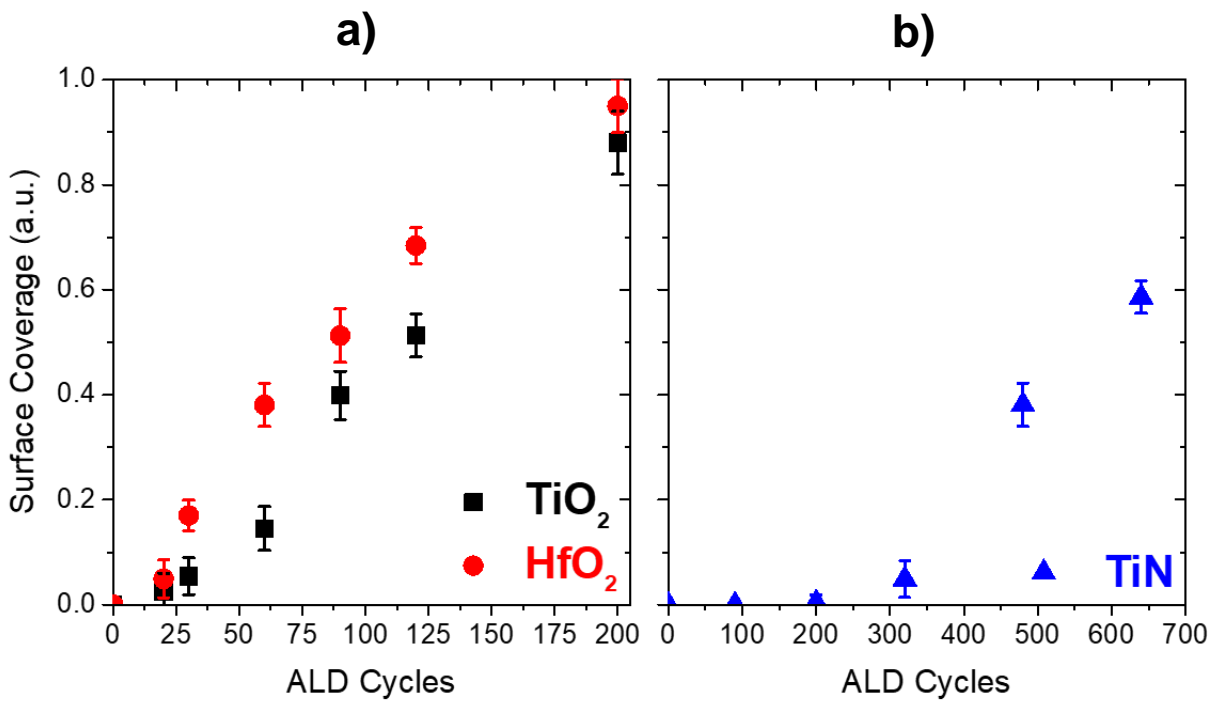


Figure 5.4: Areal surface coverage of identified a) TiO₂ and HfO₂, and b) TiN particles from top-down SEM images in Figures 5.1 (TiO₂), 5.2 (HfO₂), and 5.3 (TiN).

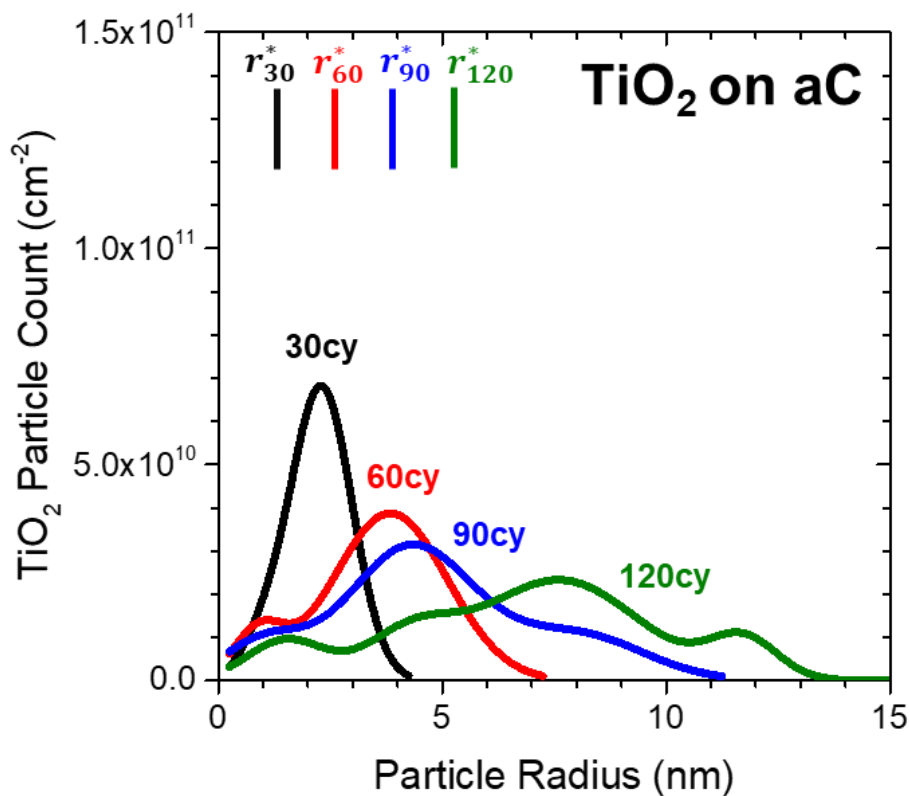


Figure 5.5: TiO₂ particle size distributions, calculated using ImageJ, given as particle count versus radius on plasma-treated aC substrates for 30 (black), 60 (red), 90 (blue), and 120 (green) cycles of Ti(OCH₃)₄ + H₂O at 250 °C. Total particle counts were normalized over an area of 1 cm². The theoretical particle radius (r_n^*), indicated using a vertical line at the expected radius, was estimated assuming a growth per cycle of 0.043 nm/cy (from spectroscopic ellipsometry measurements).

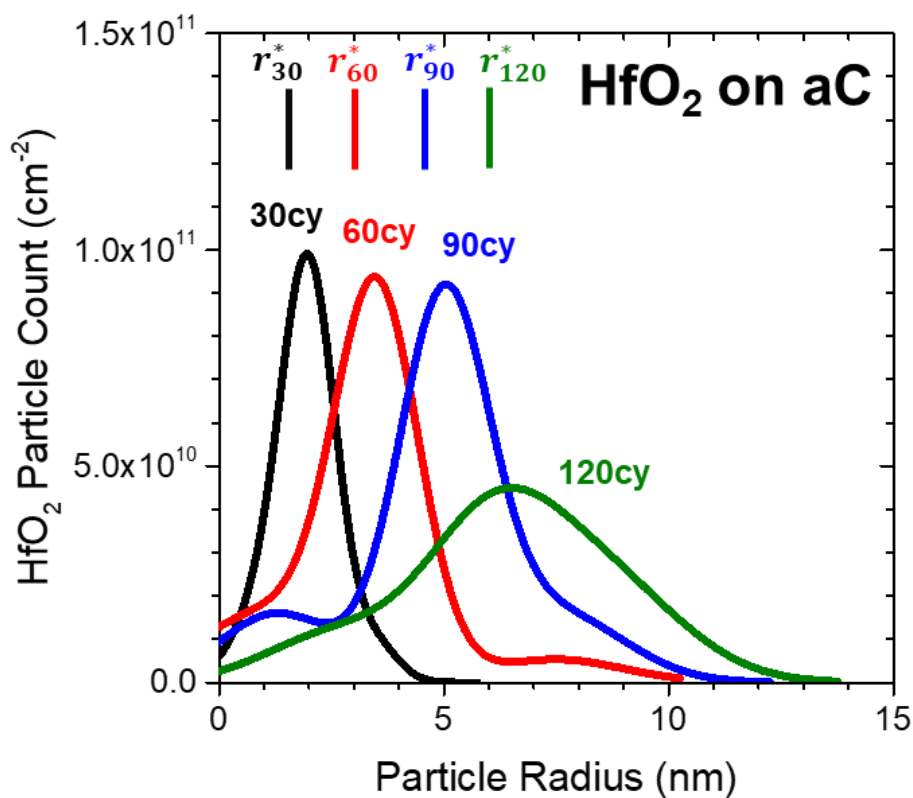


Figure 5.6: HfO₂ particle size distributions, calculated using ImageJ, given as particle count versus radius on plasma-treated aC substrates for 30 (black), 60 (red), 90 (blue), and 120 (green) cycles of HfCl₄ + H₂O at 300 °C. Total particle counts were normalized over an area of 1 cm². The theoretical particle radius (r_n^*), indicated using a vertical line at the expected radius, was estimated assuming a growth per cycle of 0.05 nm/cy (from spectroscopic ellipsometry measurements).

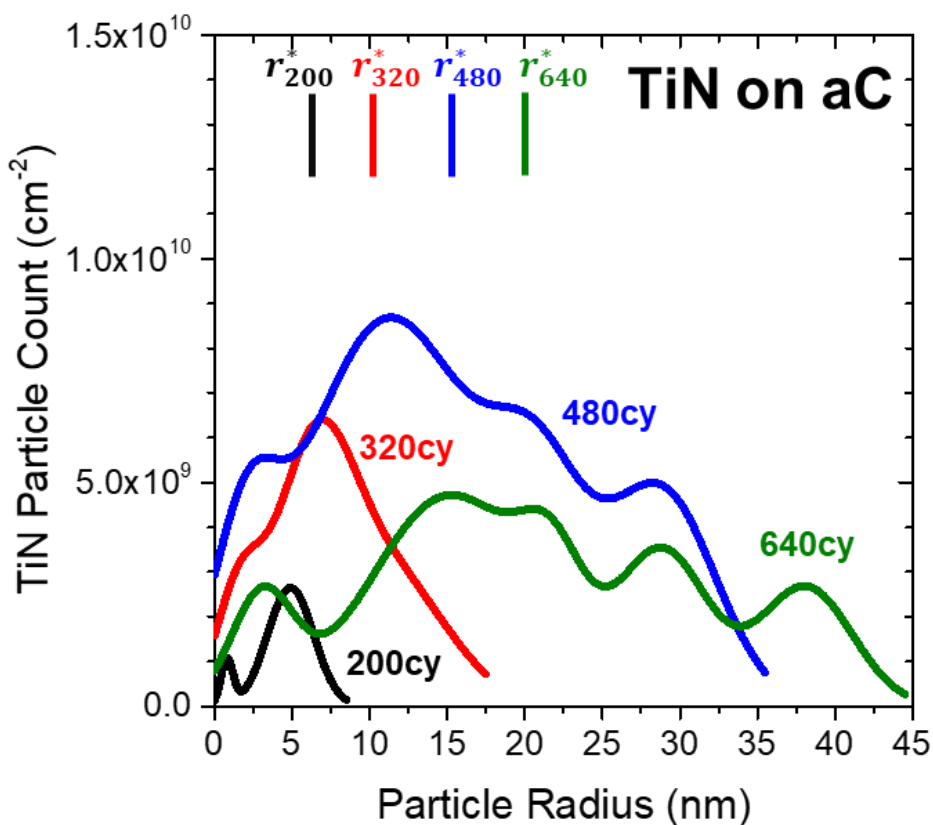


Figure 5.7: TiN particle size distributions, calculated using ImageJ, given as particle count versus radius on plasma-treated aC substrates for 200 (black), 320 (red), 480 (blue), and 640 (green) cycles of $\text{TiCl}_4 + \text{NH}_3$ at 390 °C. Total particle counts were normalized over an area of 1 cm². The theoretical particle radius (r_n^*), indicated using a vertical line at the expected radius, was estimated assuming a growth per cycle of 0.031 nm/cy (from spectroscopic ellipsometry measurements).

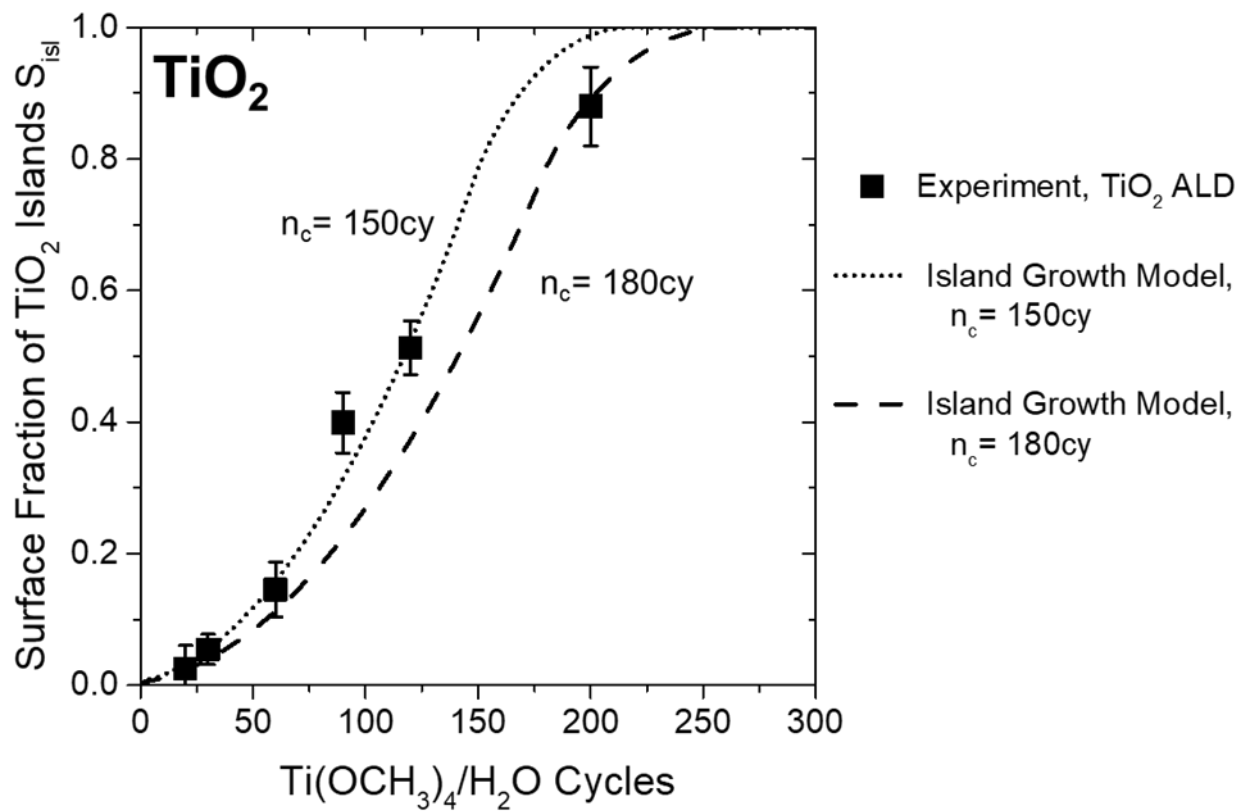


Figure 5.8: TiO₂ island surface fraction as a function of ALD cycling on plasma-treated aC. Black squares are areal coverage of TiO₂ islands calculated from SEM images in Figure 5.1, while the dotted and dashed lines correspond to the resulting fit using the Island Growth Model with layer closure parameter, n_c , equal to 150 and 180 cycles, respectively.

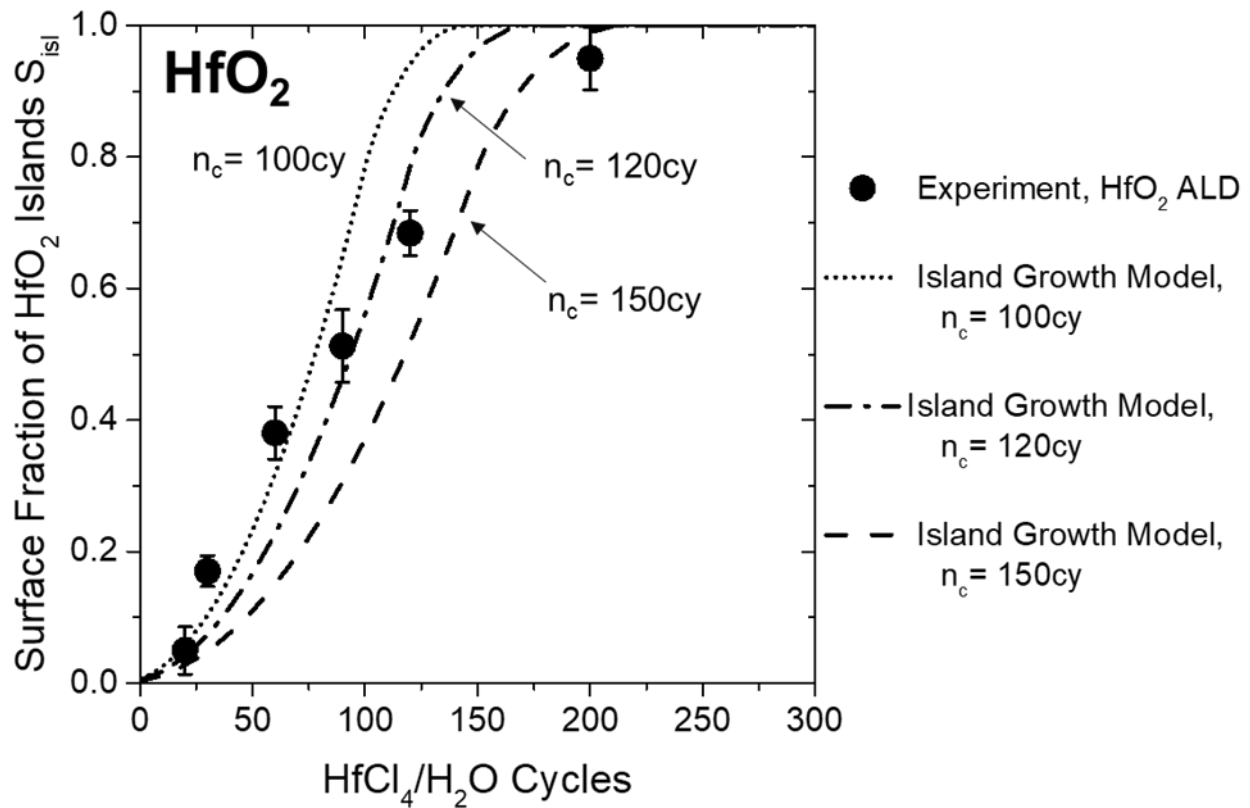


Figure 5.9: HfO₂ island surface fraction as a function of ALD cycling on plasma-treated aC. Black circles are data points from areal coverage of HfO₂ islands calculated from SEM images in Figure 5.2, while the dotted, dot-dashed, and dashed lines correspond to the resulting fit using the Island Growth Model with layer closure parameter, n_c , equal to 100, 120, and 150 cycles, respectively.

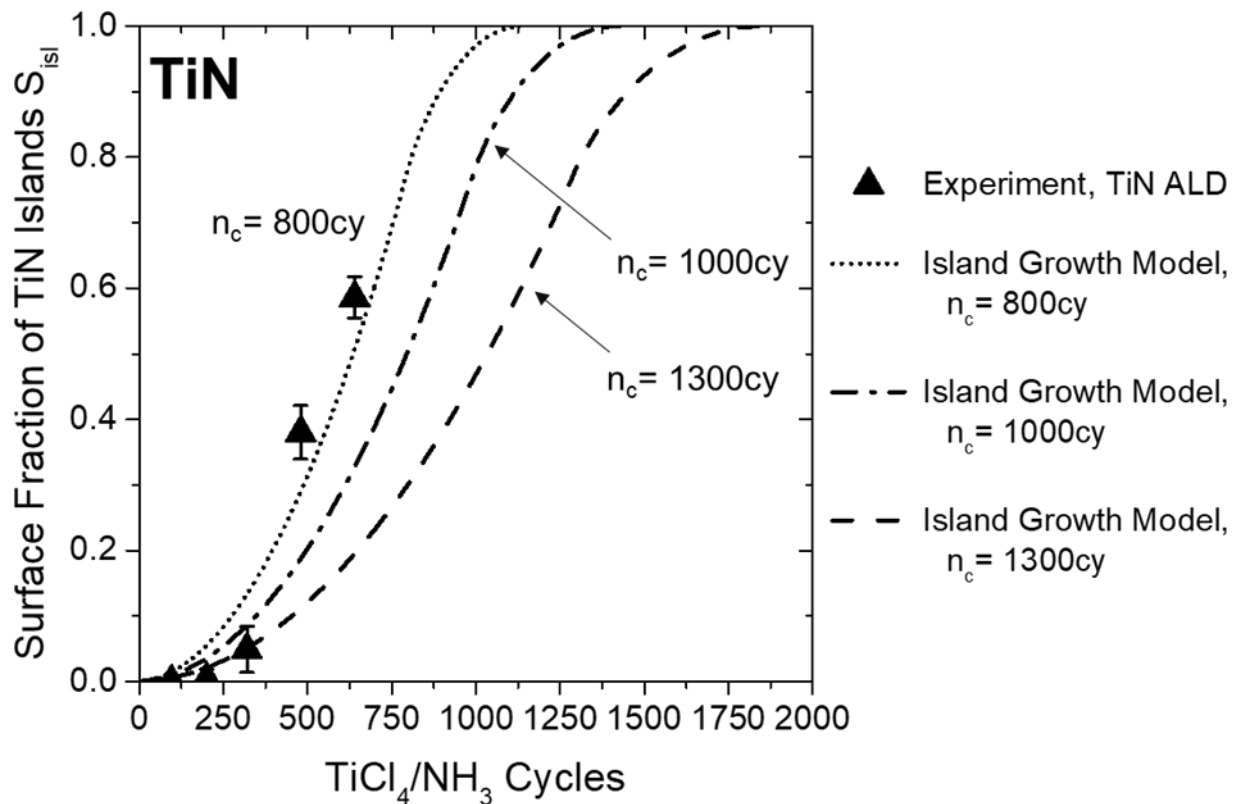


Figure 5.10: TiN island surface fraction as a function of ALD cycling on plasma-treated aC. Black triangles are data points from areal coverage of TiN islands calculated from SEM images in Figure 5.3, while the dotted, dot-dashed, and dashed lines correspond to the resulting fit using the Island Growth Model with layer closure parameter, n_c , equal to 800, 1000, and 1300 cycles, respectively.

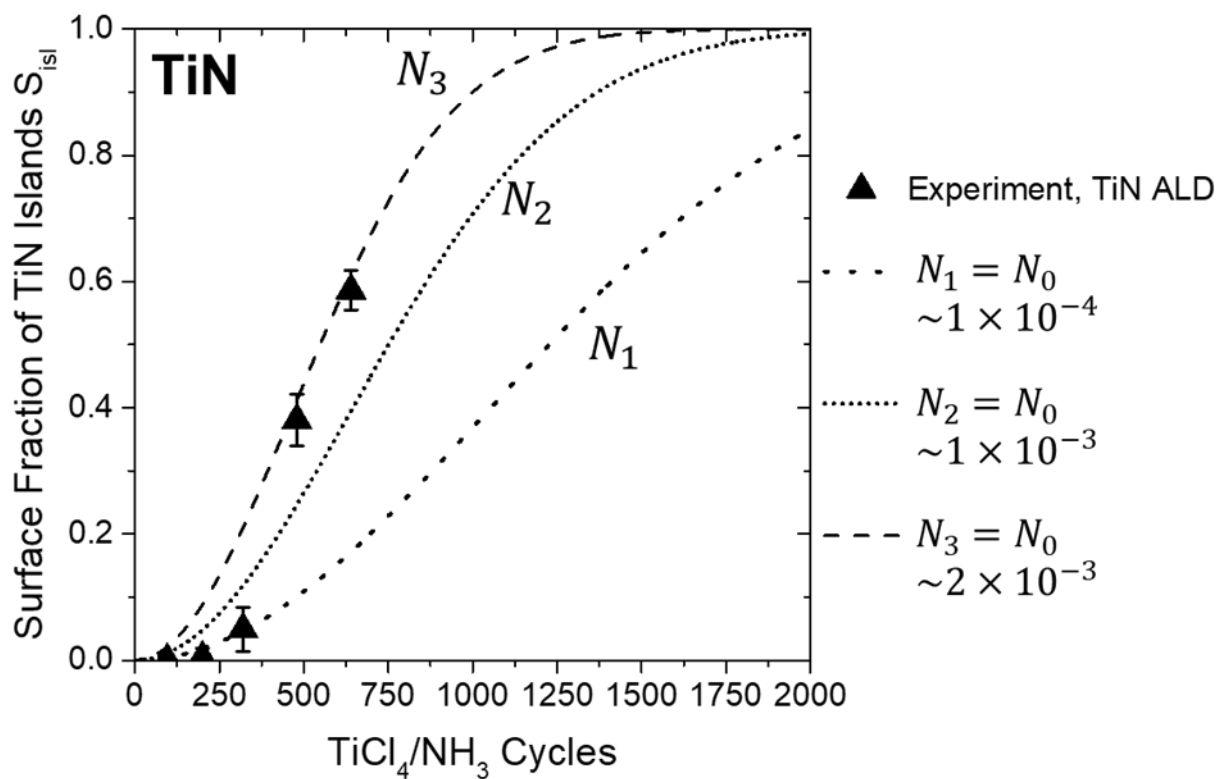


Figure 5.11: TiN island surface fraction as a function of ALD cycling on plasma-treated aC. Black triangles indicate data points from experiment, while the short-dashed, dotted, and dashed lines correspond to the resulting fit using the Avrami Equation assuming constant initial nucleation density, N_0 , equal to 1×10^{-4} , 1×10^{-3} , and $2 \times 10^{-3} \text{ nm}^{-2}$, respectively. For the model fits shown, the rate of nucleation generation parameter, \dot{N} , was set to zero.

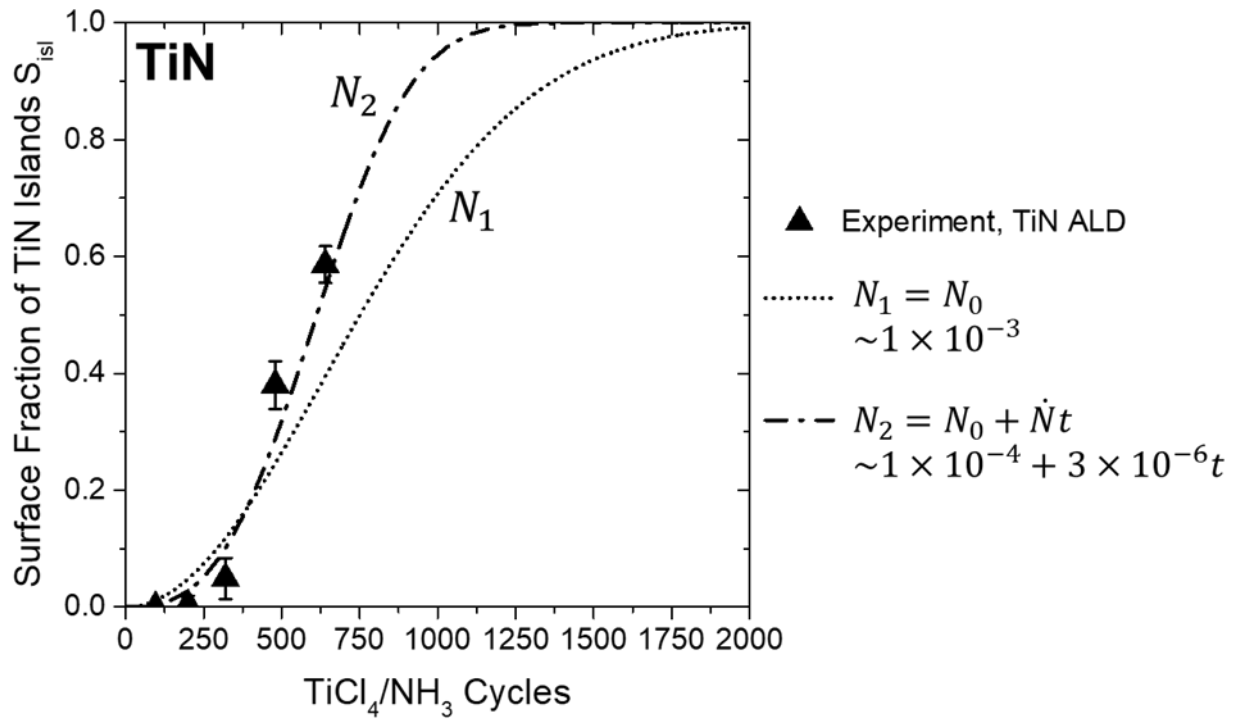


Figure 5.12: TiN island surface fraction as a function of ALD cycling on plasma-treated aC. Black triangles indicate data points from experiment, while the dotted and dashed lines correspond to the resulting fit using the Avrami Equation with nucleation functions given by N_1 and N_2 , respectively.

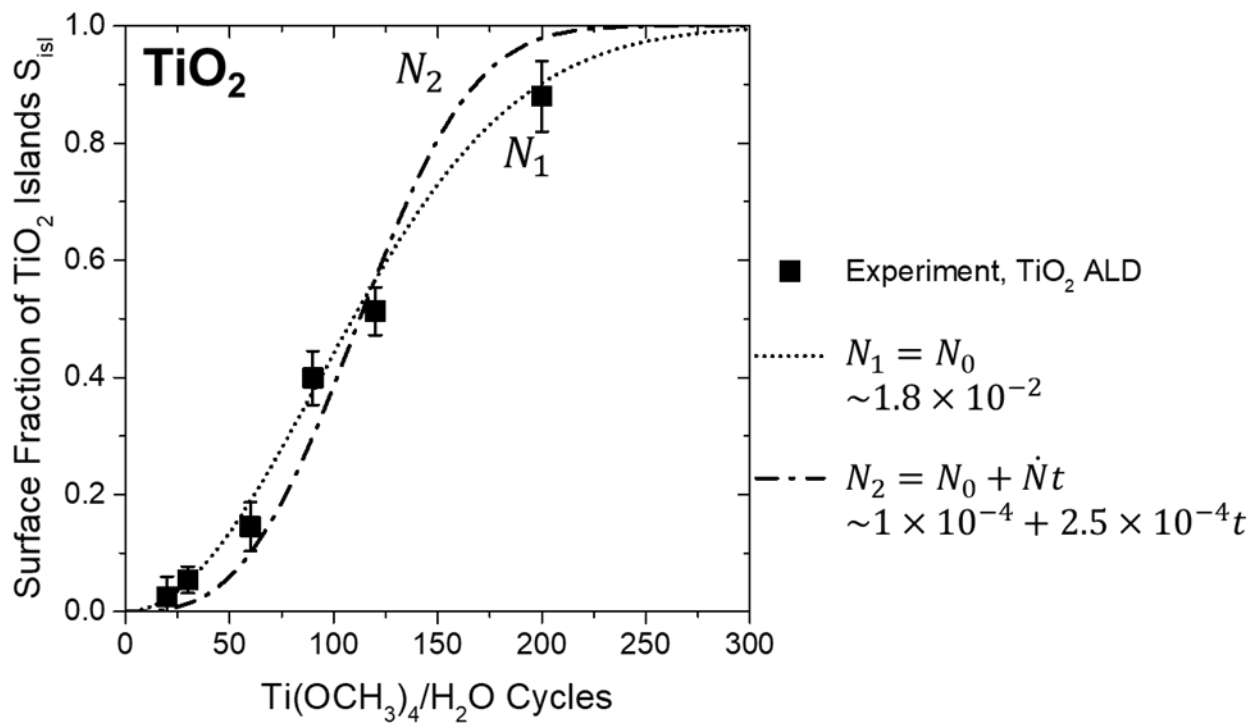


Figure 5.13: TiO_2 island surface fraction as a function of ALD cycling on plasma-treated aC. Black squares indicate data points from experiment, while the dotted and dot-dashed lines correspond to the resulting fit using the Avrami Equation with nucleation functions given by N_1 and N_2 , respectively.

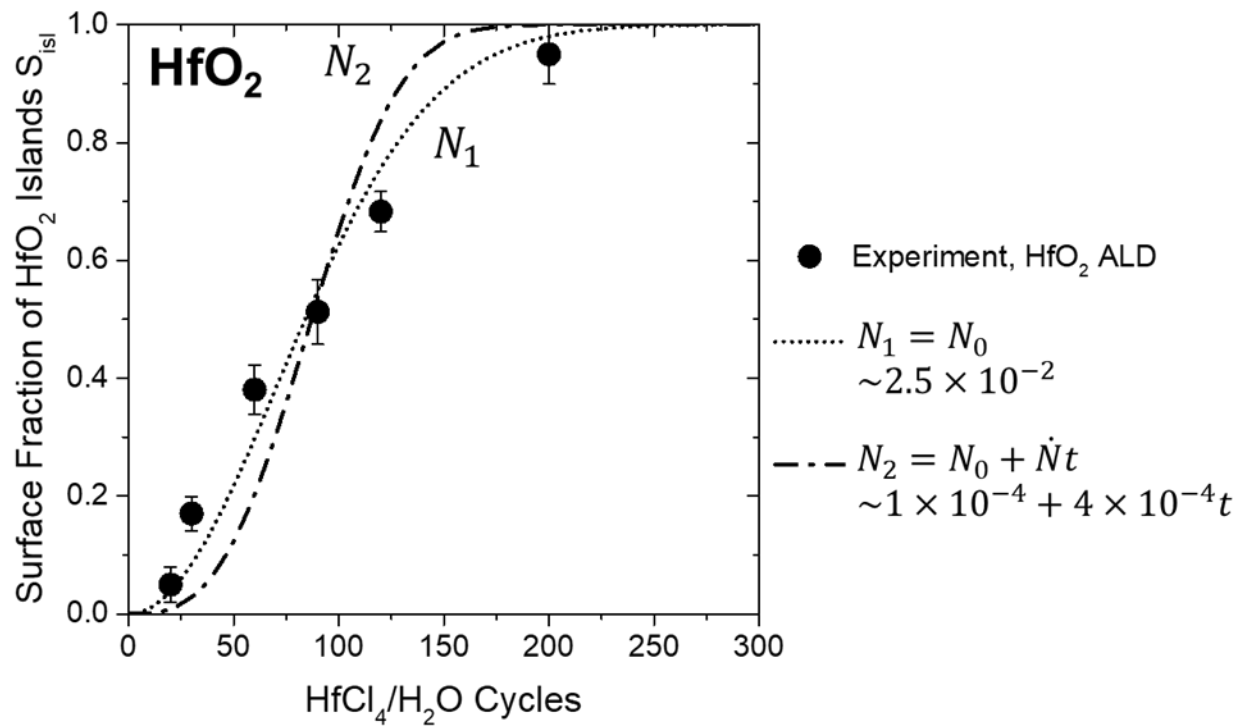


Figure 5.14: HfO₂ island surface fraction as a function of ALD cycling on plasma-treated aC. Black circles indicate data points from experiment, while the dotted and dashed lines correspond to the resulting fit using the Avrami Equation with nucleation functions given by N_1 and N_2 , respectively.

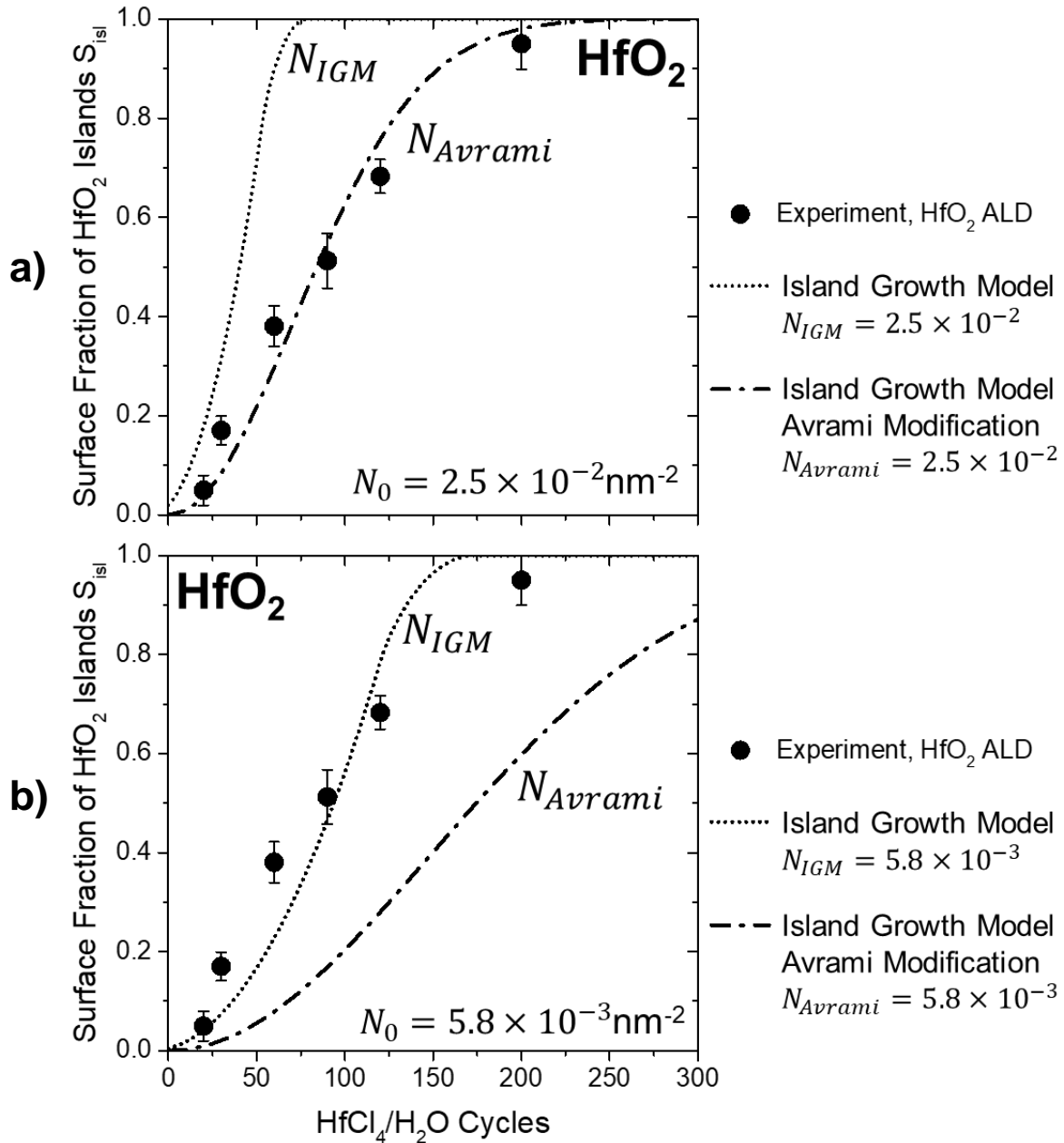


Figure 5.15: a) HfO₂ surface fraction data (black circles) with best fit using the Avrami modification (dot-dashed line) with $N_0 = 2.5 \times 10^{-2} \text{ nm}^{-2}$. Also shown is the fit calculated from the Island Growth Model (dotted line) using $N_0 = 2.5 \times 10^{-2} \text{ nm}^{-2}$. b) HfO₂ surface fraction data (black circles) with best fit using Island Growth Model (dotted line) with $N_0 = 5.8 \times 10^{-3} \text{ nm}^{-2}$. Also shown is the fit calculated from the Avrami modification using $N_0 = 5.8 \times 10^{-3} \text{ nm}^{-2}$.

5.8 Tables for Chapter 5

Table 5.1 Island Growth Model Parameters for TiO₂, HfO₂, and TiN ALD

Material	Δr (nm/cy)	r_o (nm)	n_c (cy)	b (nm)	b^{-2} (nm⁻²)	Standard Error
TiO ₂	0.043	0.5	150	13.9	5.2×10^{-3}	0.06
			180	16.5	3.7×10^{-3}	0.09
HfO ₂	0.050	0.5	100	11.1	8.1×10^{-3}	0.14
			120	13.1	5.8×10^{-3}	0.10
			150	16.2	3.8×10^{-3}	0.51
TiN	0.031	0.5	800	44.4	5.1×10^{-4}	0.08
			1000	63	2.5×10^{-4}	0.16
			1300	81.6	1.5×10^{-4}	0.11

Table 5.2 Modified Island Growth Model Best Fit Parameters for TiO₂, HfO₂, and TiN ALD

Material	Δr (nm/cy)	N_0 (nm ⁻²)	\dot{N} (nm ⁻² cy ⁻¹)	Standard Error
TiO ₂	0.043	1.8×10^{-2} 1×10^{-4}	0 2.5×10^{-4}	0.03 0.07
HfO ₂	0.050	2.5×10^{-2} 1×10^{-4}	0 4×10^{-4}	0.07 0.14
TiN	0.031	1×10^{-4} 1×10^{-3} 2×10^{-3} 1×10^{-4}	0 0 0 3×10^{-6}	0.28 0.09 0.10 0.05

5.9 References

- (1) Zeitzoff, P. M.; Huff, H. R. MOSFET Scaling Trends, Challenges, and Key Associated Metrology Issues through the End of the Roadmap. *AIP Conf. Proc.* **2005**, 788 (203), 203–213.
- (2) Kim, H. Atomic Layer Deposition of Metal and Nitride Thin Films: Current Research Efforts and Applications for Semiconductor Device Processing. *J. Vac. Sci. Technol. B Microelectron. Nanom. Struct.* **2003**, 21 (6), 2231.
- (3) Mistry, K.; Allen, C.; Auth, C.; Beattie, B.; Bergstrom, D.; Bost, M.; Brazier, M.; Buehler, M.; Cappellani, A.; Chau, R.; Choi, C.; Ding, G.; Fischer, K.; Ghani, T.; Grover, R.; Han, W.; Hanken, D.; Hattendorf, M.; He, J.; Hicks, J.; Huessner, R.; Ingerly, D.; Jain, P.; James, R.; Jong, L.; Joshi, S.; Kenyon, C.; Kuhn, K.; Lee, K.; Liu, H.; Maiz, J.; McIntyre, B.; Moon, P.; Neiryneck, J.; Pae, S.; Parker, C.; Parsons, D.; Prasad, C.; Pipes, L.; Prince, M.; Ranade, P.; Reynolds, T.; Sandford, J.; Shifren, L.; Sebastian, J.; Seiple, J.; Simon, D.; Sivakumar, S.; Smith, P.; Thomas, C.; Troeger, T.; Vandervoorn, P.; Williams, S.; Zawadzki, K. A 45nm Logic Technology with High-k+Metal Gate Transistors, Strained Silicon, 9 Cu Interconnect Layers, 193nm Dry Patterning, and 100% Pb-Free Packaging. In *IEEE International Electron Devices Meeting*; 2007; pp 247–250.
- (4) Sneh, O.; Clark-Phelps, R. B.; Londergan, A. R.; Winkler, J.; Seidel, T. E. Thin Film Atomic Layer Deposition Equipment for Semiconductor Processing. *Thin Solid Films* **2002**, 402, 248–261.
- (5) Mackus, A. J. M.; Bol, A. A.; Kessels, W. M. M. The Use of Atomic Layer Deposition in Advanced Nanopatterning. *Nanoscale* **2014**, 6 (19), 10941–10960.
- (6) Chopra, S. N.; Zhang, Z.; Kaihlanen, C.; Ekerdt, J. G. Selective Growth of Titanium Nitride on HfO₂ across Nanolines and Nanopillars.
- (7) Leskelä, M.; Ritala, M. Atomic Layer Deposition (ALD): From Precursors to Thin Film Structures. *Thin Solid Films* **2002**, 409 (1), 138–146.
- (8) Leskelä, M.; Ritala, M. Atomic Layer Deposition Chemistry: Recent Developments and Future Challenges. *Angew. Chemie Int. Ed.* **2003**, 42 (45), 5548–5554.
- (9) Anderson, V. R.; Cavanagh, A. S.; Abdulagatov, A. I.; Gibbs, Z. M.; George, S. M. Waterless TiO₂ Atomic Layer Deposition Using Titanium Tetrachloride and Titanium Tetraisopropoxide. *J. Vac. Sci. Technol. A Vacuum, Surfaces, Film.* **2014**, 32 (1), 01A114.
- (10) Kerrigan, M. M.; Klesko, J. P.; Winter, C. H. Low Temperature, Selective Atomic Layer Deposition of Cobalt Metal Films Using Bis(1,4-Di-*Tert*-Butyl-1,3-Diazadienyl)cobalt and Alkylamine Precursors. *Chem. Mater.* **2017**, 29 (17), 7458–7466.
- (11) Puurunen, R. L.; Vandervorst, W. Island Growth as a Growth Mode in Atomic Layer Deposition: A Phenomenological Model. *J. Appl. Phys.* **2004**, 96 (12), 7686–7695.

- (12) Puurunen, R.; Vandervorst, W.; Bender, H.; Conard, T.; Zhao, C.; Delabie, A.; Caymax, M.; De Gendt, S.; HeynsMinna, M.; de Ridder, M.; BrongersmaYde, H.; Dao, T.; de Win, T.; Verheijen, M.; KaiserMarko Tuominen, M. Island Growth in the Atomic Layer Deposition of Zirconium Oxide and Aluminum Oxide on Hydrogen-Terminated Silicon: Growth Mode Modeling and Transmission Electron Microscopy. *J. Appl. Phys.* **2004**, *96*, 4878.
- (13) Nilsen, O.; Mohn, C. E.; Kjekshus, A.; Fjellvåg, H. Analytical Model for Island Growth in Atomic Layer Deposition Using Geometrical Principles. *J. Appl. Phys.* **2007**, *102* (2), 24906.
- (14) Kim, K.; Lee, H.-B.-R.; Johnson, R. W.; Tanskanen, J. T.; Liu, N.; Kim, M.-G.; Pang, C.; Ahn, C.; Bent, S. F.; Bao, Z. Selective Metal Deposition at Graphene Line Defects by Atomic Layer Deposition. *Nat. Commun.* **2014**, *5*.
- (15) Hagen, D. J.; Connolly, J.; Povey, I. M.; Rushworth, S.; Pemble, M. E. Island Coalescence during Film Growth: An Underestimated Limitation of Cu ALD. *Adv. Mater. Interfaces* **2017**, *4* (18), 1700274.
- (16) Yim, S.-S.; Lee, D.-J.; Kim, K.-S.; Kim, S.-H.; Yoon, T.-S.; Kim, K.-B. Nucleation Kinetics of Ru on Silicon Oxide and Silicon Nitride Surfaces Deposited by Atomic Layer Deposition. *J. Appl. Phys.* **2008**, *103* (97), 113509–121301.
- (17) Avrami, M. Kinetics of Phase Change. I General Theory. *J. Chem. Phys.* **1939**, *7* (12), 1103–1112.
- (18) Avrami, M. Kinetics of Phase Change. II Transformation-Time Relations for Random Distribution of Nuclei. *J. Chem. Phys.* **1940**, *8* (2), 212–224.
- (19) Avrami, M. Granulation, Phase Change, and Microstructure Kinetics of Phase Change. III. *J. Chem. Phys.* **1941**, *91* (101), 198–258.
- (20) Yang, J.; McCoy, B. J.; Madras, G. Distribution Kinetics of Polymer Crystallization and the Avrami Equation. *J. Chem. Phys.* **2005**, *122* (6), 64901.
- (21) Fanfoni, M.; Tomellini, M. Avrami's Kinetic Approach for Describing Volmer Weber Growth Mode at Solid Surfaces Studied via PES and AES. *J. Electron Spectros. Relat. Phenomena* **1995**, *76*, 283–288.
- (22) Fairbairn, K.; Rice, M.; Weidman, T.; NgaiIan, C. S.; Scot Latchford, I.; Bencher, C. D.; Wang, Y. M. Method for Depositing an Amorphous Carbon Layer. 6,573,030 B1, 2003.
- (23) Tai, H.; Liao, Y. M.; Liu, W. T.; Peng, W. C.; Ying, T. H. Novel Clean Concept of Advanced Patterning Film (Amorphous Carbon) for Beyond 2xnm Generation Self-Aligned Double-Patterning (SADP) Process. *ECS Trans.* **2014**, *61* (3), 67–71.
- (24) Ponraj, J. S.; Attolini, G.; Bosi, M. Review on Atomic Layer Deposition and Applications of Oxide Thin Films. *Crit. Rev. Solid State Mater. Sci.* **2013**, *383736886* (38).

- (25) George, S. M. Atomic Layer Deposition: An Overview. *Chem. Rev.* **2010**, *110* (1), 111–131.
- (26) Lemaire, P. C.; King, M.; Parsons, G. N. Understanding Inherent Substrate Selectivity during Atomic Layer Deposition: Effect of Surface Preparation, Hydroxyl Density, and Metal Oxide Composition on Nucleation Mechanisms during Tungsten ALD. *J. Chem. Phys.* **2017**, *146* (5), 52811.
- (27) Atanasov, S. E.; Kalanyan, B.; Parsons, G. N. Inherent Substrate-Dependent Growth Initiation and Selective-Area Atomic Layer Deposition of TiO₂ Using “water-Free” Metal-Halide/metal Alkoxide Reactants. *J. Vac. Sci. Technol. A Vacuum, Surfaces, Film.* **2016**, *34* (1), 01A148.
- (28) Zhang, W.; Engstrom, J. R. Effect of Substrate Composition on Atomic Layer Deposition Using Self-Assembled Monolayers as Blocking Layers. *J. Vac. Sci. Technol. A* **2016**, *34* (1), 01A107.
- (29) Xu, Y.; Musgrave, C. B. A DFT Study of the Al₂O₃ Atomic Layer Deposition on SAMs : Effect of SAM Termination. *Chem. Mater.* **2004**, *16*, 646–653.
- (30) Vervuurt, R. J.; Karasulu, B.; Verheijen, M. A.; M Kessels, W. M.; Bol, A. A. Uniform Atomic Layer Deposition of Al₂O₃ on Graphene by Reversible Hydrogen Plasma Functionalization.
- (31) Anderson, V. R.; Cavanagh, A. S.; Abdulagatov, A. I.; Gibbs, Z. M.; George, S. M. Waterless TiO₂ Atomic Layer Deposition Using Titanium Tetrachloride and Titanium Tetraisopropoxide Waterless TiO₂ Atomic Layer Deposition Using Titanium Tetrachloride and Titanium Tetraisopropoxide. *J. Vac. Sci. Technol. A J. Vac. Sci. Technol. A* **2014**, *32* (22), 1–114.

**CHAPTER 6: AREA-SELECTIVE ATOMIC LAYER
DEPOSITION OF TiN AND TiO₂ IN SUB-50 NM aC/Si₃N₄
PATTERNS FOR ADVANCED PATTERNING
APPLICATIONS**

CHAPTER 6. Area-Selective Atomic Layer Deposition of TiN and TiO₂ in Sub-50 nm aC/Si₃N₄ Patterns for Advanced Patterning Applications

Eric Stevens,^{†,‡,§} Yoann Tomczak,[†] BT Chan,[†] Efrain Altamirano Sanchez,[†] Gregory Parsons,[‡]
Annelies Delabie^{*,†,§}

[†] Imec, Kapeldreef 75, B-3001 Leuven, Belgium

[‡] Department of Chemical and Biomolecular Engineering, North Carolina State University, 911
Partners Way, Raleigh NC 27695

[§] KU Leuven (University of Leuven), Celestijnenlaan 200F, B-3001, Leuven, Belgium

6.1 Abstract

Using a H₂ plasma pretreatment, we demonstrate the selective deactivation of aC lines sub-50 nanometer structures using 45 nm aC/Si₃N₄ line/space patterns. 3.5 nm TiO₂ and 5.8 nm TiN films were deposited on Si₃N₄ spaces with minimal particle formation on aC. We found that the selectivity loss was observed on the plasma-treated aC lines, where nucleation proceeded more readily of feature corners and edges than on blanket aC substrates. aC lines were selectively removed using oxygen plasma, leaving TiN patterns on top of Si₃N₄ with dimensions of 10-15 nm in height and 43 nm in width. We conclude that improved scaling of selectivity to nanometer scale patterns can be achieved by optimizing surface loading and extent of plasma exposure, and by further understanding shape effects in nanoscale surface plasma modification.

6.2 Introduction

The semiconductor industry is in a unique position; consumer demand for devices with better performance and more memory is continually increasing, yet the consumer still expects a lower price tag.¹ Such demands require innovations in equipment manufacturing,² deposition³⁻⁸ and etch processes,⁹⁻¹¹ and advanced patterning development.¹²⁻¹⁶ The requirement of these innovations is to typically decrease feature size, increasing the density of key components on a

single wafer, thus keeping costs low.^{17,18} In decreasing the feature size, the challenges for typical lithographic techniques become apparent, for example with increased line-edge-roughness and pattern misalignment.¹⁹

One potential strategy to address these challenges is using a tone reversal process.^{20–22} Tone reversal utilizes a sacrificial layer, such as a resist or amorphous carbon (aC), which is typically patterned using conventional lithography methods, followed by refilling the patterned regions with a desired material (e.g., TiN). By inserting (usually by deposition processing) a new material into the void space between the existing pattern, the original template material can be removed to reverse the image, or tone, created by the initial lithography step. Tone reversal has been adopted for many advanced patterning applications. One such examples is for self-aligned double patterning to extend the half-pitch resolution of patterns beyond the capabilities of traditional lithography tools.²³ Typically, these hard mask materials like TiN can be challenging to pattern using conventional methods, especially for critical dimensions of less than 50 nm. Typically, reactive ion etching is used to trim away the excess deposition on the lithography mask, leading to wasted material and potential substrate damage during dry etching. For the best device performance and scaling, the desired hard mask material would only be deposited in the void spaces between existing patterns. Such selective growth is likely only attainable by using chemisorption-based deposition processing, such as chemical vapor deposition (CVD) or atomic layer deposition (ALD), where the chemistry of the surface can dictate film growth.^{24–27}

Full realization of a single-step tone reversal will require new approaches to area-selective deposition of metal nitrides and oxides onto receptive surfaces without significant deposition onto sacrificial carbon. In our previous work, we demonstrate controlled chemical plasma modification of amorphous carbon to achieve area-selective atomic layer deposition (ALD) of TiN onto silicon

nitride (Chapter 3). We seek to apply this approach in sub-50 nm aC/Si₃N₄ line/space patterned structures on 300 mm Si wafers. We aim to investigate the selectivity attained in patterned substrates and how the results compare with blanket wafer processing. This work demonstrates the extension of an area-selective ALD process to industry-relevant applications on a demanding length scale, enabling tone reversal patterning of dielectric-on-dielectric and metal-on-dielectric material systems.

6.3 Experimental

6.3.1 Materials, Plasma, and ALD Processing

For blanket and patterned substrates, the amorphous carbon material (aC) used was Advanced Patterning Film (APF) described previously.^{28,29} High density aC films were deposited by plasma enhanced chemical vapor deposition (PE-CVD) using acetylene (C₂H₂) at 400°C on 300 mm Si (100) wafers in an Applied Materials Producer platform. In this same reactor, Si₃N₄ films were deposited by PE-CVD at 400°C using silane (SiH₄) and mixture of ammonia (NH₃) and nitrogen (N₂) plasma.

Atomic layer deposition of TiO₂ and TiN and H₂ plasma exposures were performed in an ASM Polygon 8300 cluster tool, allowing for plasma-treated substrates to be transferred without air breaks for ALD processing. TiO₂ was deposited in an ASM PULSAR cross-flow thermal ALD chamber using Ti(OCH₃)₄/Ar/H₂O/Ar (4s/8s/2s/4s) at 250°C. TiN ALD was performed in an ASM EMERALD PE-ALD chamber, the wafer chuck (bottom electrode) was heated to 390°C, while the walls and showerhead were kept at 160°C. TiN precursors, TiCl₄ and NH₃, were pulsed through the showerhead for 0.8s and 4s, respectively, separated by 1.5s Ar purges. The reagent dose and purge times for TiO₂ and TiN were selected such that linear growth with uniform thickness were observed across the entire 300 mm wafer.

In the ASM EMERALD PE-ALD chamber, a hydrogen plasma was generated at the showerhead top-electrode using a capacitively-coupled RF power source operated at 13.56 MHz. The wafer chuck was used as the counter electrode such that all plasma species were generated between the showerhead and substrate. The operating pressure was maintained at 2 Torr with an argon inert gas flow. The temperature of the bottom electrode, and thus the wafer, was set to 300°C, while the chamber walls and top electrode were maintained at 160°C. The plasma recipe began with a thermal equilibration time of 2 minutes under Ar flow. A 10 second, 10% H₂/Ar direct plasma exposure, with powers between 50 to 400W, was subjected to the wafer, followed by a 1 second Ar purge. This dosing sequence was repeated to give a total plasma exposure time of 20 seconds. Following the final exposure, the substrate was subjected to 60 seconds of 100% H₂ to passivate the surface of dangling bonds.

6.3.2 Sub-50 nm Pattern Formation

For lithographic patterning, a combination of available tools was used to form the following stack on 300 mm Si wafers: 50 nm of Si₃N₄/75 nm aC/15 nm SiO₂/67 nm BARC/105 nm photoresist. Si₃N₄ and aC films were deposited using the same processes and tool mentioned above. SiO₂ films were deposited at 75°C by plasma-enhanced ALD a proprietary Si-containing organic precursor and O₂ plasma on an EAGLE12 tool. Spin-coating of the ARC29SR BARC (Nissan Chemical Industries) and TARF-Pi6-144ME positive tone immersion material (TOK) was carried out using a SOKUDO DUO track. Subsequent lithographic exposures were done using an ASML TWINSCAN NXT:1950i 193 nm immersion scanner to print 90 nm pitch line/space patterns with a SIMEON maskset. Following lithography exposures aC/Si₃N₄ line/space patterns were created by etching away the photoresist, BARC, SiO₂, and aC layers in a LAM Kiyoo etch tool. Following plasma and ALD treatments, aC lines were removed using 60 seconds of O₂ plasma

at room temperature in a LAM Kiyo etch tool. Patterning steps are shown in Figure 6.1 in steps 1-4 (with the BARC and photoresist shown as a single layer).

6.3.3 Characterization

Patterned and blanket samples were imaged in top-down, 30° tilted, or cross-sectional mode using a scanning electron microscope (SEM, Hitachi SU8000) with a beam energy of 3 kV and a beam current of 10 pA. Samples were prepared for Transmission Electron Microscopy (TEM) imaging using a dual beam FIB/SEM Nova600i (FEI) and Ar Ion miller PIPS (Gatan). TEM images were obtained using a Tecnai F30 ST (FEI) with a FEG electron source at 300kV in TEM and STEM mode. Elemental analysis of plasma and TiN ALD treated patterned substrates was measured by Angle-Resolved X-ray Photoelectron Spectroscopy (AR-XPS) using a Theta300 system (Thermo Instruments). XPS measurements were carried out using a monochromatized Al K α X-ray source (1486.6 eV) with a spot size of 400 μ m with collection angles $22^\circ \leq \theta \leq 78^\circ$ taken perpendicular to the aC lines. Obtained XPS spectra were corrected to the C 1s peak at a binding energy of 284.5 eV. TiN thickness measurements on Si₃N₄ blanket substrates was determined using spectroscopic ellipsometry (SE) for 49 points on a 300 mm Si wafer (Aleris, KLA Tencor).

6.4 Results and Discussion

6.4.1 Formation and Plasma Treatment Processing of Sub-50nm aC/Si₃N₄ Patterned Structures

A test vehicle for area-selective ALD was created with aC lines 75 nm tall and 45 nm wide and Si₃N₄ spaces 45 nm wide, yielding a critical dimension (or CD) was 45 nm and a pitch of 90 nm. Figure 6.1 shows the steps (1-4) involved in forming the aC/Si₃N₄ patterned structures. For step 4, the SiO₂ was removed using a 1.5% dilute HF wet etch for 15 seconds. According to the standardized etch time for the tool, 10 seconds was estimated to be sufficient to remove the 15 nm

SiO₂ layer. To ensure full removal of SiO₂, and thus ALD-active hydroxyl species which would serve as undesired nucleation sites during ALD processing,^{27,30} a 15 second etch time was used.

Figure 6.2 a) shows SEM images of aC/Si₃N₄ patterns after all lithography and etch steps, essentially the starting substrate for future plasma and ALD processing. The resulting aC line dimensions, measured using image analysis software Image J are given in Table 6.1. The height measurement takes into account the observed 7 nm recess into the Si₃N₄ due to over etching during SiO₂ removal in step 4, Figure 6.1. During lithography and etch steps, substrates were exposed to air several times during transfer between tools, thus an oxide layer was expected on the Si₃N₄.³¹ This oxide layer was likely removed during the HF wet etch, and thus would explain the observed recess.

Figure 6.2 b) and c) show SEM images of aC/Si₃N₄ patterns after 400W 20s and 50s, respectively, H₂ plasma treatments, with the corresponding aC dimensions and etching reported in Table 6.1. All measurements represent an average over at least 10 separate areas on the patterned substrates. A 20 second plasma exposure resulted in ~4 nm of aC top-down etching, commensurate with what was observed for aC blanket wafers. The etching profile for the aC sidewalls was anisotropic, with lower etch rates near the bottom of the structures. Directional plasmas typically display anisotropic etching for patterned substrates with narrow critical dimensions due to radical species recombination prior to reacting with the aC surface near the bottom of high aspect ratio structures.³² Increasing the plasma exposure time to 50 seconds increased the top-down etching to ~11-12 nm (comparable to that measured for aC blanket substrates), with the sidewall etching of ~6 nm. No significant Si₃N₄ etching was observed due to H₂ plasma exposures as the recess remained constant at ~7 nm independent of plasma exposures.

With considerable sidewall etching, the aC line dimensions are expected to significantly change, for example, a 400W 50s plasma treatment reduced the width from 45 nm ~10 nm total to 35 nm width. Such sidewall etching presents a significant problem when pattern dimensions of the Si₃N₄ space are required to be less than 50 nm. Therefore, a 20 second plasma treatment was incorporated to test selective ALD growth of TiO₂ and TiN.

6.4.2 TiO₂ and TiN ALD for Bottom-Up Fill in Sub-50nm aC/Si₃N₄ Patterned Structures

6.4.2.1 Film Thickness and Growth Per Cycle

Using the aC/Si₃N₄ test vehicle shown in Figure 6.2 a), the selectivity of TiO₂ and TiN ALD in plasma-treated patterned structures was investigated. Figure 6.3 shows TEM images of plasma treated patterned substrates subjected to 30 and 75 cycles of TiO₂ ALD. Using TEM images, a thickness on the Si₃N₄ spaces was measured to be 1.7 ± 0.3 and 3.2 ± 0.2 nm for 30 and 75 cycles, respectively, corresponding to a growth rate per cycle (GPC) of 0.042 nm/cycle. The calculated GPC is comparable to the 0.043 nm/cycle obtained from ellipsometry of Ti(OCH₃)₄/H₂O on SiO₂ and Si₃N₄. For both samples, a conformal and uniform coating of the recessed Si₃N₄ was observed. TiO₂ particles on aC lines were visible for both samples, with considerable coverage for 75 cycle TiO₂ sample. Using TEM images, the maximum particle height (taken as the radius of a hemispherical particle on either the top or sidewall of the aC lines) was measured to be ~3 nm for the 75 cycle sample, and was not able to be measured for the 30 cycle sample (due to very low pixel density of particles). Furthermore, particles appeared to be larger and with higher surface coverage on the tops and corners of aC lines. This aspect will be discussed in Section 6.4.2.3.

Figure 6.4 shows TEM images of plasma-treated patterned substrates exposed to a) 200, b) 320, and c) 480 cycles of TiCl₄/NH₃ ALD. The corresponding TiN thickness obtained on Si₃N₄ spaces is shown in Figure 6.5, corresponding to a GPC of 0.031 nm/cycle. This value was

comparable to that measured using ellipsometry on SiO₂ and Si₃N₄ blanket substrates (0.031 nm/cycle). Also shown in Figure 6.5 is the maximum TiN particle radius measured on the aC sidewalls, which was consistently lower than those measured on the top surface of aC lines. Particle radii on top of aC lines was commensurate with the film thickness measured on Si₃N₄. This would imply that nucleation occurred on the top surface of aC lines during the first few cycles (as with nucleation on Si₃N₄). Conversely, smaller nuclei than the TiN thickness on Si₃N₄ would imply a delayed nucleation beyond the first few ALD cycles. When compared with the aC sidewalls, specifically near the Si₃N₄ interface, the nuclei appear to have a greater surface coverage on the top and corners of the aC lines (similar to that observed during TiO₂ ALD). These aspects will be discussed in Section 6.4.2.3.

6.4.2.2 Angle-Resolved XPS to Assess Selectivity

Isolation of Si₃N₄ and aC surfaces in sub-50 nm patterns can be challenging due to the large analysis areas of typical characterization methods (e.g., XPS, RBS, ToFSIMS, FTIR). Utilizing AR-XPS in conjunction with known pattern dimensions, aC lines can be isolated from Si₃N₄ spaces. Figure 6.6 a) shows aC/Si₃N₄ line/space patterns oriented so that photoelectrons generated during X-ray exposure are collected perpendicular to aC lines. Pattern dimensions obtained using TEM images in Figure 6.2 b) indicated a θ^* at $\sim 35^\circ$ based on pattern geometry. For $\theta > \theta^*$, photoelectrons generated from Si₃N₄ spaces need to travel through adjacent aC lines, decreasing likelihood of reaching the detector.³³ Figure 6.6 b) shows the resulting Ti at.%, obtained by aligning aC lines normal to the detector, from plasma-treated aC/Si₃N₄ line/space patterns with increasing TiN cycles. For low cycle numbers (e.g., 96 and 200 cycles TiN), Ti at.% was below $\sim 5\%$ for $\theta > \theta^*$. This drop in Ti at.% corresponds to the isolation of TiN deposited on aC lines from films on Si₃N₄ spaces. Increased TiN cycling to 320 and 480 cycles resulted in increased Ti at.%

to ~12 and 20 at.%, respectively. The obtained XPS results agree with the TEM images in Figure 6.4, where increased cycling yields high TiN particles on aC lines.

6.4.2.3 Nucleation Differences for Pattern vs. Blanket Substrates

With comparable GPC values on both blanket and patterned Si_3N_4 substrates, any nucleation discrepancies are expected to be minimal. Figure 6.7 a) shows a top-down SEM image of plasma-treated with 320 cycles of TiN on patterned substrates, with the tops of aC lines in focus. For comparison, Figure 6.7 b) and c) show the resulting TiN nucleation on plasma-treated aC blanket substrates followed by 320 and 480 cycles of TiN ALD, respectively. For the top of aC lines, image analysis revealed a TiN surface coverage of ~49% and a nuclei density of $\sim 3 \times 10^{11} \text{ cm}^{-2}$. For 320 and 480 cycles on aC blanket substrates, surface coverage of ~6% and 48%, respectively and nuclei density of $\sim 4 \times 10^{10} \text{ cm}^{-2}$ and $\sim 2 \times 10^{11} \text{ cm}^{-2}$, respectively.

The observed nucleation on the tops and corners of the aC lines could result from excess plasma damage at these sites,³⁴ or because of insufficient etch and clean steps after lithography patterning. Alternately, feature corners are generally expected to have higher surface energy than planar sites,³⁵⁻³⁷ which could favor nucleation kinetics. Further study using post-etch cleaning or atomic layer etching may help remove these defects. One possible route to minimize damage due to plasma processing would be to use a remote, rather than a direct plasma.³⁸

6.4.2.4 Tone Reversal by Selective aC Removal

Despite undesired particle nucleation on aC lines, conformal TiO_2 and TiN films were deposited on Si_3N_4 spaces. The quality of deposited films were assessed during pattern transfer by selective removal of aC lines. Using an oxygen plasma, the aC lines were removed via a combustion reaction, referred to as “ashing”, to give volatile hydrocarbon products described elsewhere.³⁹ Figure 6.8 shows tilted and cross-sectional SEM images of patterns, for a) 320 and b) 480 cycles of TiN, after aC removal. The SEM images clearly show that the aC was removed,

leaving behind TiN particles. The remaining TiN patterns were measured to be ~43 nm wide and ~10 and ~15 nm tall for 320 and 480 cycles of TiN, respectively. Considering the bottom portion of aC lines after plasma treatment, shown in Figure 6.2 b) and Table 6.1, were ~50 nm, the remaining Si₃N₄ spaces would have a width of ~40 nm (maintaining a pitch of 90 nm). Thus, the minimum width for TiN ALD was expected to also be 40 nm, comparable to that measured experimentally. For both 320 and 480 cycle samples, the thickness of TiN remaining after aC removal was similar to that measured after ALD processing (Figure 6.4 b) and c).

The top-down SEM images for 320 cycles of TiN in Figure 6.7 a) show nearly 50% aC surface exposed between TiN particles. It follows that after removal of aC, the void space remaining allows ample room for TiN particle diffusion and agglomeration.⁴⁰⁻⁴² Conversely, higher TiN surface coverage associated with 480 cycles, and likely partial coalescence allows for a more rigid TiN “arch” structure to remain after aC removal. These particles do not appear to be securely attached to the underlying substrate, as some of the “arches” have clearly broken off and are removed during sample cleaving for SEM. This would imply that a mechanical force may be suitable to remove the leftover particles, or a careful selection of solvent/acid wash to liberate particle agglomerates. Such post-aC removal clean steps is currently under investigation.

6.5 Conclusions

We demonstrated the use of a H₂ plasma pre-treatment to selectively deactivate aC lines in sub-50 nm aC/Si₃N₄ patterned wafers. We observed conformal and continuous area-selective ALD of TiN and TiO₂ on Si₃N₄ spaces with film thicknesses of 3.5 and 5.8 nm for TiO₂ and TiN, respectively. We found that the rate of TiN nucleation, resulting in selectivity loss, on the plasma-treated aC lines depended on the shape of the aC features, where nucleation proceeded more readily of feature corners and edges than on blanket aC substrates. After 320 cycles of TiN, the particle density on the top of aC lines ($\sim 3 \times 10^{11} \text{ cm}^{-2}$) was approximately one order of magnitude greater

than on blanket aC substrates. The tone reversal process was also explored by selective removal of aC lines using oxygen plasma, leaving TiN patterned on Si₃N₄. Final TiN pattern dimensions were a function of the number of ALD cycles (dictating the height), and the original space between the aC lines (determining the width). TiN patterns with the 10 and 15 nm height and 43 nm width were obtained after aC removal. Large agglomerates of particles were observed after aC removal but were partially removed during mechanical cleaving during SEM sample preparation, implying a removal by an additional etch/clean step.

6.6 Acknowledgements

The authors thank Thierry Conard, Johan Meersschaut, and Christa Vrancken (imec, Belgium) for discussions involving characterization and data analysis. The authors also thank Toby Hopf (imec, Belgium) for lithography development in creating aC/Si₃N₄ patterned structures.

6.7 Figures for Chapter 6

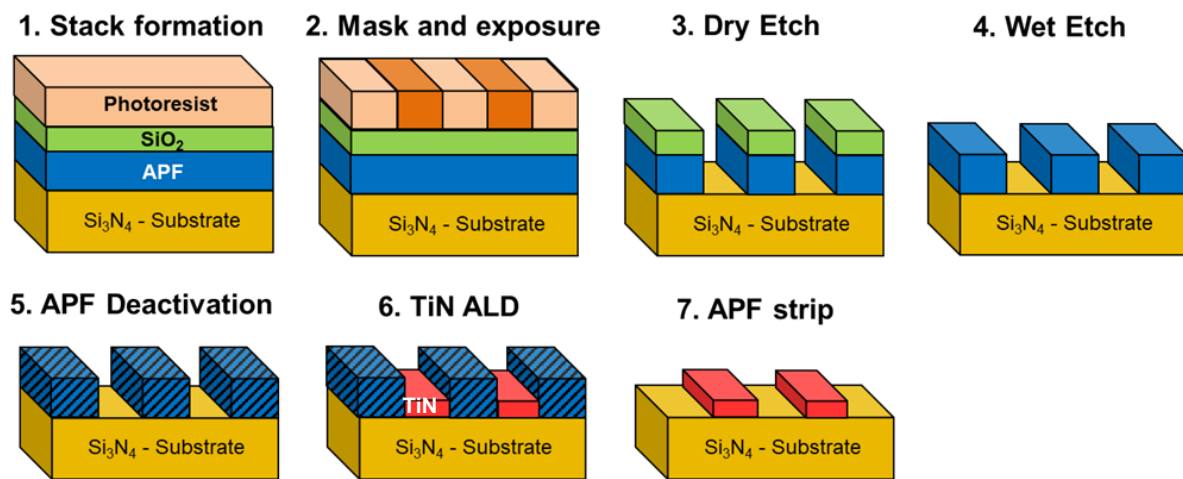


Figure 6.1: Schematic showing the steps involved in formation of aC/Si₃N₄ line/space patterns (Steps 1 – 4), where APF is an aC film. Steps 5 – 7 show the patterns after plasma, ALD, and APF strip processing, respectively.

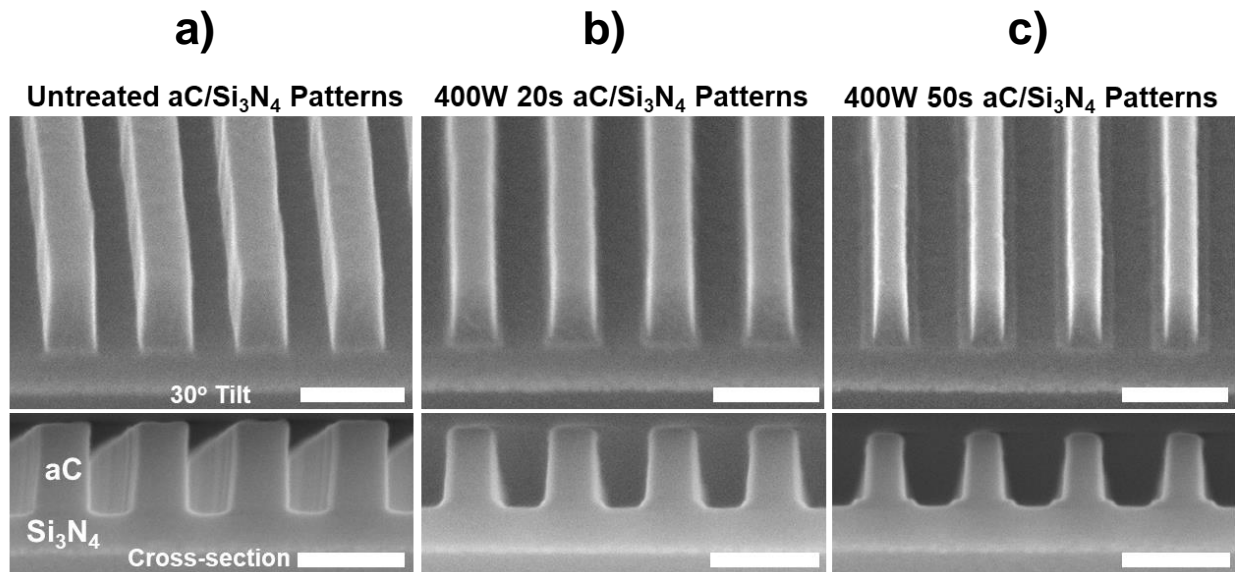
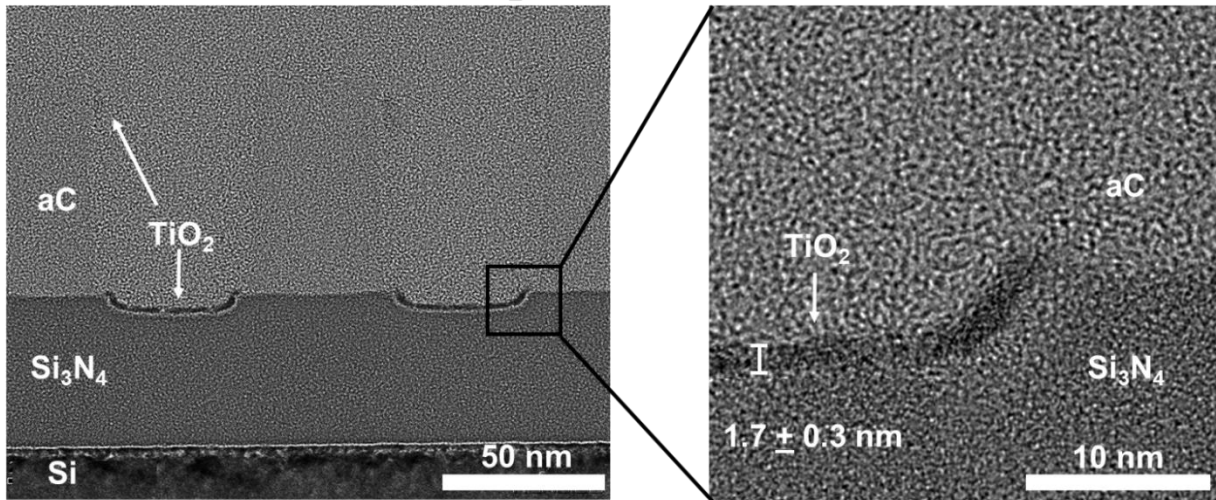


Figure 6.2: 30° tilt and cross-sectional SEM images of aC/Si₃N₄ patterned substrates after lithography and etch steps followed by a) no treatment, b) 400W 20s H₂ plasma, and c) 400W 50s H₂ plasma. Target pattern dimensions were aC line width of 45 nm, height of 75 nm, and Si₃N₄ trench width of 45 nm. All scale bars 100 nm

a) 400W 20s + 30cy TiO₂



b) 400W 20s + 75cy TiO₂

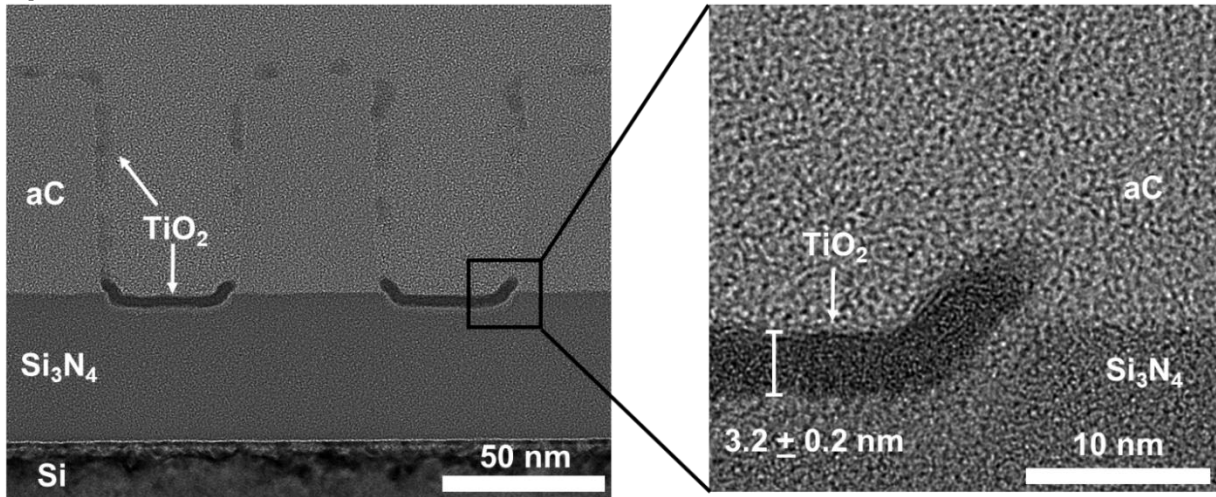


Figure 6.3: TEM images of aC/Si₃N₄ patterns subjected to 400W 20s H₂ plasma treatments at 300 °C followed by a) 30 cycles and b) 75 cycles of Ti(OCH₃)₄ + H₂O (ALD TiO₂) at 250 °C.

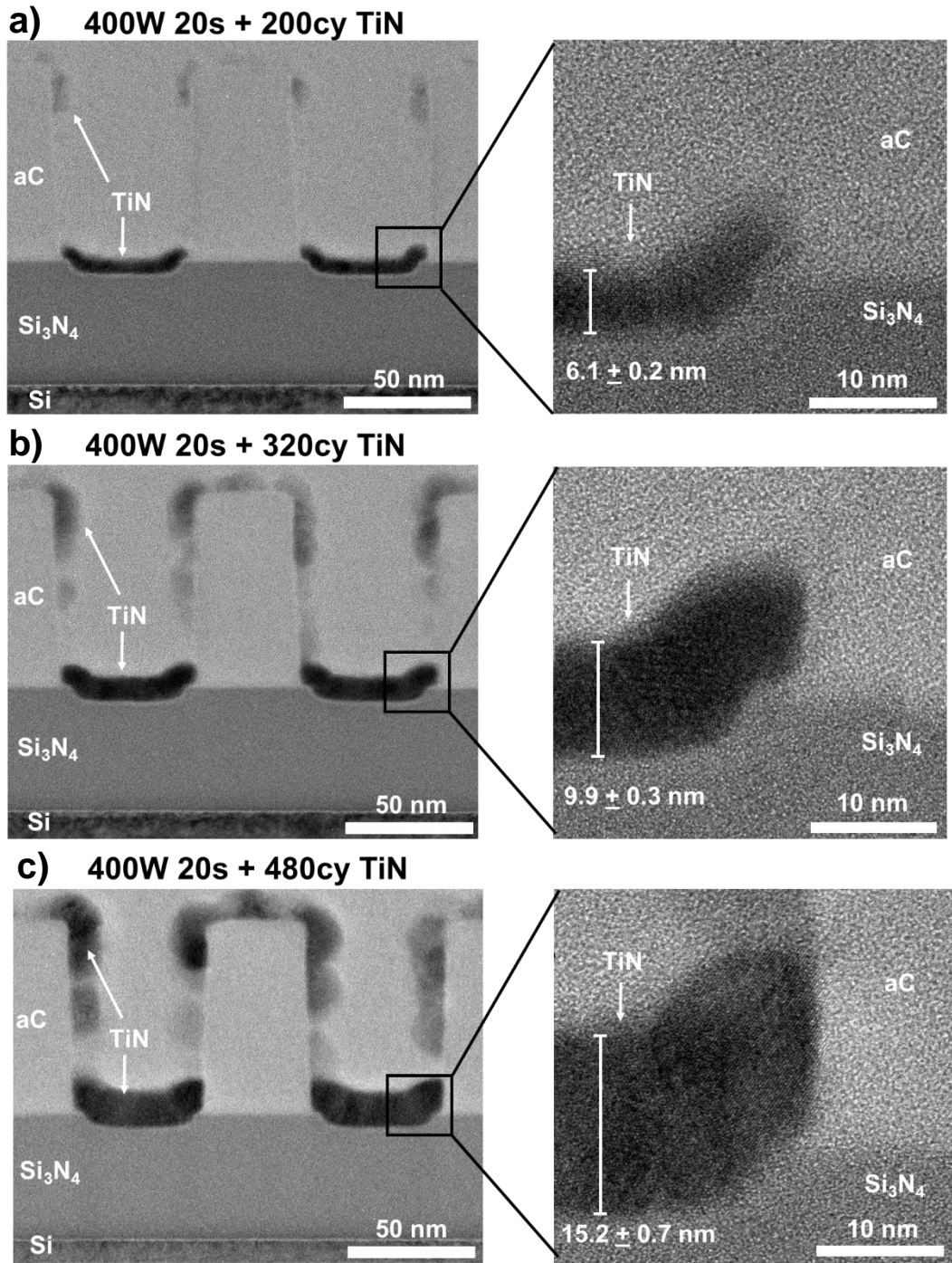


Figure 6.4: TEM images of the aC/Si₃N₄ patterns subjected to 400W 20s H₂ plasma at 300 °C followed by a) 200 cycles, b) 320 cycles, and 480 cycles of TiCl₄ + NH₃ (ALD TiN) at 390 °C.

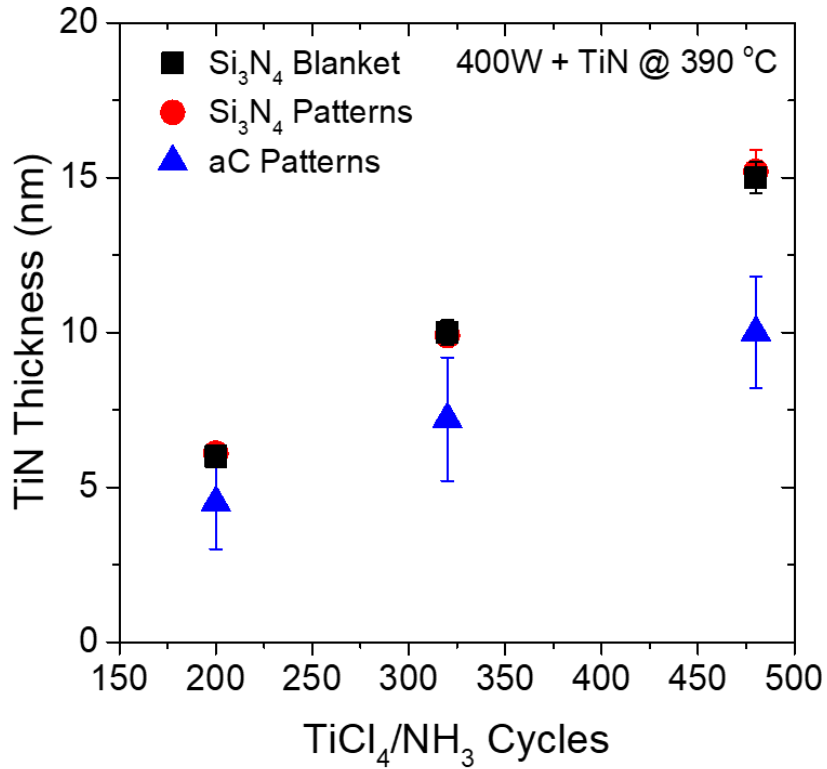


Figure 6.5: TiN thickness, measured from cross-sectional TEM images on Si_3N_4 spaces (red circles) and aC lines (blue triangles) in aC/ Si_3N_4 line/space patterns subjected to 400W 20s plasma and 200, 320, and 480 cycles of $\text{TiCl}_4/\text{NH}_3$ at 390 °C. Also shown is TiN thickness obtained by spectroscopic ellipsometry on Si_3N_4 blanket substrates (black squares).

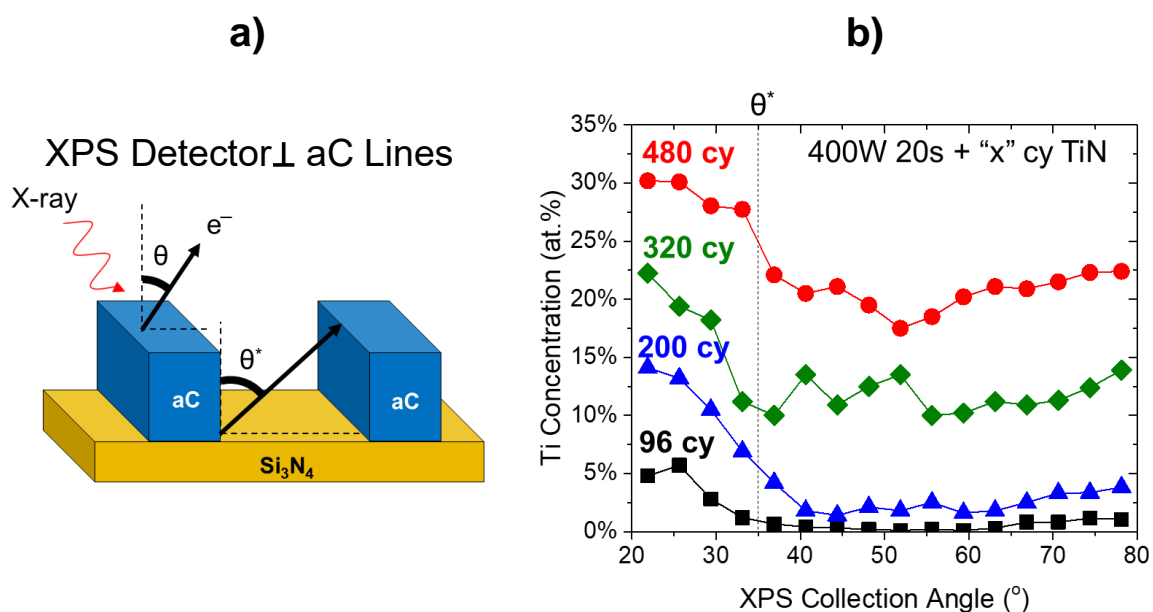


Figure 6.6: a) Schematic showing aC/ Si_3N_4 line/space patterns oriented such that the photoelectrons generated during X-ray exposure are collected perpendicular to aC lines. Angle resolved XPS was utilized, with photoelectron collection angles $22^\circ \leq \theta \leq 78^\circ$. For $\theta > \theta^*$, photoelectrons generated from Si_3N_4 spaces need to travel through adjacent aC lines. b) Resulting Ti at.%, with XPS detector perpendicular to aC lines, from plasma-treated aC/ Si_3N_4 line/space patterns subjected to 96 (black squares), 200 (blue triangles), 320 (green diamonds), and 480 (red circles) cycles of $TiCl_4/NH_3$ at $390^\circ C$. θ^* indicated at $\sim 35^\circ$ based on pattern geometry.

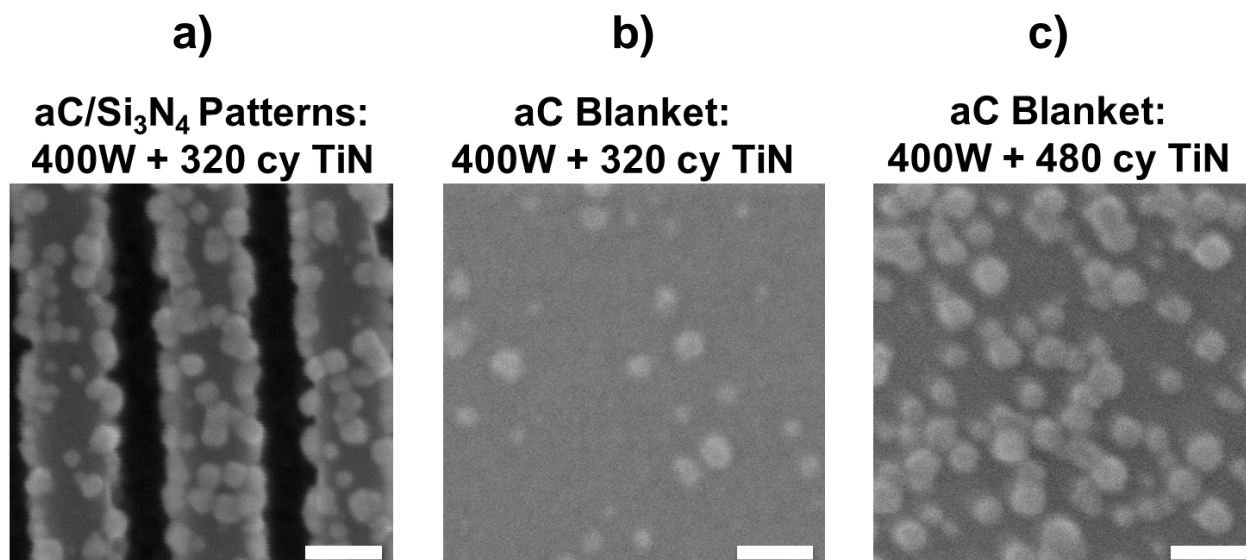


Figure 6.7: Top-down SEM images of 400W 20s H₂ plasma-treated a) aC/Si₃N₄ (tops of aC lines shown in image) patterned substrate followed by 320 cycles of TiN ALD, b) aC blanket substrate followed by 320 cycles of TiN ALD, and c) aC blanket substrate followed by 480 cycles of TiN ALD. All scale bars 50 nm.

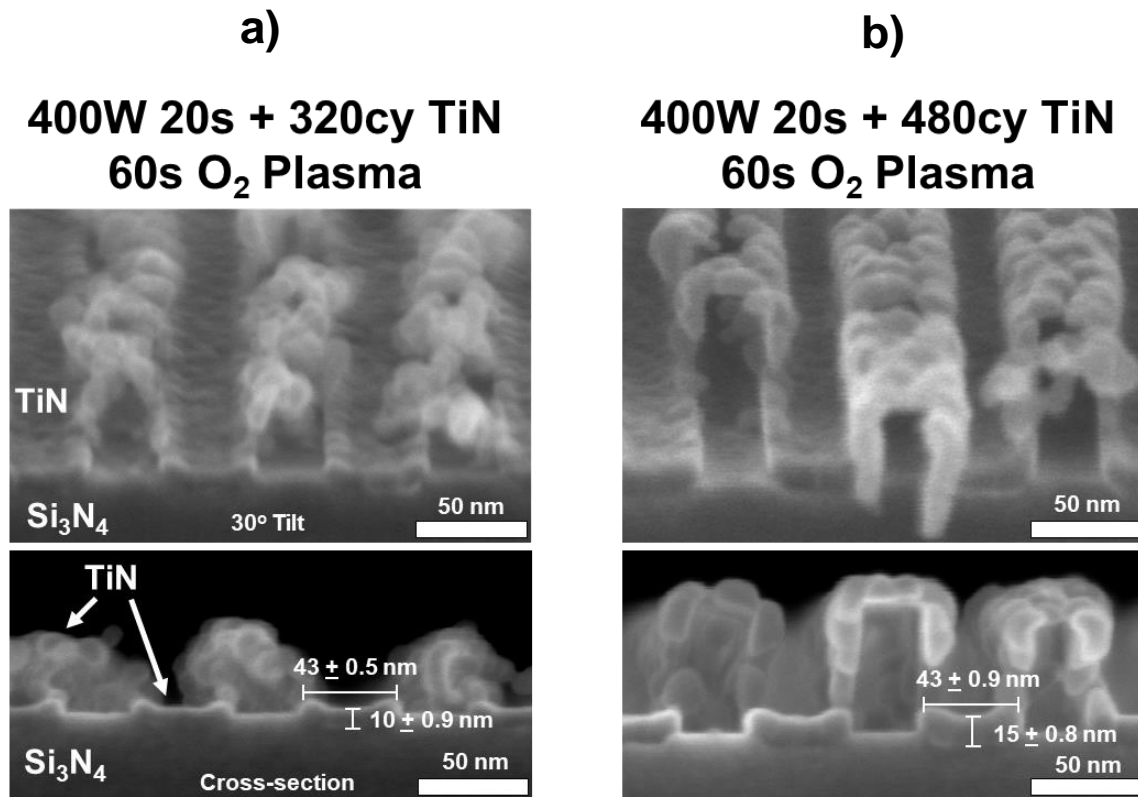


Figure 6.8: Tilted and cross-sectional SEM images of aC/Si₃N₄ substrates subjected 400W 20s H₂ plasma exposure, a) 320 and b) 480 cycles of TiN ALD, and 60 seconds O₂ plasma. Resulting structures are TiN patterned on Si₃N₄ with TiN particle contamination remaining in aC vacancies.

6.8 Tables for Chapter 6

Table 6.1 Dimensions for Untreated and Plasma-Treated aC/Si₃N₄ Patterns

Treatment	aC Height (nm)	aC Width (nm)	aC Etch Top-Down (nm)	aC Etch Sidewall (nm)
Target aC lines	75	45	-	-
Untreated aC	77.7 ± 1.1	46.5 ± 0.6 (Top) 47.6 ± 0.9 (Mid) 50.1 ± 0.7 (Bot)	-	-
400W 20s	73.6 ± 0.7	42.4 ± 1.2 (Top) 46.9 ± 1.2 (Mid) 49.9 ± 0.7 (Bot)	4.1 ± 1.3	2.0 ± 0.7 (Top) 0.4 ± 0.7 (Mid) 0.1 ± 0.5 (Bot)
400W 50s	66.5 ± 0.6	34.2 ± 0.5 (Top) 35.4 ± 0.9 (Mid) 38.5 ± 0.3 (Bot)	11.1 ± 1.2	6.1 ± 0.4 (Top) 6.1 ± 0.7 (Mid) 6.3 ± 0.4 (Bot)

6.9 References

- (1) International Technology Roadmap for Semiconductors, <http://public.itrs.net/Files/2001ITRS> http://mast-tech.com.tw/itrs_jan08.pdf.
- (2) Matsuyama, T. Exposure Tool Control for Advanced Semiconductor Lithography. *Adv. Opt. Techn* **2015**, *4* (4), 285–296.
- (3) Harper, R. Epitaxial Engineered Solutions for ITRS Scaling Roadblocks. *Mater. Sci. Eng. B* **2006**, *134*, 154–158.
- (4) Lee, A.; Fuchigami, N.; Pisharoty, D.; Hong, Z.; Haywood, E.; Joshi, A.; Mujumdar, S.; Bodke, A.; Karlsson, O.; Kim, H.; Choi, K.; Besser, P. Atomic Layer Deposition of $\text{Hf}_x\text{Al}_y\text{C}_z$ as a Work Function Material in Metal Gate MOS Devices. *J. Vac. Sci. Technol. A Vacuum, Surfaces, Film*. **2014**, *32* (1), 01A118.
- (5) Min, K. S.; Park, C.; Kang, C. Y.; Park, C. S.; Park, B. J.; Kim, Y. W.; Lee, B. H.; Lee, J. C.; Bersuker, G.; Kirsch, P.; Jammy, R.; Yeom, G. Y. Improvement of Metal Gate/high-K Dielectric CMOSFETs Characteristics by Atomic Layer Etching of High-K Gate Dielectric. *Solid. State. Electron*. **2013**, *82*, 82–85.
- (6) Xiang, J.; Ding, Y.; Du, L.; Li, J.; Wang, W.; Zhao, C. Growth Mechanism of Atomic-Layer-Deposited TiAlC Metal Gate Based on TiCl_4 and TMA Precursors. *Chinese Phys. B* **2016**, *25* (3), 37308.
- (7) Delabie, A.; Caymax, M.; Groven, B.; Heyne, M.; Haesevoets, K.; Meersschaut, J.; Nuytten, T.; Bender, H.; Conard, T.; Verdonck, P.; Elshocht, S. Van; Gendt, S. De; Heyns, M.; Barla, K.; Radu, I.; Thean, A. Low Temperature Deposition of 2D WS_2 Layers from WF_6 and H_2S Precursors: Impact of Reducing Agents. *Chem. Commun*. **2015**.
- (8) Groven, B.; Heyne, M.; Nalin Mehta, A.; Bender, H.; Nuytten, T.; Meersschaut, J.; Conard, T.; Verdonck, P.; Van Elshocht, S.; Vandervorst, W.; De Gendt, S.; Heyns, M.; Radu, I.; Caymax, M.; Delabie, A. Plasma-Enhanced Atomic Layer Deposition of Two-Dimensional WS_2 from WF_6 , H_2 Plasma, and H_2S . *Chem. Mater*. **2017**, *29* (7), 2927–2938.
- (9) Joubert, O. New Trends in Plasma Etching for Ultra Large Scale Integration Technology. *Microelectron. Eng*. **1998**, *4142*, 17–24.
- (10) Lemaire, P. C.; Parsons, G. N. Thermal Selective Vapor Etching of TiO_2 : Chemical Vapor Etching via WF_6 and Self-Limiting Atomic Layer Etching Using WF_6 and BCl_3 . *Chem. Mater*. **2017**, *29* (16), 6653–6665.
- (11) Dumont, J. W.; Marquardt, A. E.; Cano, A. M.; George, S. M. Thermal Atomic Layer Etching of SiO_2 by a “Conversion-Etch” Mechanism Using Sequential Reactions of Trimethylaluminum and Hydrogen Fluoride.

- (12) Neisser, M. Patterning Roadmap: 2017 Prospects. *Adv. Opt. Technol.* **2017**, 6 (3–4), 143–148.
- (13) Gesley, M. Mask Patterning Challenges for Device Fabrication below 100 Nm. *Microelectron. Eng.* **1998**, 41–42, 7–14.
- (14) Reboh, S.; Coquand, R.; Barraud, S.; Loubet, N.; Bernier, N.; Audoit, G.; Rouviere, J.-L.; Augendre, E.; Li, J.; Gaudiello, J.; Gambacorti, N.; Yamashita, T.; Faynot, O. Strain, Stress, and Mechanical Relaxation in Fin-Patterned Si/SiGe Multilayers for Sub-7 Nm Nanosheet Gate-All-around Device Technology. *Appl. Phys. Lett.* **2018**, 112 (5), 51901.
- (15) Nirschl, T.; Henzler, S.; Fischer, J.; Fulde, M.; Bargagli-Stoffi, A.; Sterkel, M.; Sedlmeir, J.; Weber, C.; Heinrich, R.; Schaper, U.; Einfeld, J.; Neubert, R.; Feldmann, U.; Stahrenberg, K.; Ruderer, E.; Georgakos, G.; Huber, A.; Kakoschke, R.; Hansch, W.; Schmitt-Landsiedel, D. Scaling Properties of the Tunneling Field Effect Transistor (TFET): Device and Circuit. *Solid. State. Electron.* **2006**, 50 (1), 44–51.
- (16) Zheng, Y.; Wang, H.; Hou, S.; Xia, D. Lithographically Defined Graphene Patterns. *Adv. Mater. Technol.* **2017**, 2 (5), 1600237.
- (17) Baldi, L.; Bez, R. The Scaling Challenges of CMOS and the Impact on High-Density Non-Volatile Memories. *Microsyst. Technol.* **2007**, 13 (2), 133–138.
- (18) Zeitzoff, P. M.; Huff, H. R. MOSFET Scaling Trends, Challenges, and Key Associated Metrology Issues through the End of the Roadmap. *AIP Conf. Proc.* **2005**, 788 (203), 203–213.
- (19) Horiguchi, N.; Milenin, A. P.; Tao, Z.; Hubert, H.; Altamirano-Sanchez, E.; Veloso, A.; Witters, L.; Waldron, N.; -Å Ragnarsson, L.; Kim, M. S.; Kikuchi, Y.; Mertens, H. Patterning Challenges in Advanced Device Architectures: FinFETs to Nanowires. In *Advanced Etch Technology for Nanopatterning V*; 2016; p 978209.
- (20) Yao, H.; Mullen, S.; Wolfer, E.; Mckenzie, D.; Dioses, A.; Rahman, D.; Cho, J.; Padmanaban, M.; Petermann, C.; Hong, S.; Mannaert, G.; Hopf, T.; De Simone, D.; Vangoidsenhoven, D.; Lorant, C.; Sebaai, F.; Sanchez, E. A. Spin-on Metal Oxides and Their Applications for Next Generation Lithography. *J. Photopolym. Sci. Technol.* **2016**, 29 (1), 59–67.
- (21) Ootera, Y.; Sugawara, K.; Kanamaru, M.; Yamamoto, R.; Kawamonzen, Y.; Kihara, N.; Kamata, Y.; Kikitsu, A. Nanoimprint Lithography of 20-Nm-Pitch Dot Array Pattern Using Tone Reversal Process. *Jpn. J. Appl. Phys.* **2013**, 52, 105201.
- (22) Chang, L.; Litvinov, D. Nanoimprint Lithography Tone Reversal Process Using Poly(methyl Methacrylate) and Hydrogen Silsesquioxane. *J. Vac. Sci. Technol. B, Nanotechnol. Microelectron. Mater. Process. Meas. Phenom.* **2017**, 35 (4), 41603.
- (23) Bencher, C.; Chen, Y.; Dai, H.; Montgomery, W.; Huli, L. 22nm Half-Pitch Patterning by CVD Spacer Self Alignment Double Patterning (SADP); International Society for Optics

and Photonics, 2008; Vol. 6924, p 69244E.

- (24) Kim, W.-H.; Lee, H.-B.-R.; Heo, K.; Lee, Y. K.; Chung, T.-M.; Kim, C. G.; Hong, S.; Heo, J.; Kim, H. Atomic Layer Deposition of Ni Thin Films and Application to Area-Selective Deposition. *J. Electrochem. Soc.* **2011**, *158* (1), D1–D5.
- (25) Kerrigan, M. M.; Klesko, J. P.; Winter, C. H. Low Temperature, Selective Atomic Layer Deposition of Cobalt Metal Films Using Bis(1,4-Di-*Tert*-Butyl-1,3-Diazadienyl)cobalt and Alkylamine Precursors. *Chem. Mater.* **2017**, *29* (17), 7458–7466.
- (26) Atanasov, S. E.; Kalanyan, B.; Parsons, G. N. Inherent Substrate-Dependent Growth Initiation and Selective-Area Atomic Layer Deposition of TiO₂ Using “water-Free” Metal-Halide/metal Alkoxide Reactants. *J. Vac. Sci. Technol. A Vacuum, Surfaces, Film.* **2016**, *34* (1), 01A148.
- (27) Lemaire, P. C.; King, M.; Parsons, G. N. Understanding Inherent Substrate Selectivity during Atomic Layer Deposition: Effect of Surface Preparation, Hydroxyl Density, and Metal Oxide Composition on Nucleation Mechanisms during Tungsten ALD. *J. Chem. Phys.* **2017**, *146* (5), 52811.
- (28) Fairbairn, K.; Rice, M.; Weidman, T.; Ngai Ian, C. S.; Scot Latchford, I.; Bencher, C. D.; Wang, Y. M. Method for Depositing an Amorphous Carbon Layer. 6,573,030 B1, 2003.
- (29) Tai, H.; Liao, Y. M.; Liu, W. T.; Peng, W. C.; Ying, T. H. Novel Clean Concept of Advanced Patterning Film (Amorphous Carbon) for Beyond 2xnm Generation Self-Aligned Double-Patterning (SADP) Process. *ECS Trans.* **2014**, *61* (3), 67–71.
- (30) Hu, Z.; Turner, C. H. Initial Surface Reactions of TiO₂ Atomic Layer Deposition onto SiO₂ Surfaces: Density Functional Theory Calculations. *J. Phys. Chem. B* **2006**, *110* (16), 8337–8347.
- (31) S. I. Raider, R. Flitsch, J. A. Aboaf, W. A. P. Surface Oxidation of Silicon Nitride Films. *J. Electrochem. Soc.* **1976**, *123* (4), 560–565.
- (32) Profijt, H. B.; Potts, S. E.; Sanden, M. C. M. van de; Kessels, W. M. M. Plasma-Assisted Atomic Layer Deposition: Basics, Opportunities, and Challenges. *J. Vac. Sci. Technol. A* **2011**, *29* (5), 50801.
- (33) Baschenko, O. A. Photoelectron Mean Free Path Chemical Composition Dependence and Elastic Scattering and Analyzer Acceptance Angle Finiteness Effects in Restoring Concentration Profiles from Angular Resolved X-Ray Photoelectron Spectroscopy Data. *J. Electron Spectros. Relat. Phenomena* **1991**, *57* (3–4), 297–305.
- (34) Shin, H.; Hu, C. Monitoring Plasma-Process Induced Damage in Thin Oxide. *IEE Trans. Semicond. Manuf.* **1993**, *6* (2), 96–102.
- (35) Ni, B.; Wang, X. Face the Edges: Catalytic Active Sites of Nanomaterials. *Adv. Sci.* **2015**, *2* (7), 1500085.

- (36) Freund, H. J.; Libuda, J.; Bäumer, M.; Risse, T.; Carlsson, A. Cluster, Facets, and Edges: Site-Dependent Selective Chemistry on Model Catalysts. *Chem. Rec.* **2003**, *3* (3), 181–200.
- (37) Scamehorn, C. A.; Harrison, N. M.; McCarthy, M. I. Water Chemistry on Surface Defect Sites: Chemidissociation versus Physisorption on MgO(001). *J. Chem. Phys.* **1994**, *101* (2), 1547–1554.
- (38) Viswanathan, C. R. Plasma-Induced Damage. *Microelectron. Eng.* **1999**, *49* (1), 65–81.
- (39) G. A. Antonellia, S. Reddyb, P. Subramoniumb, J. Henrib, J. Simsb, J. O’loughlinb, N.; Shammac, D. Schlosserc, T. Mountsiere, W. Guod, and H. S. Patterning with Amorphous Carbon Thin Films. *ECS Trans.* **2011**, *35* (4), 701.
- (40) Mei, H. G.; Zhao, D. W.; Wang, T. Q.; Cheng, J.; Lu, X. C. A Kinematic Model Describing Particle Movement near a Surface as Effected by Brownian Motion and Electrostatic and Van Der Waals Forces. *Sci. China Technol. Sci.* **2014**, *57* (11), 2144–2152.
- (41) Kawashima, T.; Mizutani, T.; Nakagawa, T.; Torii, H.; Saitoh, T.; Komori, K.; Fujii, M. Control of Surface Migration of Gold Particles on Si Nanowires. *Nano Lett.* **2008**, *8* (1), 362–368.
- (42) Huang, J.; Hu, G.; Orkoulas, G.; Christofides, P. D. Dependence of Film Surface Roughness and Slope on Surface Migration and Lattice Size in Thin Film Deposition Processes. *Chem. Eng. Sci.* **2010**, *65* (23), 6101–6111.

APPENDICES

**APPENDIX A1: THERMAL CHEMICAL VAPOR ETCH
SELECTIVITY OF TiO₂ VERSUS Al₂O₃ USING VAPOR
PHASE WCl₅**

APPENDIX A1. Thermal Chemical Vapor Etch Selectivity of TiO₂ versus Al₂O₃ Using WCl₅*

*The results shown in this appendix are preliminary findings, with further experiments and analysis required before drawing conclusions.

Eric C. Stevens,[†] Gregory N. Parsons^{*,†}

[†]Department of Chemical and Biomolecular Engineering, North Carolina State University, 911 Partners Way, Raleigh NC 27695

A1.1 Experimental

All ALD experiments were conducted in a homemade, hot wall, reactor operating in the viscous flow regime. All reactor lines were resistively heated to ~150–170 °C to prevent precursor condensation during the delivery process. The deposition chamber (~3.5 cm diameter 316 stainless steel tube) was resistively heated using a proportional–integral–derivative (PID) temperature controller. The deposition temperatures tested were 250 and 300 °C. The reactor utilized *in situ* quartz crystal microbalance (QCM) to monitor the process during ALD processing. Research grade nitrogen (99.999%, Machine & Welding Supply Company) was further purified (Entegris Gate-Keeper) and used as the carrier and purge gas at an operating pressure of ~1.5 Torr.

A1.1.1 ALD Precursors and Delivery

Tungsten (V) chloride (WCl₅) was obtained from industry partners and was transferred, in a N₂-filled glovebox, into a stainless-steel vessel for ALD experiments. The WCl₅ vessel was connected to the ALD reactor and, prior to initiation of ALD experiments, pumped down for ~5 minutes, at room temperature, to remove excess N₂ and ensure consistent dosing into the reactor chamber. The WCl₅ vessel was heated resistively and maintained at ~145 °C via a PID temperature

controller. WCl_5 was dosed into the deposition chamber via a three-way valve, with N_2 as the carrier gas.

Aluminum oxide (Al_2O_3) was deposited using trimethyl aluminum ($\text{Al}(\text{CH}_3)_3$, or TMA), purchased from Strem and used as received, and H_2O . The TMA vessel was not heated, but the delivery lines were kept at $\sim 150 - 170$ °C. TMA was dosed into the deposition chamber via a three-way valve, with N_2 as the carrier gas. Titanium oxide (TiO_2) was deposited using titanium tetrachloride (TiCl_4), purchased from Strem and used as received, and H_2O . The TiCl_4 vessel was not heated, but the delivery lines were kept at $\sim 150 - 170$ °C. TiCl_4 was dosed into the deposition chamber via a three-way valve, with N_2 as the carrier gas.

A1.1.2 *In situ* QCM

For QCM analysis, Au-coated quartz crystals (Inficon, 6 MHz AT-cut quartz, 0.55” diameter, unpolished) were used as received. A commercial QCM assembly (Cool Drawer, Inficon) was specially modified to allow a constant flow of ~ 0.3 Torr of N_2 to purge the back side of the quartz crystal. This modification prevented unwanted deposition during ALD processing on the electrode contacts. The modified QCM assembly was inserted into the ALD reactor, with the sensor head containing the QCM crystal positioned in the center of the deposition chamber. Before starting deposition runs, the QCM sensor was held in the reactor for $\simeq 4$ to 6 hours under dry N_2 flow at the operating pressure of 1.5 Torr to allow the sensor to reach thermal equilibrium at the desired deposition temperature. Thermal equilibrium was reached after changes in steady-state QCM frequency were less than ~ 0.5 Hz over 30 minutes. For QCM experiments, Mass change measurements were recorded using an Inficon SQM-160 controller at a sampling rate of 10 Hz.

A1.2 Results and Discussion

To understand the potential reaction pathways for WCl_5 etching of TiO_2 , thermodynamic modeling was utilized via HSC Chemistry 7.1 software. Initial species were set to 5 moles N_2 , 2

moles WCl_5 (g) and 1 moles TiO_2 (s) in a closed system, with constant pressure of 2 mbar. The temperature was increased from 25 to 500 °C, with the Gibb free energy minimized at each step. Any species with an equilibrium concentration less than 1 mmol was not shown.

Figure A1.1 shows the predicted species at equilibrium as a function of temperature. At room temperature, WCl_5 (g) reacts with TiO_2 (s) to give ~1.9 mol of WOCl_3 (s) and 1 mol of TiCl_4 (g). At temperatures above 150 °C, WOCl_3 (s) can react to form WOCl_2 (s), WOCl_3 (g), and WOCl_4 (g). For temperatures ≥ 300 °C, all solid byproducts volatilize to form WOCl_3 (g) and TiCl_4 (g). It is important to note that this model is for a closed system, which does not consider the removal of species. In an ALD reaction, byproducts are removed after each half-reaction.

TiO_2 films were grown *in situ* on Au-coated QCM crystals using 100 cycles of $\text{TiCl}_4/\text{H}_2\text{O}$ at 250 or 300 °C. Figure A1.2 shows the resulting mass change (from QCM) at 300 °C for a TiO_2 film subjected to 10 consecutive, 1 second WCl_5 doses, separated by 30 second N_2 purges. At 300 °C, the first dose results in a mass gain of ~38 ng/cm^2 , followed by a constant mass loss of ~40 ng/cm^2 . Figure A1.2 b) suggests that at 300 °C, only volatile byproducts are likely to form during WCl_5 etching of TiO_2 . The initial mass gain observed during the first WCl_5 could be due to formation of WOCl_2 (s) species, which may require additional WCl_5 dosing to react and form volatile WOCl_3 (g).

Figure A1.3 shows the resulting mass change (from QCM) at 250 °C for a TiO_2 subjected to 2 sets of 10 consecutive, 1 second WCl_5 doses, separated by 30 second N_2 purges. At 250 °C, the first dose results in a mass gain of ~25 ng/cm^2 , followed by a roughly constant mass loss of ~25 ng/cm^2 . During the first sub set of 10 doses, the mass loss decreases to ~10 ng/cm^2 for the last two doses. After a 25 minutes N_2 purge, 10 additional WCl_5 doses resulted in no mass change. Figure A1.3 b) suggests that at 250 °C, solid WOCl_2 (s) and WOCl_3 (s) byproducts are likely to form

during WCl_5 etching of TiO_2 . The initial mass gain observed during the first WCl_5 could be due to formation of $\text{WOCl}_{2(s)}$ and $\text{WOCl}_{3(s)}$ species, which may require additional WCl_5 dosing to react and form volatile $\text{WOCl}_{3(g)}$. With enough cycling, additional WCl_5 doses do not result in additional TiO_2 etching. This is likely due to an accumulation of $\text{WOCl}_{2(s)}$ and $\text{WOCl}_{3(s)}$ which may sterically hinder the WCl_5 molecule from reacting with underlying TiO_2 .

Using equation (A1.1), the average mass change (Δm) from Figures A1.2 and A1.3 and the density of TiO_2 (anatase $\text{TiO}_2 \sim 3.9 \text{ g/cm}^3$)¹, can be used to estimate the expected etch rate per cycle (EPC), in units of nm/cycle:

$$EPC = \Delta m \times \rho^{-1} \quad (A1.1)$$

Using equation (A1.1), the EPC at 300 and 250 °C was calculated to be 0.1 and 0.06 nm/cy, respectively. An estimated thickness of one TiO_2 monolayer can be calculated using equation A1.2

$$t_m = [MW / (N_A \times \rho)]^{1/3} \quad (A1.2)$$

where MW, N_A , and ρ are the molecular weight ($\text{TiO}_2 = 79.87 \text{ g/mol}$), Avagadro's number (6.022×10^{23} molecules/mol), and the density of TiO_2 (anatase $\text{TiO}_2 \sim 3.9 \text{ g/cm}^3$). Using equation (A1.2), the thickness of one TiO_2 monolayer was found to be $\sim 0.32 \text{ nm}$. With the EPC values from equation A1.1, the average etch rate can be rewritten in terms of monolayers etched per cycle. The EPC at 300 and 250 °C was thus calculated to be 0.32 and 0.20 monolayer/cy, respectively.

For etching reactions at 250 °C, the solid formation, leading to a poisoning of TiO_2 etching, could be potentially applied as a pseudo thermal atomic layer etch process.²⁻⁵ For such a process, $\sim 250 \text{ ng/cm}^2$ can be etched during 10 cycles of WCl_5 at 250°C, corresponding to $\sim 0.64 \text{ nm}$ or ~ 2 monolayers of TiO_2 . After which, the etching stops due to solid species formation. Liberation of these species can be accomplished by localized heating of the substrate, which would likely

volatilize $\text{WOCl}_{2(s)}$ and $\text{WOCl}_{3(s)}$ species to give $\text{WOCl}_{2(g)}$. This process can be repeated in a cyclic manner to give an a self-limiting etch rate of ~ 0.64 nm/cycle.

Figure A1.4 shows mass change data from QCM during 100 cycles of $\text{Al}(\text{CH}_3)_3 + \text{H}_2\text{O}$ (black) and $\text{TiCl}_4 + \text{H}_2\text{O}$ (red) at 300°C deposited on Au-coated QCM substrates followed by 30 and 50 consecutive doses of WCl_5 , respectively. Figure A1.5 a) shows a magnified region during 30 WCl_5 exposures to the Al_2O_3 surface, where the first dose resulted in a mass increase of ~ 75 ng/cm^2 . The second and third dose both resulted in a mass loss of ~ 10 $\text{ng}/\text{cm}^2/\text{cy}$ (or a total of 20 ng/cm^2), followed by no observable mass change for the remaining 27 doses. The initial mass gain is likely the formation of solid reaction byproducts, which can be partially liberated with subsequent WCl_5 doses before enough solid has accumulated to inhibit further Al_2O_3 etching. The difference between this result and TiO_2 etching at 250°C is that the ~ 0.64 nm of TiO_2 was etched during 10 cycles of WCl_5 , while a net mass increase was observed during WCl_5 doses on a Al_2O_3 surface.

Figure A1.5 b) shows a magnified region during 50 WCl_5 exposures to the TiO_2 surface, where the first dose resulted in a mass increase of ~ 40 ng/cm^2 . The remaining 49 doses resulted in a constant mass loss of ~ 12 $\text{ng}/\text{cm}^2/\text{cy}$. The initial mass gain was nearly the same as that observed in Figure A1.2. The etch rate from Figure A1.5 b), 0.03 nm/cy, was lower than that found in Figure A1.2, 0.1 nm/cy. The decreased EPC is likely due to a lesser dose during the runs that generated Figure A1.5 b) than in Figure A1.2. Despite a constant dose time and WCl_5 source temperature, a depletion of the precursor would lead to less partial pressure of WCl_5 in equilibrium in the headspace to be dosed. At 300°C this process was shown to be a chemical vapor etch, which can be defined as having a linear etch rate per cycle that does not self-limit (contrary to an atomic layer etch process). Thus, dosing less precursor would lead to a lower etch rate.

A1.3 Figures for Appendix A1

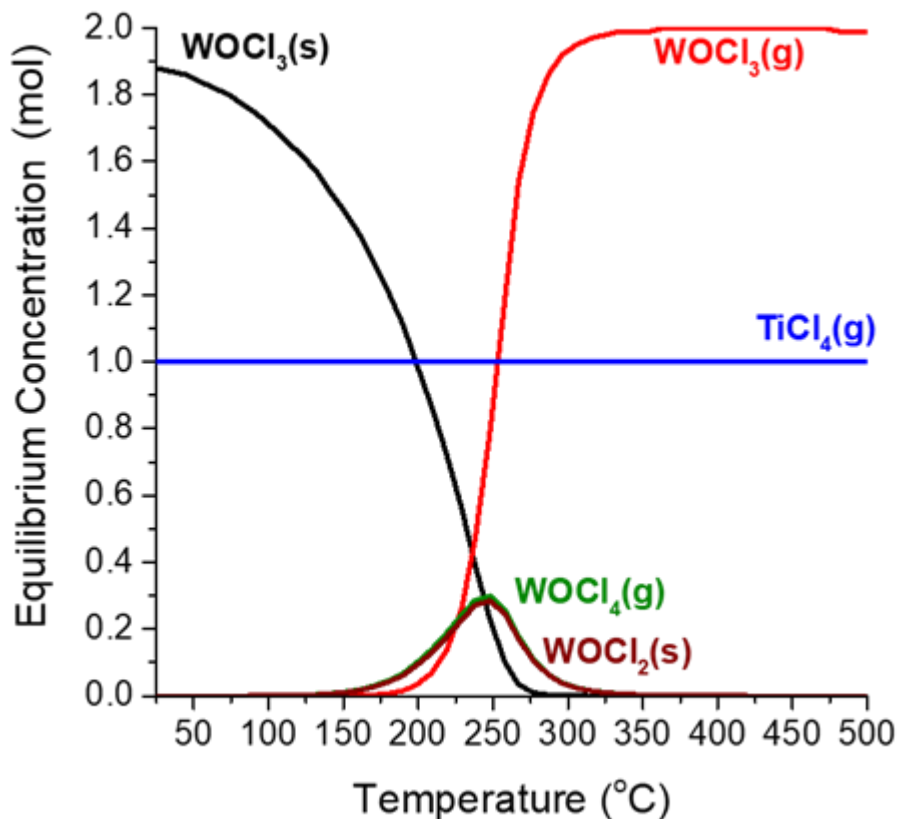


Figure A1.1: Predicted equilibrium species from the reaction of 2 moles of $\text{WCl}_5(\text{g})$ and 1 moles of $\text{TiO}_2(\text{s})$ from temperatures ranging 25 – 500 °C and pressure of 2 mbar. Only species with an equilibrium concentration greater than 1 mmol are shown. The following are the species expected at equilibrium, with their anticipated phase indicated as either (g) for gas or (s) for solid, $\text{WOCl}_3(\text{s})$ (black), $\text{WOCl}_3(\text{g})$ (red), $\text{TiCl}_4(\text{g})$ (blue), $\text{WOCl}_4(\text{g})$ (green), and $\text{WOCl}_2(\text{g})$ (brown).

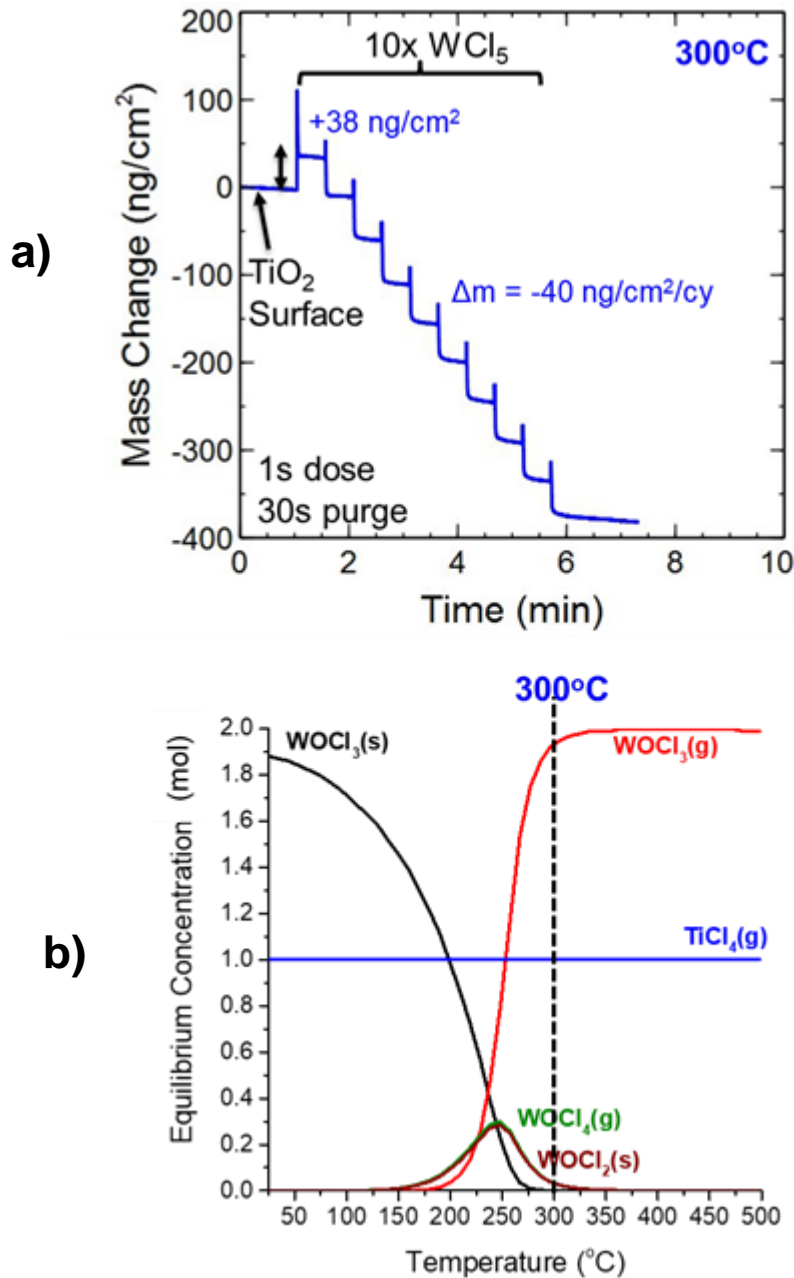


Figure A1.2: a) After 100 cycles of $\text{TiCl}_4 + \text{H}_2\text{O}$ at 300 $^{\circ}\text{C}$, 10 consecutive, 1 second doses of WCl_5 , separated by 30 second purges. Linear etch rate of $-40 \text{ ng}/\text{cm}^2/\text{cy}$. b) same as from Figure A1.1 but with vertical line indicating the etch temperature in a)

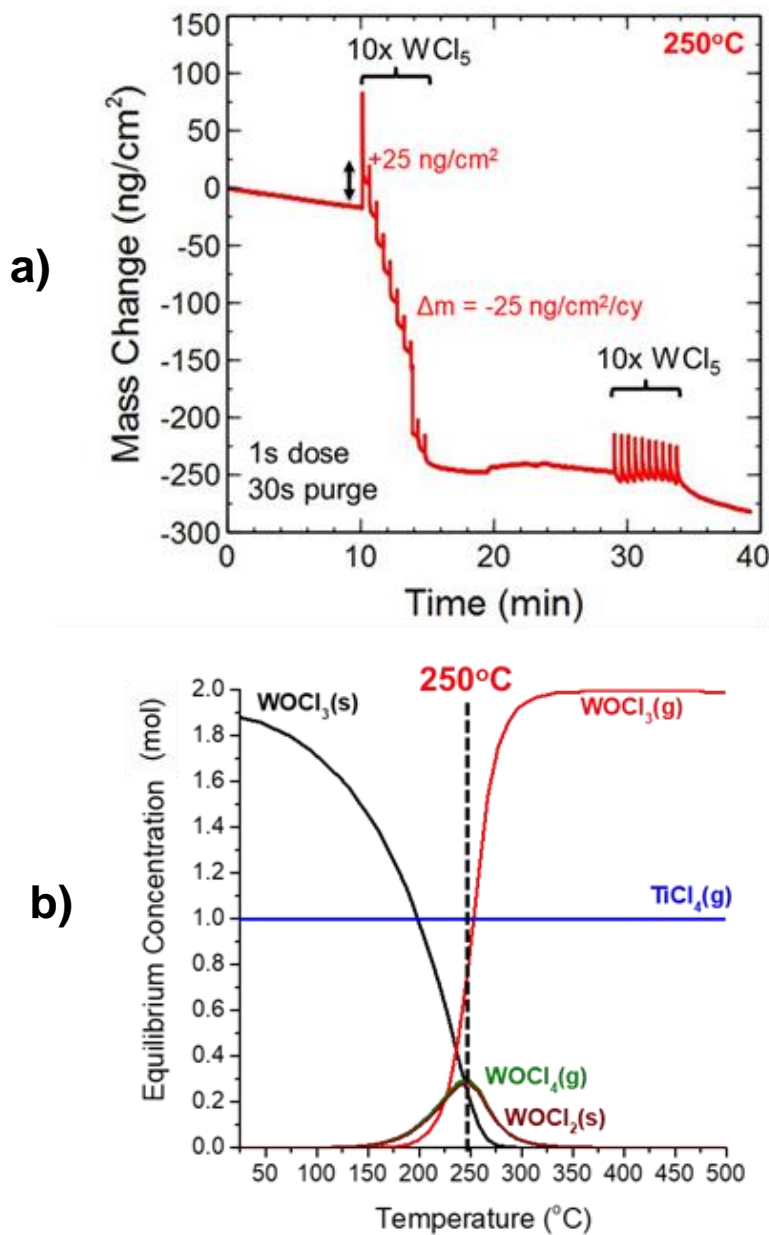


Figure A1.3: a) After 100 cycles of TiCl₄ + H₂O at 250 °C, 10 consecutive, 1 second doses of WCl₅, separated by 30 second purges. Linear etch rate of -25 ng/cm²/cy, with a decrease in etch rate to 10 ng/cm²/cy for the 9th and 10th dose. 25 minutes of N₂ purging, then 10 consecutive, 1 second doses of WCl₅, separated by 30 second purges. b) same as from Figure A1.1 but with vertical line indicating the etch temperature in a)

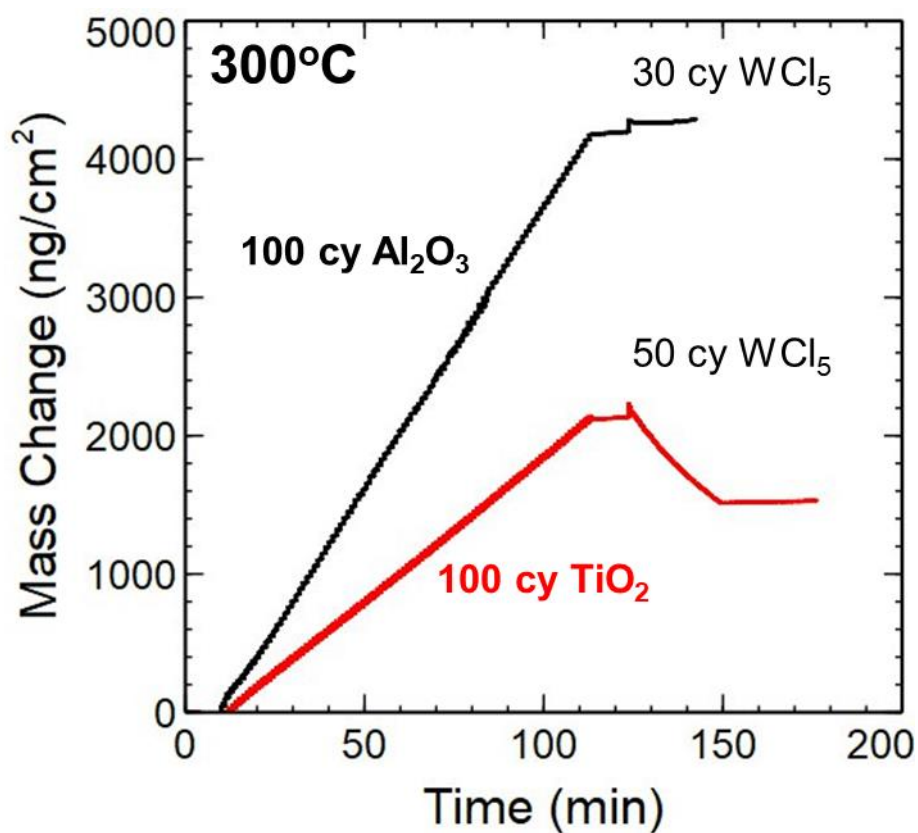


Figure A1.4: 100 cycles of Al(CH₃)₃ + H₂O (black) and TiCl₄ + H₂O (red) at 300 °C deposited on Au-coated QCM substrates followed by 30 and 50 consecutive, 1 second doses of WCl₅, separated by 30 second N₂ purges, respectively.

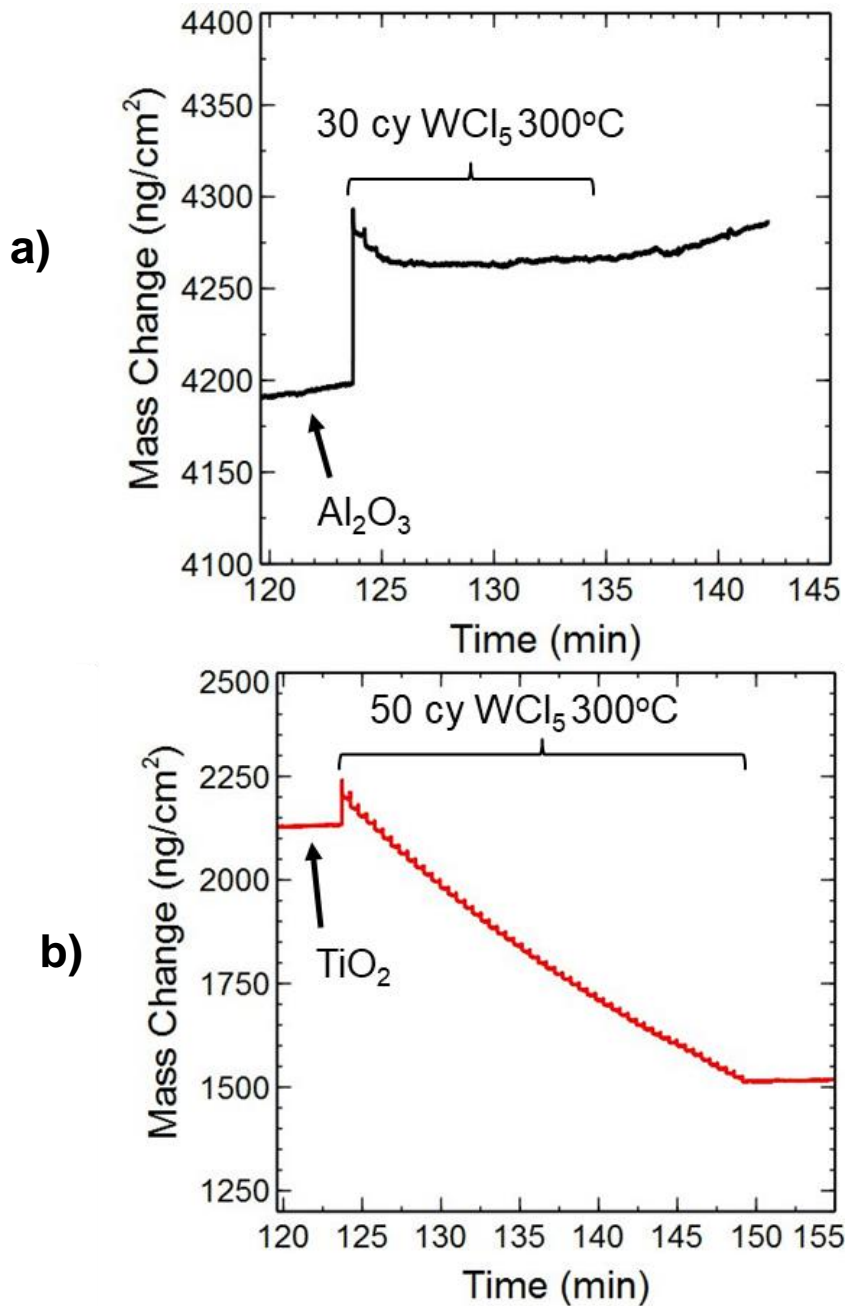


Figure A1.5: Magnified etching regions from Figure A1.4. a) 100 cycles of Al(CH₃)₃ + H₂O followed by 30 consecutive, 1 second doses of WCl₅, separated by 30 second N₂ purges. b) TiCl₄ + H₂O (red) at 300 °C followed by 50 consecutive, 1 second doses of WCl₅, separated by 30 second N₂ purges.

A1.4 References

- (1) Haynes, W. M. *Haynes, W. M. Handbook of Chemistry and Physics 96th Edition. Taylor and Francis Group, 2015, 96th ed.; 2015.*
- (2) Lee, Y.; DuMont, J. W.; George, S. M. Atomic Layer Etching of HfO₂ Using Sequential, Self-Limiting Thermal Reactions with Sn(acac)₂ and HF. *ECS J. Solid State Sci. Technol.* **2015**, 4 (6), N5013–N5022.
- (3) Dumont, J. W.; Marquardt, A. E.; Cano, A. M.; George, S. M. Thermal Atomic Layer Etching of SiO₂ by a “Conversion-Etch” Mechanism Using Sequential Reactions of Trimethylaluminum and Hydrogen Fluoride.
- (4) Lee, Y.; George, S. M. Atomic Layer Etching of Al₂O₃ Using Sequential, Self-Limiting Thermal Reactions with Sn(acac)₂ and Hydrogen Fluoride. *ACS Nano* **2015**, 9 (2), 2061–2070.
- (5) Lemaire, P. C.; Parsons, G. N. Thermal Selective Vapor Etching of TiO₂: Chemical Vapor Etching via WF₆ and Self-Limiting Atomic Layer Etching Using WF₆ and BCl₃. *Chem. Mater.* **2017**, 29 (16), 6653–6665.

**APPENDIX A2: *IN SITU* STUDY OF TITANIUM CARBIDE
BY THERMAL ALD**

APPENDIX A2. *In Situ* Study of Titanium Carbide by Thermal ALD*

*The results shown in this appendix are preliminary findings, with further experiments and analysis required before drawing conclusions.

Eric C. Stevens,[†] Gregory N. Parsons^{*,†}

[†]Department of Chemical and Biomolecular Engineering, North Carolina State University, 911 Partners Way, Raleigh NC 27695

A2.1 Experimental

All ALD experiments were conducted in a homemade, hot wall, reactor operating in the viscous flow regime. All reactor lines were resistively heated to ~150–170 °C to prevent precursor condensation during the delivery process. The deposition chamber (~3.5 cm diameter 316 stainless steel tube) was resistively heated using a proportional–integral–derivative (PID) temperature controller. The deposition temperatures tested were 200–350 °C. The reactor utilized *in situ* quartz crystal microbalance (QCM) to monitor the process during ALD processing. The upper temperature limit of 350 °C was established due to stability and material constraints of the QCM apparatus. Research grade nitrogen (99.999%, Machine & Welding Supply Company) was further purified (Entegris Gate-Keeper) and used as the carrier and purge gas at an operating pressure of ~1.5 Torr.

A2.1.1 ALD Precursors and Delivery

Titanium tetrachloride (TiCl₄) and trimethyl aluminum (Al(CH₃)₃, or TMA) were purchased from Strem and used as received. The TiCl₄ and TMA vessels were not heated, but the

delivery lines were maintained at ~ 170 °C. TiCl_4 and TMA were delivered into the deposition chamber from separate delivery lines using N_2 as the carrier gas.

A2.1.2 *In situ* QCM

For QCM analysis, Au-coated quartz crystals (Inficon, 6 MHz AT-cut quartz, 0.55” diameter, unpolished) were used as received. A commercial QCM assembly (Cool Drawer, Inficon) was specially modified to allow a constant flow of ~ 0.3 Torr of N_2 to purge the back side of the quartz crystal. This modification prevented unwanted deposition during ALD processing on the electrode contacts. The modified QCM assembly was inserted into the ALD reactor, with the sensor head containing the QCM crystal positioned in the center of the deposition chamber. Before starting deposition runs, the QCM sensor was held in the reactor for $\simeq 4$ to 6 hours under dry N_2 flow at the operating pressure of 1.5 Torr to allow the sensor to reach thermal equilibrium at the desired deposition temperature. Thermal equilibrium was reached after changes in steady-state QCM frequency were less than ~ 0.5 Hz over 30 minutes. For QCM experiments, Mass change measurements were recorded using an Inficon SQM-160 controller at a sampling rate of 10 Hz.

A2.2 Results and Discussion

To understand the TiCl_4/TMA reaction and associated byproducts as a function of temperature, thermodynamic modeling was utilized via HSC Chemistry 7.1 software. Figure A2.1 shows the predicted species at equilibrium as a function of temperature. Initial species were set to 5 moles N_2 , 1 mole $\text{TiCl}_{4(\text{g})}$, and 1 mole $\text{Al}(\text{CH}_3)_3(\text{g})$ in a closed system, with constant pressure of 2 mbar. The temperature was increased from 25 to 400 °C, with the Gibb free energy minimized at each step. Any species with an equilibrium concentration less than 1 mmol was not shown.

At room temperature, $\text{TiCl}_{4(\text{g})}$ reacts with $\text{Al}(\text{CH}_3)_3(\text{g})$ to give $\text{TiC}_{(\text{s})}$, $\text{CH}_{4(\text{g})}$, and $\text{AlCl}_{3(\text{s})}$. At temperatures above ~ 100 °C, $\text{AlCl}_{3(\text{s})}$ can react to form volatile $\text{Al}_2\text{Cl}_{6(\text{g})}$, which subsequently reacts to form $\text{AlCl}_{3(\text{g})}$ at temperatures beyond ~ 150 °C. It is important to note that this model is for a

closed system, which does not consider the removal of species. In an ALD reaction, byproducts are removed after each half-reaction.

From preliminary thermodynamic modeling results shown in Figure A2.1, deposition temperatures lower than 100 °C were not considered. Due to precursor condensation and delivery optimization, the lower temperature limit tested was 200 °C. Figure A2.2 shows the resulting mass change (from QCM) at 250, 300, and 350 °C during 200 cycles of $\text{TiCl}_4/\text{N}_2/\text{TMA}/\text{N}_2$, with dose times 1s/30s/1s/30s. The averaged mass change per cycle over 200 cycles was 80, 50, and 8 $\text{ng}/\text{cm}^2/\text{cy}$ at 350, 300, and 250 °C, respectively.

Figure A2.3 shows magnified images from Figure A2.2 for depositions at a) 350, b) 300, and c) 250 °C where resulting mass change behavior (from QCM) from individual dosing can be observed. At 350 °C, TiCl_4 exposures resulted in a mass increase of $\sim 85 \text{ ng}/\text{cm}^2/\text{cy}$, while TMA doses resulted in a mass loss of $\sim 5 \text{ ng}/\text{cm}^2/\text{cy}$. At 300 °C, TiCl_4 exposures resulted in a mass increase of $\sim 70 \text{ ng}/\text{cm}^2/\text{cy}$, while TMA doses resulted in a mass loss of $\sim 20 \text{ ng}/\text{cm}^2/\text{cy}$. At 250 °C, TiCl_4 exposures resulted in a mass increase of $\sim 16 \text{ ng}/\text{cm}^2/\text{cy}$, while TMA doses resulted in a mass loss of $\sim 8 \text{ ng}/\text{cm}^2/\text{cy}$.

To better understand dose saturation behavior, 5 consecutive sub-doses (i.e., $(\text{TiCl}_4/\text{N}_2) \times 5 / (\text{TMA}/\text{N}_2) \times 5$) of each precursor were investigated as a function of deposition temperature. Figure A2.4 shows magnified images representative of the mass change behavior over at least 50 cycles of 5 sub-doses for depositions at a) 350, b) 300, c) 250, and d) 200 °C. The resulting average mass change during each of the 5 TiCl_4 and TMA sub-doses is given in Figure A2.5 a) and b), respectively. In general, the mass increase during TiCl_4 doses approached saturation after two doses at all deposition temperatures. The first TiCl_4 dose for depositions at 350 and 300 °C resulted in a mass gain of 85 - 95 $\text{ng}/\text{cm}^2/\text{cy}$, while at 250 and 200 °C, the mass

gain was 50 - 60 ng/cm²/cy. For TMA doses, depositions at 300, 250, and 200 °C resulted in an overall mass loss, while at 350 °C dosing resulted in a mass gain.

A summary of the average mass change during TiCl₄ doses to that observed during TMA doses was calculated and presented as a function of deposition temperature in Figure A2.6. For growth at deposition temperatures of 200 and 250 °C, the ratio was 2 – 3, while at 300 and 350 °C the ratio increased to ~15 and 23, respectively. Based on previous findings, for deposition temperatures ≥ 300 °C, aluminum was found in deposited TiC films by XPS and increased with increasing temperature.¹⁻³ Previous studies also have shown that TMA degrades at temperatures ≥ 300 °C.^{4,5} Thus, the ratio of mass change during TiCl₄ and TMA dosing is likely related to the amount of Al incorporated in the films, in addition to the extent of TiCl₄ dissociative surface absorption.

Using equation (A2.1), the average mass change (Δm) from Figures A2.2 and A2.4 and the density of TiC (bulk TiC = 4.93 g/cm³)⁶, can be used to estimate the expected growth rate per cycle (GPC), in units of nm/cycle:

$$GPC = \Delta m \times \rho^{-1} \quad (A2.1)$$

Using equation (A2.1), the GPC at 350, 300, and 250 °C for single doses of TiCl₄/TMA was calculated to be 0.16, 0.10, and 0.02 nm/cy, respectively. For 5 sub-doses of TiCl₄/TMA, the calculated GPC was 0.29, 0.25, 0.14, and 0.08 nm/cy for depositions at 350, 300, 250, and 200 °C, respectively.

The estimated thickness of one monolayer of TiC can be calculated using equation (A2.2):

$$t_m = [MW / (N_A \times \rho)]^{1/3} \quad (A2.2)$$

where MW, N_A, and ρ are the molecular weight (TiC = 59.89 g/mol), Avagadro's number (6.022 $\times 10^{23}$ molecules/mol), and the density of TiO₂ (bulk TiC = 4.93 g/cm³). Using equation (A2.2),

the ideal TiC monolayer thickness was found to be ~ 0.27 nm. With the GPC values from equation A2.1, the average GPC can be rewritten in terms of monolayers grown per cycle. The GPC at 350, 300, and 250 °C for single doses of TiCl₄/TMA was calculated to be 0.60, 0.37, and 0.06 monolayer/cy, respectively. For 5 sub-doses of TiCl₄/TMA, the calculated GPC was 1.0, 0.90, 0.52, and 0.30 monolayer/cy for depositions at 350, 300, 250, and 200 °C, respectively. The GPC calculations above assume the bulk density of TiC, which is likely to vary as a function of deposition temperature and corresponding aluminum incorporation.

A2.3 Figures for Appendix A2

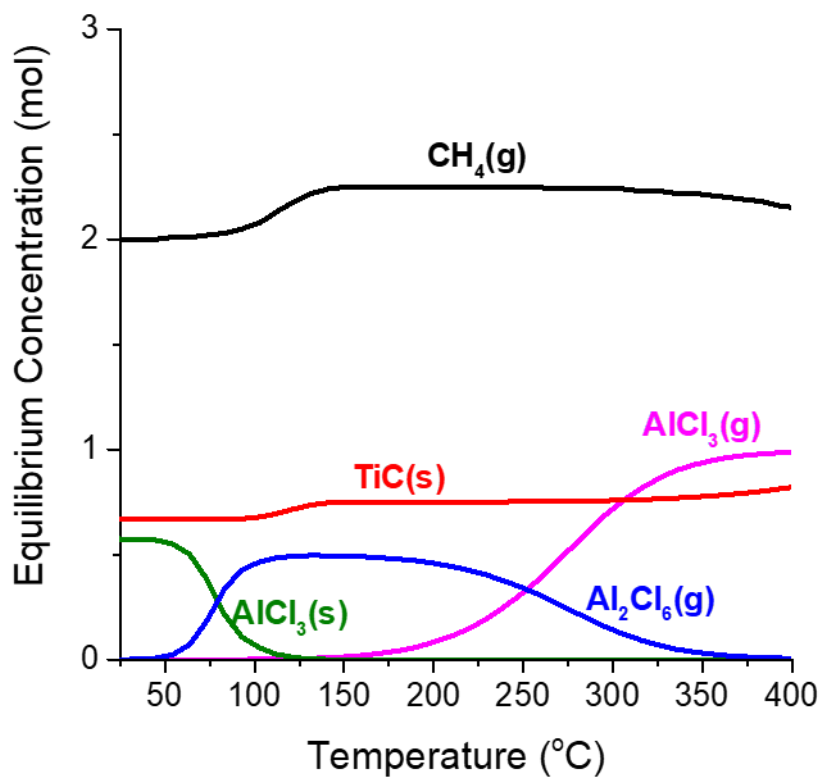


Figure A2.1: Predicted equilibrium species from the reaction of 1 mole of $\text{TiCl}_{4(g)}$ and 1 mole of $\text{Al}(\text{CH}_3)_3(g)$ from temperatures ranging 25 – 400 °C and pressure of 2 mbar. Only species with an equilibrium concentration greater than 1 mmol are shown. The following are the species expected at equilibrium, with their anticipated phase indicated as either (g) for gas or (s) for solid: $\text{CH}_4(s)$ (black), $\text{TiC}(s)$ (red), $\text{AlCl}_3(g)$ (pink), $\text{AlCl}_3(s)$ (green), and $\text{Al}_2\text{Cl}_6(g)$ (blue).

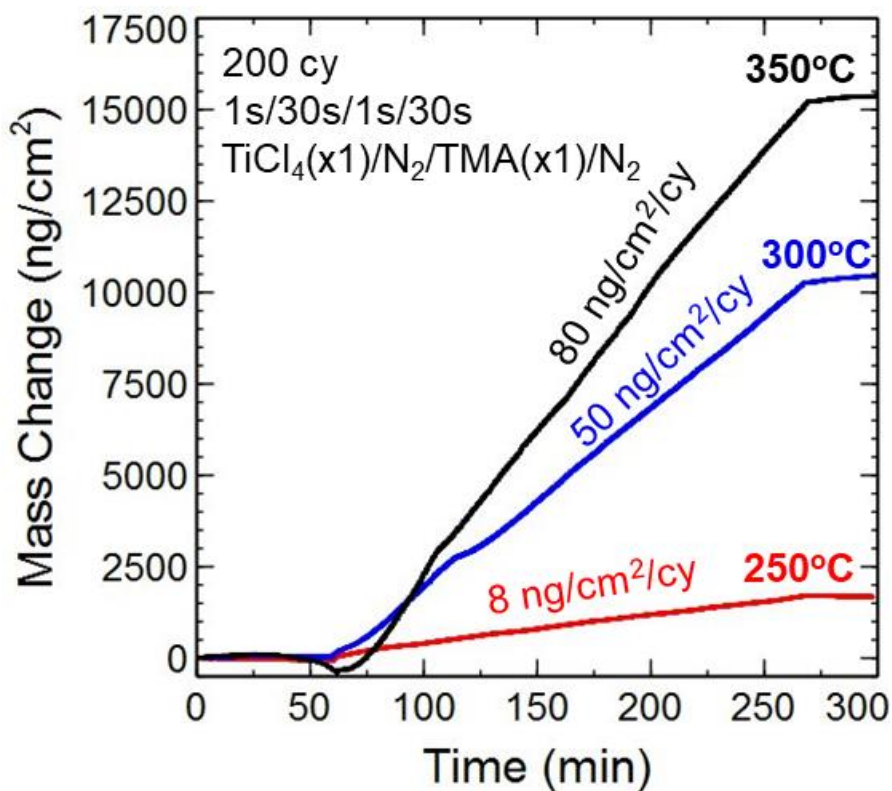


Figure A2.2: QCM results showing the mass change (ng/cm²) versus process time (minutes) for 200 cycles of TiCl₄/N₂/TMA/N₂, with dose times 1s/30s/1s/30s, at 350 °C (black), 300 °C (blue), and 250 °C (red). For each temperature, the average mass change per cycle is given above the corresponding curve in units of ng/cm²/cy.

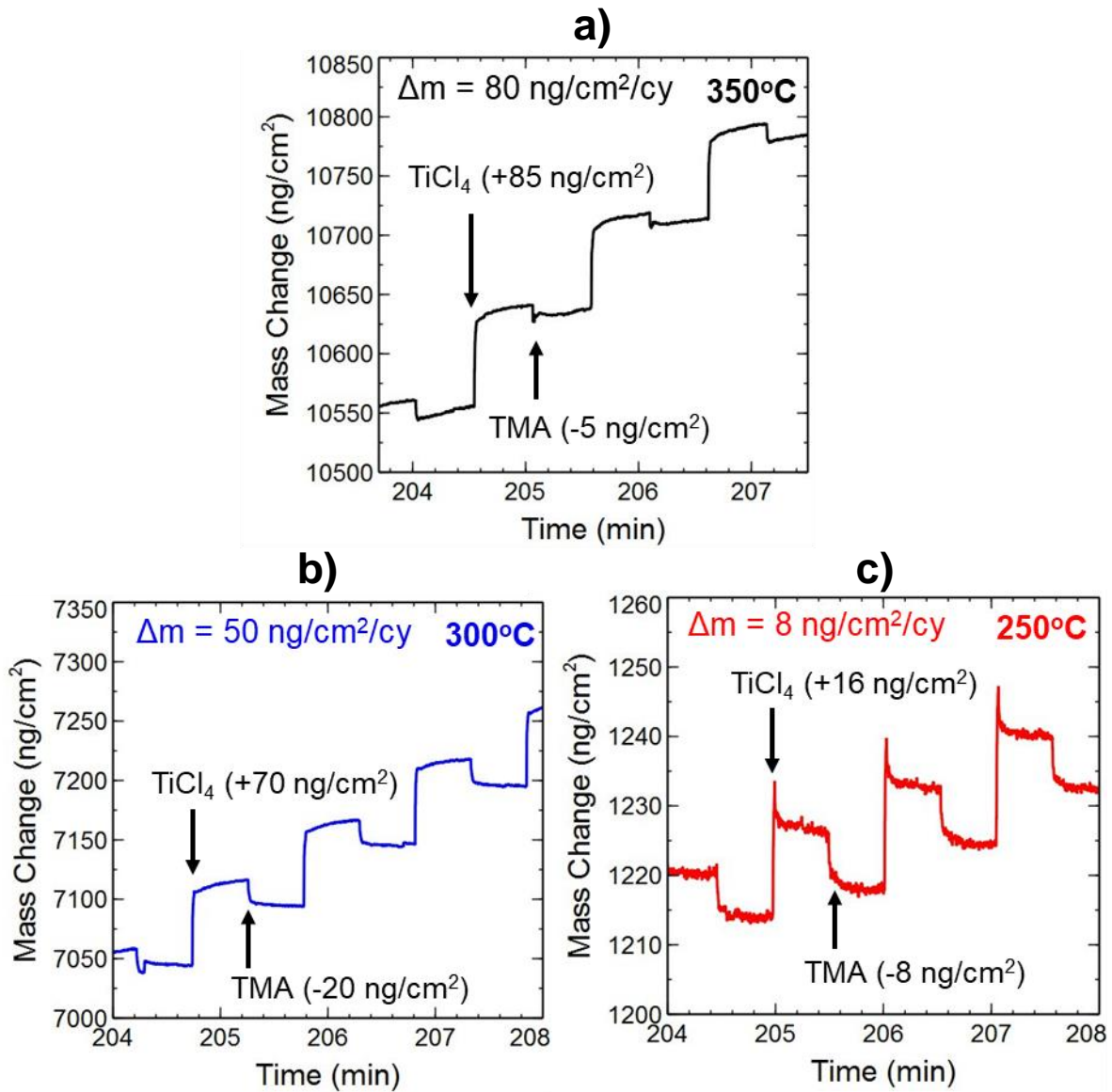


Figure A2.3: QCM results showing the magnified mass change (ng/cm^2) versus process time (minutes) from Figure A2.2 for 200 cycles of $\text{TiCl}_4/\text{N}_2/\text{TMA}/\text{N}_2$, with dose times 1s/30s/1s/30s, at a) 350°C (black), b) 300°C (blue), and c) 250°C (red). For each deposition temperature, a representative TiCl_4 and TMA dose are shown with arrows, along with the average mass change.

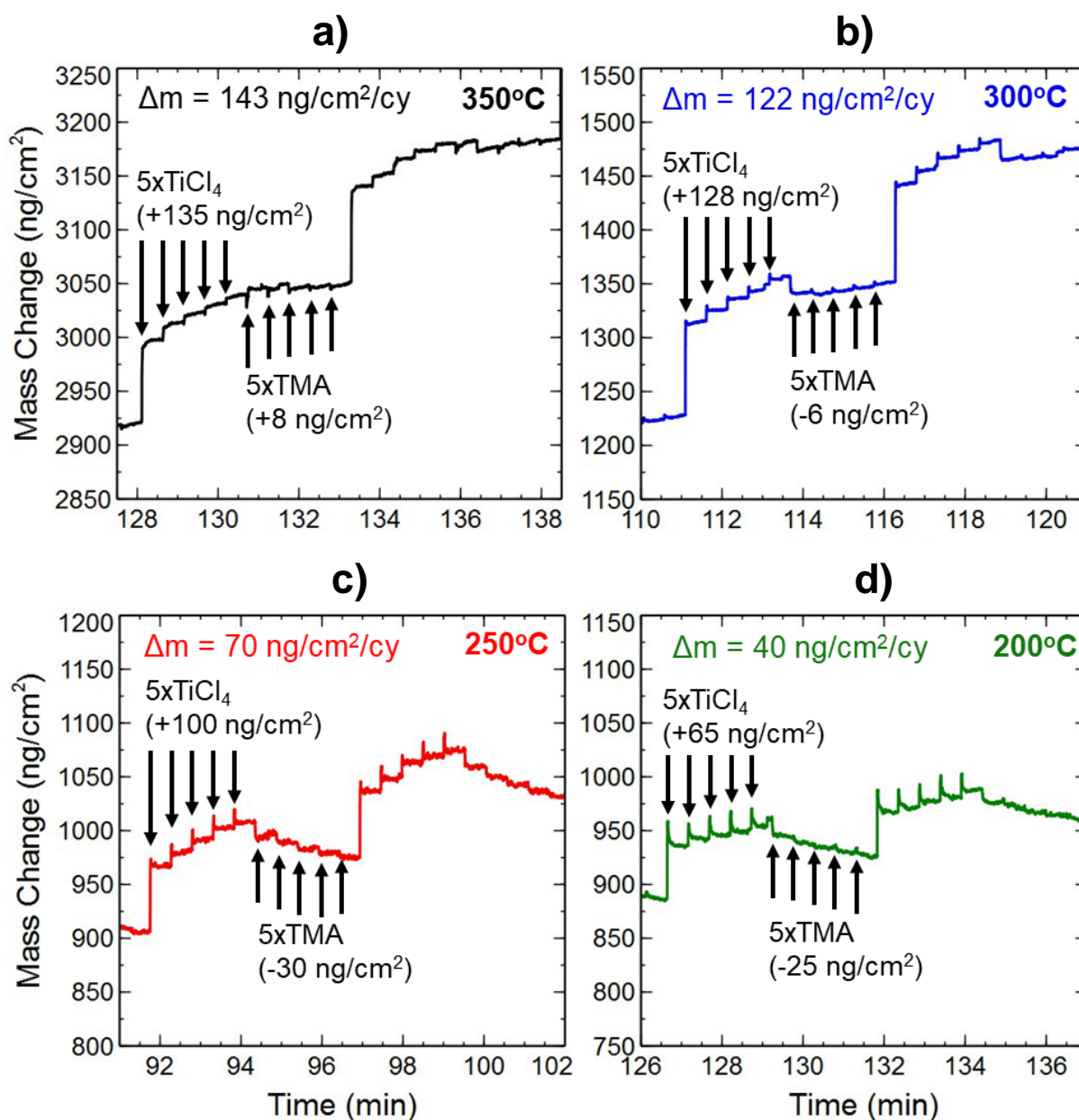


Figure A2.4: QCM results showing the mass change (ng/cm²) versus process time (minutes) for 5 sub-doses, i.e., (TiCl₄/N₂)×5/(TMA/N₂)×5, with dose times (1s/30s)×5/(1s/30s)×5, at a) 350 °C (black), b) 300 °C (blue), c) 250 °C (red), and d) 200 °C (green). For each deposition temperature, representative TiCl₄ and TMA doses are indicated with arrows, along with the cumulative mass change.

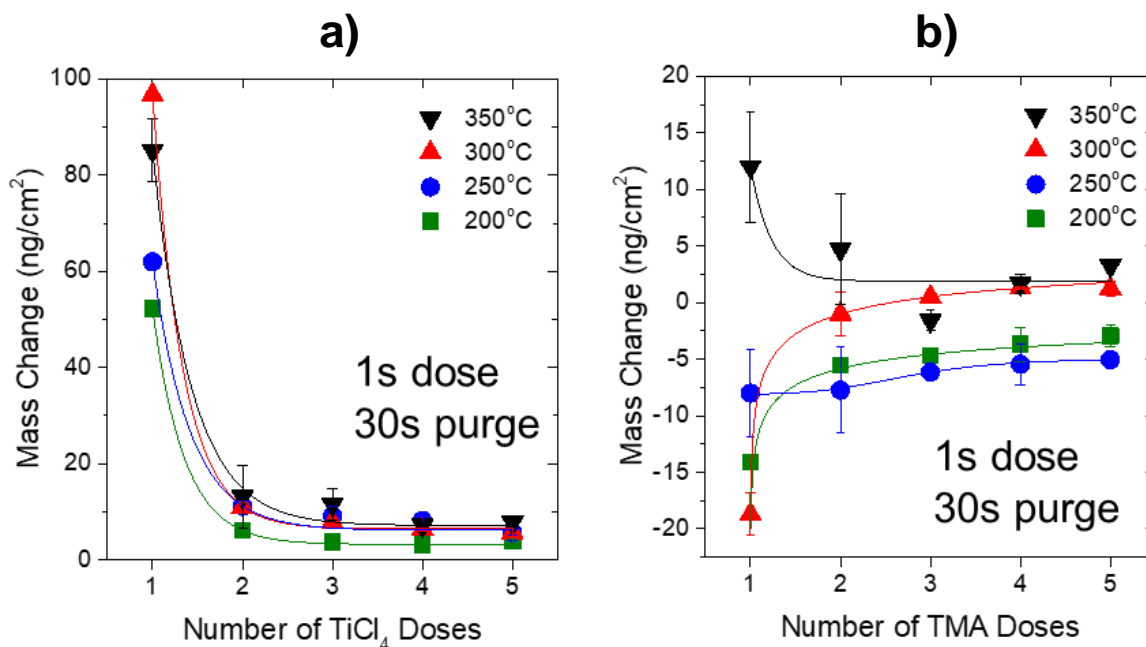


Figure A2.5: QCM results showing the average mass change (ng/cm²) versus number of a) TiCl₄ of b) TMA sub-doses. Data were averaged from over at least 50 cycles of (TiCl₄/N₂)×5/(TMA/N₂)×5, with dose times (1s/30s)×5/(1s/30s)×5, at 350 °C (black upside-down triangles), 300 °C (red triangles), 250 °C (blue circles) and 200 °C (green squares).

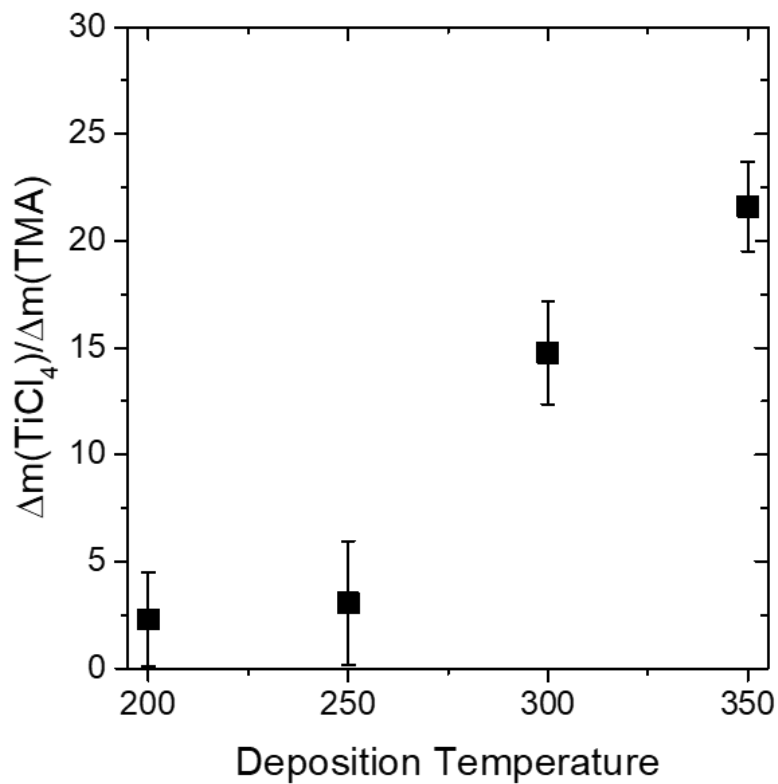


Figure A2.6: Ratio of the averaged mass changes (absolute value), obtained from QCM, during 5 sub doses of TiCl_4/TMA at 200, 250, 300, and 350 °C. Data were averaged from over at least 50 cycles of $(\text{TiCl}_4/\text{N}_2) \times 5 / (\text{TMA}/\text{N}_2) \times 5$, with dose times $(1\text{s}/30\text{s}) \times 5 / (1\text{s}/30\text{s}) \times 5$.

A2.4 References

- (1) Xiang, J.; Ding, Y.; Du, L.; Xu, C.; Li, T.; Wang, X.; Li, J.; Zhao, C. Investigation of N Type Metal TiAlC by Thermal Atomic Layer Deposition Using TiCl_4 and TEA as Precursors. *ECS J. Solid State Sci. Technol.* **2016**, 5 (5), P299–P303.
- (2) Xiang, J.; Ding, Y.; Du, L.; Li, J.; Wang, W.; Zhao, C. Growth Mechanism of Atomic-Layer-Deposited TiAlC Metal Gate Based on TiCl_4 and TMA Precursors. *Chinese Phys. B* **2016**, 25 (3), 37308.
- (3) Xiang, J.; Zhang, Y.; Li, T.; Wang, X.; Gao, J.; Yin, H.; Li, J.; Wang, W.; Ding, Y.; Xu, C.; Zhao, C. Investigation of Thermal Atomic Layer Deposited TiAlX (X = N or C) Film as Metal Gate. *Solid State Electron.* **2016**, 122, 64–69.
- (4) Puurunen, R. L.; Lindblad, M.; Root, A.; Outi I. Krause, A. Successive Reactions of Gaseous Trimethylaluminium and Ammonia on Porous Alumina. *Phys. Chem. Chem. Phys.* **2001**, 3 (6), 1093–1102.
- (5) Yamashita, S.; Watanuki, K.; Ishii, H.; Shiba, Y.; Kitano, M.; Shirai, Y.; Sugawa, S.; Ohmi, T. Dependence of the Decomposition of Trimethylaluminum on Oxygen Concentration. *J. Electrochem. Soc.* **2011**, 158 (2), H93.
- (6) Haynes, W. M. *Haynes, W. M. Handbook of Chemistry and Physics 96th Edition. Taylor and Francis Group, 2015, 96th ed.; 2015.*